



---

MOIST RAYLEIGH BÉNARD  
CONVECTION

---

**Prasanth Prabhakaran**



# Moist Rayleigh Bénard Convection

## Dissertation

for the award of the degree  
“Doctor of Philosophy”  
Division of Mathematics and Natural Sciences  
at the Georg-August-Universität Göttingen

within the doctoral degree program

Physics of Biological and Complex Systems  
of the Göttingen Graduate School of Neurosciences, Biophysics, and  
Molecular Biosciences (GGNB)  
of the Georg-August University School of Sciences (GAUSS)

submitted by

**Prasanth Prabhakaran**  
from Chennai, India  
Göttingen, 2018

## THESIS COMMITTEE:

**Prof. Dr. Eberhard Bodenschatz (Referee)**

Department of Fluid Physics, Pattern Formation and Biocomplexity  
Max Planck Institute for Dynamics and Self-Organization

**Prof. Dr. Andreas Tilgner (Co-Referee)**

Institute of Geophysics  
Georg-August-University Göttingen

**Prof. Dr. Jens Niemeyer**

Institute of Astrophysics  
Georg-August-University Göttingen

## MEMBERS OF THE EXAMINATION BOARD:

**Prof. Dr. Eberhard Bodenschatz (Referee)**

Department of Fluid Physics, Pattern Formation and Biocomplexity  
Max Planck Institute for Dynamics and Self-Organization

**Prof. Dr. Andreas Tilgner (Co-Referee)**

Institute of Geophysics  
Georg-August-University Göttingen

## OTHER MEMBERS OF THE EXAMINATION BOARD:

**Prof. Dr. Jens Niemeyer**

Institute of Astrophysics  
Georg-August-University Göttingen

**Dr. Michael Wilczek**

Theory of Turbulent Flows  
Max Planck Institute for Dynamics and Self-Organization

**Prof. Dr. Ulrich Parlitz**

Biomedical Physics Group  
Max Planck Institute for Dynamics and Self-Organization

**Prof. Dr. Marcus Müller**

Institute for Theoretical Physics  
Georg-August-University Göttingen

Date of oral examination: 16.10.2018

# Affidavit

Hereby, I declare that the presented thesis has been written independently and with no other sources and aids than quoted.

Parts of this thesis and few figures have been published in the journal article:

**Prabhakaran, P.**, Weiss, S., Krekhov, A., Pumir, A., & Bodenschatz, E. (2017). “*Can hail and rain nucleate cloud droplets?*”. *Physical review letters*, 119(12), 128701.

Göttingen, 24.08.2018



# Contents

<b>Abstract</b>	<b>1</b>
<b>1 Introduction</b>	<b>3</b>
1.1 Motivation . . . . .	3
1.2 Rayleigh-Bénard convection . . . . .	5
1.3 Pattern formation . . . . .	7
1.4 Secondary Nucleation in Clouds . . . . .	9
1.5 Overview . . . . .	11
<b>2 Experimental Setup</b>	<b>13</b>
2.1 Apparatus . . . . .	13
2.2 Phase diagram . . . . .	17
2.3 Filling Procedure . . . . .	19
2.4 Flow visualization . . . . .	20
2.4.1 Shadowgraphy . . . . .	22
2.4.2 Beam splitter setup . . . . .	22
2.4.3 Mirror unit . . . . .	22
<b>3 Pattern Formation in Moist Convection</b>	<b>27</b>
3.1 Experimental Details . . . . .	27
3.2 Thick Cell . . . . .	29
3.2.1 Transients . . . . .	29
3.2.2 Statistically Steady State . . . . .	32
3.2.2.1 Small $\Delta T$ - Low Thermal Driving . . . . .	34
3.2.2.2 Large $\Delta T$ - High Thermal Driving . . . . .	39
3.2.3 Spectral Analysis . . . . .	42
3.2.4 Steady State Statistics . . . . .	45
3.3 Theoretical Considerations . . . . .	49
3.3.1 Surface tension and gravity . . . . .	49
3.3.2 Marangoni Forces and Gravity . . . . .	51

3.3.3	Evaporation-condensation effects . . . . .	53
3.4	Discussion: Thick Cell . . . . .	55
3.5	Thin Cell . . . . .	57
3.6	Medium Cell . . . . .	64
3.7	Discussion: Thin, Medium and Thick Cell . . . . .	67
3.8	Summary . . . . .	73
<b>4</b>	<b>Can Rain and Hail Nucleate Cloud Droplets?</b>	<b>75</b>
4.1	Laboratory Atmosphere . . . . .	75
4.2	Experimental Observations . . . . .	76
4.3	Homogeneous Nucleation . . . . .	82
4.3.1	Classical Nucleation Theory (CNT) . . . . .	83
4.3.2	Comparison With The Experiment . . . . .	86
4.3.3	Heat Transfer From a Falling Drop . . . . .	86
4.4	Clouds in a Lab . . . . .	89
4.5	Atmospheric Implications . . . . .	93
4.5.1	Earth's Atmosphere . . . . .	93
4.5.2	Deep Convective Systems . . . . .	96
4.5.3	Secondary Nucleation in Clouds . . . . .	97
4.6	Conclusion . . . . .	99
<b>5</b>	<b>A Secondary Ice Nucleation Mechanism in Clouds</b>	<b>101</b>
5.1	Experimental Setup . . . . .	101
5.2	Experimental Observations . . . . .	104
5.3	Wake Analysis . . . . .	108
5.3.1	Warm conditions . . . . .	108
5.3.2	Droplet activation . . . . .	111
5.3.3	Cold conditions . . . . .	119
5.3.3.1	Ice nucleation . . . . .	119
5.3.3.2	Droplet activation . . . . .	121
5.4	Atmospheric Implications . . . . .	123
5.4.1	Secondary Ice Nucleation . . . . .	123
5.4.2	Cloud Engineering . . . . .	129
5.5	Conclusion . . . . .	130
<b>6</b>	<b>Additional Observations: Drop Fragmentation, Leidenfrost Patterns and Boundary Layer Visualization</b>	<b>131</b>
6.1	Drop Fragmentation . . . . .	131
6.2	Leidenfrost Drops . . . . .	134

---

6.3	Boundary Layer Visualization . . . . .	140
<b>7</b>	<b>Summary and Outlook</b>	<b>147</b>
7.1	Summary . . . . .	147
7.2	Outlook . . . . .	150
7.2.1	Secondary Nucleation . . . . .	150
7.2.2	Laboratory-Scale Clouds . . . . .	150
7.2.3	Moist Pattern Formation . . . . .	150
	<b>List of Figures</b>	<b>153</b>
	<b>Bibliography</b>	<b>163</b>
	<b>Acknowledgment</b>	<b>171</b>
	<b>Curriculum Vitae</b>	<b>173</b>



# Abstract

Clouds play an important yet poorly understood role in weather forecasting and climate change. The objective in the present work is to establish a laboratory-scale experiment for simulating clouds in the Earth's atmosphere. The experiments are conducted in a moist Rayleigh-Bénard convection (RBC) system. In this thesis we investigate three different problems associated with moist convection.

In the first problem, we investigate the effects of phase change on the Rayleigh Taylor instability (RTI) in a thin film. We use Sulphur Hexafluoride ( $\text{SF}_6$ ) as the working fluid at conditions where  $\text{SF}_6$  exists in both liquid and vapor phases. We report on the patterns formed at the cold top plate due to the condensation of moist  $\text{SF}_6$  from the bottom plate. We observe two different regimes in this experiment. In regime 1, the bottom plate was covered with a layer of liquid  $\text{SF}_6$ . We show that the condensed liquid layer at the top plate forms hexagonal patterns if the imposed temperature difference is sufficiently large. These patterns drip periodically into the liquid pool at the bottom plate. In regime 2, we eliminate the liquid  $\text{SF}_6$  layer on the bottom plate by adjusting the pressure in the convection cell. We show that the liquid layer at the top plate is stable if the evaporative effects below the liquid layer is sufficiently large. We show that under appropriate conditions, the liquid layer at the top plate form hexagonal surface pattern with nearly no dripping.

In the second problem, we report results from a moist convecting cloud chamber with a  $\text{SF}_6$ -Helium binary mixture as the working fluid, where  $\text{SF}_6$  models the moist component in the Earth's atmosphere (water vapor), and He models the dry components (Nitrogen, Oxygen etc.). We observe that under appropriate conditions, micro-droplets nucleate in the wake of a large cold drop falling through a supersaturated  $\text{SF}_6$ -He atmosphere. We show that the micro-droplets are formed in the cold wake of the large drop through homogeneous nucleation. We extend our results to the atmospheric clouds, and our model calculations suggest that under supersaturated conditions, falling hailstones/graupel and large rain drops may significantly enhance the nucleation of cloud droplets in their wake. We also show that under appropriate conditions a stable horizontal layer of cloud micro-droplets was established in the convection chamber. The layer was formed between the supersaturated and sub-saturated volumes in the chamber.

In the third problem, we examine the possibility of a novel secondary ice nucleation mechanism in deep convective clouds. These experiments are inspired by the wake nucleation experiments in the SF<sub>6</sub>-He binary mixture. The experiment is conducted in a cloud chamber using a mixture of air and water vapor as the working fluid. In this experiment, we investigate the heterogeneous nucleation of micro-droplets and ice crystals in the wake of a warm drop. We show that the evaporative supersaturation attained in the wake of the warm drop was sufficient to activate water droplets and ice nuclei. We model the flow field behind the warm drop and use that to calculate the growth of a droplet from a nucleus to an activated droplet behind the drop. We extend this model to atmospheric clouds and conduct a detailed study on various parameters that affects the activation of water droplets and ice crystals. Our analysis shows that in the wake of a hailstone/graupel in the wet growth regime, the ice crystal concentration increases from 1 per liter to 5 per liter at a temperature of  $-15^{\circ}\text{C}$ . This may partly explains the enhanced ice concentrations observed in deep convective systems. Based on these results we propose a new technique for cloud engineering.

We also conduct a preliminary investigation of three additional problems. First, we examine the role of humidity in the fragmentation of drops during free fall conditions. Our observations suggest that in a supersaturated environment, the critical Weber number for a drop to become unstable may increase. Similarly, in a sub-saturated environment the critical Weber number may decrease. Second, we examine the dynamics of chimney formation in Leidenfrost drops of various sizes. We observe that the number of chimneys in a drop increases with the size of the drop. Above a critical size, the chimneys also grow in size by merging with other chimneys. Third, we propose a new technique for visualizing the flow structure of the diffusive wall layer in RBC using Helium bubbles.

# 1 Introduction

Rain and clouds have fascinated mankind for millennia. Artists and writers impressed by their visual and auditory beauty have used them extensively in their works. For instance, in a Sanskrit poem “Meghaduta” (Cloud Messenger) by Kalidasa, an exiled bureaucrat sends a message to his wife with the aid of passing clouds [1, 2]. Different cultures attribute different significances to rain. Civilizations and cultures world over have adapted their habits/activities to rainfall patterns (see [3] for details). In fact, in most cultures throughout history, rainfall is considered as a gift of God(s) owing to their agrarian societal heritage [3]. In India, there is a separate season associated with the onset of rainfall due to the seasonal reversing of the wind directions along the southwest coast and is called the monsoon season. The agricultural practices, religious festivals, and even the school schedules are influenced by the rainfall patterns and their associated seasonal variations. The beauty and moods of the monsoon rains are described well by the “Malhaar” (loosely translates to monsoon) raaga - a melodic note in the Indian classical music [4].

In the present day, clouds and rainfall are topics of immense scientific interest due to their profound role in climate change and weather prediction [5–9]. An Accurate forecast of rainfall patterns is especially important for tropical countries. For instance, in a country like India, where agriculture is an important part of the economy, the accurate prediction of the monsoons can have a significant impact on the economic health of the country [10, 11].

## 1.1 Motivation

Clouds are an example of a complex system with interactions between flow turbulence, microphysics (thermodynamics, phase transition) and radiation [8, 9]. The scales involved in the underlying turbulent flow range from about a millimeter to more than a kilometer. In contrast, the size of cloud droplets range from about a micrometer to a few millimeters [12]. The large scale dynamics of the flow dictate the dilution rate of clouds. And latent heat released at the small scales can influence the evolution of the large scale features in convective clouds [9]. Due to these complex interactions, clouds

are difficult to model, and thus are marked as one of the biggest uncertainties in weather and climate modelling [6, 12, 13]. Clouds are listed as one of the “most urgent scientific problems requiring attention” according to Intergovernmental Panel on Climate Change (IPCC 1996) [12, 14]. An Estimate suggests that an increase in the short wave-cloud forcing can mitigate the effects of greenhouse gases since industrial revolution [1, 15].

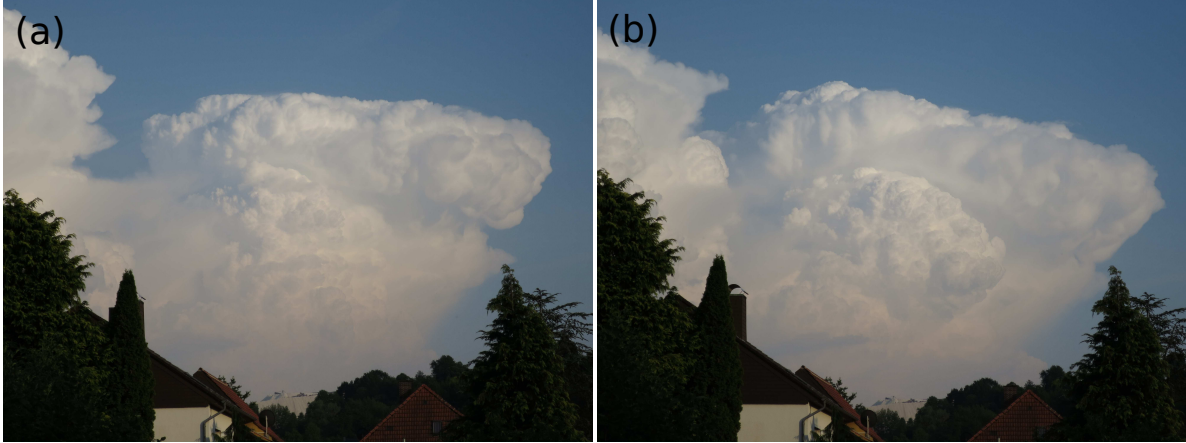


**Figure 1.1:** (a) Developing cumulonimbus cloud near Goettingen. Photo taken on July 4, 2015 at 17:53 UTC. (b) Same cloud as in (a) but four minutes later. Image courtesy - Dr. Oliver Schlenzcek, MPIDS, Goettingen.

A cloud is defined as an aggregate of particles of water (liquid/solid) in the atmosphere [16]. They occur in a variety of shapes and sizes, and play an important role in atmospheric circulation. For instance, the cumulus or cumulonimbus clouds play an important role in tropical convection. These clouds act as a conveyor belt, transporting water vapor and heat across the troposphere [1]. Figure 1.1 shows a developing cumulonimbus cloud. Cloud formation begins with the ascent of an air parcel along slopes of a hill/mountain or in the form of an isolated plume from a hot patch on the surface of the Earth [17]. As it rises, its temperature decreases due to adiabatic expansion. At a certain height, the rising parcel reaches its dew point temperature. This is called the cloud condensation level (CCL) [17]. Additional ascent results in the nucleation of cloud droplets and ice crystals. In the absence of ice particles, the cloud droplets grow initially through condensation of water vapor on the droplets [18]. Above a critical diameter, these droplets grow through collision and coalescence with other droplets [12]. The later stages of growth are strongly influenced by the fine scale structure of the underlying turbulence as it plays an important role in initiating precipitation in warm clouds (clouds with cloud top temperature above  $0^{\circ}\text{C}$ ) [12].

The formation of cloud droplets and ice particles releases latent heat into the cloud system which may fuel further ascent of the cloud. This off-source buoyancy generated from the latent heat may influence the dilution rate of these clouds by altering the large scale coherent motions in them [9]. These complex dynamics and the large separation

between scales ( $\mu\text{m}$  - km) have restricted the number of laboratory experiments in cloud research. As a consequence, most of the available data are based on field campaigns and numerical simulations.

Laboratory-scale experiments can be and are conducted to study individual features in a cloud. In a recent laboratory experiment, the effect of latent heat release on entrainment in a cumulus cloud was investigated [9]. They found that the off-source addition of buoyancy disrupts the coherent structures in the cumulus cloud flow, and this shuts off the entrainment process in the flow. Further details on these experiments and related numerical simulations to understand the entrainment behavior in a cumulus cloud are discussed in [19]. Experiments were conducted to investigate the effect of aerosol concentration on the size distribution in a turbulent moist convection chamber [20]. They showed that the mean droplet diameter and the width of the droplet size distribution decreases as the aerosol concentration was increased. These studies show that increased aerosol concentration may delay/suppress precipitation formation in polluted clouds until ice nucleation is initiated. Similar experiments on the micro-physical aspects of clouds such as the activation of cloud nuclei are also conducted in moist wind tunnels [21]. Ice nucleation and secondary ice production experiments are also conducted in static cloud chambers, e.g., AIDA [22]. An overview on the available laboratory scale cloud research facility is presented in [23].

The objective of the present work is to establish a reliable laboratory-scale cloud model to understand the formation of clouds in a clean environment in the absence of aerosols. Droplets can nucleate on the surface of a nuclei (heterogeneous nucleation) or through random aggregation of molecules (homogeneous nucleation) under appropriate conditions. In the Earth's atmosphere, water droplets are nucleated by heterogeneous nucleation. In our experimental model we eliminate the role of nuclei, and hence rely on homogeneous nucleation for forming new droplets. We use Sulphur Hexafluoride ( $\text{SF}_6$ ) and Helium (He) as the working fluid in the experiment. We operate the experiment close to the critical line of  $\text{SF}_6$ -He mixture to favour homogeneous nucleation. Later, the observations from the  $\text{SF}_6$ -He environment were extended to atmospheric conditions with aerosols. The experiments were conducted in a Rayleigh-Bénard convection (RBC) setup. The key construction details are discussed in chapter 2

## 1.2 Rayleigh-Bénard convection

The convective processes in the Earth's atmosphere are driven by the insolation received from the Sun. The solar radiation heats up the Earth's surface and triggers turbulent convection that transports water vapor across the atmosphere. As was stated in the previous section, we use a RBC experiment to create our laboratory atmosphere with  $\text{SF}_6$  and He as the working fluids. A RBC experiment consists of a fluid layer confined

between two horizontal plates separated vertically by a distance  $H$ . The top plate is cooled and the bottom plate is heated. The imposed temperature gradient across the top (cold) and bottom (hot) plate drives the convective flow in the experiment. Figure 1.2 (a) shows a schematic of a classical RBC experiment. If the fluid properties in the convection cell do not vary significantly with temperature, then the RBC system is characterized by two parameters: Rayleigh number  $Ra = \frac{g\alpha\Delta TH^3}{\nu\kappa}$ , which represents the ratio between buoyancy force and the diffusive force, and Prandtl number  $Pr = \frac{\nu}{\kappa}$ , which represents the ratio between the thermal and momentum diffusion time scales where  $g$  is the magnitude of acceleration due to gravity,  $\alpha$  is the coefficient of thermal expansion,  $\Delta T$  is the temperature difference across the convection cell,  $H$  is the height of the convection cell and  $\nu$  ( $\kappa$ ) is the kinematic viscosity (thermal diffusivity) of the working fluid. At  $Pr = 1$ , convection is initiated at  $Ra \approx 1708$ , and above  $Ra \sim 10^5$  the flow is considered turbulent. At sufficiently low  $Ra$ , the velocity field consists of periodic up-welling and down-welling regions that represent the convection rolls. As  $Ra$  increases, the flow field becomes chaotic, thus disturbing the periodic arrangement of the convection rolls. Further increase in  $Ra$  renders the flow turbulent, and the heat is transported between the two plates through plumes originating from the boundary layers at the two plates. These plumes are transported along the upwelling and down-welling regions in the flow field that represents the large scale circulation (LSC). The LSC has similar characteristics as the convection rolls in the low  $Ra$  regime [24].

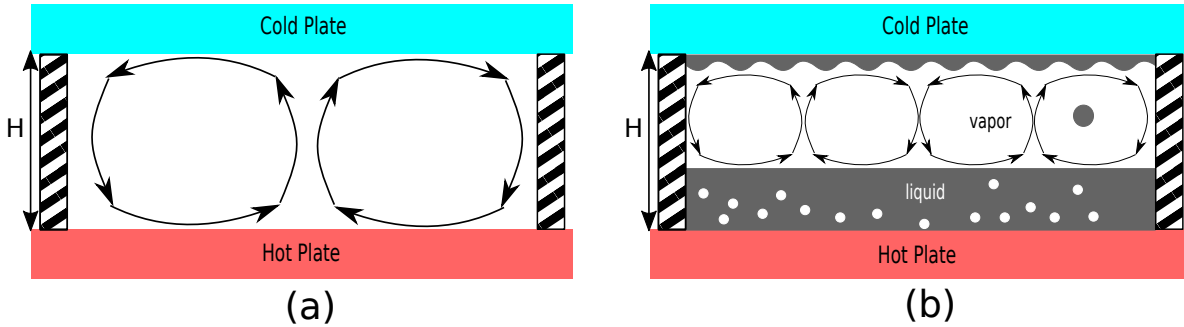


**Figure 1.2:** (a) Schematic of classical RBC. (b) Schematic of moist RBC. The arrows represent the LSC in the cell.

In our experiments,  $\text{SF}_6$  exists in both liquid and vapor phases. The flow structure and the heat transport mechanisms are vastly different and more complex than the classical Boussinesq RBC. The bulk of the heat transport occurs through phase change [25]. A schematic of the moist convection setup is shown in Fig. 1.2 (b). The liquid and vapor phases can be treated as two separate convection cells and both of them undergo convective motions with large scale circulations in both liquid and vapor phases. In the case of a boiling liquid layer at the bottom plate, there is an additional buoyancy source due to the rising bubbles. This may alter the characteristics of the LSC in the liquid

pool. Moreover, the rising warm SF<sub>6</sub> vapor condenses on the top plate. The liquid film on the top plate undergoes Rayleigh-Taylor like instability (RTI) as it is gravitationally unstable.

### 1.3 Pattern formation

Pattern forming systems are pervasive in nature. Pattern formation has significance in all aspects of our lives (scientific application to art/literature). Patterns in a system or object may indicate the absence of spatial/temporal homogeneity [26]. Since the seminal paper on morphogenesis by Alan Turing [27], several pattern forming systems have been identified in physics, biology and chemistry [28]. The patterns observed in different systems have similar characteristics, and developing a detailed understanding of their behaviour is of significant importance [28]. In fluid dynamics, RBC close to the onset of convection has been used as a model system for pattern formation studies [29]. The variation of the spatial structure of the convection roll in RBC has been studied both experimentally and theoretically [29]. These ideas can also be extended to study superstructures in turbulent flows. The characteristic properties of these superstructures/very large scale motions in turbulent RBC is similar to those in a non-linear chaotic pattern forming system [24]. Similarly, the large scale roller motions in a turbulent mixing layer is attributed to the Kelvin-Helmholtz instability in a shear layer [30, 31].

In this thesis we investigate the pattern forming instability in a system with a density gradient across an interface. Interfaces with a density gradient subjected to a destabilizing gravitational field undergoes RTI [32–34]. RTI occurs in an accelerating system when the acceleration is directed against the density stratification [34, 35]. RTI has important applications in systems with strong density gradients like in astrophysics, oceanography. In the presence of a liquid interface, the surface tension may stabilize the interface. Viscosity plays an important role in the dynamics of thin films with a wall on one side when the thickness of the liquid layer is smaller than the viscous length  $(\frac{\nu^2}{g})^{\frac{1}{3}}$ , where  $\nu$  is the kinematic viscosity and  $g$  is the acceleration due to gravity [34, 36]. Thin films have important applications in the field of biophysical, physical and engineering systems [37]. For instance, the tear layer in the eye [37, 38] and surface protection layers such as paints etc. [37]. The liquid-vapor interface or the liquid-liquid interface in the thin film limit may exhibit a variety of shapes and structures. A thorough investigation is required to understand their dynamics under various conditions. A detailed review is available in [37]. We focus only on a thin film on a horizontal plate destabilized by gravity.

A thin film can be stabilized using a variety of forces. A constant surface tension results in a long wavelength instability [34, 37]. This problem was investigated experi-

mentally using silicone oil [34]. The initial transients result in a hexagonal pattern until the film starts to drip. The pattern wavelength scales with the capillary length  $((\frac{\sigma}{\Delta\rho g})^{\frac{1}{2}})$ . The pattern symmetry is gradually lost once dripping sets in. The experiments were repeated with a porous top plate with a constant mass flow rate across the plate [36, 39]. Several different regimes were obtained depending on the flow rates. Under certain flow rates they observed a stable hexagonal pattern on the lower side of the plate with a continuous liquid column falling from each pattern. A similar observation was made in a one dimensional system [40]. The patterns were more dynamic in nature when the flow rates were increased, and beyond a certain critical flow rate the liquid columns become chaotic. A further increase in the flow rate resulted in the formation of liquid sheets due to the merging of neighbouring liquid columns [39].

In the absence of a continuous flow across the top plate, a temperature gradient imposed across the thin film alters the dynamics of the liquid layer and may suppress dripping [41, 42]. To do this, the direction of the temperature gradient must oppose the direction of the acceleration vector, i.e., the temperature of the liquid-vapor interface is warmer than the temperature at the plate. The surface tension at the interface decreases with temperature. As a consequence the Marangoni forces oppose the effects of gravity. It was found that the liquid layer is stable if the imposed temperature gradient is large enough [42]. However, the layer was unstable to long wavelength perturbations. The observations were consistent with the predictions from the the linear stability analysis [42]. These experiments show that thermo-capillary effects may stabilize a thin film on a plate subjected to a destabilizing gravitational field. More details on this mechanism are discussed in Chapter 3.

An additional stabilization mechanism involves the effect of phase change (evaporation-condensation effects). This problem has been investigated theoretically under the thin film assumption and lubrication approximation [43]. A temperature gradient is imposed across the thin film. The liquid-vapor interface is assumed to be in equilibrium with the vapor phase below the film. Their calculations showed that the film layer was stable if the magnitude of the evaporation-condensation effect was sufficiently large. The rupture of the film, i.e., the thickness of the film approaching zero, was prevented by the condensation effects, and the evaporation effects suppressed the increase in the thickness of the film. Under certain conditions, the thin film interface deforms into a regular stable hexagonal patterns [43]. In this thesis we conduct experimental investigations on the effects of evaporation and condensation on the thin film underneath a cold top plate in a moist RBC system. More details on this mechanism are discussed in Chapter 3.

## 1.4 Secondary Nucleation in Clouds

Nucleation is a key process in clouds. In particular, formation of ice phase in mixed phase clouds have tremendous significance in cloud dynamics and precipitation formation [44]. Initiating the ice phase formation in developing cumulus clouds was used in the past to locally induce precipitation, and thus alter the cloud dynamics. Following the laboratory success in initiating ice phase formation using dry ice and Silver Iodide (AgI) [45, 46], several field campaigns were carried out with the objective of enhancing precipitation from clouds [47, 48]. In almost every case, addition of ice initiating agents resulted in rapid growth of the cloud followed by abundant rainfall in the immediate neighbourhood. Since then several investigations have been carried out to understand the nucleation process in clouds and their effects on the life cycle of a cloud system [44, 49]. The significance of ice phase in clouds is that under cold conditions the ice supersaturation is higher than the liquid water supersaturation. The variation of vapor pressure as function of temperature for ice phase and supercooled liquid water phase is shown in Fig. 1.3. At temperatures below  $0^{\circ}\text{C}$ , the vapor pressure in the ice phase decreases at a faster rate compared to the supercooled liquid water. This results in a higher supersaturation relative to ice at sub-zero temperatures. Due to a higher ambient supersaturation, ice particles grow diffusively at a faster rate than the liquid droplets, and hence initiate precipitation. Moreover, additional latent heat is released through glaciation which may influence the development of the cloud [9]. In the mixed phase clouds, if the vapor pressure falls below liquid water saturation, then the ice particles grow diffusively at the expense of cloud droplets. This process is called the “Wegener Bergeron Findeisen” process [44], and is responsible for the punch hole clouds (also known as fallstreak hole) [50].

A long standing question in mixed phase clouds is the anomaly between the measured ice nuclei concentrations and the measured ice particle concentrations [44]. Measurements show that the ice particle concentrations is quite often several orders of magnitude higher than the measured ice nuclei concentrations [44, 53–56]. This discrepancy has led to experimental investigations in search of new ice nucleation/production mechanisms. These are called secondary ice production (SIP) mechanisms. We provide a brief overview on various SIP mechanisms. A detailed review is available in [53].

Hallet-Mossop (H-M) process also known as rime splintering, is the most widely investigated SIP mechanism [53, 57]. It was found that several splinters of ice are generated when a cylinder coated with a layer of ice (a surrogate for a graupel or snowflake) is moved rapidly in an environment containing several supercooled droplets. Based on several experiments, it was concluded that the H-M process was active only in the temperature range of  $-3^{\circ}$  to  $-8^{\circ}\text{C}$  in the presence of liquid cloud droplets with diameters larger than  $25\ \mu\text{m}$  and smaller than  $13\ \mu\text{m}$  [53]. The peak splinter production

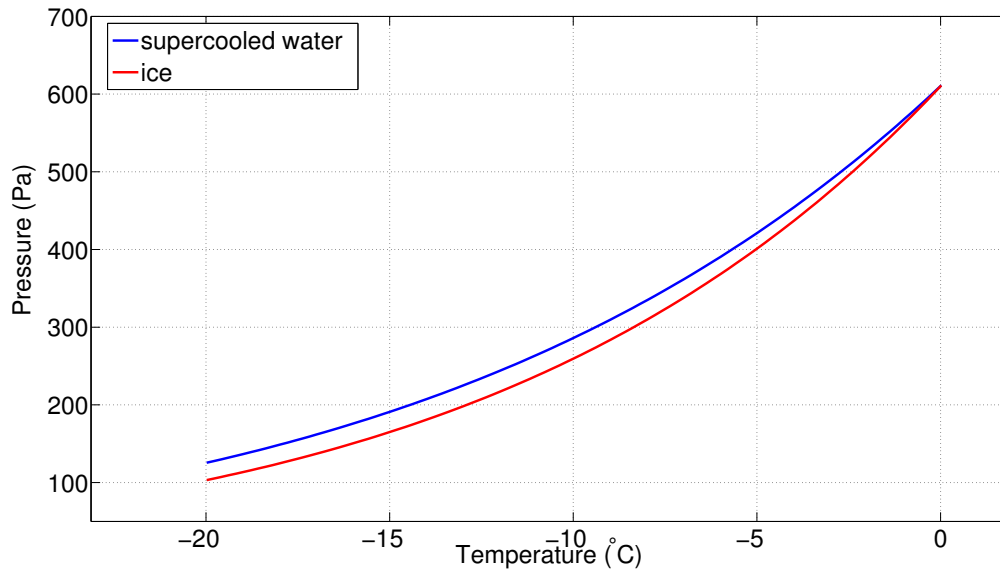


**Figure 1.3:** Variation of vapor pressure as function of temperature in supercooled water and ice [51, 52].

was observed at a relative velocity of 2–4 m/s [55]. Several experiments were conducted to understand the physics behind the H-M process [53]. Some argued that the thermal shock due to the temperature difference between the substrate and the drop caused splintering [58]. A few others argued that symmetric freezing of droplets resulted in the build up of internal pressure. This was relieved by the flowing of unfrozen liquid through the cracks in the outer frozen shell, resulting in the formation of a protuberance that breaks into splinters under appropriate conditions [53, 59]. Despite many experiments, there is still no consensus among the researchers about the underlying mechanism for the formation of ice splinters [53].

Other SIP mechanisms include evaporation induced fragmentation [60, 61]. These experiments showed that under sub-saturated conditions, the narrow bridges in a snowflake may sublime, forming additional ice particles. Another possible ice multiplication mechanism involves collisions of ice particles. Laboratory investigations present evidence for splinter formation based on collision induced fragmentation of ice particles [62]. The fragile needle like structures may breakup on impact with other ice particles at temperatures where the H-M process is active [63]. An additional SIP mechanism that is currently being explored in detail is the shattering of large freezing droplets [53, 64]. This mechanism is most efficient in the temperature range of  $-10$  to  $-15$  °C and can operate over a broader temperature range compared to other SIP mechanisms [53, 64].

Several SIP mechanisms have been explored under controlled laboratory conditions, but there is no consensus among the researchers regarding their importance in an at-

atmospheric cloud [53]. Field campaigns were attempted to conduct a consistency check and also to quantify the effect of various SIP mechanisms. The major uncertainties in the field measurements are due to the probe limitations and the effect of the aircraft on the cloud as multiple passes through the cloud is required to quantify the effect of H-M process [53, 65]. A few field measurements showed that the ice concentrations measured in the cloud could not be attributed to the H-M process as the cloud glaciation rate was faster than the observations in the laboratory, the temperature conditions were outside the H-M process range, and small ice particles were found alongside frozen droplets, which was inconsistent with H-M process observations in the laboratory [53, 54, 66]. Similar observations were reported in recent experimental observations [67, 68]. Correlations were found between the freezing of large (1 mm) supercooled drops and high ice particle concentrations due to SIP [53, 67]. They also suggest that the secondary ice particles may have been produced through the drop shattering process.

A large eddy simulation (LES) with size resolved micro-physics models, suggested that evaporation of drops may trigger nucleation of ice particles [69]. Similar ideas were suggested in the past based on simple numerical calculations of the supersaturation field in the neighbourhood of a growing graupel/hailstone [70]. They predicted that the induced evaporative supersaturation may activate ice nuclei. This prediction is consistent with the formation of satellite droplets in the neighbourhood of a large freezing droplets observed in laboratory experiments [71–73]. It was speculated that this transitional supersaturation may enhance the number of activated ice nuclei in the neighbourhood of a growing hydrometeor or a freezing drop.

The discussion so far suggests that additional investigations are required to understand the importance of secondary ice nucleation in atmospheric clouds. In this thesis, we investigate the possibility of secondary nucleation of droplets and ice crystals in the wake of falling hydrometeors (hailstones/graupel/large drops) in clouds.

## 1.5 Overview

The primary objective of this work is to establish a reliable laboratory model for studying clouds and investigate nucleation in the wake of falling hydrometeors. We also conduct a systematic study on the dynamics of a thin film on the cold top plate in a RBC system. The remainder of the thesis is organized into 5 chapters. In chapter 2 we discuss the key features of the experimental setup. In chapter 3 we report the dynamics of the thin film on the cold top plate. In chapter 4 and 5 we present the nucleation of cloud droplets and ice particles in the wake of cold and hot drops. In chapter 6 we provide a brief overview of additional interesting experimental observations. We end the thesis with a brief summary and outlook.



## 2 Experimental Setup

In this chapter we present the layout of the experimental apparatus, the phase diagram of the working fluid and the flow visualization techniques employed. We use Sulphur-Hexafluoride ( $\text{SF}_6$ ) and Helium (He) as the working fluid. During the course of the experiments the conditions were set such that the working fluid coexisted in two phase.

### 2.1 Apparatus

The experimental apparatus was constructed in Cornell university and a detailed documentation of the apparatus is available in Plapp (1997) [74]. This apparatus was designed and used for studying pattern formation close to the onset of convection [74–78]. Only an overview of the experimental setup is presented here along with the key modifications essential for the present study.

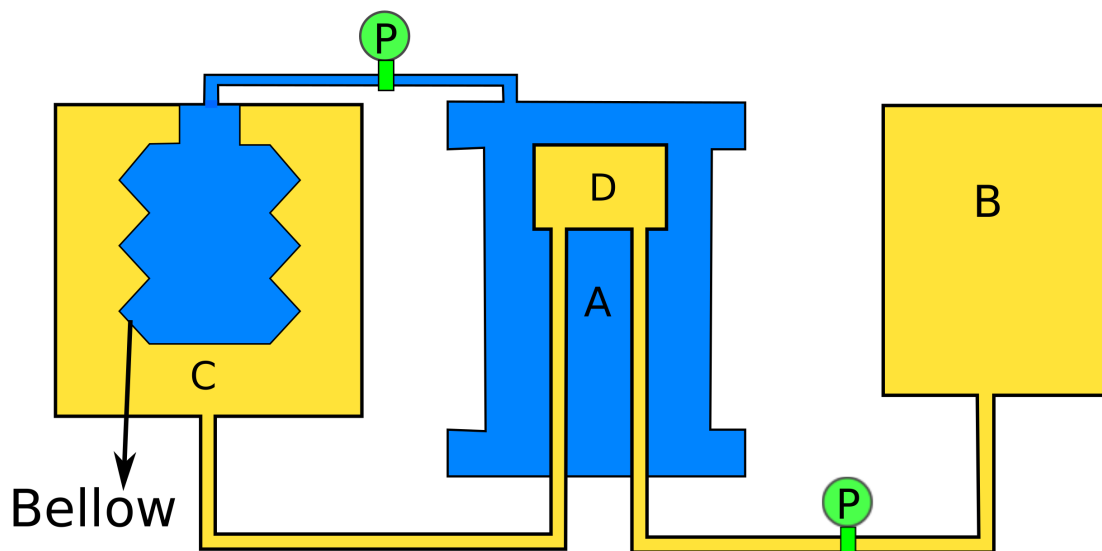


**Figure 2.1:** A schematic representation of the experimental setup. (A) Main pressure vessel (B) Pressure regulation vessel (C) Pressure equilibration vessel (D) convection vessel inside the main pressure vessel.  $\text{P}$  represents the pressure gauge attached to the water and gas side of the experiment. The gas side is marked in yellow and the water side is marked in blue.

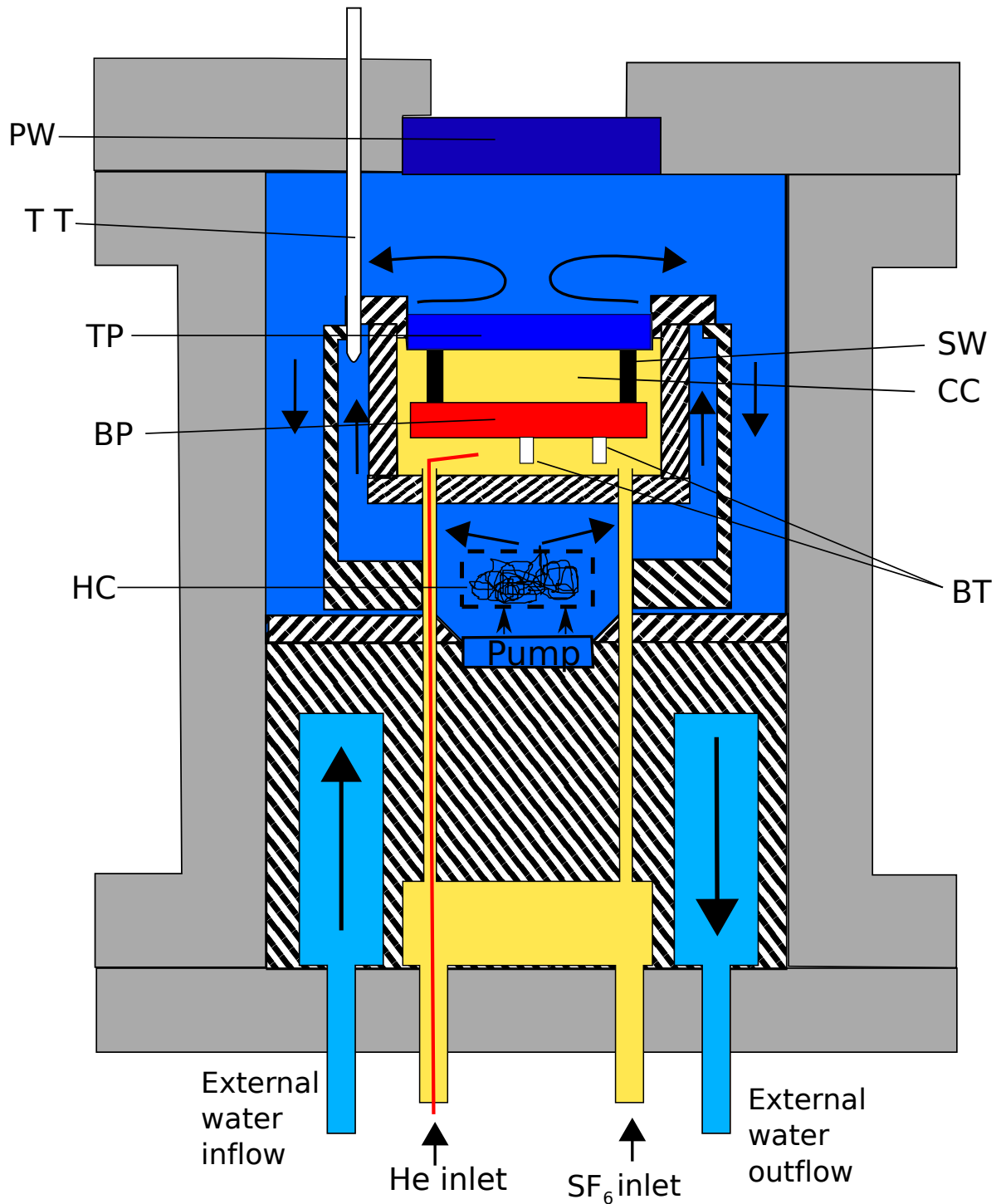


**Figure 2.2:** A schematic of the main pressure vessel. The two different water circuits are marked in different shades of blue. Arrows indicate the direction of the flowing water. PW - Sapphire pressure window, TT - Top plate thermistor, BT - bottom plate thermistors, CC - convection cell, SW - side wall of the convection cell, BP - bottom plate, TP - top plate, HC - heating coil. The different shades of blue separates the internal and the external water circuit. A more detailed account on the design is available in [74, 78]

The setup was certified to operate up to a pressure of 130 bars. A schematic of the experimental setup is shown in Fig. 2.1. The setup consists of three units: a main

pressure vessel, a pressure regulating vessel and a pressure equilibration vessel. The gas side and the internal water circuit were maintained at the same pressure via a bellow in the pressure equilibration vessel. Figure 2.2 shows a schematic of the main pressure vessel. The main pressure vessel was attached to the head of a milling machine. The main pressure vessel houses the convection cell. The convection cell consists of a top plate made of mono-crystalline sapphire and a bottom plate made of mono-crystalline silicon. Both plates have a diameter of 101.6 mm, a thickness of 9.5 mm and were polished to a flatness of  $\lambda/4$  ( $\lambda$  is around 633 nm). The cell height was varied depending on the nature/type of the experiment. An Ohmic foil heater was glued to the bottom of the silicon plate to heat the plate to a desired temperature. The whole convection cell was placed in a temperature controlled water bath. The bath temperature was controlled by using a heating wire and an external water circuit connected to a chiller (Thermoscientific Neslab) for heat exchange. The top plate temperature was regulated by circulating water on its top surface. The water was circulated using an aquarium pump. The water flows over the top plate through a flow distributor for better heat exchange, thus resulting in a nearly homogeneous temperature across the plate. The external water circuit was operated at atmospheric pressure. The chiller was also used to define the base temperature for the experiment. The flow directions in the water circuits are marked in Fig. 2.2. The top plate temperature was estimated based on the temperature in the water bath near to the top plate. At the bottom plate, two ceramic thermistors were attached using a spring for the precise measurement of the temperature. Four similar thermistors were also placed at different locations close to the pump in the water bath for precise temperature control. Please note that due to the placement of the thermistors and finite conductivities of the top and bottom plates a precise measurement of the temperature difference across the convection cell was not possible. Moreover, in the two-phase experiments additional heat loss effects come into play due to phase change. If the imposed temperature difference across the cell was sufficiently high then boiling is initiated at the bottom plate (both on the top and bottom surface of the bottom plate). This results in an unaccounted heat loss from the bottom plate. As a consequence, the measured temperature difference was an over estimation of the temperature difference across the convection cell (between the top of the bottom plate and the bottom of the top plate).

The pressure-regulating vessel was used to maintain a set pressure during the course of the experiment. The pressure vessel contained  $\text{SF}_6$  in two phase. The temperature of the vessel was controlled using an external heat exchanger connected to a chiller (Thermoscientific Neslab) and a foil heater inside the vessel. The temperature in the vessel determined the equilibrium vapor pressure in the experiment. The pressure regulation vessel was disconnected for experiments where the bottom plate was covered with a layer

of liquid SF<sub>6</sub>, as the pressure in the experiment was determined by the temperature of the liquid-vapor interface inside the cell. The pressure equilibration vessel was used to equilibrate the pressure between the gas side and the water side. This was essential for the pattern formation experiments as it prevents the bending of the top plate in the cell. A bellows with a cylindrical shape was used for pressure equilibration (Fig. 2.1). The sidewall of the bellows are flexible and can deform when subjected to net pressure difference across walls. One side of the bellows was filled with the working fluid and the other side was filled with water. The bellows underwent deformation to compensate for the changes in pressure on either side. The compressibility of water is very small. As a consequence the volume change encountered due to the variation in pressure was rather small. A pressure difference of 50 bars results in a volume change of  $\approx 2$  ml per litre of water under the assumption that no gas was present in the water. This was ensured by lowering the pressure on the water side to the vapor pressure of water for a long time before filling the cell with SF<sub>6</sub>. This concept of pressure equilibration was developed by de Bruyn *et al* [79].

A Keithley 2000 digital multimeter with a resolution up to 7.5 digits was used for electrical measurements. It was kept in a temperature-controlled box with a desiccant (silica) to avoid drifts in the measurement due to temperature and humidity fluctuations. The whole experiment was computer controlled and the communication was established through a GPIB and RS 232 interface. A Proportional-Integral-Differential (PID) control loop was used for temperature and pressure regulation during the course of the experiment. The control loop computes the amount of voltage required for maintaining the set temperature and pressure. This voltage was sent to the Agilent power supply connected to the heaters of the bottom plate and the pressure regulation vessel, which supplied the required voltage. A Sensotec pressure transducer (model S-TJE) was used to measure the pressure. An additional Heise Bourdon tube gauge (0 – 1000 psi, model CM) was connected to the gas side. The temperature regulation was stable up to 10 mK and the pressure regulation was stable up to 1 psi. The thermistors were calibrated against Pt-100 thermistor (PT-103-70H, Lakeshore electronics) with an accuracy of 20 mK.

The experimental observations discussed in the later chapters were acquired with cells of three different heights. Various side walls were used depending on the nature of the experiment. The various convection cells used in the experiments are classified into four categories: (i) Type 1 (thick cell) - the cell had a square planform of length  $L = 65$  mm and a height  $H = 21.26 \pm 0.5$  mm. The side walls were made of acrylic with a thickness of 1 mm. The side wall was insulated using open cell foam. Thermal conductivity of acrylic is larger than that of SF<sub>6</sub>. The pores in the insulation material were filled with SF<sub>6</sub> vapor/liquid. As a consequence the side wall conductivity was as

low as that of the working fluid in the cell. (ii) Type 2 (thick cell) - the cell has a square planform of  $L \approx 62$  mm and a  $H \approx 22$  mm. The lateral side wall was made of acrylic with mirrors embedded onto it. This was one of the major design changes in the apparatus to provide lateral optical access into the cell. The construction details are discussed in section 2.4.3. (iii) Type 3 (medium cell) - the cell has a circular planform with a diameter of 80 mm and  $H$  was about 2 mm. The side wall was made of paper slips of thickness about  $50 - 100 \mu\text{m}$ . The paper slips were stacked together to attain the desired cell height and were glued together at 3 points. (iv) Type 4 (thin cell) - the cell design was similar to Type 3. The cell height was reduced to about 0.5 mm.

## 2.2 Phase diagram

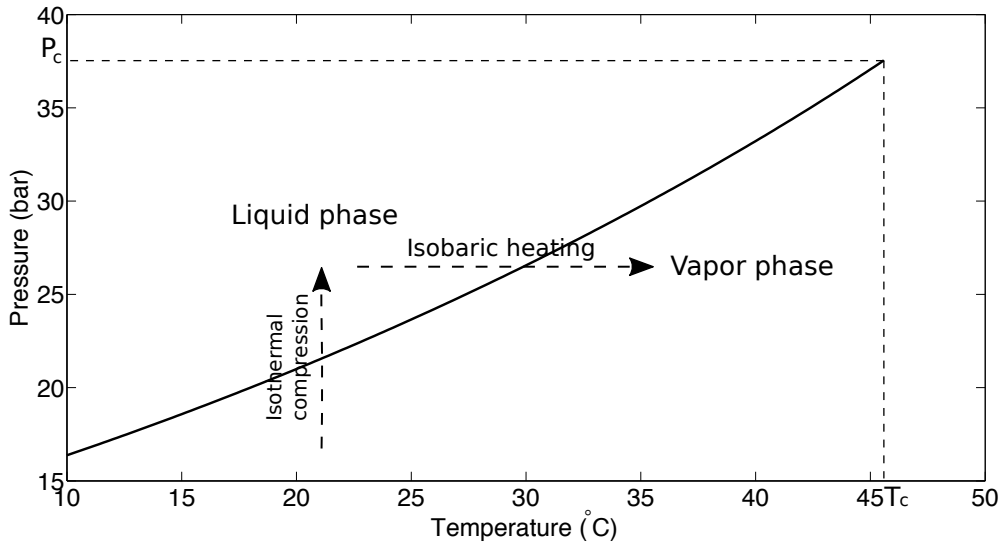


**Figure 2.3:**  $T - P$  phase diagram of  $\text{SF}_6$ . Solid black line represents the liquid-vapor coexistence line.  $P_c$  and  $T_c$  represent the critical pressure and temperature respectively. The data was obtained from the NIST database [80].

A single component fluid can exist in a solid, liquid and/or in a vapor phase under equilibrium conditions. We used Sulphur Hexafluoride ( $\text{SF}_6$ ) and Helium (He) as the working fluid in the experiments. The temperatures in the experiments varies between  $10^\circ\text{C}$  and  $50^\circ\text{C}$ . In this temperature range,  $\text{SF}_6$  can exist in both liquid and vapor phase depending on the pressure. Helium on the other hand exists only in the gaseous state under these conditions. The phase diagram for pure  $\text{SF}_6$  and  $\text{SF}_6$ -He binary mixture are represented using pressure  $P$ , temperature  $T$  and composition as the independent variables.

Figure 2.3 shows the  $T - P$  phase diagram for pure  $\text{SF}_6$ . The thick black line is the liquid-vapor curve or the saturation curve for  $\text{SF}_6$ . This line separates the liquid phase from the vapor phase. The region above this line represents liquid phase and the region

below is the vapor phase. Isothermal compression can alter the phase from vapor to liquid. Isobaric heating can alter the phase from liquid to vapor. If the fluid exists in both liquid and vapor phase then the state of the system is uniquely determined either by the pressure or the temperature along the saturation curve. As we move up along the liquid-vapor coexistence line, the density of the liquid phase decreases and that of the vapor phase increases until the critical point is reached. At the critical point the liquid and vapor phase are indistinguishable and have the same density. Beyond this point the fluid is in the supercritical state. For SF<sub>6</sub> the critical temperature is 45.583 °C and the critical pressure is 37.55 bars.

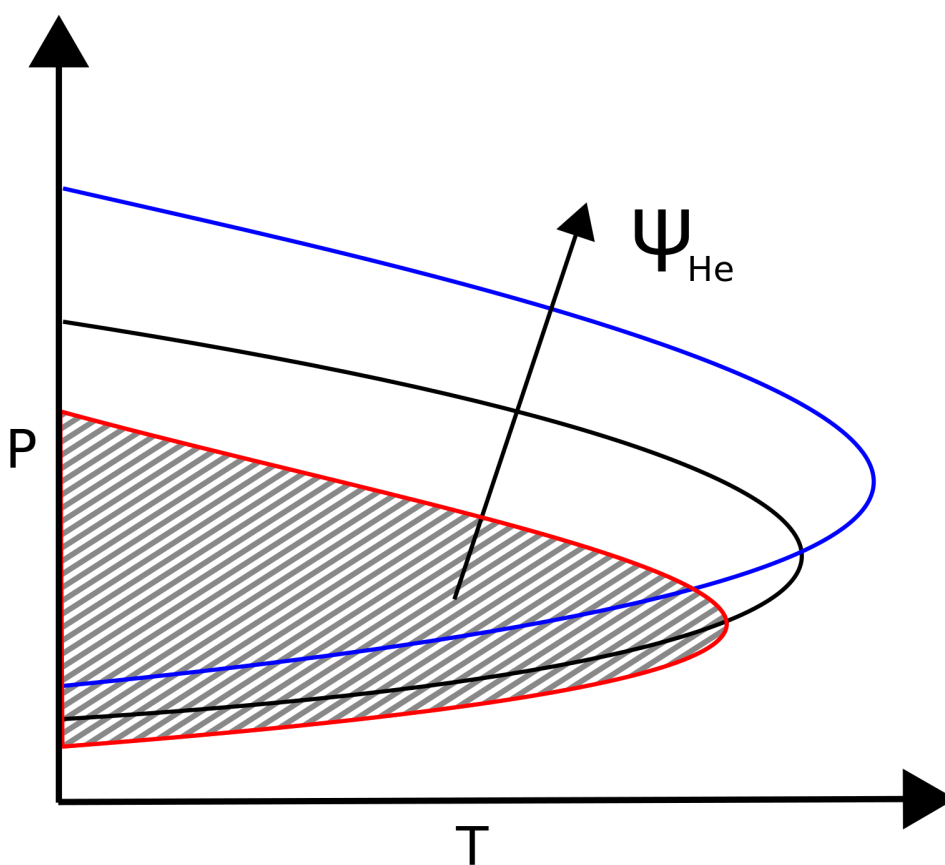


**Figure 2.4:** Schematic representation of the phase diagram of SF<sub>6</sub>-He binary mixture.  $\psi_{He}$  represents the mole fraction of helium in the mixture. The shaded region represents the two phase region for the red curve which corresponds to a certain concentration of He.

In a binary mixture the phase of the system is described by three independent variables: pressure, temperature and composition of the mixture. As a consequence the phase diagram of a binary mixture has three independent axes, i.e., a 3 dimensional diagram. The composition is represented by the mole fraction of one of the constituents  $\psi$ . In the present experiment, the binary mixture was composed of SF<sub>6</sub> and He and the

exact composition was not known. Only an estimate was obtained using an indirect method (about 25% of He, see chapter 4 for details). Moreover, the phase diagram represents the state of a fluid system in thermal equilibrium. In the experiments discussed here, there always exists a net heat flux across the fluid system. Despite these limitations, an idea of the phase diagram was useful in conducting the experiments. An account on the phase diagram of Xenon-Helium (Xe-He) mixture is provided in [81]. The phase diagram of the SF<sub>6</sub>-He mixture is similar to that of Xe-He mixture as the molecular mass of SF<sub>6</sub> and Xe are similar. To the best of our knowledge we are not aware of a detailed characterization of the phase diagram of the SF<sub>6</sub>-He mixture. Partial information is available based on some of the cloud chamber experiments [78, 82]. In Fig. 2.4 we only show a schematic of the phase diagram of a binary mixture. The details discussed here are based on the Xe-He mixture.

The two phase region for a certain concentration of He is shown in Fig. 2.4. Instead of a line as was the case in single phase, in the binary mixture the two phase region is spread over an area for a given concentration of He. As the concentration of He increases the area occupied by the two phase region also increases. In a binary system a critical point does not exist, instead we have a locus of critical points or a critical curve. In some binary mixtures the critical line connects the critical points of the pure components (e.g. ethane-heptane [83]) . In systems like Xe-He mixtures we do not know if the critical curve connects the critical points of the pure components [81]. From the available data it appears that the critical curve departs from the critical point of Xe with a positive slope away from the critical point of He [81]. These effects come into play when the pressure and temperature in the system are significantly higher than the critical pressure and critical temperature of the pure components, hence are not of much interest to the experiments presented in this thesis.

## 2.3 Filling Procedure

The first step was to ensure that the experiment has enough water on the water-side for the bellows to act as a pressure equilibration device. Furthermore, to reduce the compressibility of water it was necessary to ensure that the water does not contain any dissolved gases in it. For this the gas-side and water-side of the experiment was pumped down to the vapor pressure of liquid water at room temperature and then pumped back to atmospheric pressure. This process was repeated several times, and in the last two cycles the gas side was supplied with clean SF<sub>6</sub>. In this process any stray water vapor or Nitrogen present in the gas side was eliminated and the required amount of water was filled in.

The mean temperature in the experiment was varied from 22 °C to 45 °C across the liquid vapor co-existence line. The gas side of the experiment was connected to a

bottle of clean SF<sub>6</sub> (purity - 99.999% by volume), which was at a pressure of 22 bars at room temperature. The experiment was cooled to a temperature (around 18 °C) below the room temperature to ensure a continuous flow from the bottle to the setup without an additional pump. The pressure-regulating vessel was maintained at a temperature around 10 °C. The liquid SF<sub>6</sub> filled in this vessel was later used to pump in SF<sub>6</sub> if not enough SF<sub>6</sub> was available inside the cell at higher mean temperatures. Furthermore, the temperature of pressure regulation vessel was varied to adjust the height of the liquid-vapor interface inside the convection cell. As was mentioned earlier, the temperature in the lower and upper half of the experiment can be regulated independently. The temperatures were adjusted such that the lower half of the cell was filled with liquid SF<sub>6</sub> and the liquid vapor interface exists only inside the convection cell. We disconnected the pressure regulation vessel from the convection cell during experiments with a layer of liquid SF<sub>6</sub> on the bottom plate. The pressure inside the cell was determined by the temperature of the liquid-vapor interface and an additional external regulation was not required. But in the experiments with no liquid layer on the bottom plate the pressure regulation vessel was used for regulating the pressure in the chamber. This provides better control in regulating the saturation ratio (ratio of the vapor pressure and saturation vapor pressure) inside the convection cell.

In the experiments with He and SF<sub>6</sub>, He was pumped into the cell through a Teflon tube shown in Fig. 2.2. The long Teflon tube was made of three smaller tubes and were connected using a copper tube. The connections were not leak tight and as a consequence, the He was released into the liquid SF<sub>6</sub> pool just below the cell and was well mixed in the liquid phase. Addition of Helium significantly alters the position of the liquid-vapor interface inside the cell. The temperature of the pressure-regulating vessel was adjusted to compensate for this change. This procedure aids the smooth operation of the experiment without much interruption.

## 2.4 Flow visualization

The dynamics in the convection cell were observed using various visualization techniques. Three prominent techniques are discussed in this section. The main pressure vessel has a sapphire window of thickness  $\approx 2.5$  cm and a diameter of  $\approx 10$  cm. This provides optical access into the convection cell. Two different cameras were used for image acquisition - namely QI-Cam Fast 1394, operated at a resolution of  $1392 \times 1040$  pixel at 10 fps (frames per second) and Phantom 65 gold, operated at a maximum resolution of  $4096 \times 2048$  pixels at 140 fps [84].

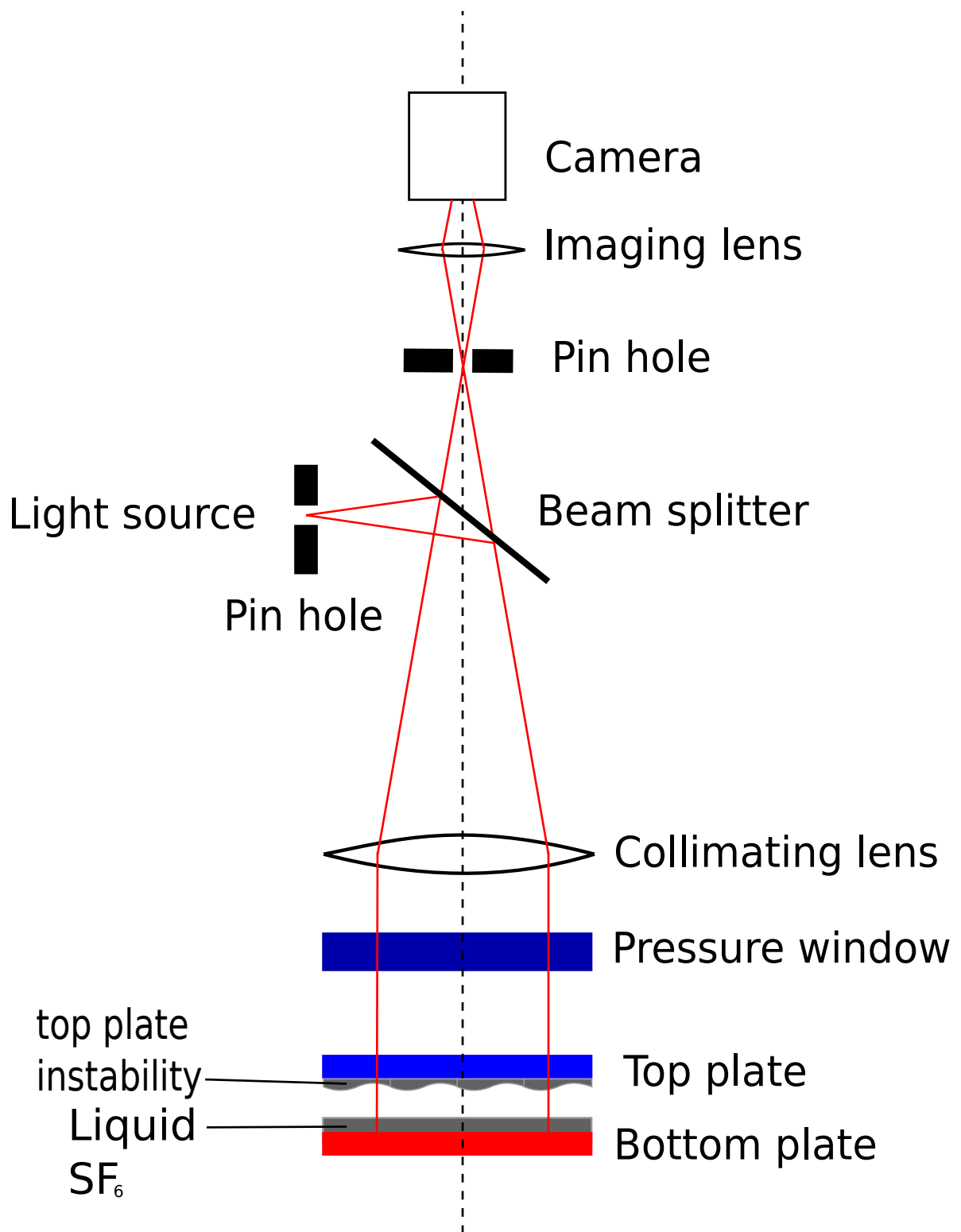


Figure 2.5: Schematic representation of the shadowgraph setup.

### 2.4.1 Shadowgraphy

Shadowgraphy is a popular visualization technique in fluid systems with refractive index variations [79, 85]. A schematic of the visualization setup is shown in Fig. 2.5. A detailed description of the shadowgraph setup is discussed in [74, 79, 86]. A red LED was used as the light source. The LED was coupled into the shadowgraph via an optical fibre. The light was deflected into the collimating tube using a beam splitter. The light was collimated using a telescopic lens of diameter 12 cm. The light from the optical fiber was placed at the focal length of the collimating lens which was about 60 cm. The collimated beam was strongly altered by the liquid layer pattern at the top plate. The drop like deformations in the liquid layer at the top plate act as a lens array. Depending on the focal plane chosen, these drop like deformations of the liquid layer appear as a bright or dark circular patch. On top of the shadowgraph setup, a CCD camera with a Nikon lens was mounted. The location of the focal plane was adjusted by moving the lens and camera independently.

### 2.4.2 Beam splitter setup

A schematic of the visualization setup is shown in Fig. 2.6. A similar visualization strategy was used by Winkel (2015) [78]. An array of  $5 \times 2$  white LED BOSCH Professional GLI DeciLED was attached to the cross beam above the main pressure vessel. The incoming light beam passes through a diffuser plate resulting in a relatively uniform light intensity, followed by a 50/50 beam splitter and into the convection cell through the top sapphire. The light reflected from the bottom plate was directed towards the camera using the beam splitter. Different lens and camera combinations were used depending on the experimental requirement.

### 2.4.3 Mirror unit

The visualization strategies discussed so far provide only a top view of the dynamics in the convection cell. The convection cell was re-designed with the objective of providing lateral optical access into the convection cell. The new cell had a square planform. The side walls of the convection cell were made of acrylic with two sets of mirrors embedded on to them at an angle of  $45^\circ$ . A cross-section of the mirror unit assembly is shown in Fig. 2.7 and a detailed orthographic projection is shown in Fig. 2.9. The whole unit was made of acrylic. The mirror assembly consists of 9 units: a mirror holder and 8 wall blocks that form the side walls of the convection cell. Each wall of the cell consists of an upper and a lower block. The interface between the upper and lower blocks form the mirror surface and were machined using a special diamond milling tool (S117 - Supermini 105 with diamond cutting inserts) to provide a fine finish. The mirror surface on the upper block was coated with a thin layer of Aluminum, thus making it reflective.

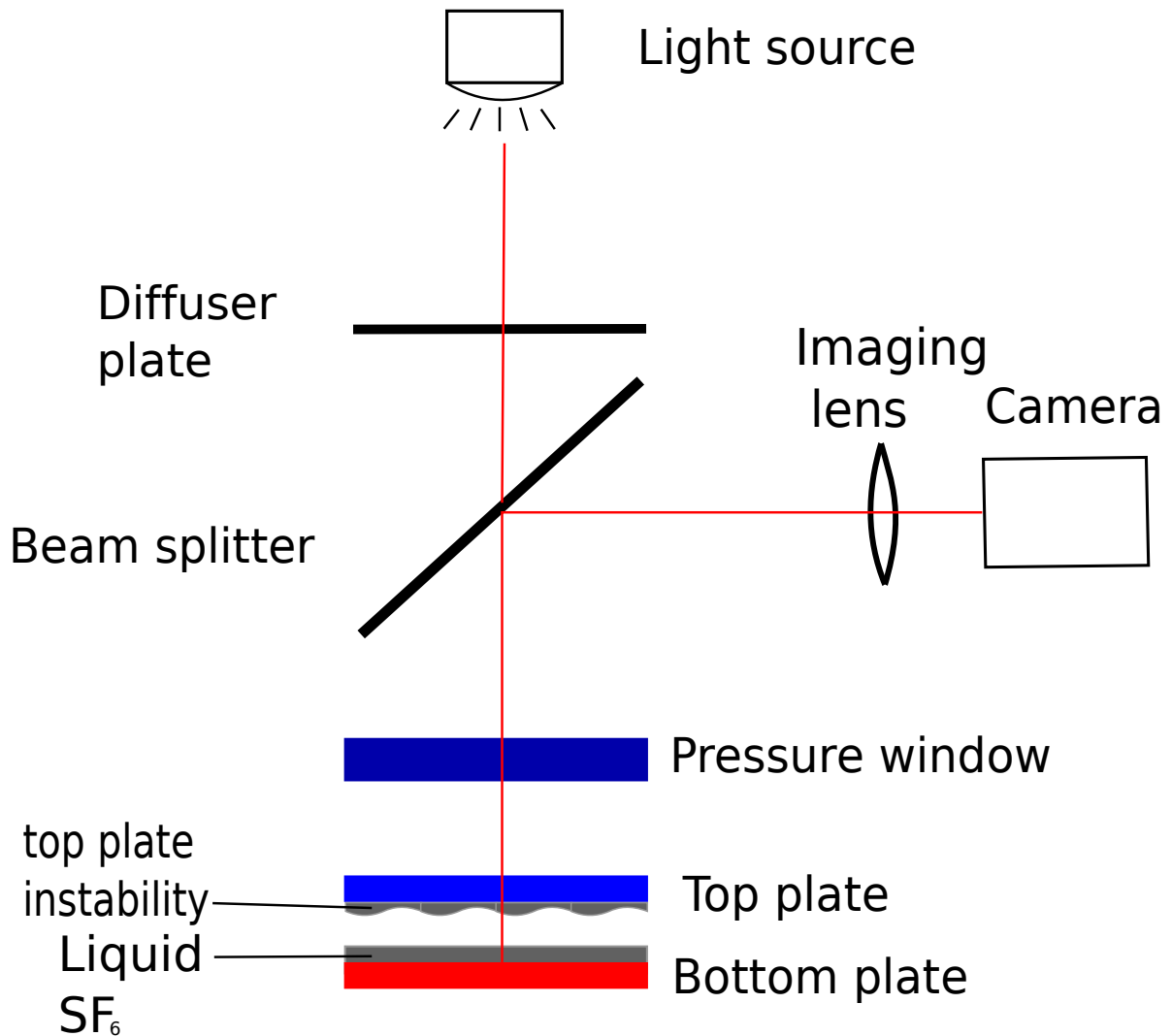


**Figure 2.6:** Schematic representation of the beam splitter setup.

This surface acts as a mirror and provides lateral optical access into the convection cell. The blocks were designed such that one set of mirrors provided optical access to the lower half of the cell and the other set provided access into the upper half of the cell. This was ensured by adjusting the height of the wall blocks as shown in Fig. 2.9. Each set of mirrors form a complementary pair. The light source was placed on top of one of these mirrors and the camera was placed above the complementary mirror. A schematic of this arrangement is shown in Fig. 2.8. The side walls also had a scale engraved on the front part of the mirror piece, thus allowing us to locate the height of the liquid vapor interface. The mirrors were held in position using the guide ways in the mirror holder. The mirror blocks have an elongated protrusion on the rear side which slide along the guide ways in the mirror holder. The lateral edges of the mirror blocks are set at an angle of  $45^\circ$  as shown in the top view in Fig. 2.9. These angled edges keep the mirror blocks stable. The tolerance levels were adjusted such that the entire assembly results

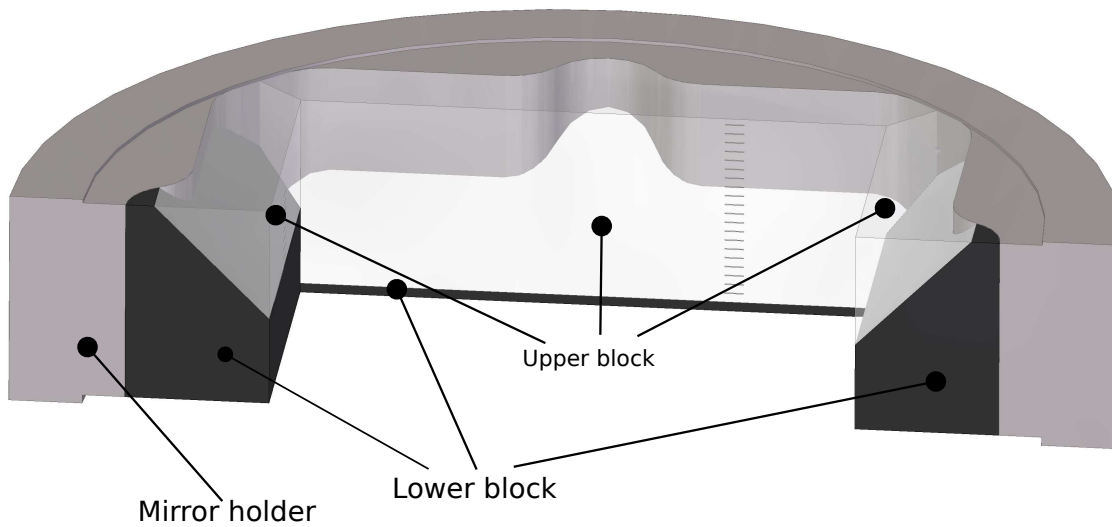


**Figure 2.7:** Cross section of the mirror unit assembly. The lower blocks are colored in black and the upper blocks are semi-transparent. The mirrors are located at the interface between the lower and upper block. See Fig. 2.9 for scale. Image courtesy: Dr. Artur Kubitzek

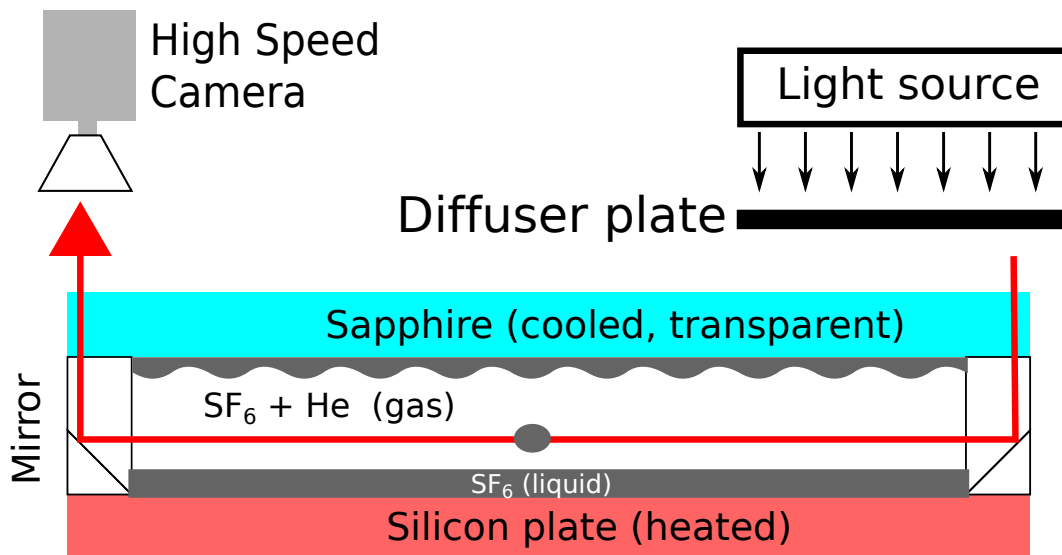


**Figure 2.8:** Schematic representation of the mirror unit flow visualization strategy.

in a tight fit.

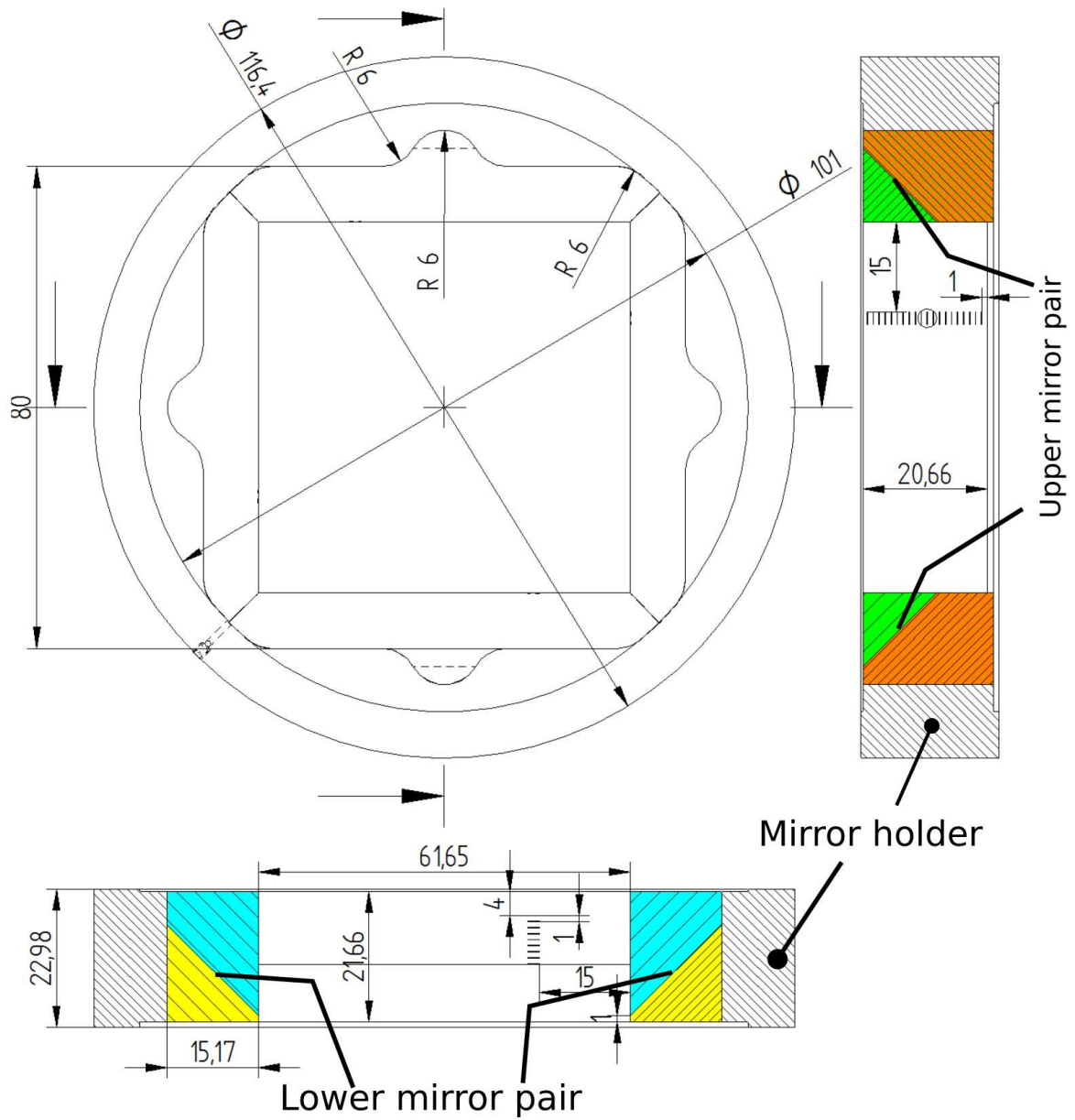


**Figure 2.9:** Orthographic projection of the mirror unit. All dimensions are in mm. Image courtesy: Dr. Artur Kubitzek



# 3 Pattern Formation in Moist Convection

In this chapter, we investigate pattern formation in a two-phase Rayleigh-Bénard convection system. We study the patterns formed in a thin condensed liquid layer at the cold top plate. We first report the laboratory observations under different conditions. Later we compare our observations with the theoretical predictions.

## 3.1 Experimental Details

Figure 3.1 represents a schematic of the flow patterns inside the convection cell. We use SF<sub>6</sub> as the working fluid. The temperature and pressure were adjusted such that a part of the cell was filled with liquid SF<sub>6</sub>. Once the temperature difference is imposed, the warm saturated SF<sub>6</sub> vapor rises from the liquid-vapor interface, and condenses on the cold top plate forming a layer of liquid SF<sub>6</sub>. The thickness of this layer increases over time and above a critical thickness it becomes unstable. We investigate the nature of this instability. If the imposed temperature gradient is sufficiently large then the liquid pool on the bottom plate starts to boil. This restricts the temperature difference across the convection cell due to an additional heat transport mechanism associated with phase change.

Several parameters are involved in this experiment. The difference in temperature between the bottom and top plate ( $\Delta T = T_b - T_t$ , where  $T_b$  and  $T_t$  are the bottom and top plate temperatures respectively) is one of the most important parameters that we regulate.  $\Delta T$  was varied by keeping  $T_t$  constant and changing only  $T_b$ . The experiment was operated across the liquid-vapor coexistence line, and  $T_t$  was varied from 22°C to the critical temperature of SF<sub>6</sub>, thus, allowing us to vary the material parameters. Experiments were conducted at three different cell heights  $H$ :  $21.26 \pm 0.5$  mm,  $1.8 \pm 0.1$  mm,  $0.46 \pm 0.05$  mm and are henceforth referred to as thick, medium and thin cell respectively. An additional parameter is the height of the liquid level  $h$ , above the bottom plate.

Different lateral boundaries were used throughout the experiments with the objective

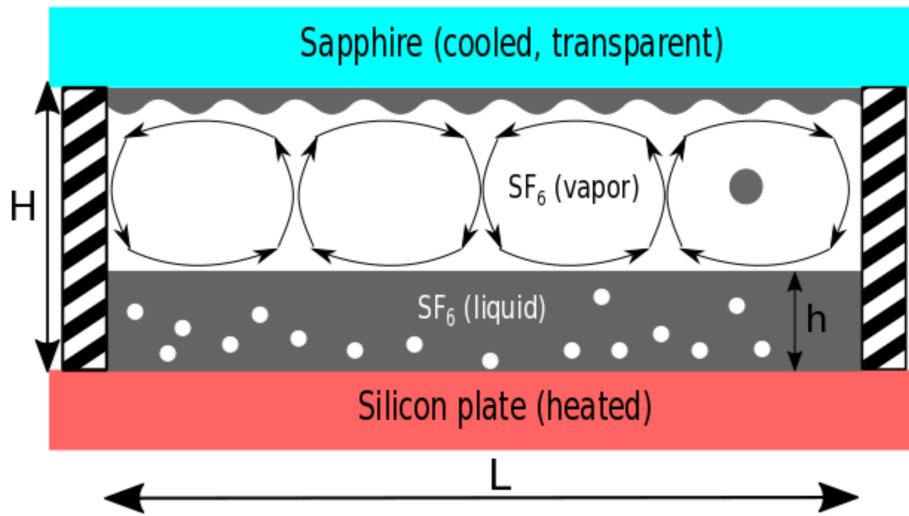


**Figure 3.1:** A schematic of the flow field inside the convection cell. The hatched region represents the lateral side walls. Grey region represent liquid SF<sub>6</sub> and the white region between the top and bottom plate represents SF<sub>6</sub> vapor . The arrows indicate large scale circulation in the vapor region.  $H$  - height of the cell,  $L$  - width of the cell,  $h$  - height of the liquid layer above the bottom plate

of providing nearly adiabatic side walls. In the experiments with the thick cell, a 1 mm thick acrylic wall with a square planform was used as the lateral boundary. These walls were covered with open cell polyurethane for additional insulation. The sidewalls had a height  $H \approx 22$  mm and a width  $L \approx 65$  mm. These were later replaced with acrylic side walls with embedded mirrors to provide side view into the cell. In this experiment, the side wall mirrors were used for measuring the height of the liquid pool above the bottom plate (see Chapter 2 for details).

The experiment was modified to accommodate a convection cell of  $H \approx 0.5$  mm for the thin cell and  $H \approx 2$  mm for the thick cell. The side walls were made of paper slips with a circular planform of diameter  $\approx 80$  mm. The distance between the top and bottom plate was measured to be  $0.46 \pm 0.05$  mm in the thin cell and  $1.8 \pm 0.1$  mm in the thick cell using an interferometer. The bottom plate used in the present experiment was made out of mono-crystalline silicon and was different from that of the thick cell experiment. In the thick cell experiment the silicon plate had a thin layer of gold to enhance the reflectivity from the bottom plate. Other details about the setup are similar to that of the thick cell experiments. Two different types of flow visualisation techniques were used in studying the patterns: shadowgraphy and a simple beam splitter setup (see Chapter 2 for additional details).

## 3.2 Thick Cell

### 3.2.1 Transients

We start with the transient observations in the thick cell. The sequence of images in Fig. 3.2 shows the development of a thin liquid film underneath the top plate. The images were acquired using the shadowgraph. Prior to the experiment, the top and bottom plate temperatures were initially set to  $22.00^\circ\text{C}$ . The pressure in the cell was adjusted such that the cell was nearly saturated with  $\text{SF}_6$  vapor. The bottom plate was not covered with liquid  $\text{SF}_6$ , *i.e.*,  $h = 0$ . The top plate temperature regulation was switched off. As a consequence  $T_t$  decreases over time as the temperature of the heat exchanger used for temperature regulation was around  $17^\circ\text{C}$  (see Chapter 2 for details). The temporally evolving  $\Delta T$  initiates convection in the cell. At the instances when the images in Fig. 3.2 were acquired, the Rayleigh number  $Ra = g\alpha\Delta TH^3/\nu\kappa$  was high enough for the flow to be turbulent as can be seen from the plume structure in Fig. 3.2. The underlying convective motion transports warm vapor to the cold top plate where the vapor condenses resulting in the formation of a liquid film. The development of the film is visible in Fig. 3.2 (a-c). The film was developing from the lateral boundaries towards the center. The movement of the contact line towards the centre of the top plate is visible in Fig. 3.2 (a-c). Near the contact line, the curvature in the film acts like a lens and as a consequence there is a variation in the intensity of the transmitted light.

Over time the film gets thicker due to the condensation of  $\text{SF}_6$  vapor and above a critical thickness the film becomes unstable, resulting in stripe patterns. The film is thicker near the lateral boundaries than at the center of the cell. Consequently, the film becomes unstable near the cell wall, and the instability propagates inwards as depicted in Fig. 3.2 (d). The propagation of the instability towards the center is visible in Fig. 3.2 (d-f). The spacing between the stripes is nearly uniform throughout the propagation of the instability, thus indicating that there exists a dominant growing mode. Over time these one dimensional stripe and axisymmetric patterns break down into two dimensional drop like deformations of the liquid film as shown in Fig. 3.2 (g-i). These drops grow over time due to the continuous supply of vapor until they pinch-off from the liquid film.

A similar image sequence is shown in Fig. 3.3. In this experiment, the system state was changed from  $T_t = 22^\circ\text{C}$ ,  $\Delta T = 0^\circ\text{C}$  to  $T_t = 22^\circ\text{C}$ ,  $\Delta T = 0.30^\circ\text{C}$ . The bottom plate was covered with a layer of liquid  $\text{SF}_6$ . It takes about a few seconds before the bottom plate temperature attains its set point temperature. We note that the evolution of the instability is similar to the experiments shown in Fig. 3.2. The amount of vapor transported towards the cold top plate per unit time is higher in the present case, as

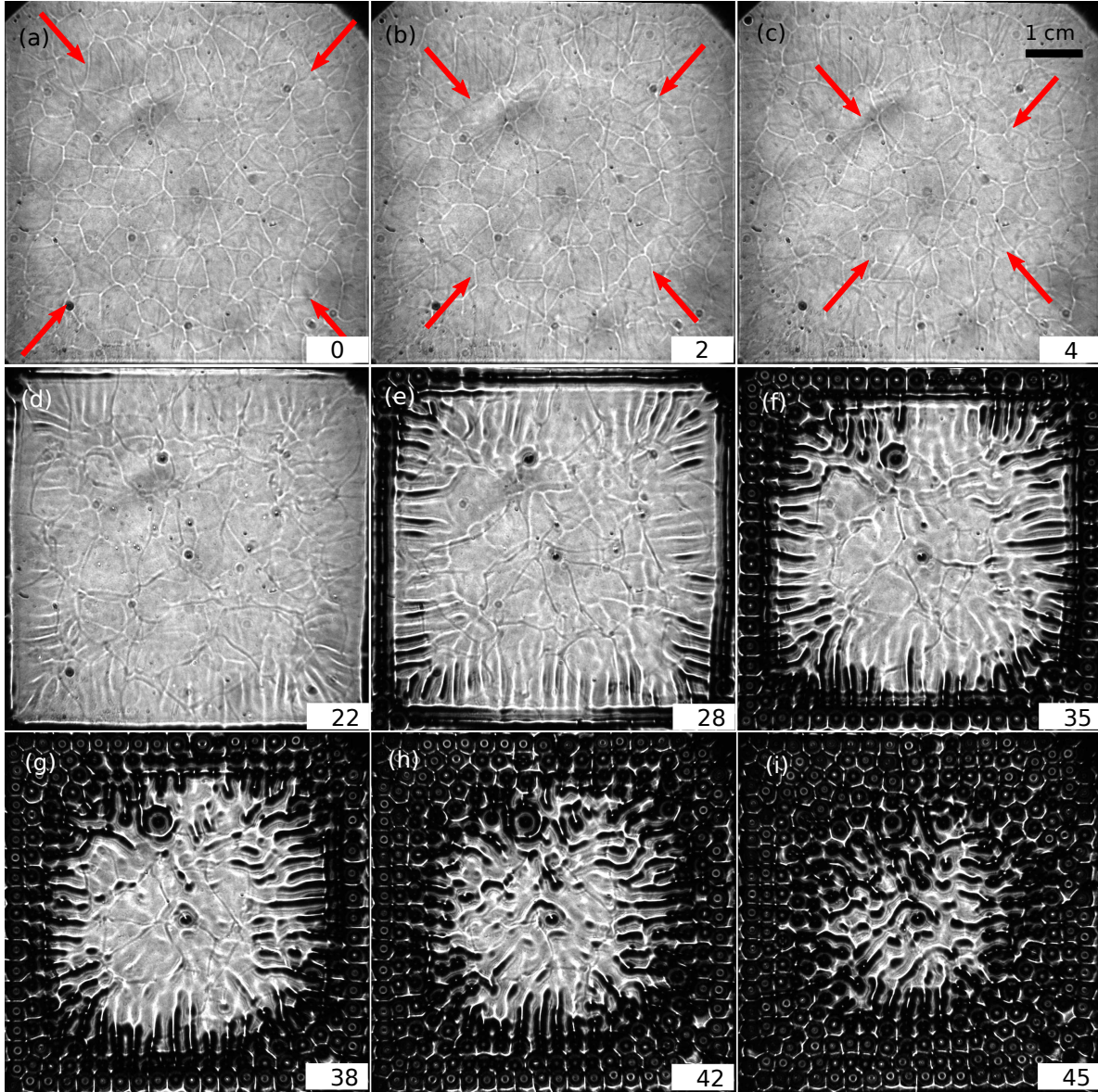


**Figure 3.2:** Thick cell.  $T_b = 22.00^\circ\text{C}$  and  $T_t < T_b$ . (a-c) Propagation of the contact line of the liquid layer below the top plate towards the center is marked using red arrows. (d-f) Propagation of the instability towards the center. (g-i) Break up of stripe and axisymmetric patterns into drops like deformations. Time stamp (in seconds) for each of these images is shown in the bottom right corner of the image.

the imposed temperature gradient is larger than in the experiment shown in Fig. 3.2. This explains the faster development of the instability in Fig. 3.3 as compared to the experiment in Fig. 3.2. In Fig. 3.3 (a-c) we see the development of an axisymmetric pattern. We see a new drop forming in Fig. 3.3 (a), probably due to the presence of a dust particle or some other impurity on the surface. A short time later, we see the formation of an axisymmetric pattern triggered by the primary drop (Fig. 3.3 (b and c)). Over time, this pattern breaks into an array of drops arranged in a hexagonal manner with the primary drop at the center as shown in Fig. 3.3 (d and e). This trend continues

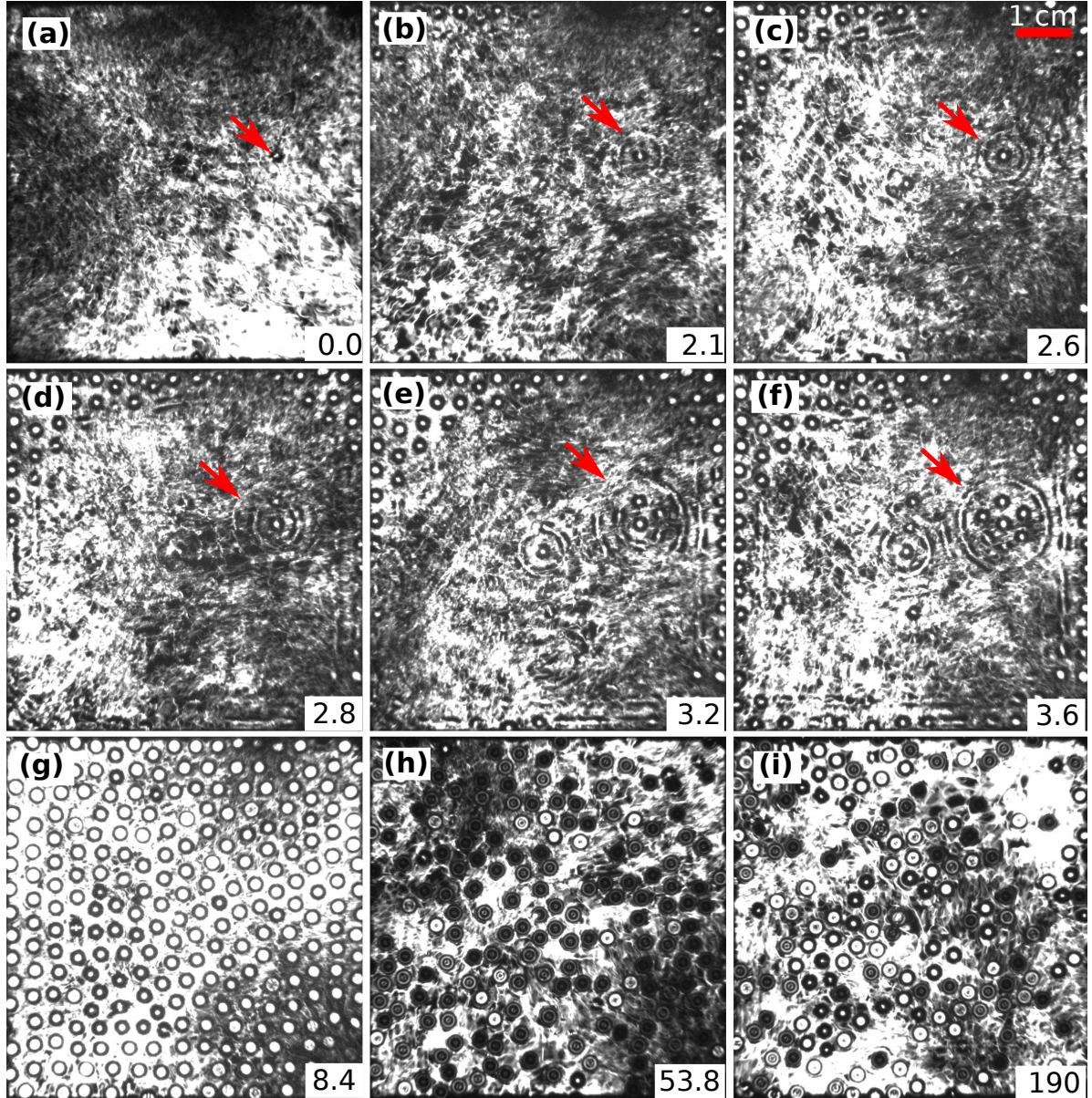


**Figure 3.3:** Evolution of the liquid layer below the top plate in the thick cell at  $T_b = 22.30$  °C,  $T_t = 22.00$  °C and  $P \approx 22.4$  bar. Time (in seconds) for each of these figures is indicated on the bottom right corner. Please note that the time stamp indicates the time from (a) and not the absolute time in the experiment. (a-c) evolution of the secondary azimuthal mode from a primary drop. (d-f) breakup of an azimuthal mode into drop like structures. (g-i) loss in symmetry due to dripping.

until the subsequent patterns interact with the nearby stripes or axisymmetric patterns. Figure 3.3 (g) shows a combination of the stripe like patterns and the axisymmetric arrangement of drops resulting in an organised arrangement with nearly hexagonal symmetry. The liquid layer continues to grow, as more vapor condenses onto the top plate, thus resulting in dripping. This results in a loss of symmetry and reduction in the height of the liquid layer locally. More defects start to develop in the arrangement over time (Fig. 3.3 (g-i )) until the rate of vapor condensation on the top plate was balanced

by the mass lost through dripping. The steady state observations are discussed in the next sub-section. The transient dynamics are similar in all experiments under different thermal conditions and so will not be discussed any further.

### 3.2.2 Statistically Steady State

Strictly speaking the term “steady state” is not appropriate in the context of this experiment as the system never attains steady state due to the continuous condensation and dripping of drops from the liquid layer above. Nevertheless, we use the phrase “steady state” in the sense that the net mass flux from/to the liquid layer attains a stationary state or a quasi-steady state. Figure 3.4 shows a sequence of images highlighting the effects of  $\Delta T$  on the steady state of the patterns. The  $T_t$  was maintained at 24.00 °C in all the cases and  $\Delta T$  was varied between 0.5 °C and 3.0 °C, and corresponding variations in the pressure was also observed (see figure caption for details). The pressure was maintained within  $\pm 0.05$  bar once the experiment attained stationary state. The fluctuations in pressure was predominantly due to the boiling of liquid SF<sub>6</sub> at the bottom plate and also due to the response time of the bottom plate temperature regulation loop.

The rate of boiling at the bottom plate increases with temperature difference and as a consequence, the rate of mass transferred onto/from the liquid layer was also enhanced. In Fig. 3.4 we observe that the stationary state arrangement of drops appeared more organised as  $\Delta T$  was increased. The hexagonal symmetry observed in the transient was re-established with the increase in thermal driving ( $\Delta T$ ). It is unusual to see that the symmetry in the pattern increases with the thermal driving. Let us look at the stationary state dynamics of two contrasting situations: (1) small  $\Delta T$ , resulting in a random arrangement of drops (Fig. 3.5 (a,b)), and (2) with sufficiently large  $\Delta T$  resulting in hexagonal patterns (Fig. 3.5 (d,e)). It is important to note that the term “small” and “large”  $\Delta T$  are used in a relative sense and strongly depend on the material properties of the fluid. At a fixed top plate temperature, a  $\Delta T$  is considered “large” or “small” depending on whether the corresponding steady state arrangement of drops contain an organized hexagonal symmetry or not. For example, at  $T_t = 22.00$  °C, a  $\Delta T = 0.5$  °C is considered “small” as it was not sufficient to form regular patterns. On the other hand, the same  $\Delta T$  was sufficient to generate hexagonal patterns at  $T_t = 42.00$  °C and is considered as “large”. In the following sections, we will refer to an experiment as “small”  $\Delta T$  when the imposed temperature gradient was not large enough to form organized patterns and as “large”  $\Delta T$  when the imposed temperature gradient was large enough to form organized hexagonal patterns. The drop like deformation in the liquid layer at the top plate is henceforth referred to as “drop” in this chapter.

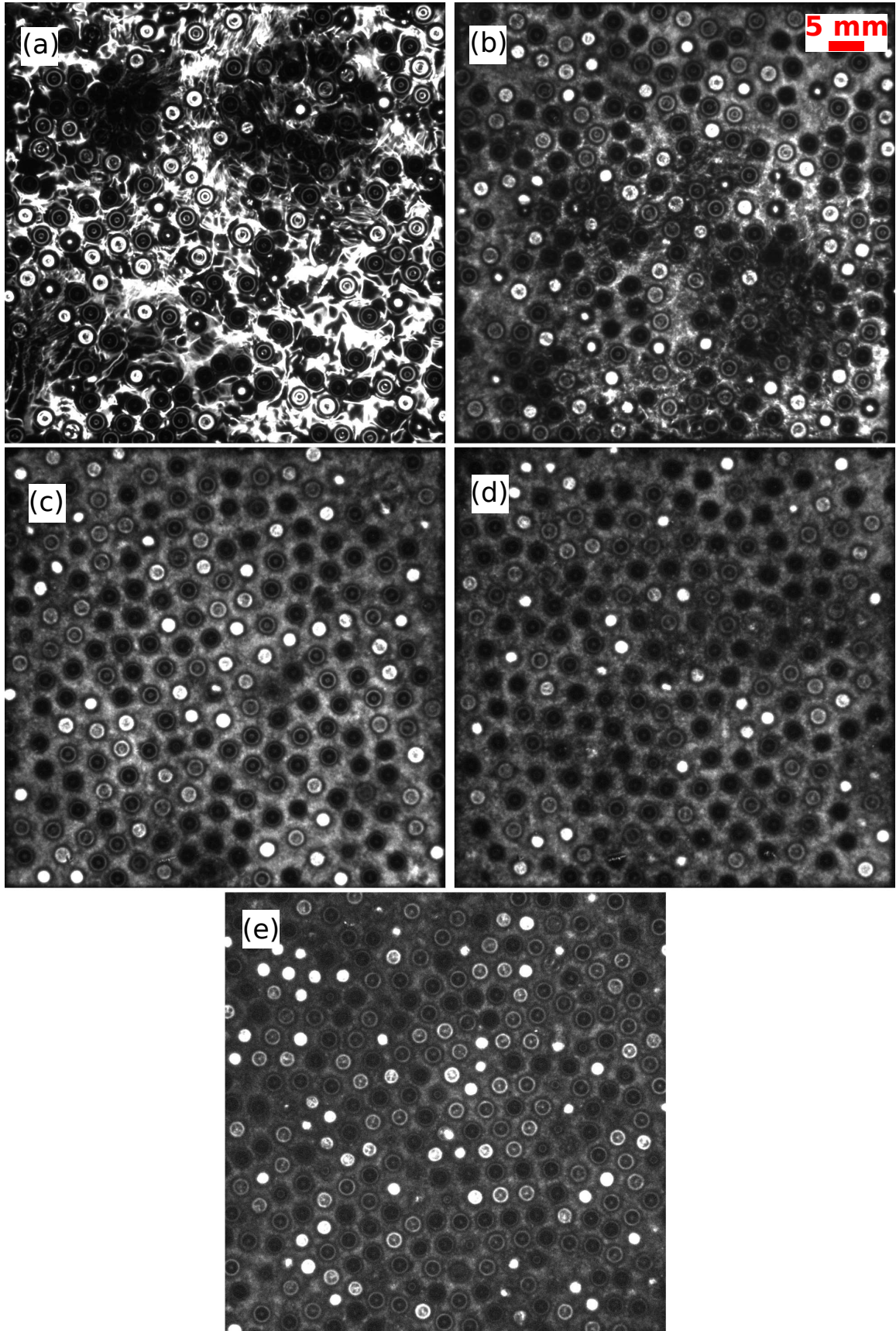


**Figure 3.4:** Effect of  $\Delta T$  on the patterns in the thick cell under steady conditions.  $T_t = 24.00^\circ\text{C}$ . (a)  $\Delta T = 0.55^\circ\text{C}$ ,  $P = 23.4$  bar, (b)  $\Delta T = 1.30^\circ\text{C}$ ,  $P = 23.5$  bar, (c)  $\Delta T = 2.05^\circ\text{C}$ ,  $P = 23.9$  bar, (d)  $\Delta T = 2.55^\circ\text{C}$ ,  $P = 24.0$  bar and (e)  $\Delta T = 2.90^\circ\text{C}$ ,  $P = 24.1$  bar. Scale bar is shown in (b) for all images.

### 3.2.2.1 Small $\Delta T$ - Low Thermal Driving

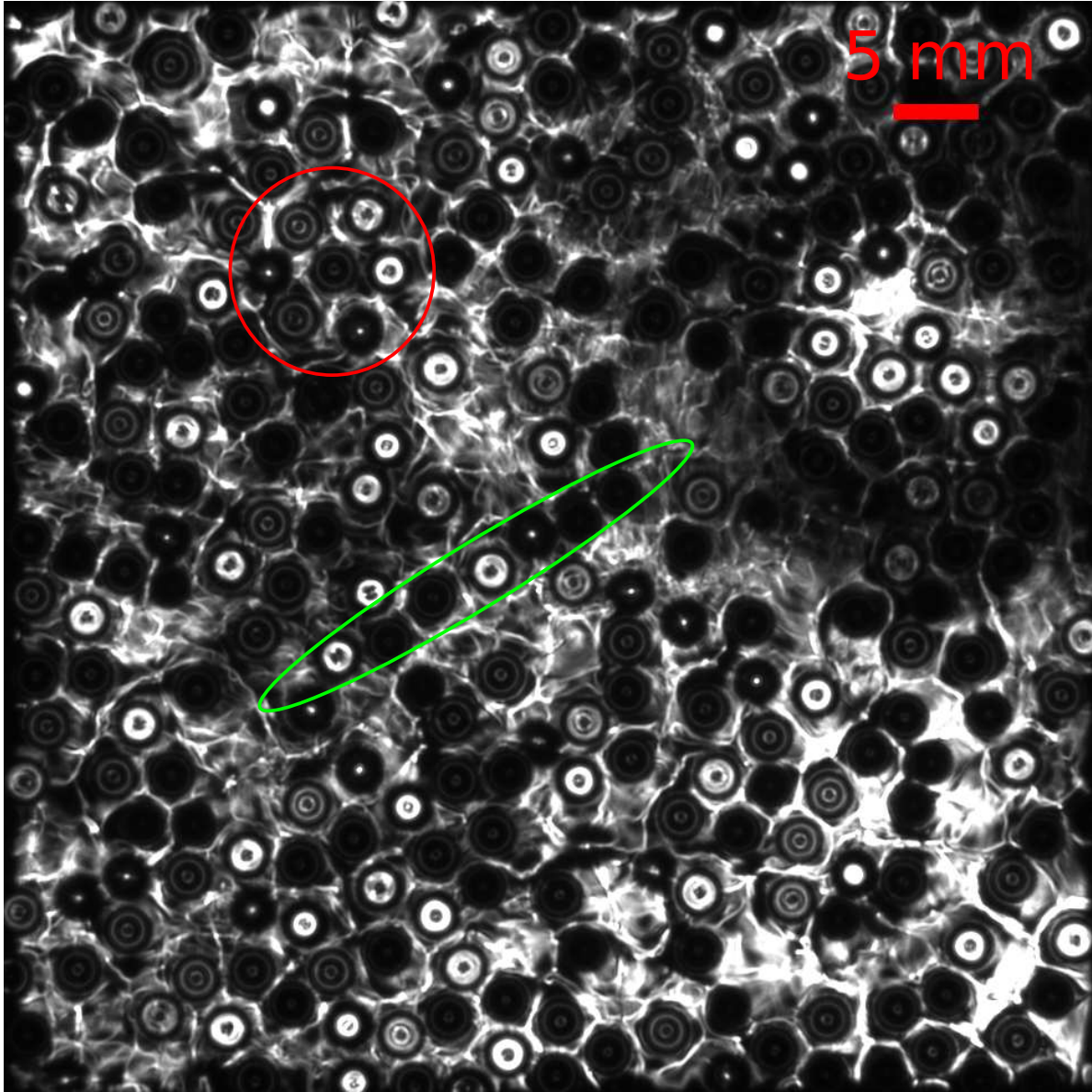


**Figure 3.5:** Thick cell - small  $\Delta T$ : Arrangement of drops in the thin liquid layer at the top plate at  $T_t = 28.00$  °C,  $\Delta T = 0.55$  °C and  $P = 25.5$  bar. An isolated hexagonal cluster of drops is marked in red and an isolated linear arrangement (stripe) of drops is marked in green.

Figure 3.5 shows a snapshot from an experiment where  $\Delta T$  was not large enough to generate hexagonal patterns. The  $T_t$  was set to 28.00 °C and a temperature difference of  $\Delta T = 0.55$  °C was imposed across the plates. The underlying convection in the vapor phase was not visible as the thin liquid layer at the top plate masked the convective motions. The axisymmetric black patches in the background was due to the dripping of drops from the liquid layer. Surface waves were generated as these drops fell into the liquid pool above the bottom plate. These waves or disturbances cast a shadow in the background, thus, locally affecting the intensity contrast caused by the drop-like

deformations in the liquid layer on the top plate. The arrangement of the pattern in Fig. 3.5 are non-periodic (random). There are some isolated clusters of drops with a nearly hexagonal symmetry (one such cluster is marked in the Fig. 3.5). There are also some isolated stripes consisting of an array of drops (one such stripe is marked in green in Fig. 3.5). The formation of a new drop in the liquid layer is shown in the sequence presented in Fig. 3.6. The deformation of the liquid layer before the formation of a drop is visible in Fig. 3.6 (a and b). The emergence of the drops are visible in Fig. 3.6 (b, c and d).

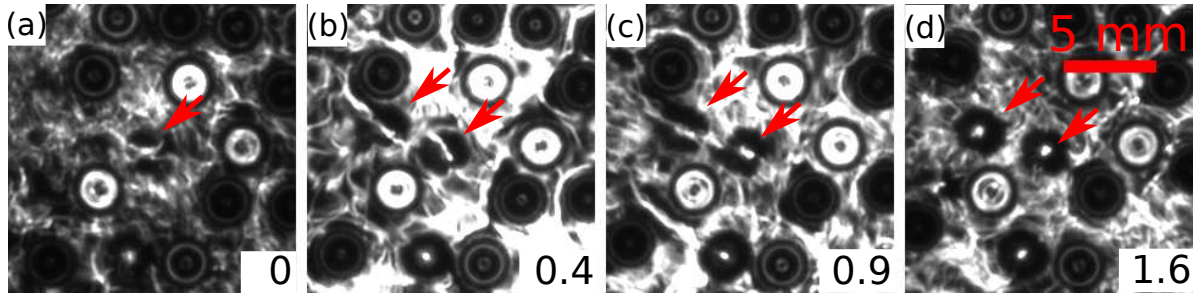
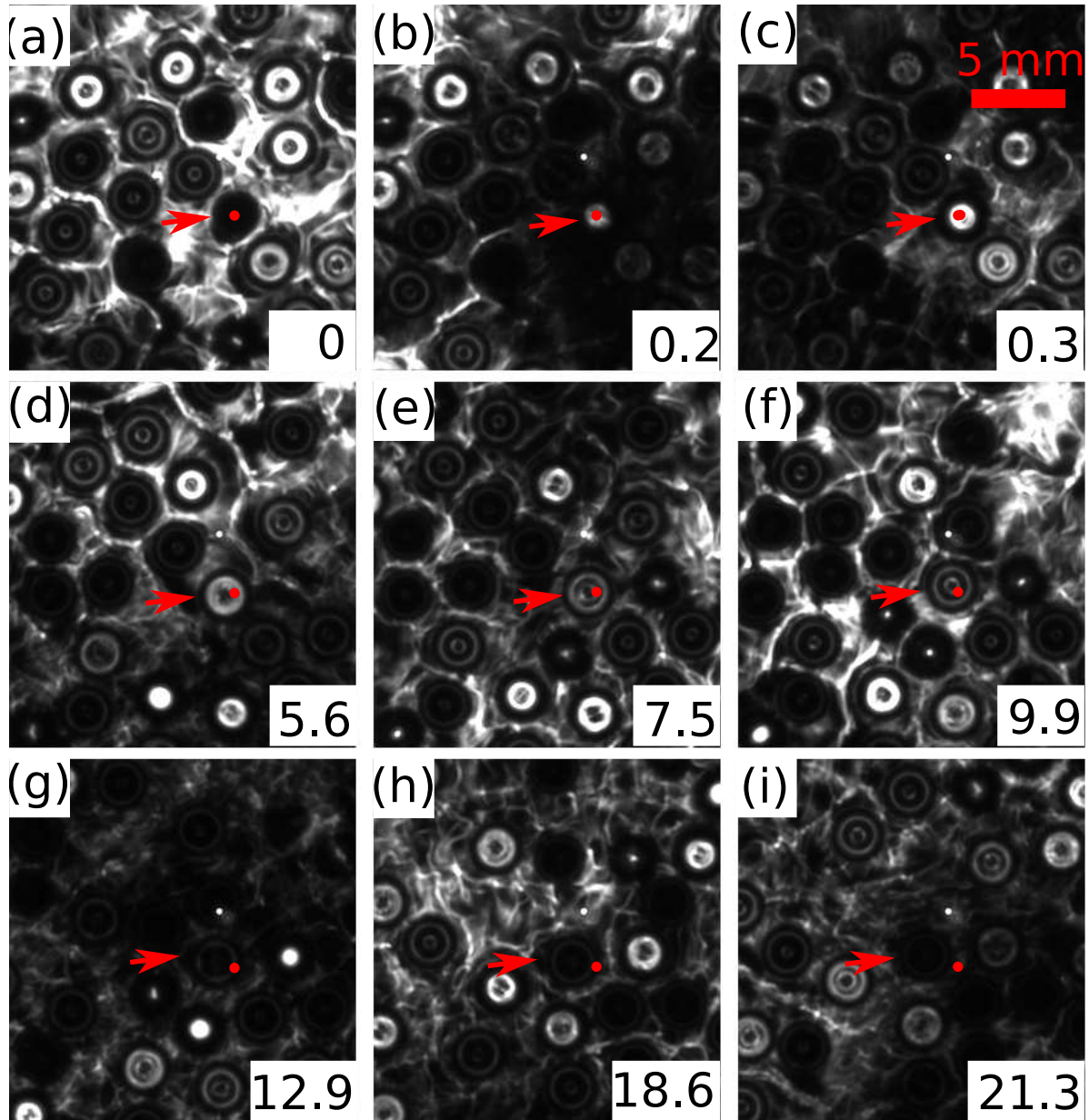


**Figure 3.6:** Thick cell - Formation of drops in the liquid layer at the top plate. (a, b) Deformation of the liquid film. (c, d) Deformations develop into drops. See Fig. 3.5 for the experimental conditions.

Figure 3.7 and Fig. 3.8 shows the evolution of a drop in the liquid layer at the top plate. A drop in the liquid layer acts as a lens, and as it grows, the focal length of the lens changes. A drop appears bright if the transmitted light was focused on to the image plane. In the present arrangement of the camera lens system, a newly formed drop appears bright, and the intensity of the drop decreases as it grows. A drop appears black just before it detaches from the liquid layer. The intermediate stages were of different intensities on the gray scale with some fringes inside the drop.

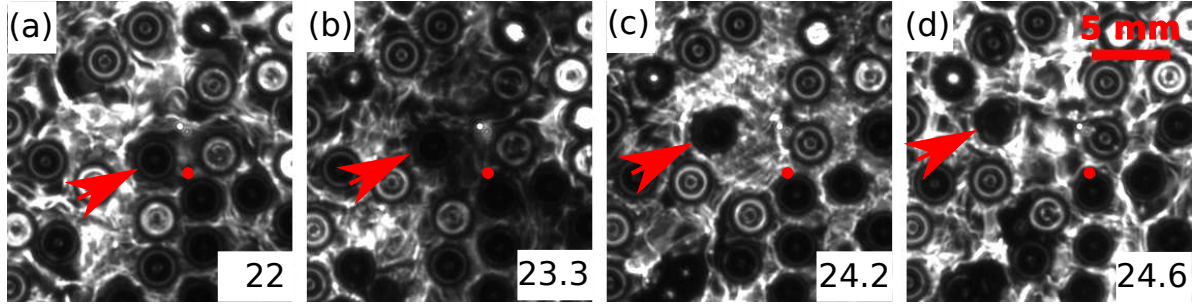
Figure 3.7 (a, b) shows a large drop detaching from the liquid layer on the top plate. The variation in the intensity of the drop from dark to bright is visible from Fig. 3.7 (a and b). Moreover, the background intensity around the drop also changes from bright to dark. This was due to the formation of surface waves from the falling of the drop into the liquid pool below. The propagation of the wave fronts are visible in Fig. 3.7 (b, c). In the next few seconds shown in Fig. 3.7 (d-f), the drop moves about 2 mm from its origin. During this time, the drop develops fringes in its core due to the variation in its focal length. Over time the intensity of the fringes decreases and the core of the drop appears black (Fig. 3.7 (g-i)). The drop grows due to the condensation of vapor on its surface and also due to material flux from the surrounding liquid layer. The drift velocity of the drop increases once it attains a certain critical size (not measured here). The drop moves around until it drips. The rapid drift and final dripping is shown in Fig. 3.8 (a-d).

The variation in the position of a drop as a function of time is shown in Fig. 3.9.

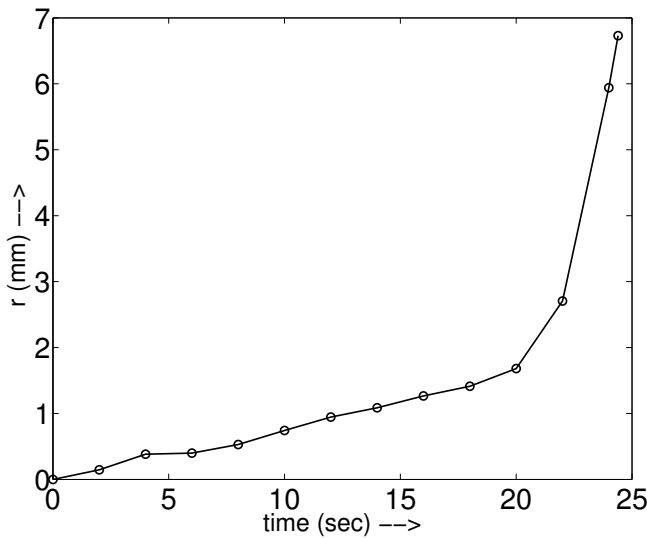


**Figure 3.7:** Thick cell: Sequence of images depicting the evolution of a drop in the liquid layer at the top plate. See Fig. 3.5 for experimental conditions. The red dot indicates the location where the drop was formed and the arrow indicates the drop under discussion. Time stamp in seconds is shown in the bottom right corner of each image.

$t = 0$  indicates the time when the drop was formed. The location marked in Fig. 3.7 (b) was used as the origin for the drop.  $r$  is the displacement of the drop from its origin. The flow in the vapor phase was turbulent. Please note that  $Ra$  was not explicitly calculated as the temperature distribution across the liquid pool and the vapor phase was not measured. The approximate Rayleigh number based on the cell height and the vapor phase properties was around  $Ra \approx 10^7$ . From Fig. 3.9, we infer that the displacement of the drop was not significant in the initial stages of its development as opposed to the later stages. A possible reason could be that as the drop grew in



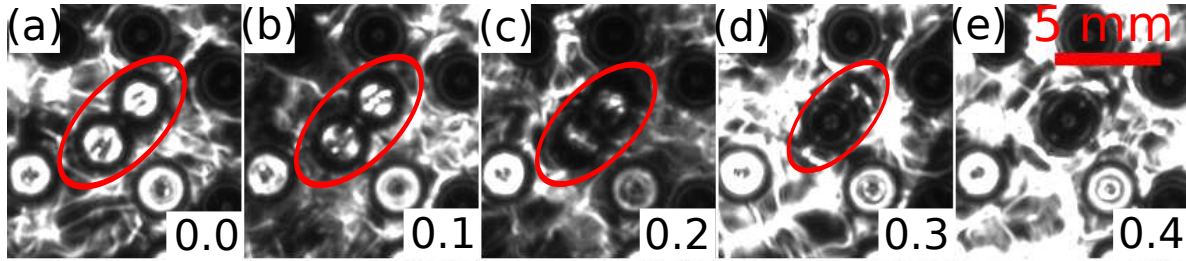
**Figure 3.8:** Thick cell - Drifting of a drop in the liquid layer. See Fig. 3.5 caption for experimental conditions. The red dot indicates the location where the drop originated (Fig. 3.7(b)) and the arrow indicates the drop under discussion. Time stamp (continuation from Fig. 3.7) in seconds is shown in the bottom right corner of each image.



**Figure 3.9:** Displacement of the drop discussed in Fig. 3.7 & 3.8 from its origin as a function of time.

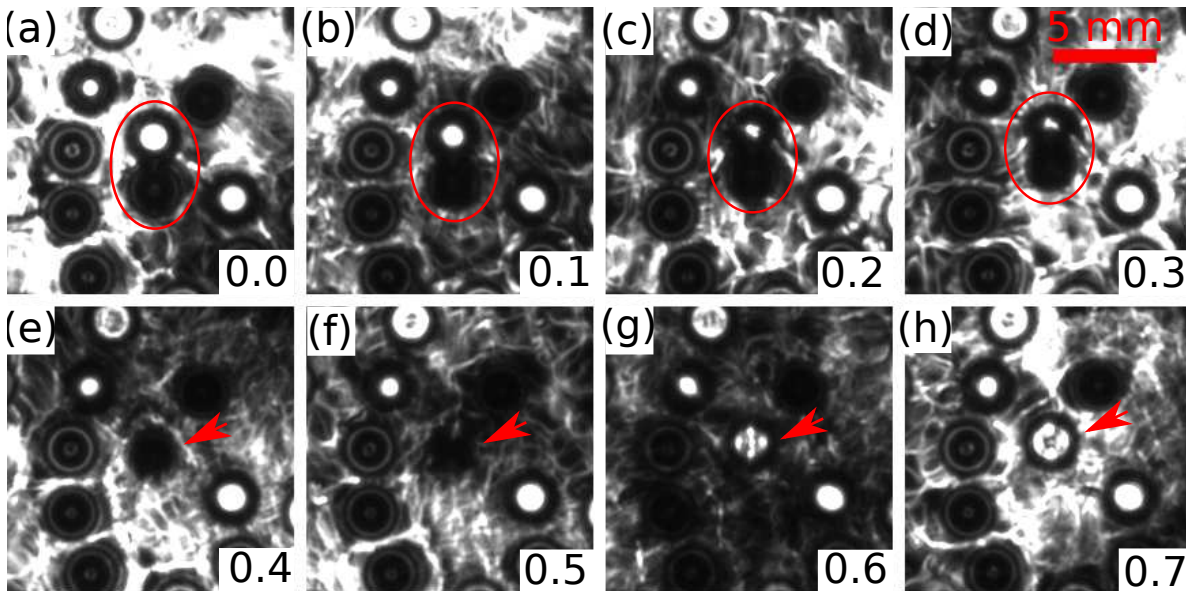
size, it interacted with the underlying flow, and was pushed around by the convective circulations in the vapor region until it detaches from the liquid layer. In a classical RBC system, in the plane of LSC, the horizontal velocity increases with the distance from the top plate in the boundary layer [87]. Assuming that the velocity field here is similar to that in a classical RBC system, the enhanced velocity encountered by the large drops could be responsible for their drift. There exists the possibility that the drifting of drops was due to the inclination of the top plate. The drop under discussion moved towards the upper left corner, but the trajectory encountered some deviations from a straight line. These deviations may also be due to the disturbances in the liquid layer. Please note that the direction in which a drop drifts depends on its location. Nevertheless, the evolution of all the drops in the liquid layer are similar to the drop described above.

As stated above, drops larger than a certain size drifts around in the liquid layer until



**Figure 3.10:** Merging of two drops (within the red oval) of nearly equal diameters. See Fig. 3.5 caption for experimental conditions. Time stamp in seconds is shown on the bottom right corner of each image.

they drip. As these drops move, they may collide with other drops in the neighbourhood. Figure 3.10 shows the merging of two drops of equal size in the liquid layer. In Fig. 3.10 (a, b) two (primary) drops are visible. From the intensity of the drops in Fig. 3.7 we infer that the primary drops in Fig. 3.10 (a,b) were relatively small. We see that the distance between the drops has decreased from Fig. 3.10 (b) to Fig. 3.10 (c). In fact, it is not easy to distinguish the primary drops in Fig. 3.10 (c, d). The resultant drop post merger is marked in Fig. 3.10 (e) and the average intensity of the drop is significantly lower than the primary drops, thus, indicating that the size of the drop post merger is comparable to a drop in its final stages before it drips down. Please note that the final drop did not drip immediately post merger.



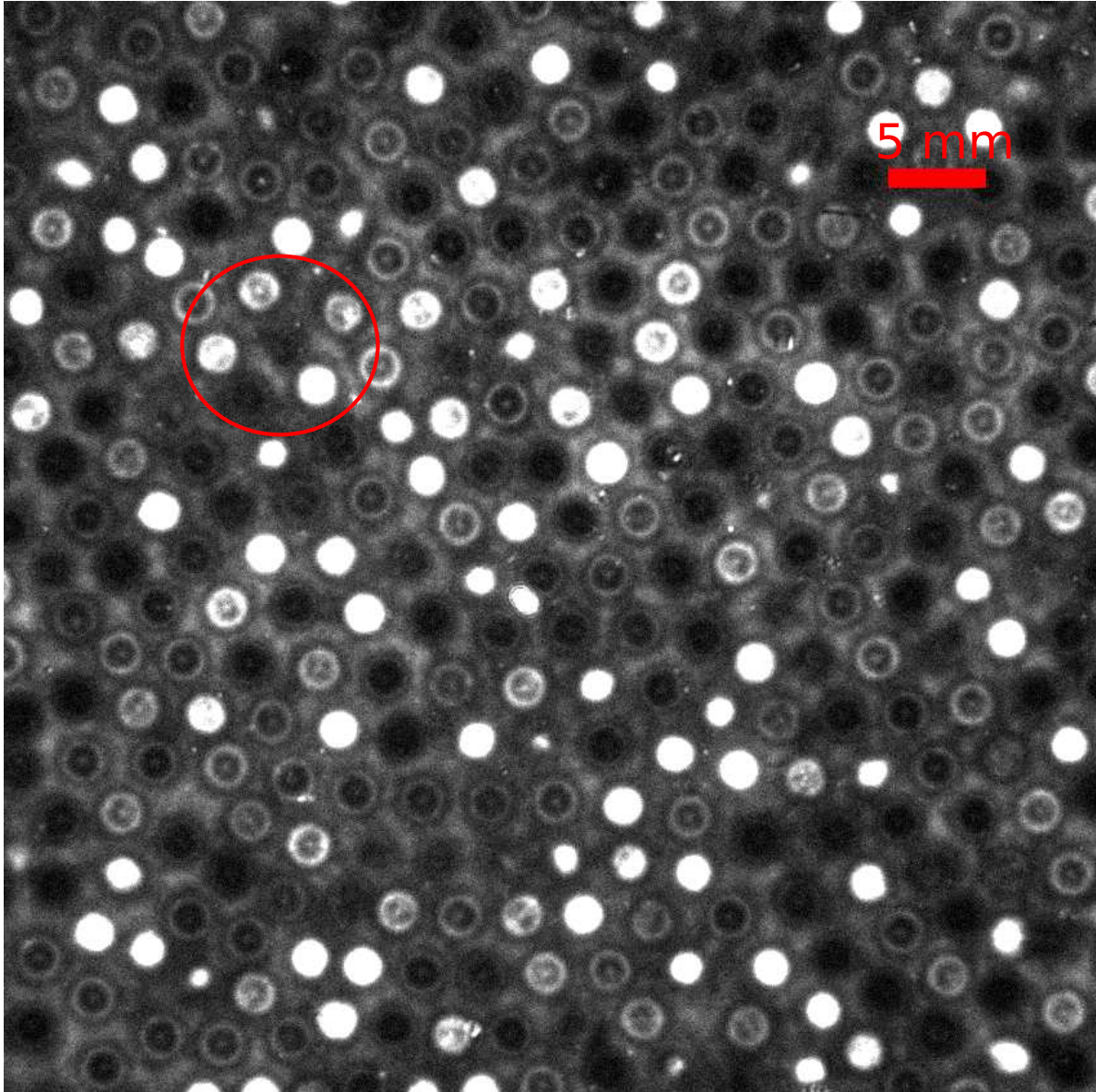
**Figure 3.11:** Thick cell - (a-d) Merging of two drops of different sizes. (e-f) Post merger evolution of the drop. See Fig. 3.5 caption for experimental conditions. Time stamp in seconds is shown in the bottom right corner of each image.

Figure 3.11 shows the dynamics associated with the merging of two drops of different sizes. The primary drops in Fig. 3.11 (a) appear with different grey scale intensities in the shadowgraph image. One of them is a large drop, i.e., large enough to drift around,

and the other drop is small, and is in its initial stages of development. In Fig. 3.11 (a-d), we notice that the difference in distance between the two drops decreases over time, as the larger drop moves towards the smaller drop. The final drop is visible in Fig. 3.11 (e) with very low intensity, indicating that the drop is about to drip. The dripping of the merged drop and the formation of a new drop is shown in the image sequence presented in Fig. 3.11 (e-h). The splash and the associated surface waves are visible in Fig. 3.11 (g, h). The size of the final drop depends on the size of the primary drops. If the primary drops were small then the final drop does not drip immediately. On the other hand, if at least one of the primary drops were sufficiently large then the resulting final drop drips down immediately.

### 3.2.2.2 Large $\Delta T$ - High Thermal Driving

Figure 3.12 shows an instantaneous snapshot from an experiment where  $\Delta T$  was large enough to generate spatially periodic patterns in the liquid layer at the top plate. The  $T_t$  and  $\Delta T$  were set to 28.00 °C and 3.00 °C respectively. The large temperature difference between the two plates triggered boiling in the liquid pool at the bottom plate. The formation of bubbles scatters all the light entering into the convection cell. As a consequence, the background has a lower intensity (Fig. 3.12) as compared to the non-boiling liquid pool case in Fig. 3.5. The random distribution of bubbles in the liquid pool results in a uniform background intensity which aids image processing. The shadow cast by the surface waves in the background is not visible in Fig. 3.12. The variation in the intensity of the drops in Fig. 3.12 is similar to that in Fig. 3.5. The arrangement of drops on the top plate has hexagonal symmetry, with almost every drop surrounded by six neighbouring drops. At certain locations defects in the pattern causes a drop to have five or seven neighbours instead of six. One such defect is marked in Fig. 3.12. The drops shown in Fig. 3.12 are at different stages of development. If a drop drips from the liquid layer then it will not be visible until a new drop is formed at the same location. Some of these defects disappears if we look at an image processed over time. One such image is shown in Fig. 3.13(a), showing the top view of the full convection cell, where each pixel represents the maximum intensity over 30 frames (3 seconds). Figure. 3.13 (a) shows that there are some disturbances in the drop arrangement close to the four corners of the cell and as we move towards the centre of the cell, the patterns appear to be stationary. The four corners are near the edge of the top plate and hence are subjected to additional dynamics associated with the boundaries which may influence the movement of the patterns. For the analysis presented in the thesis, only the patterns near the center of the cell are used. The drops in the liquid layer drift in a particular direction due to the inclination of the top plate or due to the underlying large scale convective flow. The drift is better visible by extending the duration for detecting the



**Figure 3.12:** Thick cell - large  $\Delta T$ : Arrangement of drops in the liquid layer under the top plate in the thick cell at  $T_t = 28.00^\circ\text{C}$ ,  $P = 26.6$  bar and  $\Delta T = 3.00^\circ\text{C}$ . Red circle - a defect in the arrangement.

maximum value at each pixel. Figure 3.13 (b) shows an image generated by processing over 200 images (20 seconds). The drifting of the drops become apparent as white stripes. The drift directions are marked in the figure. Not all drops are moving in the same direction. It appears that the drift motion was a combination of the inclination of the top plate and also the underlying convection in the vapor phase. The inclination of the top plate was unavoidable due to the complexity of the experiment.

Let us look at the local dynamics of the drops in the present system. Figure 3.14 shows the dynamics of a hexagonal patch of drops. Figure 3.14 (a) shows the formation of a drop in the core of the hexagonal patch under consideration and Fig. 3.14 (i) shows the dripping of the core drop, thus, completing a cycle (from formation to dripping).

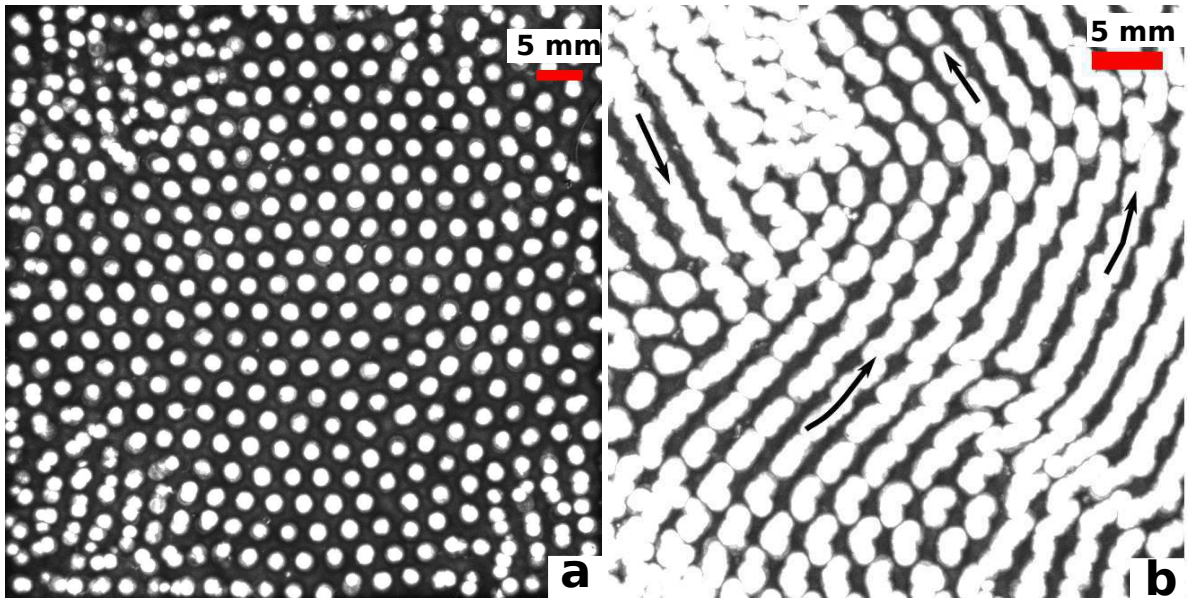


**Figure 3.13:** Thick cell: Drop arrangement processed over time. Each pixel represents the maximum intensity over a certain duration of time. See Fig. 3.12 for the experimental conditions. (a) Image processed over 3 seconds. (b) Image processed over 20 seconds. The arrows indicate the drift direction of the drops.

The surrounding drops were at various stages of development. The remaining images shows the intermediate stages of these drops. The intensity variation of the drop in the large  $\Delta T$  case is similar to the small  $\Delta T$  case shown in Fig. 3.5. These drops move slightly about their mean position, but the net drift during the course of a single cycle was not significant, which is in contrast to the small  $\Delta T$  case (Fig. 3.7).

From Fig. 3.13 we infer that the net displacement of a drop in a cycle at large  $\Delta T$  is rather low and is comparable to the size of the drop. We make use of this information to construct the intensity history of a given drop. Figure 3.15 shows the variation in gray-scale intensity of a drop as a function of time. From this plot we calculate the average time period of dripping for this drop to be about 2 seconds. The time period for a drop in the large  $\Delta T$  experiment in Fig. 3.12 is much smaller than the period calculated for the small  $\Delta T$  experiment in Fig. 3.5 (about 24 seconds). This may explain why the drops do not drift significantly in the large  $\Delta T$  case. These drops act as a high Stokes number particle subjected to a shear flow. So the time required for a drop to respond to the imposed shear, i.e., the response time of the drop, is quite high. If the life cycle of the drop is significantly smaller than the response time, then the drop will drip before it starts to drift. As a consequence, the drops drift significantly under the influence of gravity and the underlying convective flow in the small  $\Delta T$  case due to a relatively long development timescale compared to the large  $\Delta T$  case.

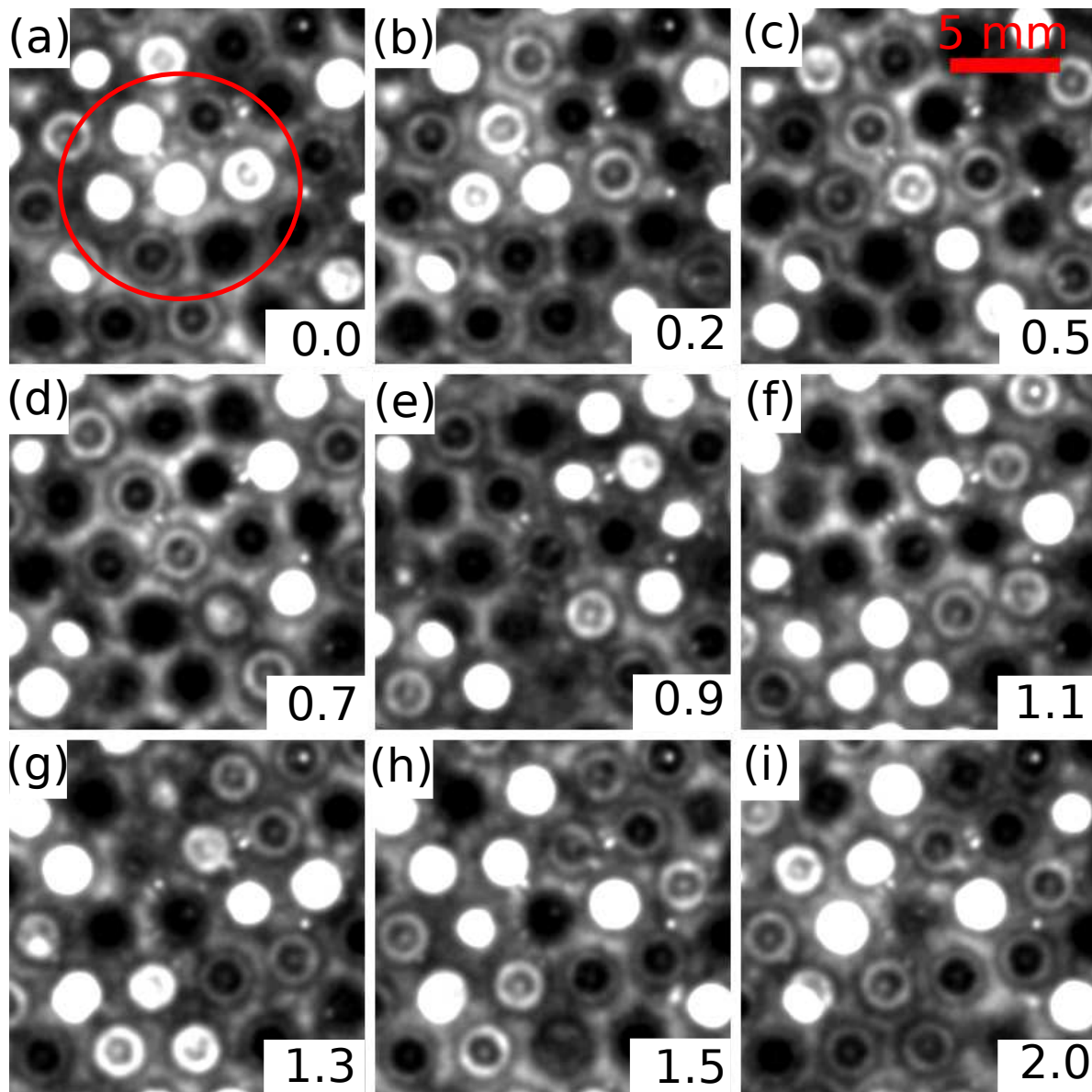


**Figure 3.14:** Thick cell - large  $\Delta T$  - Temporal dynamics of a hexagonal patch in Fig. 3.12. See Fig. 3.12 for experimental details.

### 3.2.3 Spectral Analysis

In this section we look at the Fourier transform of the patterns in the large  $\Delta T$  experiment. Figure 3.16 (a) shows the central part of Fig. 3.13 (a) and thus is nearly undisturbed by the disturbances close to the lateral boundaries. The image was processed to identify the centre of mass of each drop. Later, the image was reconstructed with a black background and a peak at the center of each drop. This reduces the noise from the background and also from the oscillations of the drop. A sample snapshot of the reconstructed image is shown in Fig. 3.16 (b). The power spectrum of the reconstructed image is shown in Fig. 3.17 (a). Six distinct peaks are visible and they represent

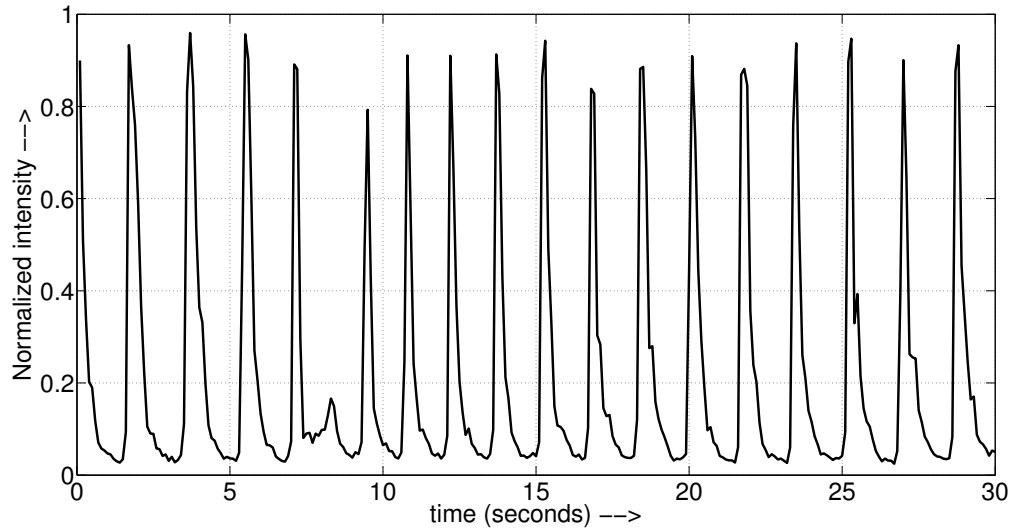


**Figure 3.15:** Intensity variation of a drop in Fig. 3.12 as a function of time

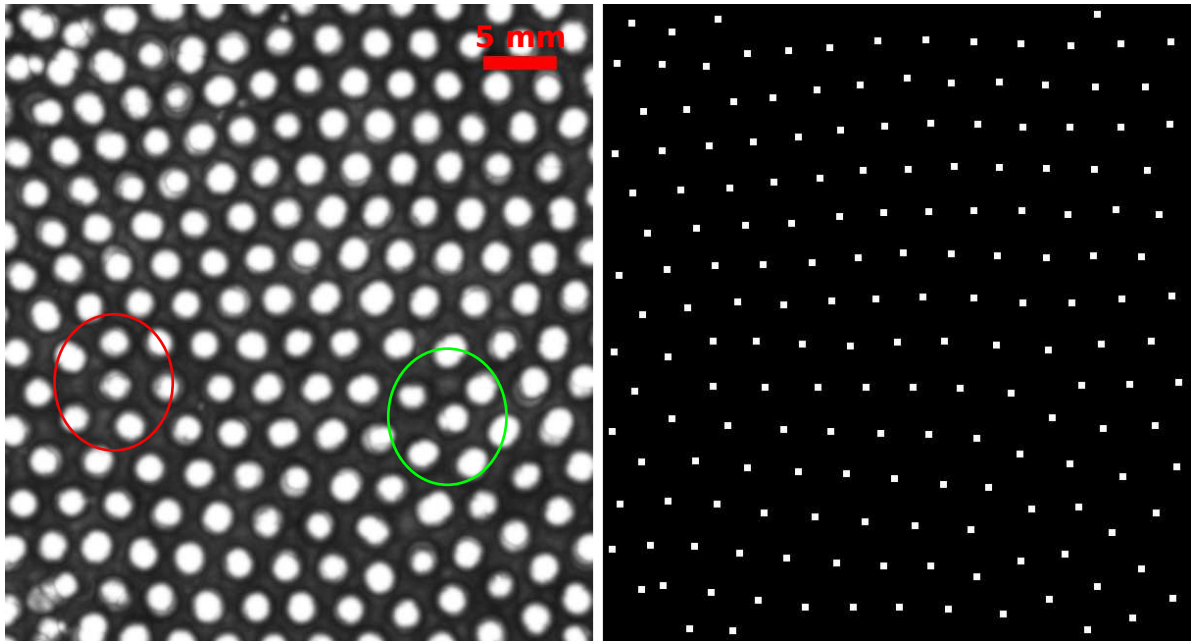


**Figure 3.16:** (a) Averaged image from Fig. 3.13 (a). The circles mark some of the defects in the pattern. (b) Processed image with the identified drop centers.

three different wave vectors. Each wave vector has two peaks corresponding to  $\mathbf{k}$  and  $-\mathbf{k}$ . The wave vectors are marked in Fig. 3.17, and the inverse Fourier transform of these vectors are shown in Fig. 3.18 (a-c). Each of these vectors correspond to stripe pattern inclined at  $120^\circ$  from each other. These stripe patterns combine together to form the hexagonal lattice. Please note that the images in Fig. 3.18 are contrast enhanced for the sake of clarity. The stripes are nearly straight with some wavy undulations. These undulations indicate the disorganization in the hexagonal pattern.

The defects in Fig. 3.16 are visible in stripe patterns in Fig. 3.18 (a-c). A defect

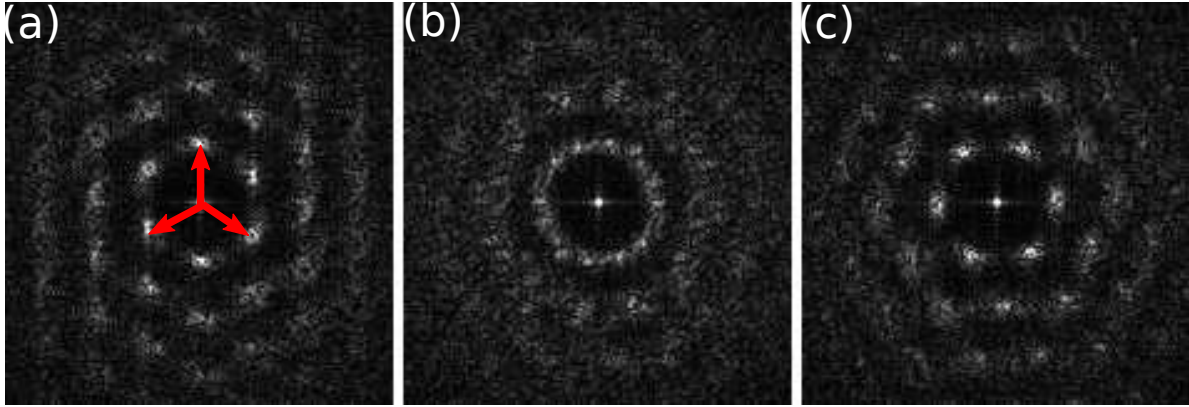


**Figure 3.17:** 2D power spectrum of the drop arrangement on the top plate in the large  $\Delta T$  experiments. (a) 2D power spectrum of Fig. 3.16 at  $t = 0$ . The arrows represent the wave vectors; (b)  $t = 63$  seconds and (c)  $t = 111$  seconds.

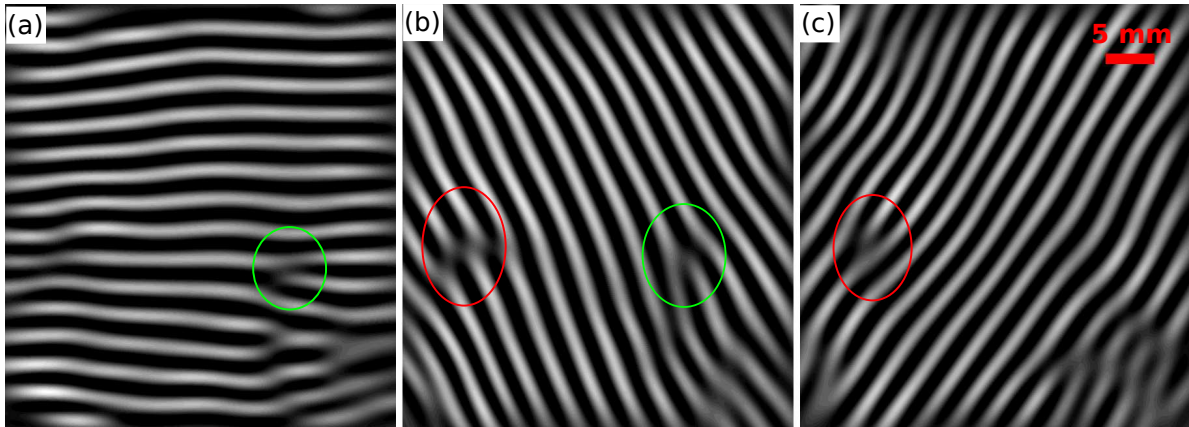


**Figure 3.18:** Inverse Fourier transform of the wave vectors marked in Fig. 3.17(a). The defect locations are marked in red and green.

is defined as a localized irregular arrangement in a pattern. A defect location is identified as the crossing of two stripes or the termination of a stripe within the cell [79]. These are dislocation defects among two of the stripe patterns that form the hexagonal lattice structure [79]. One such defect location is marked in Fig. 3.16 and Fig. 3.18. Figure 3.17(a, c) shows the magnitude of the Fourier transform of the patterns at two separate instants (111 seconds apart). An intermediate stage about 63 seconds after the Fig. 3.17(a) is shown in Fig. 3.17(b) and it does not contain six distinct peaks as in Fig. 3.17(a, c). We note that the peaks have shifted by about 30 degrees in the anti-clockwise direction between Fig. 3.17(a) and Fig. 3.17(c). Over time the stripes appear to be exhibiting azimuthal motion which may be due to the large scale flows in the convection cell.

Figure 3.19 depicts the propagation of defects in the liquid layer using a single stripe pattern. Merging of two or more drops result in the formation of a defect in the pattern arrangement. One such distorted stripe pattern is visible in Fig. 3.19 (b). This defect

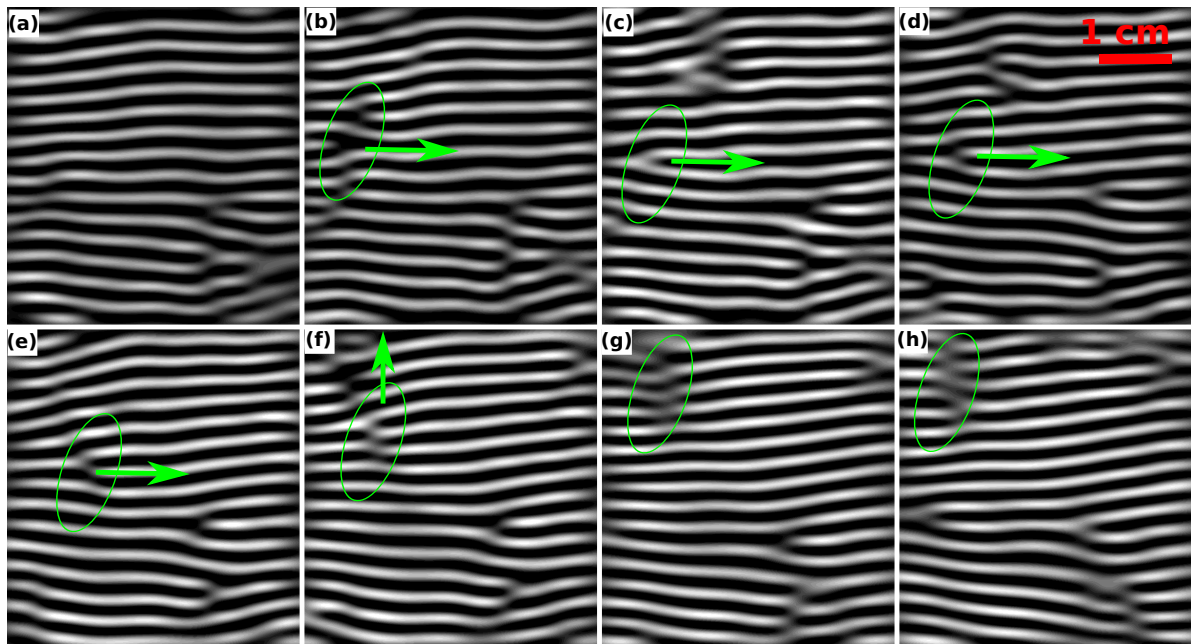


**Figure 3.19:** Time lapse of the Fourier transform of a single wave vector. The time difference between each image is 100 ms. The green oval marks a defect location and the green arrow indicates the propagation direction of the defect.

originated due to the merging of two drops. This results in the formation of a void in the packing, which initiates the movement of neighbouring drops to fill the void. As a consequence, the defects propagate to a different stripe structure as shown in Fig. 3.19 (b-g). The defects drift until a new drop is formed in its neighbourhood, thus re-establishing the symmetry in the stripe pattern. The movement of the defects may result in other drop coalescence events.

### 3.2.4 Steady State Statistics

So far we have discussed the experimental observations for a particular top plate temperature and two different bottom plate temperatures. Figure 3.20 presents the conditions for all the experiments conducted in the thick cell that resulted in a hexagonal pattern in the stationary state. The experiments were conducted such that  $T_t$  was kept constant and  $\Delta T$  was varied until the hexagonal patterns were established. In principle, the experiments could have been conducted with a constant  $T_b$  and variable  $T_t$ , but the time required to vary  $T_t$  was significantly greater ( $\approx 30$  minutes per  $^\circ\text{C}$ ) than the time required to vary  $T_b$  ( $\approx 1$  minute per  $^\circ\text{C}$ ). The thick black curve in Fig. 3.20 represents the liquid vapor coexistence line for  $\text{SF}_6$ . The red and blue dots represent the bottom and top plate conditions respectively. The red dots are in the vapor phase in almost every case, thus suggesting that the liquid layer on the bottom plate was boiling. Note that the bottom plate was always covered with a condensed liquid layer. The thin black line joining the red and blue dots represent the mean pressure during the experiment.

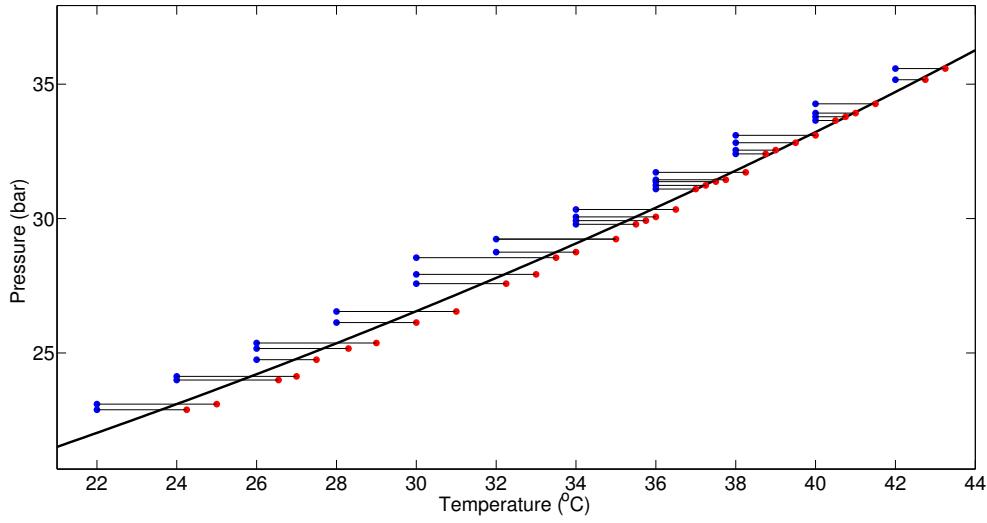


**Figure 3.20:** Measurement overview - thick cell.  $\bullet$ ,  $T_t$ ;  $\bullet$  -  $T_b$ . The thick black curve indicates the liquid-vapor coexistence curve for  $\text{SF}_6$  and the line connecting the top and bottom plate conditions represent the pressure in the experiment.

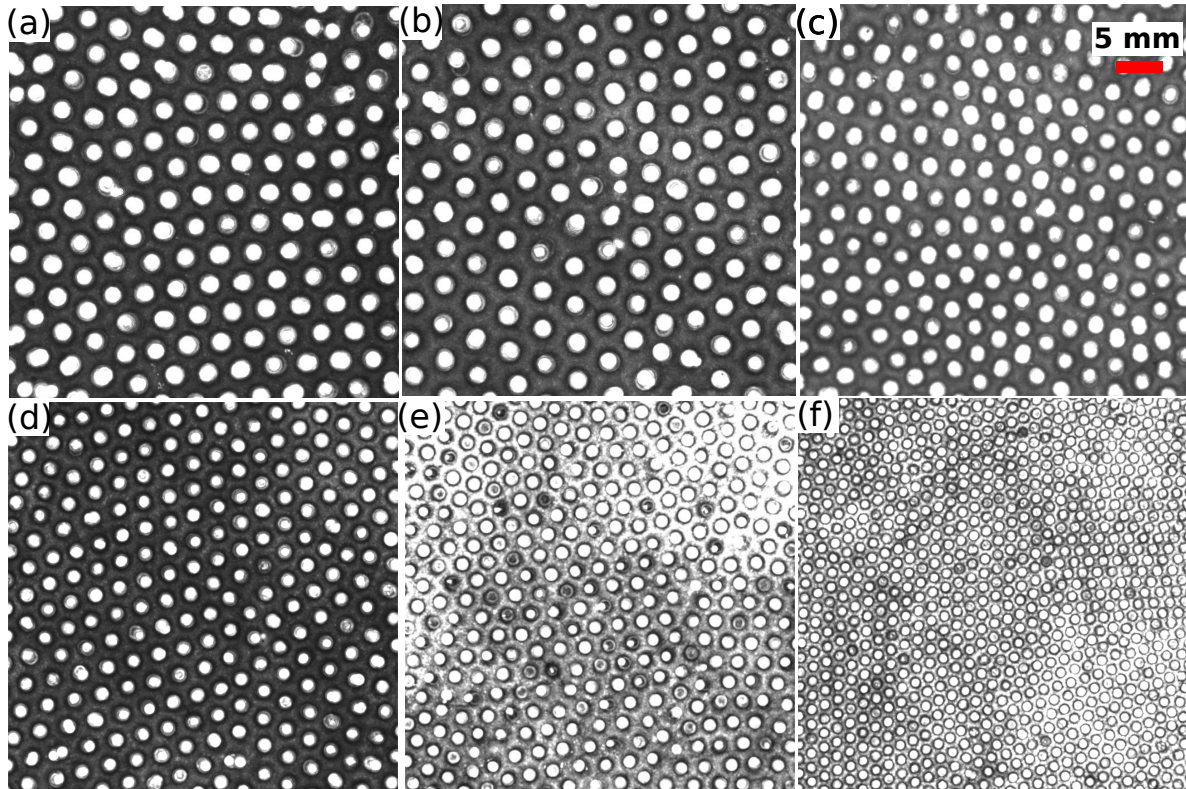


**Figure 3.21:** Stationary state patterns under different conditions across the liquid-vapor coexistence curve. (a)  $T_t = 22.00$  °C,  $\Delta T = 3.00$  °C,  $P = 23.1$  bar. (b)  $T_t = 26.00$  °C,  $\Delta T = 2.30$  °C,  $P = 25.2$  bar. (c)  $T_t = 30.00$  °C,  $\Delta T = 3.00$  °C,  $P = 27.9$  bar. (d)  $T_t = 34.00$  °C,  $\Delta T = 1.50$  °C,  $P = 29.8$  bar. (e)  $T_t = 38.00$  °C,  $\Delta T = 1.00$  °C,  $P = 32.5$  bar. (f)  $T_t = 42.00$  °C,  $\Delta T = 0.50$  °C,  $P = 35.2$  bar.

Figure 3.21 shows a sequence of images representing the stationary state patterns under various thermodynamic conditions covering the entire range of the liquid-vapor

coexistence line accessed in the experiment. The images shown here were processed over a duration of 3 seconds to eliminate the effects of dripping and also to reduce the background noise. Each pixel represents the maximal intensity over a duration of 3 seconds. We note that the hexagonal symmetry is obtained for all top plate temperatures. The temperature difference required to attain the hexagonal pattern decreases as the the top plate temperature was increased. The symmetry in the pattern arrangement increases with the top plate temperature. This maybe due to the decrease in the imposed  $\Delta T$ . Lower  $\Delta T$  results in a lower thermal driving and also a lower rate of boiling.

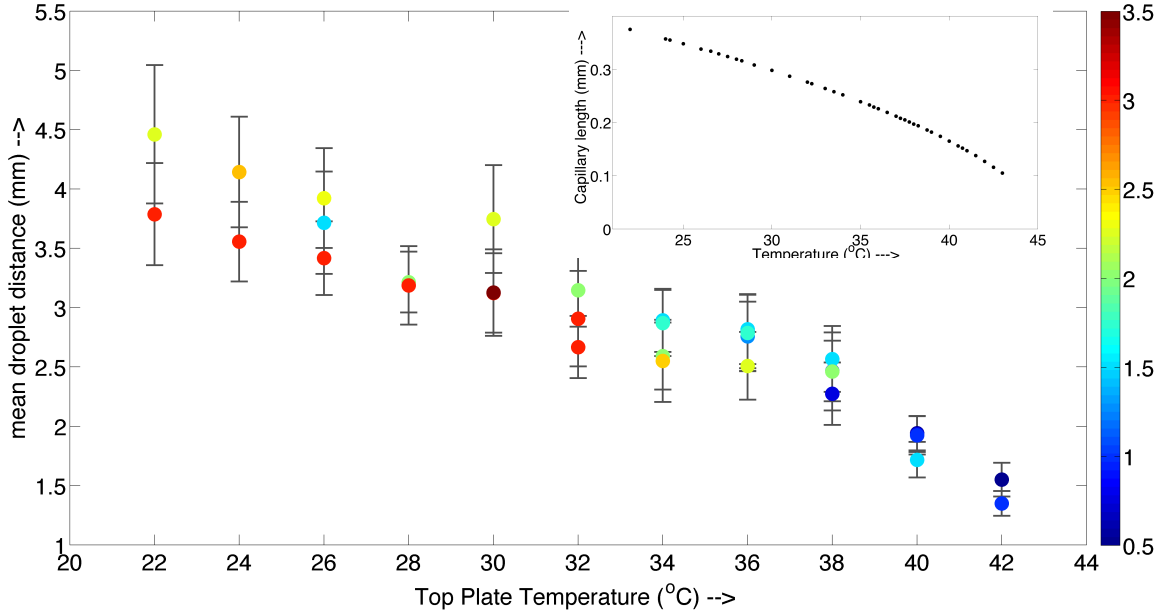


**Figure 3.22:** Variation of mean distance between drops as a function of the top plate temperature. The inset shows the variation of capillary length as a function of temperature. Color code represents  $\Delta T$ .

Figure 3.22 shows the mean distance between the drops as a function of the top plate temperature and . From Fig. 3.22 we infer that the mean distance between the drops decreases with the increase in  $T_t$ . For a fixed  $T_t$ , the mean distance between the drops decreases as the  $\Delta T$  was increased. The inset in Fig. 3.22 shows the variation of the capillary length  $l_c = \sqrt{\frac{\sigma}{(\rho_l - \rho_v)g}}$  as a function of the temperature, where  $\sigma$  is the surface tension,  $\rho_l$  is the density of the liquid phase,  $\rho_v$  is the density of the vapor phase and  $g$  is the acceleration due to gravity. We note that the variation in the mean drop distance as a function of the top plate temperature is similar to the variation in the capillary length. Figure 3.23 depicts the variation in the pattern wavelength  $\lambda$  as a function of the top plate temperature. The pattern wavelength decreases with temperature similar to the mean distance between the drops. Figure 3.24 shows the wavelength in the pattern normalized with the capillary length as a function of  $T_t$ . In principle, the capillary length used for normalization should be calculated based on the fluid properties at the

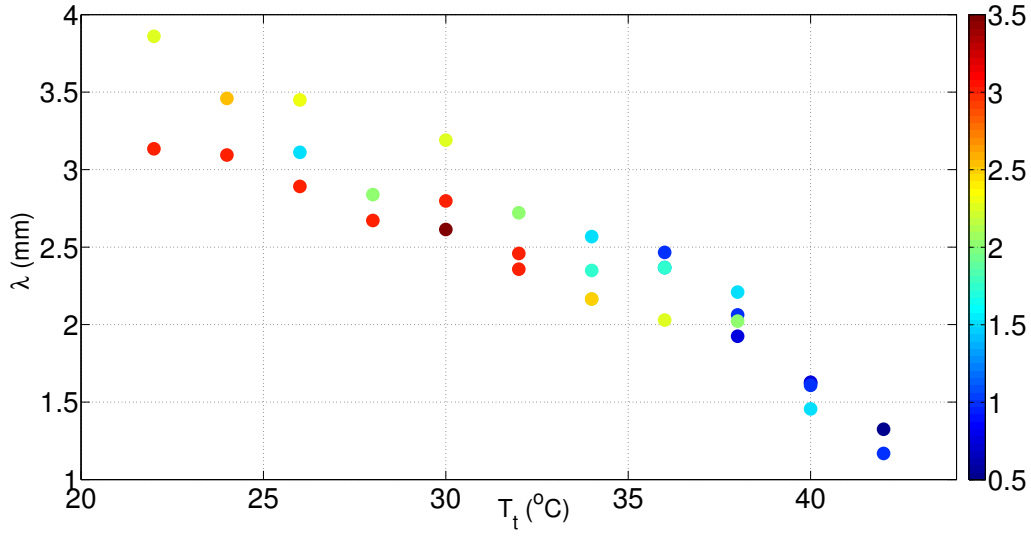


**Figure 3.23:** Variation of the pattern wavelength as a function of the top plate temperature. Color code represents  $\Delta T$ .

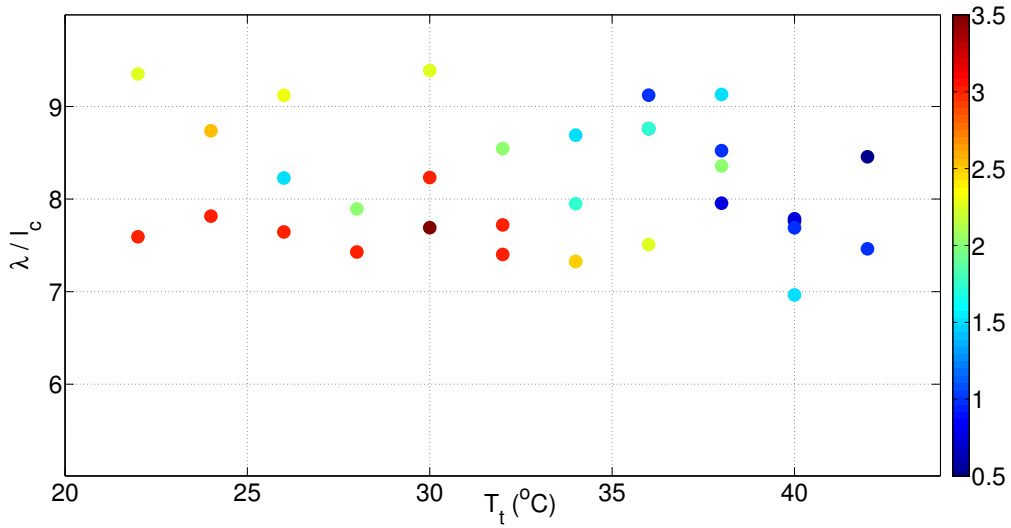


**Figure 3.24:** Normalized (with capillary length) pattern wavelength as a function of the top plate temperature. Color code represents  $\Delta T$ .

interface temperature, which was not possible to measure in the present experimental setup. So, the capillary length was calculated based on the fluid properties at the top plate temperature. The pattern wavelength at different top plate temperatures scale with the capillary length with the scaling pre-factor between 7 and 9. Figure 3.25 shows the variation of dripping frequency as a function of the top plate temperature. At a given  $T_t$ , the dripping frequency increases with the increase in  $\Delta T$ , and for a fixed  $\Delta T$ , the dripping frequency increases with the increase in  $T_t$ .

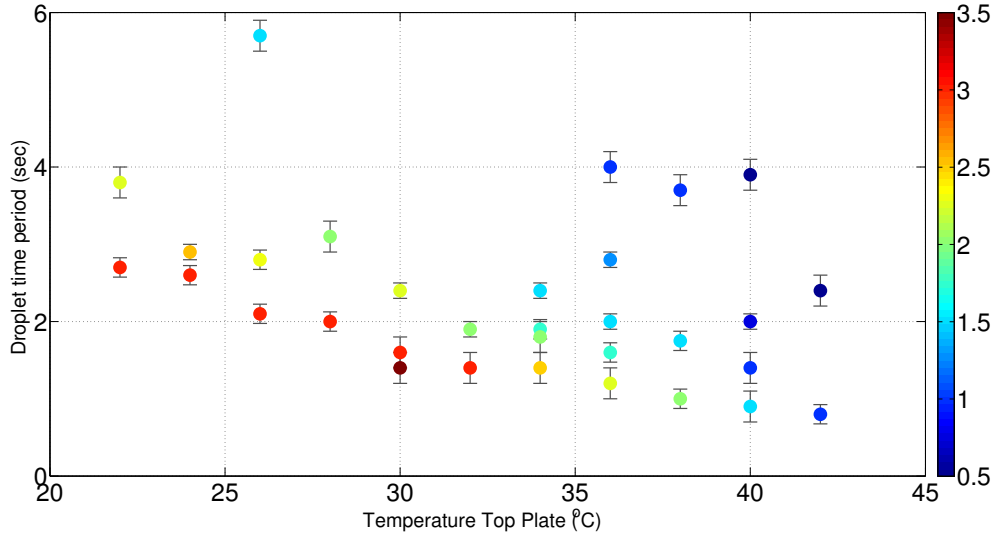


**Figure 3.25:** Dripping time period as a function of  $T_t$ . Color code represents  $\Delta T$ .

### 3.3 Theoretical Considerations

Rayleigh-Taylor instability (RTI) arises in a system where a fluid interface across which a density gradient exists, is subjected to a destabilizing gravity field. Such a scenario can also be created in accelerating systems if the density stratification is adverse or unstable, i.e., the direction of acceleration is towards the lighter fluid from the heavier fluid [33]. In the case of liquids, surface tension plays an important role in the dynamics of the system. The interface is unstable to small perturbations [32, 33]. A considerable amount of literature is available on this particular topic and a detailed review was presented in Chapter 1. In the present system, the liquid layer condensing on the cold top plate was destabilized by gravity. The surface tension stabilizes the liquid-vapor interface. The layer was heated from below and as a consequence, Marangoni stresses may also play a role in stabilizing the interface. Moreover, the condensation/evaporation effect plays an important role in the evolution of the interface.

#### 3.3.1 Surface tension and gravity

Let us start with the simplest systems where gravity destabilizes the liquid layer, and surface tension stabilizes the liquid layer. Only an overview of the basic equations are presented here. The detailed derivation is discussed in [34, 37, 88]. Figure 3.26 (a) shows a schematic of the Rayleigh-Taylor instability in thin films. The film is subjected to a destabilizing gravity field.  $h(x, y, z, t)$  represents the height of the liquid layer from the top plate. As the film is thin, viscous effects cannot be ignored [34], and in the limit of very low Reynolds number  $Re = \frac{U_o h_o}{\nu} \ll 1$  where  $h_o$  is the mean height of the interface,  $U_o$  is the velocity scale in the system,  $\nu$  is the kinematic viscosity of the liquid

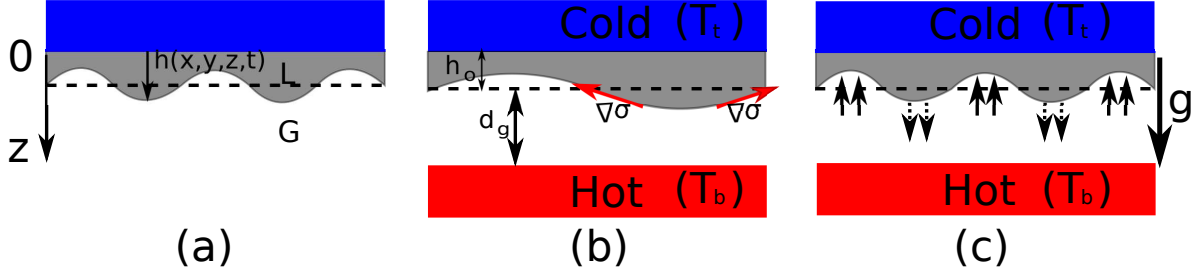


**Figure 3.26:** Rayleigh Taylor instability - (a) gravity vs surface tension and viscosity (b) gravity vs Marangoni forces (c) gravity vs evaporation-condensation: upward arrows indicate condensation and downward arrows indicate evaporation. Dashed line represents the mean position of the interface.

layer, the inertial effects are ignored. As a consequence, the dynamics in the liquid layer is governed by the Stokes equations (Eq. 3.1 - Eq. 3.3).

$$\mu \nabla^2 \mathbf{u} + \mu \frac{\partial^2 \mathbf{u}}{\partial z^2} = \nabla P \quad (3.1)$$

$$\mu \nabla^2 w + \mu \frac{\partial^2 w}{\partial z^2} = \frac{\partial P}{\partial z} - \rho g \quad (3.2)$$

$$\nabla \cdot \mathbf{u} + \frac{\partial w}{\partial z} = 0 \quad (3.3)$$

where  $\mathbf{u}$  is the horizontal components of the velocity,  $w$  is the vertical component of velocity,  $\nabla$  represents the gradient along the horizontal plane  $(x, y)$ ,  $P$  is the pressure field,  $\mu$  and  $\rho$  are the dynamic viscosity and the density of the liquid layer respectively, and  $g$  is the acceleration due to gravity. At the plate, i.e., at  $z = 0$ , no slip boundary conditions are applicable and at the interface, i.e.,  $z = h(x, y, z, t)$ , the following boundary conditions are used:

$$\text{no flux condition: } w = \frac{\partial h}{\partial t} + \mathbf{u} \cdot \nabla h \quad (3.4)$$

$$\text{zero stress: } \mathbf{T}(\mathbf{n}, \mathbf{t}) = 0 \quad (3.5)$$

where  $\mathbf{T}$  is the stress acting on the liquid vapor interface and  $\mathbf{n}$ ,  $\mathbf{t}$  are the unit normal and unit tangent to the interface respectively. In the thin film limit where the deflection of the mean interface position is small compared to the capillary length, the governing equations are simplified using lubrication approximation [89, 90]. Ignoring the higher order terms, the stokes equations reduce to

$$\frac{\partial P}{\partial x} = \mu \frac{\partial^2 u}{\partial z^2} \quad (3.6)$$

$$\frac{\partial P}{\partial z} = \rho g \quad (3.7)$$

$$\nabla \cdot \mathbf{u} + \frac{\partial w}{\partial z} = 0 \quad (3.8)$$

$$(3.9)$$

At  $z=h$ :

$$\frac{\partial \mathbf{u}}{\partial z} = 0 \quad (\text{zero shear stress}) \quad (3.10)$$

$$P_a - P = \sigma \nabla^2 h \quad (\text{zero normal stress}) \quad (3.11)$$

where  $P_a$  is the ambient pressure and  $\sigma$  is the surface tension of the interface. These equations are integrated to obtain the velocity and pressure field.

$$P = P_a - \rho g(h - z) - \sigma \nabla^2 h \quad (3.12)$$

$$u = \frac{1}{2\mu} z(2h - z) \nabla(\rho g h + \sigma \nabla^2 h) \quad (3.13)$$

The evolution equation for the interface is obtained by integrating the mass conservation equation along  $z$  direction from 0 to  $h$ .

$$\int_0^h \nabla \cdot \mathbf{u} + w \Big|_{z=0}^{z=h} = 0 \quad (3.14)$$

Making use of the no-slip, no flux conditions and the Leibniz's rule we obtain

$$\frac{\partial h}{\partial t} + \nabla \cdot \int_0^h \mathbf{u} dz = 0 \quad (3.15)$$

Using Eq. 3.13 in Eq. 3.15, we obtain the evolution equation for the interface position

$$\frac{\partial h}{\partial t} + \frac{1}{3\mu} \nabla \cdot [h^3 \nabla(\rho g h + \sigma \nabla^2 h)] = 0 \quad (3.16)$$

Using appropriate scales, Eq. 3.16 in a non-dimensional form is written as

$$\frac{\partial h}{\partial t} + \nabla \cdot \left[ \frac{G}{3} h^3 \nabla h + \frac{S}{3} h^3 \nabla^2 \nabla h \right] = 0 \quad (3.17)$$

where  $G = \frac{gd^2}{\nu U_o}$  is the Gravity number accounting for the gravitational effects,  $S = \frac{\sigma d}{\mu U_o}$  is the Capillary number accounting for the surface tension.

### 3.3.2 Marangoni Forces and Gravity

In the experiments discussed in this chapter so far, the temperature difference across the liquid layer played an important role. As a consequence, Marangoni effects may play an additional role in the evolution of the interface. A schematic of the system is shown in Fig. 3.26(b). In a Rayleigh-Taylor like scenario, liquids with  $\sigma_T = -\partial\sigma/\partial T > 0$  have a stabilizing effect if the top plate is cooler than the bottom plate, and can suppress dripping from the liquid layer [42]. If the interface is perturbed, the region close to the top plate, i.e., the colder region will have higher surface tension than the warmer region

near to the bottom plate (as the surface tension decreases with temperature). As a consequence, the liquid from the warm region is pulled towards the cold region, thus, opposing the destabilizing effects of gravity. To account for the effects of the thermo-capillary stresses an additional term is included in Eq. 3.17. The interface equation in the non-dimensional form is written as [42, 91]

$$\frac{\partial h}{\partial t} + \nabla \cdot \left[ \frac{G^*}{3} h^3 \nabla h + \frac{S^*}{3} h^3 \nabla^2 \nabla h - \frac{M}{2} \frac{Q h^2 \nabla h}{(Q - Fh)^2} \right] = 0 \quad (3.18)$$

where  $M = (h_o \sigma_T \Delta T / \rho \nu \kappa) (1 + d_g \kappa / h_o \kappa_g)^{-1}$  is the Marangoni number for the liquid layer,  $G^* = g h_o^3 / \nu \kappa$  is the Galileo number and  $S^* = \sigma h_o / \rho \nu \kappa$  is the inverse Crispation number, two-layer Biot number  $F = (\kappa / \kappa_g - 1) (1 + d_g \kappa / h_o \kappa_g)^{-1}$  and  $Q = 1 + F$ .  $\Delta T$  is the temperature difference across the two layers as shown in Fig. 3.26 (b). The geometrical details are shown in Fig. 3.26 (b).  $h_o$  ( $d_g$ ) and  $\kappa$  ( $\kappa_g$ ) are the height and thermal conductivity of the liquid (gas) layer respectively. The definition of  $G^*$  and  $S^*$  are different from  $G$  and  $S$  in Eq. 3.17 as different scales were used for normalization. Please note that no explicit velocity scale was used for normalization in Eq. 3.18. To account for the thermal effects, an additional energy equation along with the appropriate boundary conditions was solved to obtain the temperature distribution in the liquid-gas layer. A detailed account on the derivation of Eq. 3.18 is discussed in [37, 91].

A linear stability analysis of a thin film using Eq. 3.18 shows that the interface is stable if the imposed temperature difference ( $\Delta T$ ) is larger than  $\Delta T_c$  [42].  $\Delta T_c$  is the critical temperature difference below which the liquid layer is unstable.  $\Delta T_c$  is defined as

$$\Delta T_c = \frac{2 \rho g d^2}{3 \sigma_T} \frac{(1 + d_g \kappa / d \kappa_g)^2}{(\kappa / \kappa_g) (1 + d_g / d)} \quad (3.19)$$

The non-dimensional growth rate is given as

$$\gamma(q) = \frac{G}{3} q^2 \left[ \epsilon - \left( \frac{q}{q_{cap}} \right)^2 \right] \quad (3.20)$$

Here,  $\epsilon = (\Delta T_c - \Delta T) / \Delta T_c$  is the reduced temperature difference,  $q$  is the wave number of the imposed disturbance and  $q_{cap} = \sqrt{\rho g d^2 / \sigma}$  is the capillary wave number. A schematic of the dispersion relation is shown in Fig. 3.27 (a) for both stable and unstable conditions. These relations were tested experimentally and for  $\Delta T > \Delta T_c$  a stable flat interface was observed [42]. In the unstable configuration the fastest growing mode was  $q^* = q_{cap} \sqrt{\epsilon / 2}$ .  $q^*$  approaches zero as  $\Delta T$  approaches  $\Delta T_c$ , thus indicating that it is a long wavelength instability. These are also called type II instabilities in the pattern formation literature [28]. In such systems, the wavelength increases over time due to the coarsening of the patterns.

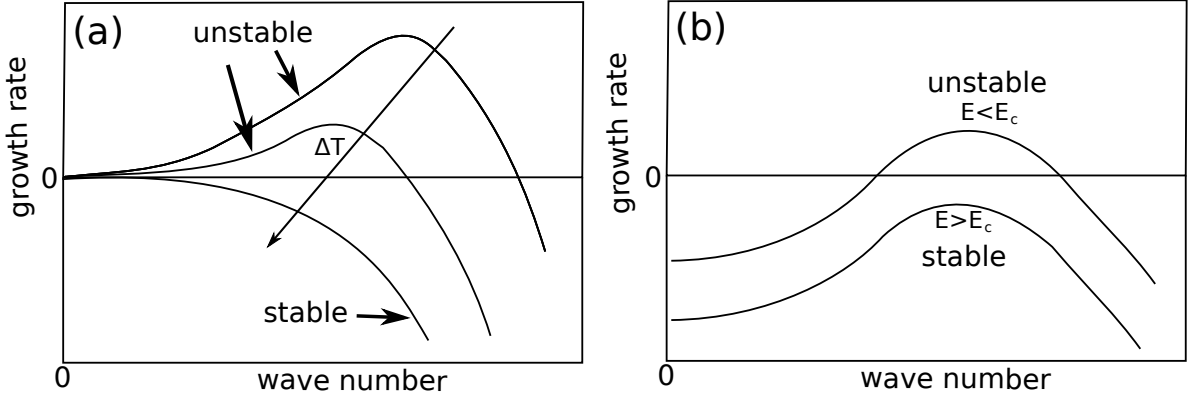


**Figure 3.27:** Dispersion curve - (a) gravity vs Marangoni forces (b) gravity vs evaporation-condensation

### 3.3.3 Evaporation-condensation effects

In the observations discussed in this chapter, phase change plays an important role in the evolution of the instability and the patterns. The mechanisms discussed so far do not account for the effects of phase change. In this sub-section we discuss the influence of phase change (evaporation-condensation) on the nature of the instability. The details presented here are based on [43].

A schematic of the system is presented in Fig. 3.26 (c). The liquid-vapor system is heated from below and cooled from above. The conditions are set such that the vapor layer is in equilibrium with the liquid layer, i.e., the vapor is saturated *w.r.t* the temperature of the liquid-vapor interface. The interface is flat initially (the dashed line in Fig. 3.26(c)). When the interface is deflected from its initial position (the continuous line in Fig. 3.26 (c)), the crest moves towards the cold top plate and the trough moves towards the hot bottom plate. The imposed vertical temperature gradient reduces the temperature of the crest and increases the temperature of the trough compared to the interface temperature at  $t = 0$ . The vapor in the neighbourhood of the crest is locally supersaturated due to the reduced crest temperature, resulting in condensation. On the contrary, the vapor in the neighbourhood of the trough is locally subsaturated resulting in evaporation. The evaporation-condensation process continues until equilibrium conditions are re-established. The evaporation-condensation process acts as a stabilizing mechanism that suppresses the destabilizing effects of gravity. Note that the thermo-capillary effects are ignored in this discussion.

The lubrication limit and thin film approximations are valid for this system. An additional term is included in the evolution equation of  $h$  (Eq. 3.15) to account for evaporation and condensation effects:

$$\frac{\partial h}{\partial t} + \nabla \cdot \int_0^h \mathbf{u} dz + \frac{J}{\rho} = 0, \quad (3.21)$$

where  $J$  is the mass transfer rate across a unit area measured in  $kg/(m^2s)$ , and it is a function of various thermodynamic parameters and fluid properties. The functional form for  $J$  is approximated using the Hertz-Knudsen law [43]

$$J(T, P_s) = \alpha(P_s(T) - P)\sqrt{\frac{M}{2\pi\kappa_B T}}, \quad (3.22)$$

where  $P_s$  is the saturation vapor pressure at a given temperature  $T$ ,  $P$  is the vapor pressure of the liquid in the vapor phase,  $M$  is the molecular mass of the working fluid,  $\kappa_B$  is the Boltzmann constant and  $\alpha$  is the accommodation coefficient to account for the experimental conditions with a value not more than 1. The vapor pressure in the system is assumed to be constant. The temperature of the interface decreases as the interface is deflected towards the top plate. As a consequence, the local saturation pressure  $P_s$  also decreases, thus, causing condensation. Similarly, if the interface is deflected towards the bottom plate, the localized sub-saturation causes evaporation. From Eq. 3.22 and Eq. 3.21, we realize that condensation increases  $h$  and evaporation decreases  $h$ . Assuming a linear temperature profile in the vertical direction, the expression for  $J$  is re-written as

$$J(T_I) \approx \alpha^*(T_s - T_t)\frac{h - d}{d}, \quad (3.23)$$

where  $d$  is the equilibrium thickness,  $T_s$  is the temperature of the interface under equilibrium conditions and  $\alpha^* = \alpha\sqrt{m/(2\pi\kappa_B T)}(dP_s/dT)_{T_s}$  is the modified accommodation coefficient.

Neglecting capillary effects and using thin film approximation, the evolution equation for the height is written in the non-dimensional form as

$$\frac{\partial h}{\partial t} = -\nabla[(h^3 + h^3\nabla^2)\nabla h] - E(h - 1), \quad (3.24)$$

where  $E$  is the evaporation number which accounts for the evaporation-condensation effects. The horizontal coordinates are normalized using the capillary length, height using equilibrium thickness  $d$  and time using the time scale  $\tau = 3\sigma\mu/(\rho^2g^2d^3)$  [43]. The evaporation number is defined as

$$E = \frac{\alpha^*\tau}{\rho} \frac{T_I - T_t}{d} \quad (3.25)$$

where  $T_I$  is the interface temperature. A linear stability analysis of Eq. 3.24 reveals that for  $E \geq E_c = 0.25$ , the liquid layer is stable, and for  $E < E_c$ , a pattern forming instability occurs with a critical wave number  $q_c^2 = 1/4$ . The dispersion relation is plotted in Fig. 3.27(b) and is similar to Rayleigh-Benard convection close to onset [35]. It is a finite wavelength instability (Type I) and through numerical simulations it was established that in the non-linear limit there was no coarsening, unlike in the non-

evaporating system [43]. It was observed that a regular stationary hexagonal pattern was formed if the value of  $E$  was close to  $E_c$  and the mean pattern wavelength scales with the critical wavelength [43].

### 3.4 Discussion: Thick Cell

The experimental observations presented so far shows that under appropriate conditions a thin liquid layer condensing on the cold top plate results in a stationary regular patterns with hexagonal symmetry for large  $\Delta T$  only. The mean wavelength of the patterns scales with the capillary length. The patterns were stationary but not stable. The drops grew over time and periodically dripped into the liquid pool at the bottom plate. Nevertheless, in the stationary non-linear regime the patterns have a well-defined periodicity, which suggests that the underlying dynamics have an inherent wave number selection mechanism.

The theoretical discussion in the previous section summarized various Rayleigh-Taylor like instability configurations with three different stabilization mechanisms - surface tension, thermo-capillary effects and evaporation-condensation effects. The first two mechanisms result in a long wavelength instability. These configurations have been investigated experimentally. In the transient evolution of a thin liquid layer, hexagonal patterns were observed [34, 42]. These transient patterns scale with the capillary length similar to the present experimental observations. Once dripping sets in, the pattern symmetry was lost [34, 42] and the liquid layer thickness decreases over time until only a large drop remains. So, dripping effectively results in mass loss from the liquid layer and hence reduces the thickness of the layer until it attains the critical thickness. Over time, the thickness of the layer becomes smaller than the critical thickness required for RTI, which results in a large drop. It was observed that if the imposed  $\Delta T$  across the layer was sufficiently large, then the Marangoni forces suppresses dripping from the layer resulting in one large drop at the top plate. These large structures were unstable to long wavelength perturbations [42].

The evaporation-condensation model (BM model) causes a finite wavelength instability that results in a hexagonal pattern in the non-linear regime if the evaporation number  $E$  was close to 0.25. The numerical calculations showed that the liquid layer was stable for  $E > 0.25$  [43]. This model however does not account for dripping, as dripping cannot be modeled using the thin film equation. A linear temperature profile was assumed in the vertical direction, and the distribution of temperature and vapor pressure was assumed to be uniform in the horizontal plane. Moreover, the BM model assumes that the temperature of the liquid-vapor interface was in equilibrium with the vapor pressure. This model predicts a final hexagonal pattern that scales with the critical wavenumber  $k_c = 0.71$  (non dimensionalized using capillary length). The normalized wave number  $k^*$

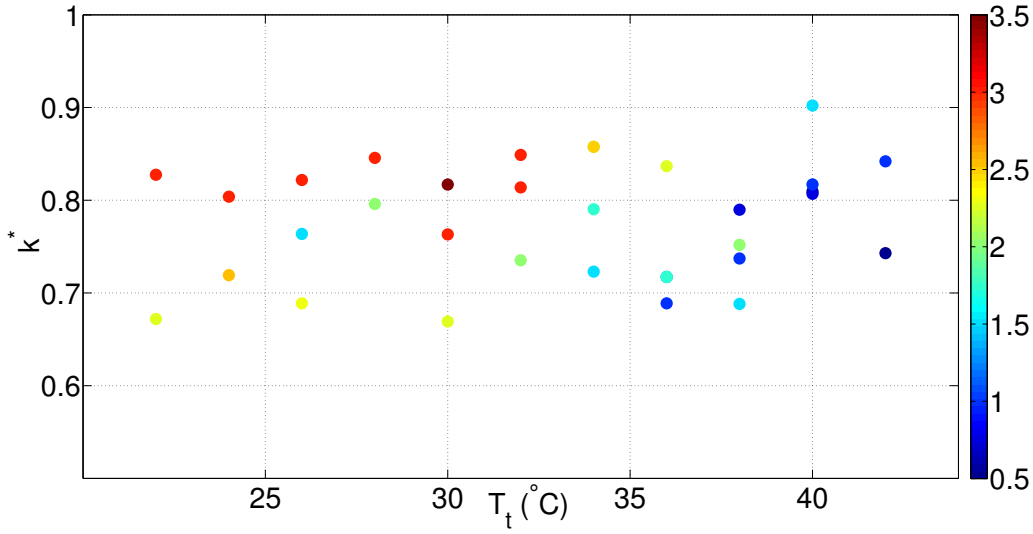


**Figure 3.28:** Variation of non-dimensional wavenumbers obtained from the Fourier analysis of the experiments in Fig. 3.24 as a function of  $T_t$ . The color code represents the  $\Delta T$ .

$= \frac{2\pi l_c}{d_p}$ , where  $d_p$  is the wavelength of the patterns, as a function of  $T_t$  for the “large”  $\Delta T$  experiments is plotted in Fig. 3.28. Please note that the capillary length was calculated based on material properties evaluated at the top plate temperature as the interface temperature was not measured. Most of the values for the normalized wavenumber lie between 0.65 and 0.85. For a given  $T_t$ , the largest  $k^*$  corresponds to the highest  $\Delta T$ . This may be due to the fact that the capillary length for each of these experiments at a given  $T_t$  is different since the interface temperature is higher than  $T_t$ . The scatter in the data may reduce if the mean interface temperature was known. The interface temperature was not measured in these experiments.

In the experiments discussed in this chapter so far, most of the assumptions from the BM model are not applicable. The Rayleigh number was high enough for the flow in the vapor phase to be turbulent. This violates the assumption of a uniform distribution of temperature and vapor in the horizontal plane due to the convective plumes in the system. The temperature profile in the vertical direction was not linear. It is not easy to determine the temperature distribution inside the cell due to the presence of a boiling liquid layer at the bottom plate. Not many experiments or numerical studies have been carried out in a two-phase convection system and only little information is available regarding the distribution of temperature. Therefore, we rely on a description of the classical turbulent convection [92]. Since the liquid layer above the bottom plate was boiling, there was a continuous supply of vapor, and on average the vapor phase was supersaturated, in contrast to the BM model where a saturated environment was assumed at the interface.

Despite these differences between the experimental conditions and the theoretical

assumptions, the characteristics of the final patterns are similar. In an ideal situation, the appropriate experiment is a system where the thickness of the liquid layer can be regulated, as the evaporation number  $E$  is inversely proportional to the fourth power of the thickness. The thickness of the liquid layer on the top plate cannot be regulated in the experiment discussed so far as there was a continuous supply of vapor from the liquid pool at the bottom plate. Moreover, the vapor phase below the thin layer was supersaturated. From Eq. 3.21 we know that in a supersaturated environment, the growth of the layer cannot be restricted. Consequently, the liquid layer thickness is always above the critical thickness and hence continuously undergoes RTI. The drop like structures grow until dripping sets in. The thin film approximation is not applicable once dripping sets in.

We modified the convection cell design for a better comparison with the BM model. The previous setup only accounts for the condensation effects and not the evaporative effects. The continuous supply of vapor from the liquid layer at the bottom plate needs to be cut-off to create a volume of sub-saturation above the bottom plate. This is ensured by eliminating the liquid layer at the bottom plate. Moreover, the effects of convection and turbulence have to be suppressed to achieve a linear vertical temperature gradient. This was ensured by the reduction of the cell height.

### 3.5 Thin Cell

Figure 3.29 shows a snapshot from the thin cell experiments. A simple beam splitter setup was used for flow visualization (see section 2.4.2 for details). The black patch on the upper and lower half of the image was due to the shadow cast by the beam-splitter. In this particular experiment,  $T_t$  and  $T_b$  were set to 24.00 °C and 32.00 °C respectively. The pressure was set to 23.7 bars and was adjusted such that there was no liquid layer on the bottom plate, but was high enough for SF<sub>6</sub> to condense on the top plate. The absence of a liquid layer at the bottom plate renders part of the cell sub-saturated. The average height of the sub-saturated region can be adjusted by varying the vapor pressure inside the cell.

The drops in Fig. 3.29 exhibit hexagonal symmetry with some defects. The inset in Fig. 3.29 shows the 2D power spectrum of the pattern, and it contains six distinct peaks. The pattern was nearly stationary with minor drift probably due to a small inclination of the cell. The underlying flow was convecting as the  $\Delta T$  close to the onset  $Ra$  was not sufficient to establish a stable pattern. The drops appear to be ‘jittery’ due to the underlying convection in the vapor layer. The diameter of the drops increases with the distance from the cell center and is largest near the lateral boundaries. This variation may be due to a radial temperature gradient across the top and bottom plate. An important outcome of this experiment was that dripping was nearly suppressed. The

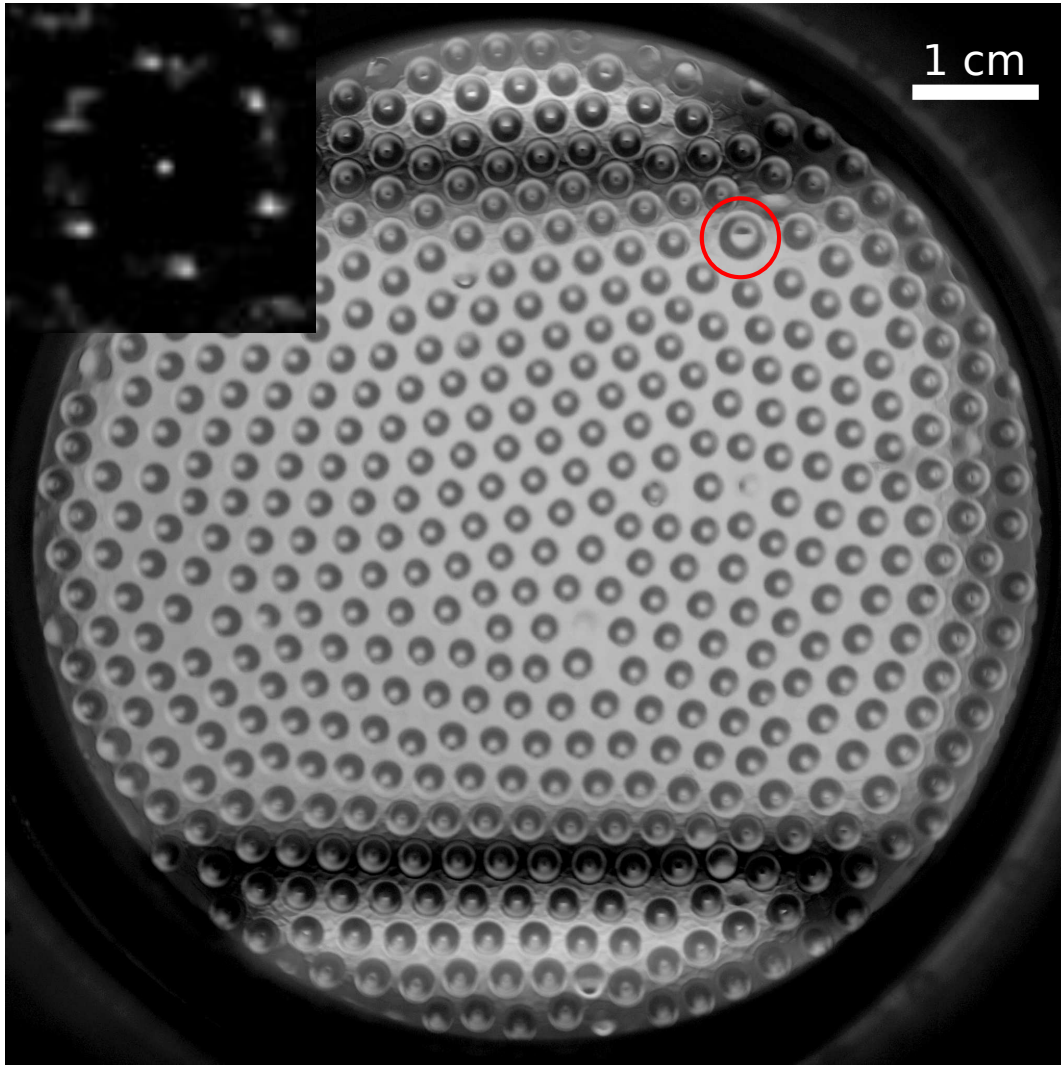


**Figure 3.29:** Thin cell: Hexagonal arrangement of drops in the liquid layer below the top plate.  $T_t = 24.00$  °C,  $T_b = 32.00$  °C and  $P = 23.7$  bars. The drop inside the red circle is an outcome of a merger event between 3 drops. The inset in the top left corner shows the 2D power spectrum of the hexagonal arrangement.

sub-saturation obtained in the lower part of the cell due to the elimination of the liquid layer at the bottom plate was sufficient to nearly suppress dripping. There were some occasions when the drops dripped. For instance, a few drops merged together to form a large drop that was unstable. But its occurrence was rare - about 1 drop dripped over 3 minutes. More frequent but aperiodic dripping was observed for smaller drops. For instance, one small drop dripped 3 times within 15 seconds and then stopped dripping thereafter. Nevertheless, the number of drops that dripped were quite small ( $< 5\%$  over a period of 3 minutes) compared to the total number of drops at the top plate.

Figure 3.30 presents a sequence of images capturing a merger event resulting in the formation of large drops in the liquid layer. One such large drop is marked in Fig. 3.29. Figure 3.30 (a-c) shows the coalescence of three drops. The resulting single merged

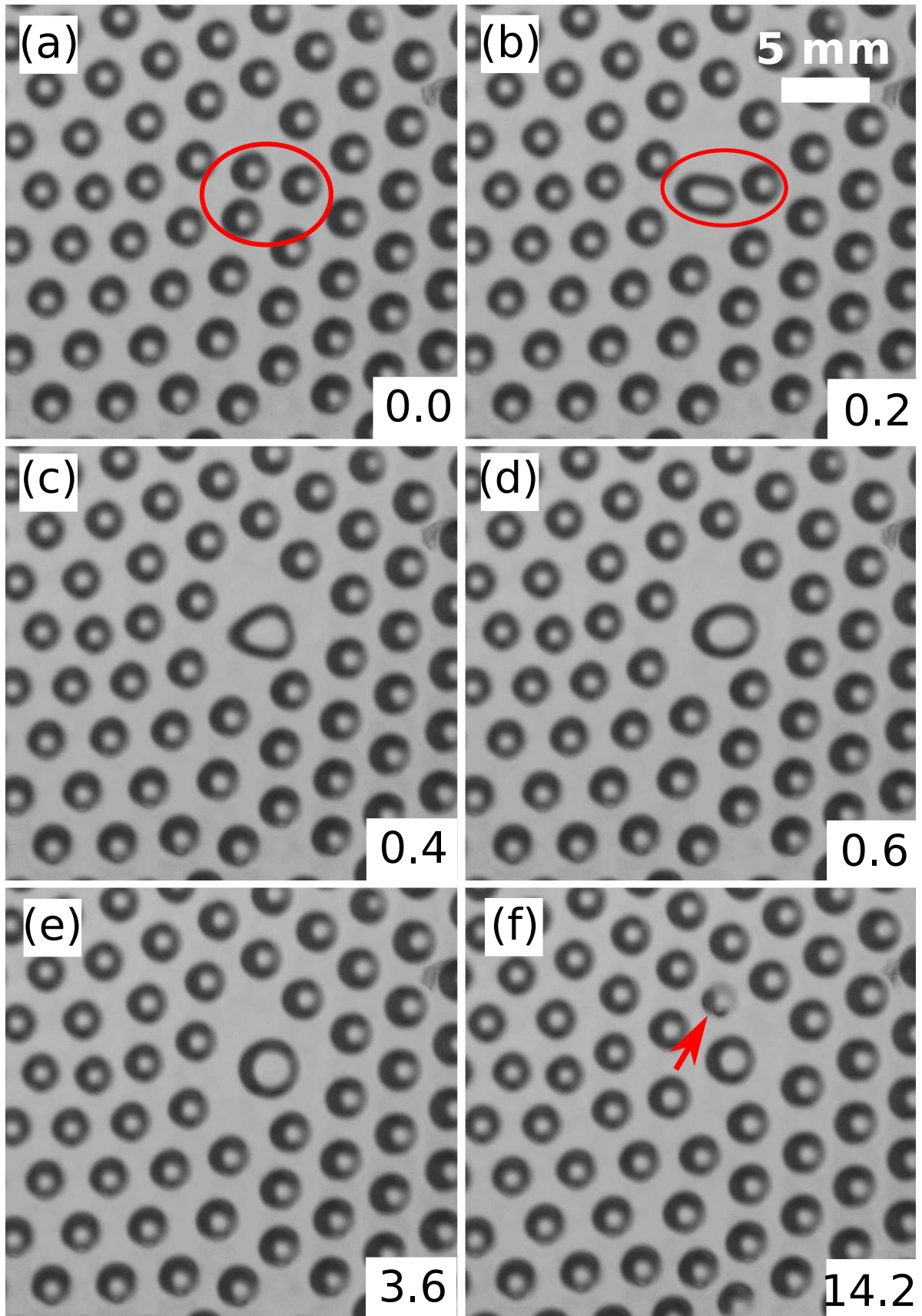
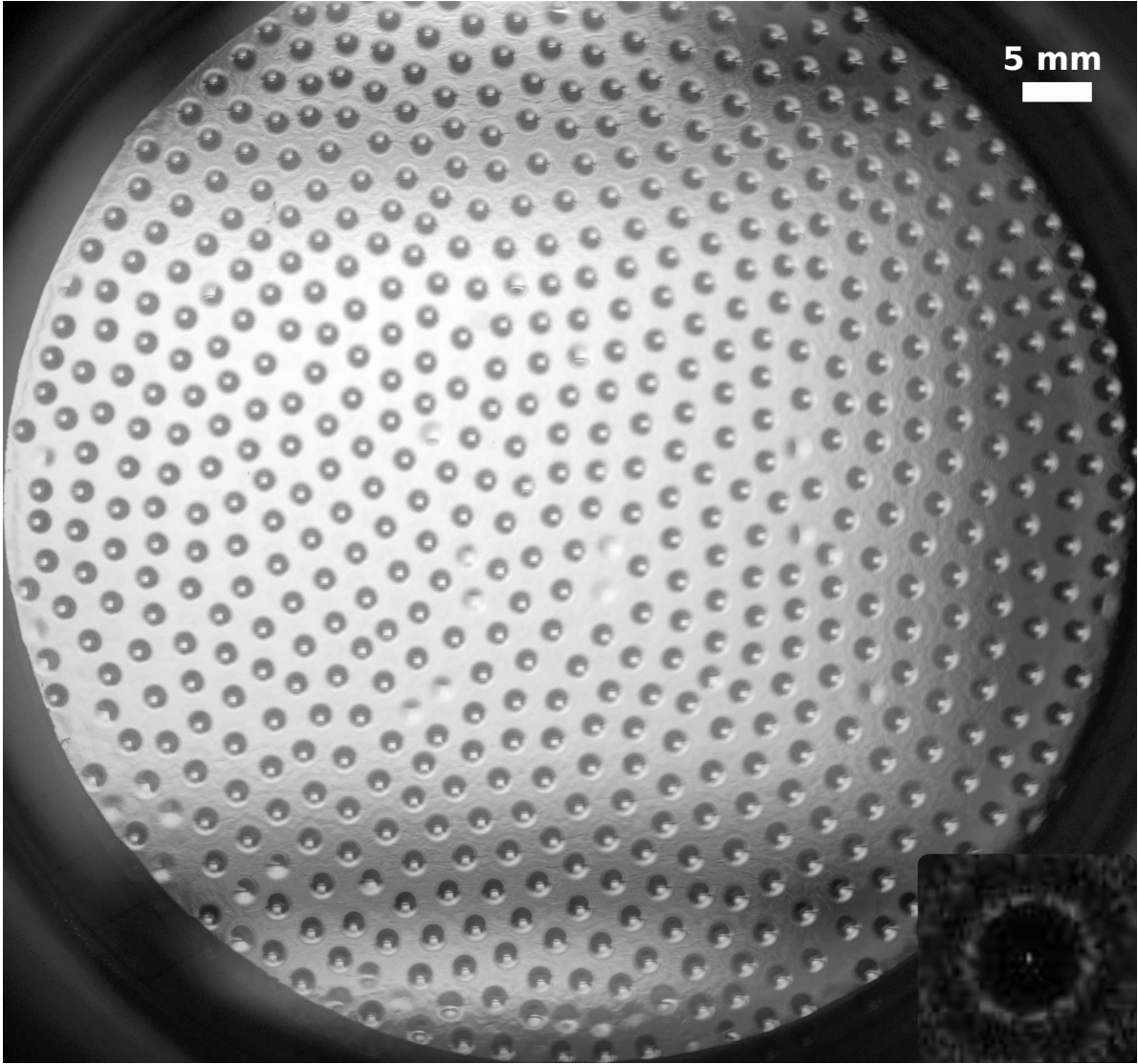


**Figure 3.30:** Formation of a large drop through coalescence. The red oval circumscribes the merging drops. The red arrow in (f) marks the formation of the new drop. Time stamp in seconds is indicated in the bottom right corner of each image. See Fig. 3.29 for experimental conditions.

drop is shown in Fig. 3.30 (d). Fig. 3.30 (b and c) shows the capillary oscillations exhibited by the coalesced drop. The merger events of the type discussed above result in the formation of voids/defects in the pattern arrangement. Over time, these voids in the packing are filled by the formation of new drops or by the rearrangement of the neighbouring drops similar to the thick cell experiments. The genesis of a new drop is marked in Fig. 3.30 (f). In the thick cell experiments, the merger events were followed by dripping. In the present case, Fig. 3.30(a-f) shows that merger results in a large drop that gradually shrinks back to its equilibrium size. The shrinking is attributed to mass loss through evaporation. The merging process results in a large drop extending into the sub-saturated zone. This results in partial evaporation of the drop. The evaporation process continues until the equilibrium size was re-established.

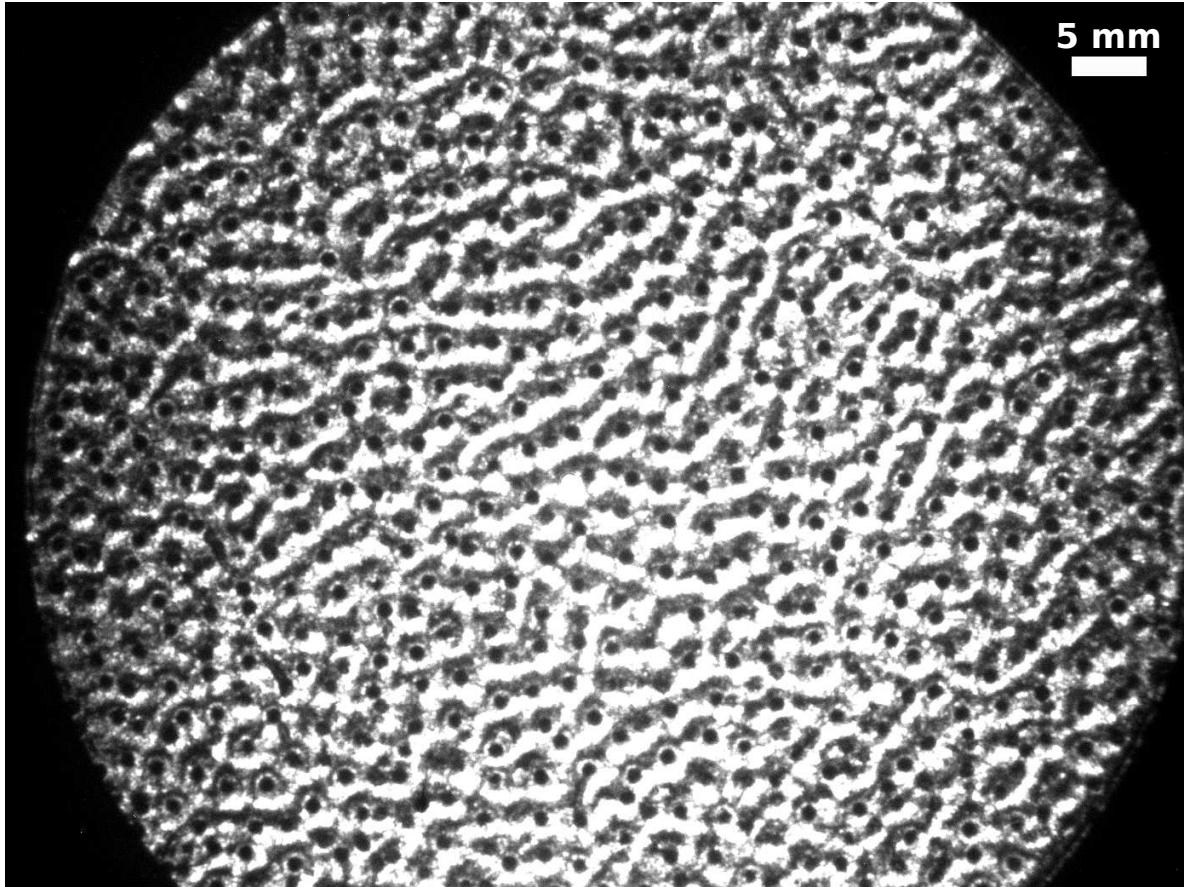
The evaporation effects discussed above explains the reduction in size of a large diameter drop. Nevertheless, it does not explain how such a large drop remained attached to the liquid layer. As was mentioned earlier, the smaller drops drip more frequently than the large drops. In the case of small drops, the dripping frequency was not periodic (unlike in the thick cell case with a supersaturated vapor in the lower part) and the location where dripping occurred was quite random. A plausible argument may be that the level of local sub-saturation or the local evaporation number  $E$  may not have been large enough to stabilize these drops. As a consequence, the growth of a drop was not arrested, thus resulting in dripping. Dripping in the present experiment is a quick process compared to the evaporative effects (based on the time stamps in Fig. 3.30). It appears that other effects not accounted for so far may aid in stabilizing such large drops. The Leidenfrost effect may play a role in make such large drops stable. If  $T_b$  was high enough (greater than the Leidenfrost temperature), then the vapor evaporating from the drop may produce a cushioning effect [93]. This may provide additional stability to such large drops.

Figure 3.31 shows an instantaneous snapshot of the arrangement of the drops on the top plate at a higher mean temperature compared to Fig. 3.29.  $T_t$  and  $T_b$  were set to 32.00 °C and 40.00 °C respectively. The pressure was set to 28.3 bar. The inset in Fig. 3.31 shows the magnitude of the two dimensional Fourier transform of the image. A well-defined mean distance between the patterns exist, but distinct peaks are not visible in the Fourier space. The diameter of the drops has decreased compared to Fig. 3.29 due to the increase in the mean temperature. The drops oscillate/jitter a lot more compared to the drops in the experiment shown in Fig. 3.29. This may have been due to the increased turbulence intensity in the underlying convective flow in the vapor layer. The material parameters change with temperature. Dynamic viscosity and thermal conductivity do not change significantly, but the density  $\rho$  of the vapor phase increases with temperature, and the Rayleigh number is proportional to  $\rho^2$ . In



**Figure 3.31:** Thin cell: Arrangement of drops in the liquid layer below the top plate.  $T_t = 32.00\text{ }^\circ\text{C}$ ,  $T_b = 40.00\text{ }^\circ\text{C}$  and  $P = 28.3$  bars. The inset on the bottom right corner shows the 2D power spectrum of the drop arrangement.

the experiment shown in Fig. 3.31 the Rayleigh number in the vapor layer is estimated to be 70000 (about 3 times the Rayleigh number in Fig. 3.29). As a consequence the flow field in the vapor layer is chaotic and may influence the arrangement of drops at the top plate. A similar image is shown in Fig. 3.32 where  $T_t$  was set to  $41.00\text{ }^\circ\text{C}$  and the bottom plate was supplied with a constant heat flux. The mean bottom plate temperature was  $\approx 47.5\text{ }^\circ\text{C}$  and the mean pressure was  $\approx 34.7$  bar. The patterns and the underlying convective flow was visualized using the shadowgraph setup. The drops at the the top plate appear as black circles. The chaotic roll structure of the underlying convective flow is visible in Fig. 3.32 as the long white and dark stripes. The drops in the liquid layer are aligned with the structure of the convection rolls. No organization is visible in the arrangement of the drops in Fig. 3.32 as these drops drift along with the



**Figure 3.32:** Thin cell: Arrangement of drops in the liquid layer below the top plate.  $T_t = 41.00\text{ }^\circ\text{C}$ ,  $T_b \approx 47.50\text{ }^\circ\text{C}$  and  $P \approx 34.7$  bars. Image was acquired using the shadowgraph setup.

underlying convection rolls. From this image it is not possible to say if the drops are aligned along the upwelling plumes or the down-welling plumes.  $\Delta T$  in this experiment was comparable to the experiments in Fig. 3.29 & 3.31, but the turbulence intensity was much higher due to higher thermal driving ( $Ra \approx 5 \times 10^5$ ).

Figure 3.33 shows a snapshot from an experiment at thermal conditions similar to that in Fig. 3.32. The top temperature is the same in both experiments. The bottom temperature was increased to  $T_b \approx 48.5\text{ }^\circ\text{C}$  and the corresponding pressure is  $P \approx 34.8$  bars. Flow visualization was done using the beam splitter technique. The difference between Fig. 3.32 and Fig. 3.33 is that no drops are visible in the center of the cell in the latter experiment. The increase in the bottom plate temperature seems to have eliminated the drops near the cell center. As we move towards the lateral boundaries the drops are visible. This is attributed to the radial temperature gradient across the cell. A few drops are marked in Fig. 3.33. A shadowgraph image under similar conditions is shown in Fig. 3.34 (see figure caption for the experimental conditions). The convection rolls are visible in the central region of the cell but the drops are not discernible in the centre. It appears that the top plate was free of drops around the center of the cell.

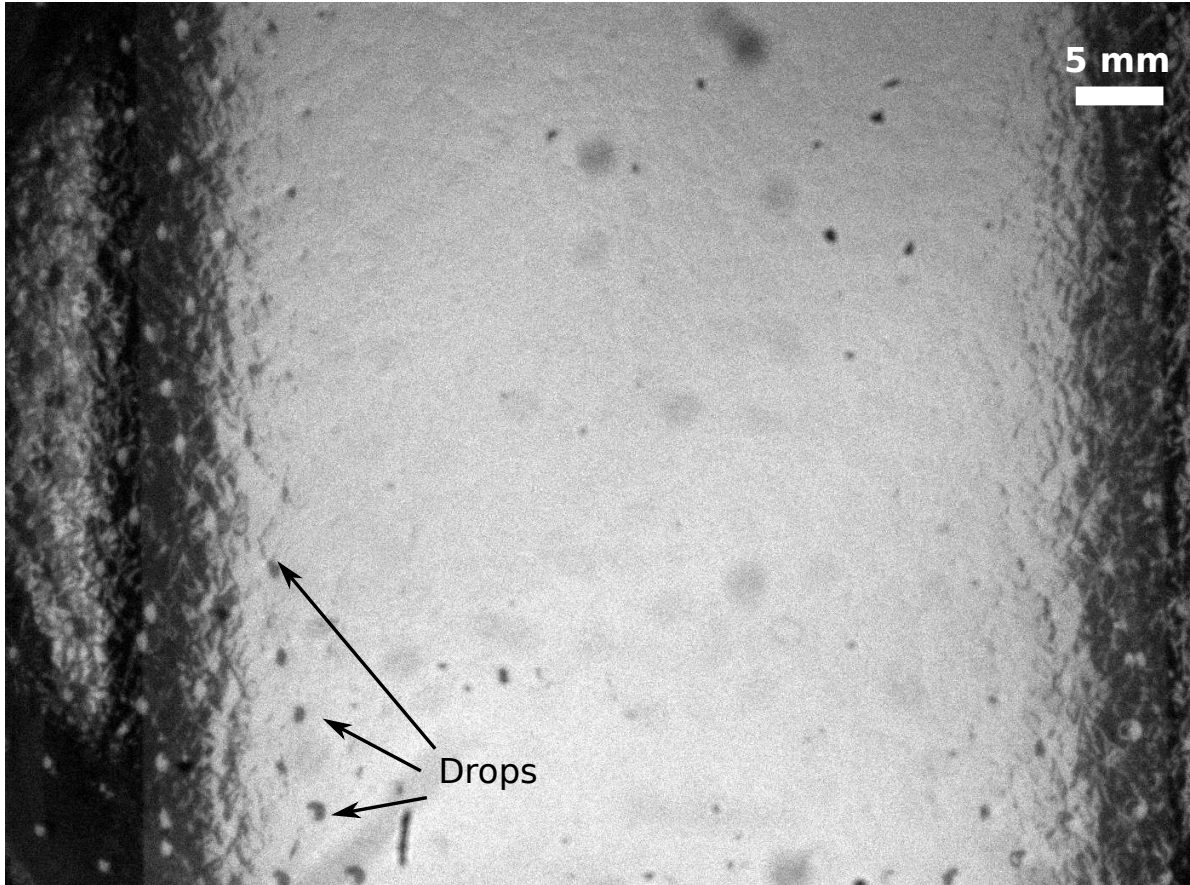


**Figure 3.33:** Thin cell: Arrangement of drops in the liquid layer below the top plate.  $T_t = 41.00$  °C,  $T_b \approx 48.5$  °C and  $P \approx 34.8$  bars. Central portion has no drop like deformations.

Either the liquid layer around the centre of the top plate was stable, or the liquid layer was not present. We show later that the top plate was indeed covered with a layer of liquid  $\text{SF}_6$ .

The liquid layer or the saturation level inside the cell can be adjusted by regulating the pressure inside the convection cell. The liquid layer above the bottom plate can be established by increasing the pressure inside the cell such that vapor and liquid phase co-exist. As was stated earlier, wettability of liquid  $\text{SF}_6$  on the silicon plate improves with increasing temperature. Experiments with a liquid  $\text{SF}_6$  layer at the bottom plate were conducted only at mean temperatures close to the critical temperature. One such case is shown in Fig. 3.35 (see figure caption for the experimental conditions). The drops are arranged in a hexagonal lattice and the mean distance between the patterns is about 1 – 1.2 mm and is comparable to the mean distance in the thick cell experiments shown in Fig. 3.22. The drops grew over time and dripped periodically into the liquid layer at the bottom plate. The dynamics in the presence of a liquid layer on the bottom plate is similar to those discussed in the thick cell experiments, and so will not be discussed here.

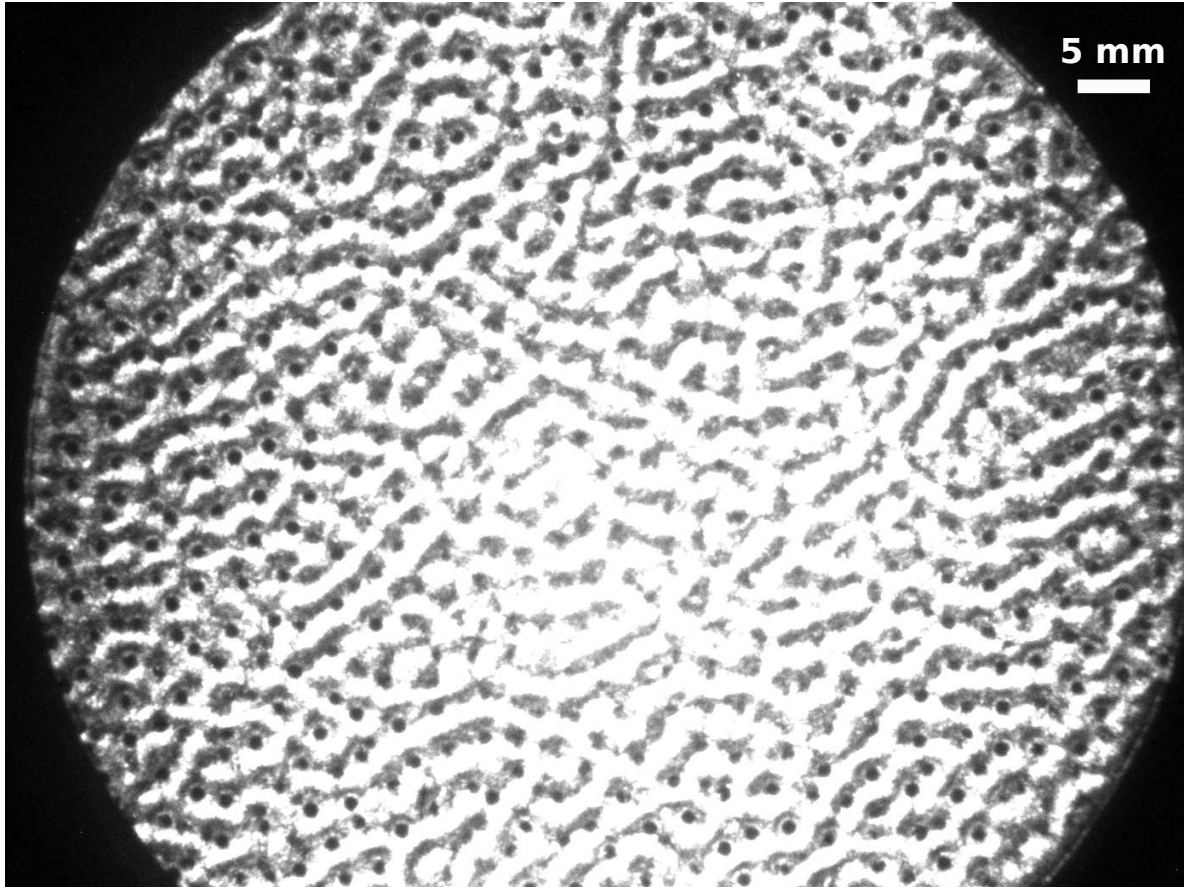


**Figure 3.34:** Thin cell: Arrangement of drops in the liquid layer below the top plate.  $T_t = 41.00$  °C,  $T_b \approx 50$  °C and  $P \approx 34.9$  bars.

### 3.6 Medium Cell

Figure 3.36 shows the effect of vapor pressure on the arrangement of drops in the liquid layer at the top plate in the medium cell (cell height  $\approx 2$  mm) experiments.  $T_t$  and  $T_b$  were set to 35.00 °C and 35.50 °C respectively. The pressure increases by 0.1 psi per image in Fig. 3.36 (a-f). Please note that in all these experiments the liquid layer at the top plate was unstable and dripped. In most cases dripping occurred after the merger of two drops. No liquid layer was present on the bottom plate in Fig. 3.36 (a-c). As the pressure was increased further, isolated islands of liquid SF<sub>6</sub> appeared on the bottom plate as shown in Fig. 3.36 (d and e). In Fig. 3.36 (f) the bottom plate was completely covered with a layer of liquid SF<sub>6</sub>. The number of drops in the liquid layer at the top plate increased with the increase in vapor pressure. Figure 3.36(b and c) shows isolated stripes and clusters of drops, and on average each of these stripes/clusters contained about 3 to 5 drops in them. These drops appear to be aligned along the convection rolls as was shown in the thin cell experiment in Fig. 3.32. Thus, an increase in vapor pressure results in the formation of new drops along these rolls as long as the bottom

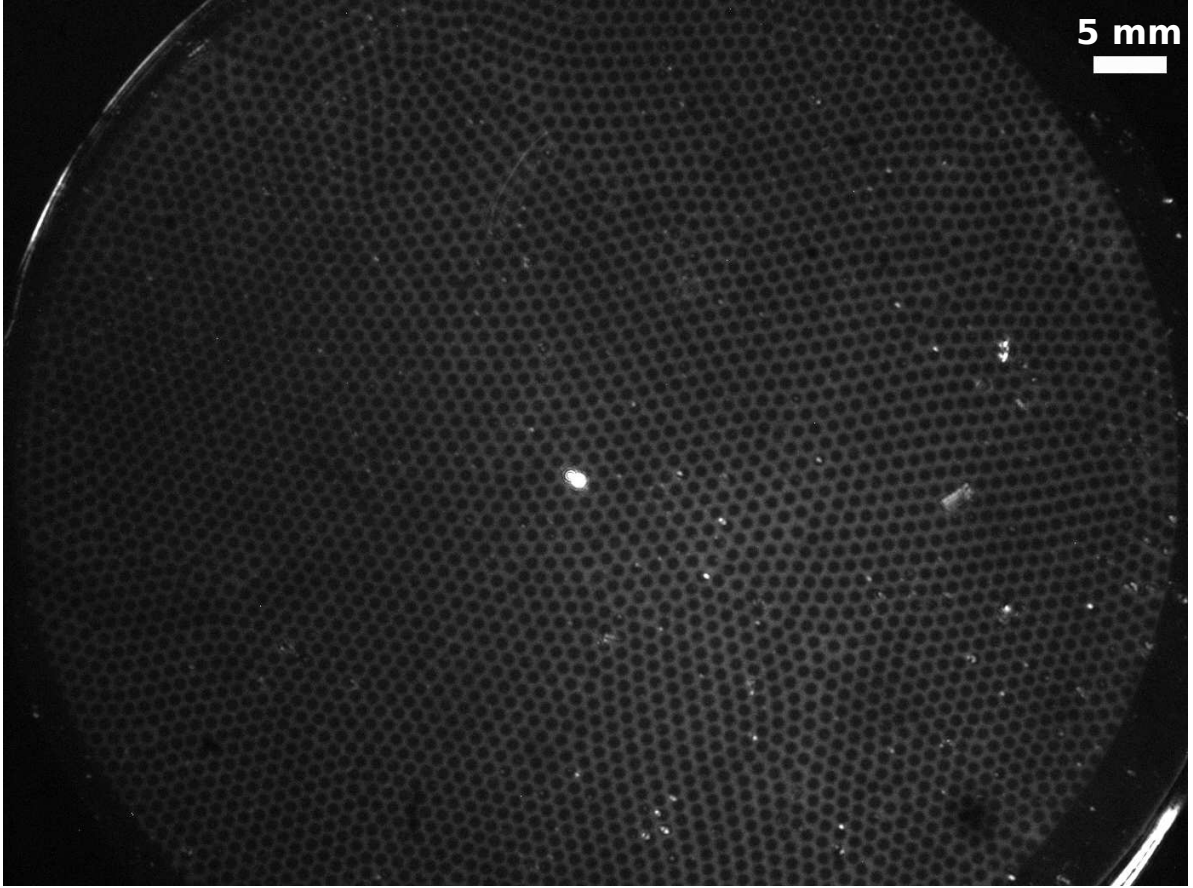


**Figure 3.35:** Thin cell: Arrangement of drops in the liquid layer on the top plate.  $T_t = 42.00$  °C,  $T_b = 43.80$  °C and  $P = 36.1$  bars. The bottom plate is covered with a layer of liquid  $\text{SF}_6$ .

plate was not covered with a layer of liquid  $\text{SF}_6$ . The presence of an isolated patch or a layer of liquid  $\text{SF}_6$  on the bottom plate ensures continuous supply of vapor locally. This renders the vapor phase locally supersaturated (Fig. 3.36(d, e)). This increases the number of drops in the liquid layer drastically and these drops are not aligned along the convection rolls. Their dynamics were similar to the thick cell experiments discussed earlier. The chaotic motion of these drops was suppressed once the liquid layer was established at the bottom plate (Fig. 3.36(f)). The drops are more organized and drip periodically from the liquid layer. If  $\Delta T$  was large enough (not shown here), the arrangement of drops have a hexagonal symmetry, similar to the experiments in the thick cell.

Figure 3.37 shows a snapshot from an experiment with a higher thermal driving compared to the experiment in Fig. 3.36(b, c). The top plate temperature was the same in both the experiments.  $\Delta T$  in Fig. 3.37 was about 28 times higher than the experiment in Fig. 3.36. The arrangement of drops in both the experiments are similar with some isolated stripes/clusters composed of 3 to 5 drops. The number of such stripes/clusters appear to be smaller in Fig. 3.37 compared to Fig. 3.36. This may be

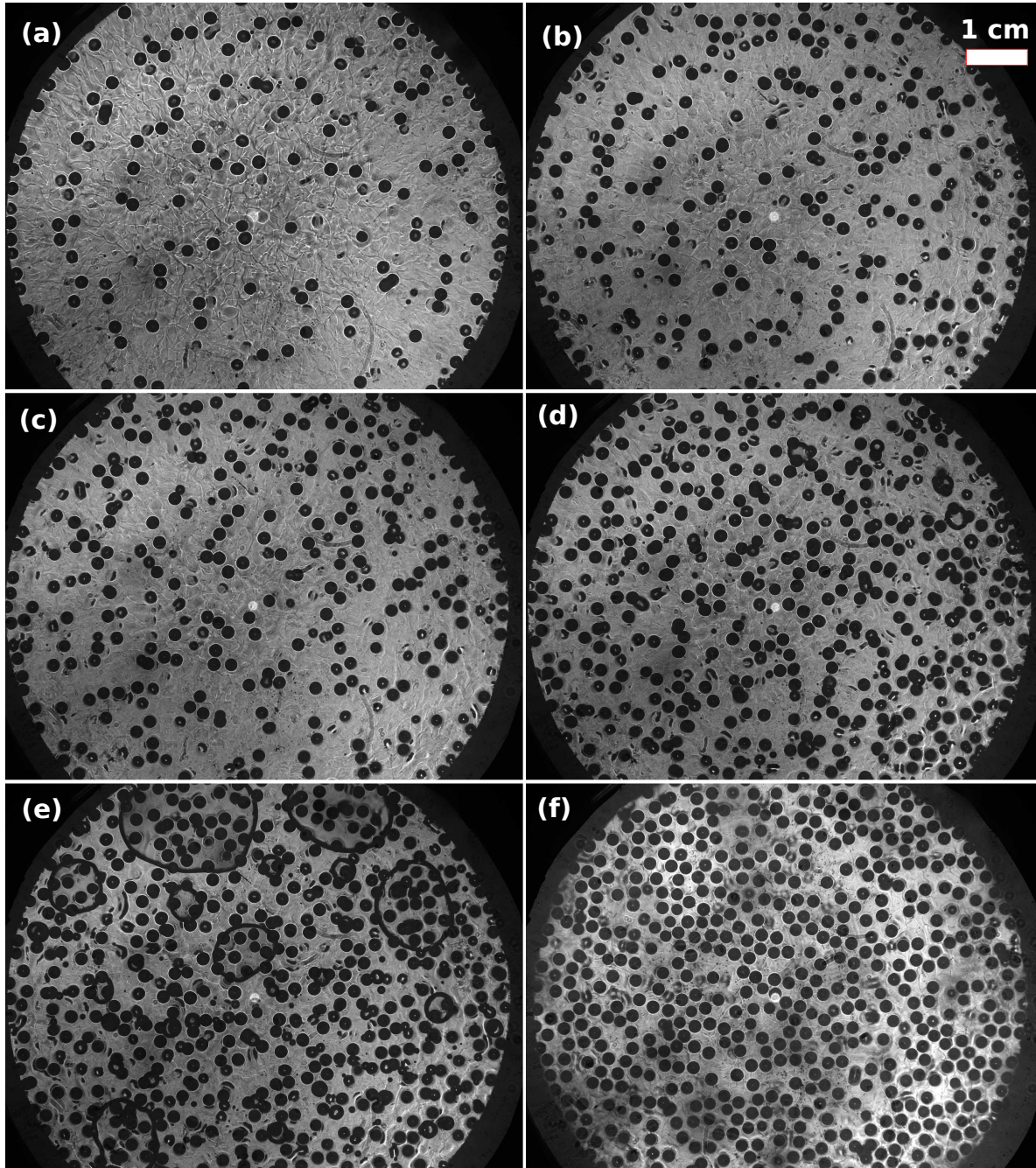


**Figure 3.36:** Medium cell - Effect of vapor pressure on the arrangement of drops in the liquid layer on the top plate.  $T_t = 35.00$  °C,  $T_b = 35.50$  °C. Pressure in (a) 433 psi, (b) 433.1 psi, (c) 433.2 psi, (d) 433.3 psi, (e) 433.4 psi and (f) 433.5 psi.

related to enhanced thermal driving in the vapor layer. Studies have shown that as  $Ra$  increases the wavelength of the large scale circulation also increases [24]. The drops appears to be arranged along the stagnation zones where the plumes were ejecting or impacting. As a consequence, the mean distance between the stripes/clusters of drops also increases with  $Ra$  due to the corresponding increase in the size of the convection rolls. Moreover, the temperature difference across the cell was not sufficient to suppress

dripping from the liquid layer at the top plate. Dripping occurred predominantly after the merging of two or more drops in the liquid layer.

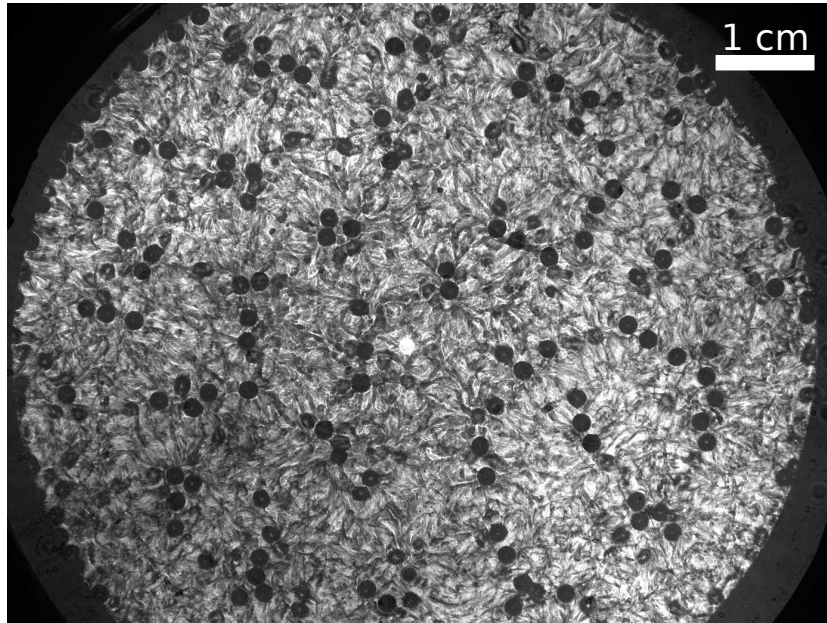


**Figure 3.37:** Medium cell: Arrangement of drops in the liquid layer on the top plate.  $T_t = 35.00$  °C,  $T_b = 49.00$  °C and  $P = 445$  psi. No liquid layer on the bottom plate.

### 3.7 Discussion: Thin, Medium and Thick Cell

The observations from the thin and medium cell experiments discussed in the previous section suggests that the presence/absence of a liquid pool above the bottom plate makes a significant difference to the patterns on the top plate. The elimination of the liquid layer on the bottom plate restricts the continuous supply of vapor onto the liquid layer at the top plate. As a consequence, the lower part of the cell was sub-saturated. The sub-saturated environment resulted in the evaporative effects playing a role in the dynamics of the liquid layer at the top plate. These effects were absent in the thick cell experiments. The reduced cell height also decreased  $Ra$  in the system thus lowering the turbulence intensity in the cell. These conditions are consistent with the assumptions in the BM model. In the thin cell experiments under certain conditions the dripping from the top plate liquid layer was nearly arrested. The positioning of drops on the top plate had a hexagonal symmetry with nearly no dripping, provided the thermal driving in the vapor phase was not strong. The hexagonal symmetry was lost as the mean temperature in the experiment was increased. This is attributed to the increase in  $Ra$  in the vapor layer. Dripping from the liquid layer was suppressed at all mean temperatures if the imposed temperature difference across the thin film was sufficiently large.

Let us attempt to explain some of these observations using the BM model. Figure 3.29 & Fig. 3.31 shows the quasi-stationary patterns in the thin cell experiments. Organized patterns were observed only in these two cases. The mean distance between the rolls in Fig. 3.29 & Fig.3.31 are 3.0 mm & 2.6 mm respectively and the corresponding non-dimensional wave numbers (normalized using the capillary length based on the top plate temperature) are 0.83 & 0.78 respectively. These values are consistent with those reported in the thick cell experiments in Fig. 3.28. The BM model predicts a steady state hexagonal pattern with a non-dimensional wavenumber of 0.71 if  $E < E_c$ .  $E$  was not calculated for these experiments as the liquid layer thickness was not measured. Attempts were made to measure the thickness of the liquid layer using a laser interferometer, but the signal was distorted by the underlying convection and no quantifiable information was obtained. Despite these limitations, the observations are qualitatively consistent with the predictions from the BM model.

The variation in the mean pressure inside the cell alters the thickness of the liquid layer. For the sake of simplicity let us consider a diffusive temperature profile inside the cell. The top plate has a stable layer of liquid that was in equilibrium with its environment, i.e.,  $E > E_c$  and  $P = P_s(T_I)$ . If the vapor pressure in the system was increased from  $P$  to  $P + \Delta P$  and  $\Delta T$  remains unchanged, then the interface temperature  $T_I$  should increase such that  $P_s(T_I) = P + \Delta P$ . Since  $\Delta T$  is unchanged, the liquid layer thickness should increase through condensation until an equilibrium condition is re-established. The condensation rate is dictated by the vapor pressure and the interface temperature (Eq. 3.22). Similarly, a decrease in pressure would result in a reduction in the thickness of the liquid layer.

The difference in the vapor pressure and  $\Delta T$  between Fig. 3.32 and Fig. 3.33 may explain the absence of drops at the centre of the top plate in Fig. 3.33. The increase in pressure resulted in a corresponding increase in the thickness of the liquid layer. As was mentioned earlier, the evaporation number is proportional to the fourth power of the average thickness. As a consequence, the increase in thickness lowers the evaporation number, thus, destabilizing the liquid layer, which in turn affects the pattern symmetry (BM Model). Similarly, lowering the pressure with fixed  $\Delta T$  would enhance the evaporation number. It was also observed in some of the experiments (not shown here) that the drops shrunk in diameter and eventually disappeared as the pressure was successively lowered. They disappear first in the center. With a further reduction in the vapor pressure the patterns closer to the boundaries start to disappear. A similar scenario is shown in Fig. 3.33 and Fig. 3.34 where the region around the centre appears to be void of drops. In these experiments, the liquid film thickness was controlled by varying the bottom plate temperature. Nevertheless, the effects are similar whether we vary the pressure or  $\Delta T$  as they are coupled to the evaporation number through Eq. 3.25.

In the experiments in Fig. 3.32 and Fig. 3.34,  $\Delta T$  was varied and the pressure was not regulated. As a consequence, the pressure varies due to the changes in  $\Delta T$ . Let us assume a linear temperature profile in the cell. No drops were dripping from the liquid layer at the top plate. So we assume that the liquid layer was stable and was in equilibrium with the vapor phase. This implies that  $T_I$  corresponds to the dew point temperature in the chamber. In Fig. 3.32, Fig. 3.33 and Fig. 3.34, the interface temperatures are 42.0 °C, 42.1 °C and 42.25 °C respectively. For the ease of calculation we assume the cell height to be 0.5 mm, and this gives a liquid layer thickness of 0.077 mm, 0.073 mm and 0.067 mm respectively. If  $E^*$  is the evaporation number in Fig. 3.32, then the evaporation numbers in Fig. 3.33 and Fig. 3.34 are  $1.36E^*$  and  $1.92E^*$  respectively. As we increase  $\Delta T$  across the cell, the evaporation number increases, and thus stabilizes the liquid layer.

One could argue that there was no liquid layer around the center of the top plate in Fig. 3.33 and Fig. 3.34. For this statement to be true, the temperature at the lower surface of the top plate at the center should be above the dew point temperature in the cell. The measured pressure for the experiments in Fig. 3.34 was  $34.9 \pm 0.07$  bar, and the corresponding saturation temperature was  $42.25 \pm 0.09$  °C. Please note that the uncertainty in the measurements reported here are the maximum and minimum values within which the variable fluctuated. The top plate temperature in the present experiment was set to 41.00 °C. As was mentioned in Chapter 2, the top plate thermistor measures the temperature of the cooling water and not the temperature at the lower side of the top plate. The experiments under discussion was operated at a constant heat flux mode. Let us assume that all the heat added to the bottom plate was transferred to the top plate without any loss at the lower side of the bottom plate or the side walls. The bottom plate was supplied with 27.7 Watts. So the temperature difference across the top plate using Fourier's heat conduction equation is

$$\Delta T_{top} = \frac{Qd_{top}}{\lambda A_{top}} \quad (3.26)$$

where  $\lambda$  is the thermal conductivity of the sapphire ( $\lambda = 38$  W/(m-K) at 25 °C),  $d_{top} = 9.5$  mm is the thickness of the top plate,  $A_{top}$  is the surface area of the top plate and  $Q$  is the heat flux. Using Eq. 3.26 we obtain the temperature difference across the top plate  $\Delta T_{top} \approx 0.9$  °C. This is the maximum possible temperature difference across the top plate under the assumption that the present convection cell is well insulated along the lateral side walls and also along the lower side of the bottom plate. Using the calculated value of  $\Delta T_{top}$ , the average temperature at the underside of the top plate is around 41.9 °C and is lower than the dew point temperature. As a consequence, the surface of the top plate has to be coated with a layer of liquid SF<sub>6</sub>. It is important to note that the insulations at the side walls and that around the bottom plate are

not adequate to provide an adiabatic boundary condition. The side walls in the thin cell experiments were made out of paper with thermal conductivity of  $0.06 \text{ W}/(\text{m}\cdot\text{K})$  which is about three times higher than  $\text{SF}_6$  in the vapor phase at a temperature of  $30^\circ\text{C}$ . Conduction through the sidewalls introduces temperature inhomogeneity at the top and bottom plates. Moreover, additional heat loss occurred from the lateral sides of the bottom and top plates. As a consequence, the coldest and warmest points on the top and bottom plates are at the center. This implies that  $\Delta T$  across the convection cell was highest at the center of the cell, and decreases radially as we move towards the sidewalls. In terms of evaporation number  $E$ ,  $E$  is the highest at the cell center, and decreases as we move radially outwards. Under appropriate conditions, the evaporation number at the interface can be varied radially such that part of the liquid layer was stable and in the rest of the layer it was unstable. This explains a stable (no drop) liquid layer at the center and an unstable layer away from the center in Fig. 3.33 and Fig. 3.34.

The observation of a hexagonal arrangement of drops with nearly no dripping in the liquid layer at the top plate in the thin cell experiments are consistent with the predictions of BM theory although the critical thickness was not measurable due to experimental limitations. It was also observed that as  $Ra$  in the vapor layer was increased, the arrangement of the patterns were influenced by the underlying convection. This was evident from the shadowgraph images shown in Fig. 3.32. Moreover, the thin and medium cell experiments showed that the arrangement of the drops at the top plate in the absence of a liquid layer at the bottom plate was strongly influenced by the underlying structure of the convection rolls. The drop like structure originates due to the instability of the liquid layer, and is swept around by the underlying convection rolls. The shear encountered by the drop is minimal near upwelling or down-welling region in a large scale circulation in RBC. As a consequence the drops are aligned along the convection rolls in an RBC system. The shift in the spacing between the drops as a function of Rayleigh number was also demonstrated in the medium cell experiments. The BM model neglected the influence of convection in the vapor layer. So this model cannot be used for studying the effect of shear on the thin liquid layer underneath the top plate. An additional forcing term should be included in the thin film equation (Eq. 3.24). The forcing term should be coupled with the convection in the vapor layer to explain these observations.

The Rayleigh numbers in the experiments conducted in the thick cell were at least 100 times higher than in the experiments using thin and medium cells. It is interesting to note that the hexagonal patterns at the top plate with a supersaturated vapor layer was not strongly influenced by the convective motions in the vapor layer. This was discussed briefly in Section 3.2.2. The main argument was that the drop development

time scales were much shorter than the time scales of the large scale circulations. This may well be true as the equivalent Stokes number for these drops are significantly greater than zero. It may be interesting to see how these drops are arranged under conditions close to the critical point of SF<sub>6</sub>. As we approach the critical point the density difference between the liquid and vapor phase decreases and this would reduce the Stokes number of these drops. Experiments were conducted to investigate these effects, but no quantifiable observations were obtained due to critical opalescence and vigorous boiling of the liquid layer at the bottom plate. Another possible explanation is that the large scale circulation was much weaker in the experiments with a layer of liquid covering the bottom plate compared to the dry bottom plate experiments. In the presence of a boiling liquid layer the majority of heat and mass was transported through phase change (boiling/condensation). The buoyant bubbles may disrupt the large scale circulations in the liquid phase which in turn may slow down the circulation in the vapor phase. We varied the height of the liquid layer above the bottom plate to test the effect of the weakening of the large scale circulation. But this did not have any strong influence on the hexagonal patterns at the top plate. This does not rule out the possibility of the weakening of the large scale circulations. Additional experiments and numerical calculations are required to understand the role of boiling and falling drops on the large scale circulation.

It is also interesting to note that the patterns in the liquid layer at the top plate with a supersaturated vapor layer below, called regime 1, and the patterns in the thin cell experiments with a sub-saturated vapor layer below, called regime 2, have similar non dimensional wave numbers in the stationary state. In the absence of coarsening in the long-time limit, it appears that the dynamics of the pattern at the top plate in regime 1 and regime 2 are governed by a mechanism similar to the evaporation/condensation mechanism in the BM model. The central point in the BM model was that the evaporation-condensation effects prevented the coarsening of the patterns in the long-time limit. In the BM model, the evaporation-condensation effects were modeled using the Hertz-Knudsen law (see section 3.3.3) which represents the mass transfer between different phases across the interface. This mass transfer may occur through different mechanisms, and evaporation-condensation is one such mechanism. In the experiments with a liquid layer at the bottom plate, the vapor phase was supersaturated due to the continuous supply of warm vapor from the boiling liquid pool. Therefore, condensation effects are relevant in transferring mass into the liquid layer at the top, but the evaporation effects do not play any role. Continuous condensation results in uninhibited growth of the liquid layer, thus resulting in dripping. Dripping represents a loss of mass from the liquid layer. Dripping unlike evaporation, is an intermittent yet periodic process. When averaged over time, its effect may be similar to those

of evaporation. So dripping stabilizes a liquid layer that exceeds a critical thickness. Dripping dynamics cannot be modeled using the thin film approximation as it violates the assumptions and boundary conditions used in formulating the evolution equation for the interface position (Eq. 3.24). Moreover, dripping results in the formation of capillary waves in the liquid layer which may influence the alignment of the drop like deformations.

Let us assume that the capillary waves generated due to dripping do not influence the dynamics in the liquid layer strongly. With this assumption in place, the evolution equation for the interface (Eq. 3.24) as proposed in the BM model can be retained locally with  $J$  representing the net mass flux added or lost from the liquid layer per unit time. The time integral of  $J$  should be zero under steady state conditions. From the discussions so far, it appears that the net mass flux (in one direction) plays a crucial role in dictating the dynamics, and a regular hexagonal patterns are established if the mass flux exceeds a critical value. In regime 1, the role of  $\Delta T$  was to enhance the mass transfer rate by increasing the supersaturation in the vapor phase. In principle, these observations can be reproduced by having a continuous mass supply to the top plate without any of the thermal effects and one should see a hexagonal arrangement of the liquid interface at the top plate. Experiments on this idea have been conducted in the past using a porous plate [36, 39]. In these experiments a continuous mass flux of silicone oil across a porous plate was maintained. The dynamics observed in these experiments were similar to the ones described here in the context of a supersaturated vapor phase. In these experiments, the liquid layer was not dripping, instead there was a continuous liquid column from the unstable thin layer to the liquid pool below. This can be attributed to the relatively high mass flow rate in these experiments. A similar situation can be created in our experiments as well if enough power can be supplied to the bottom plate to enhance the boiling rate/mass flux. This would require modification of the present experimental setup and hence was not attempted. Moreover, in these experiments there was no temperature gradient across the liquid layer and no turbulent convection in the gas layer below.

In the porous plate experiments, three different regimes were identified based on the flow rates [36, 39]. In the first regime, the liquid layer was dripping and in the second regime, the layer had liquid columns. In both cases a hexagonal arrangement of columns/drops was observed. In the third regime, a chaotic disordered arrangement of columns was observed, and thus this regime was called the turbulent regime. The flow rate was increasing from the first to the third regime. In our experiments with a layer of liquid covering the bottom plate (also known as regime 1) we identify two sub-regimes - small and large  $\Delta T$ . In the small  $\Delta T$  regime, the imposed temperature difference was not large enough to transport enough vapor to render the entire layer unstable.

As a consequence we observed a disorganized (random) arrangement of drops on the top plate. In the large  $\Delta T$  regime, the drops were arranged in a hexagonal lattice with periodic dripping. We did not observe any loss in symmetry as we increased the thermal driving. Similar observations were also reported in the experiments with SF<sub>6</sub>-He binary mixture close to the critical point of SF<sub>6</sub> [78].

Experiments and associated discussions so far have revealed that the evaporation-condensation effects, and their equivalent condensation-dripping effects, have prevented the coarsening of the patterns in the long-time limit in the thin liquid layer at the cold top plate. Similar observations have been reported from models using Cahn-Hilliard equations. Cahn-Hilliard equations are used for modeling phase separation in a binary mixture [94]. Bestehorn and Merkt (2006) [43] reported that in a simplified form of an extended Cahn-Hilliard system, in the presence of evaporation-condensation effects, the stationary solutions have a finite wavelength. A similar model was used for the suppression of Ostwald ripening in active emulsions within the framework of a Cahn-Hilliard system [95]. The evaporation-condensation effects were replaced with chemical reactions. These reactions generate a drop material out-flux/influx similar to the evaporation-condensation effects in our experiments. This effect stabilizes droplets of a certain size in emulsions, and thus suppresses Ostwald ripening.

### 3.8 Summary

The experimental observations and the subsequent discussions highlighted the effects of phase change on the RTI of a thin film in a moist RBC experiment. The experiments were classified into two regimes depending on the saturation ratio in the vapor layer below the liquid layer at the top plate. In regime 1, the vapor layer is supersaturated, and in regime 2, the vapor layer is sub-saturated. In regime 1, we observed two different sub-regimes depending on the imposed temperature gradient: small  $\Delta T$  and large  $\Delta T$ . In the small  $\Delta T$  experiments, the patterns in the liquid layer at the top plate did not have spatial periodicity. On the other hand, in the large  $\Delta T$  experiments, the patterns at the top plate had a hexagonal lattice structure with a well-defined wavelength. These patterns grew over time due to the continuous condensation of SF<sub>6</sub> vapor and dripped periodically into the liquid layer at the bottom plate. In regime 2, the liquid layer at the bottom plate was eliminated and also the cell height was reduced to suppress the  $Ra$  in the vapor layer. This rendered the lower part of the cell sub-saturated. Under appropriate conditions it was observed that the liquid layer at the top plate was stabilized against gravity by the evaporation-condensation effects. The dripping from the liquid layer at the top plate was nearly suppressed due to the evaporative effects in the vapor layer, and stable hexagonal patterns were observed at the top plate if the  $Ra$  in the vapor layer was low. The non-dimensional wave number of this pattern is similar

to the pattern wave number obtained in the large  $\Delta T$  experiments in regime 1. As the  $Ra$  in the vapor layer was increased, the patterns were influenced by the convective motions in the vapor layer. At very high  $Ra$ , it was observed that the spatial periodicity in the liquid layer at the top plate was lost, and the drops in the layer were aligned along the convection rolls in the vapor phase. The observations from the experiments with no liquid layer on the bottom plate were compared with the theoretical prediction from Besthorn and Merkt (2006) (BM model) [43]. The experimental observations were qualitatively consistent with the theoretical predictions. In the low  $Ra$  experiments, the non-dimensional wave number  $\approx 0.8$ , observed in the hexagonal pattern is consistent with the predicted value of 0.7. The BM model predicted that if the evaporation number was high enough, then the liquid layer at the top plate can be stabilized against gravity. Furthermore, it was also predicted that close to the critical evaporation number, the patterns in the liquid layer were arranged in a hexagonal lattice structure with no coarsening in the long-time limit. This was demonstrated experimentally for the first time in the present work. Additional work is required to extend the BM model to account for the effects of shear from the underlying convective flow in the vapor phase.

# 4 Can Rain and Hail Nucleate Cloud Droplets?

In this chapter we discuss the possibility of a new mechanism for the nucleation of cloud droplets in a deep convective cloud. We present laboratory observations and a simple model to explain these observations. Later, we extend this model to check if a similar mechanism carries over to atmospheric clouds.

## 4.1 Laboratory Atmosphere

The Earth's atmosphere consists of various gases like Nitrogen, Oxygen, water vapor etc. Of all these gases, only water vapor undergoes phase change under the temperature and pressure range of the atmosphere. The composition of Earth's atmosphere can be separated into two parts: the moist component composed of saturated water vapor and the dry component composed of all the other dry gases. In our experiment, we used SF<sub>6</sub> and Helium to mimic the Earth's atmosphere. The temperature and pressure were adjusted such that SF<sub>6</sub> exists in both liquid and vapor phase, thus, playing the role of water vapor in the Earth's atmosphere. Helium, on the other hand, does not undergo phase change under the laboratory conditions, thus, mimicking the dry component in the Earth's atmosphere. The advantage of using SF<sub>6</sub> is that a relatively small amount of supersaturation is sufficient to trigger homogeneous nucleation [82].

Addition of Helium alters the nature of the flow. Boiling of SF<sub>6</sub> on the bottom plate was suppressed due to the increased atmospheric pressure. Moreover, Helium has very high thermal diffusivity (about ten times greater than SF<sub>6</sub> vapor at 25 °C) and hence reduces the Rayleigh number of the flow. A convection cell of rectangular planform was used for this experiment. The sidewalls were made of acrylic with mirrors embedded on them. The mirror unit was used for flow visualization (please see section 2.4.3 for details). A schematic of the cell is shown in Fig. 4.1.

## 4.2 Experimental Observations

The bottom plate was warmed up to a temperature  $T_b$ , while the top plate temperature was kept at  $T_t < T_b$ . The pressure and temperature were adjusted such that a layer of liquid  $\text{SF}_6$  formed on the top plate of the cell. Evaporated  $\text{SF}_6$  vapor rose from the liquid-gas interface, and condensed on the top plate creating a thin liquid  $\text{SF}_6$  layer that continuously underwent RTI. The thin layer grew over time and resulted in the dripping of  $\text{SF}_6$  drops that fell through the  $\text{SF}_6$ -He gas layer into the liquid pool at the bottom. The dynamics of this layer was discussed in chapter 3.

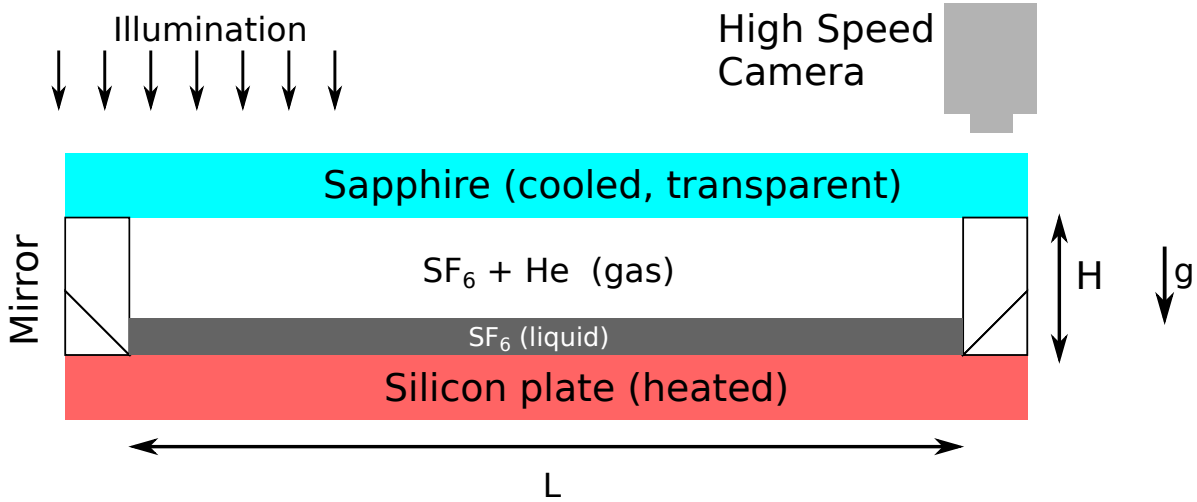


**Figure 4.1:** Schematic of the convection cell. Mirrors were embedded into the acrylic side walls. Only the two mirrors covering the lower half of the cell are shown for clarity.

Figures 4.2-4.6 shows the dynamics observed using the side wall mirrors in the convection cell under various pressures and temperatures. The flow parameters for each of these figures are mentioned in the respective figure captions. As was discussed in section 2.4.3, the sidewall mirrors consist of two parts, one providing visual access to the upper half of the cell and the other part providing visual access to the lower half. Figure 4.2 to 4.4 shows the dynamics in the upper half of the cell. These figures show a big drop pinching off from the liquid layer attached to the top plate. In the process, the stem connecting the mother drop and the liquid layer undergoes Rayleigh-Plateau instability [35], thus, generating additional satellite drops. These drops collide and bounce off or coalesce with the mother (or primary) drop (Figs. 4.2, 4.4). These drops deform due to the pressure distribution caused by the free fall. The extent of deformation is a function of the Weber number  $We = \rho U_t^2 d / \sigma$  where  $\rho$  is the density of the ambient gas,  $U_t$  is the terminal velocity of the drop,  $d$  is the diameter of the drop. In almost all cases presented here we observe nucleation of new droplets in the wake of the large cold drop. The number of nucleated droplets depend on the temperature difference between the two plates, the mean temperature and also on the liquid level

above the bottom plate.

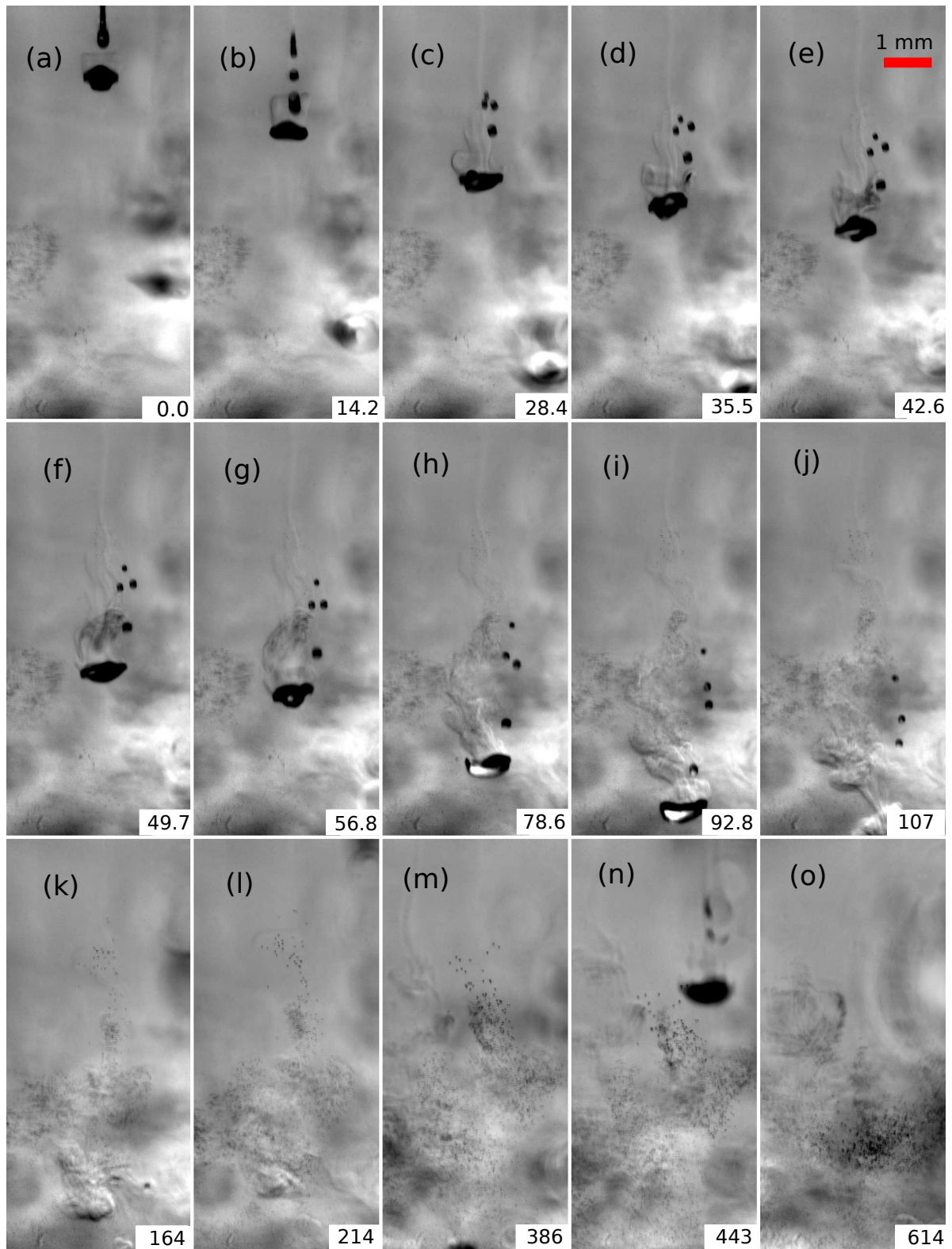


**Figure 4.2:** Contrast enhanced image sequence highlighting the dynamics in the upper half of the cell.  $T_t = 40.00$  °C,  $T_b = 45.00$  °C and  $P = 47.1$  bar. The time stamp (in ms) for each sub-figure is shown at the bottom-left corner. (a) and (b) shows the pinch-off instability and the formation of satellite drops. (c-o) nucleation in the wake of cold drop.

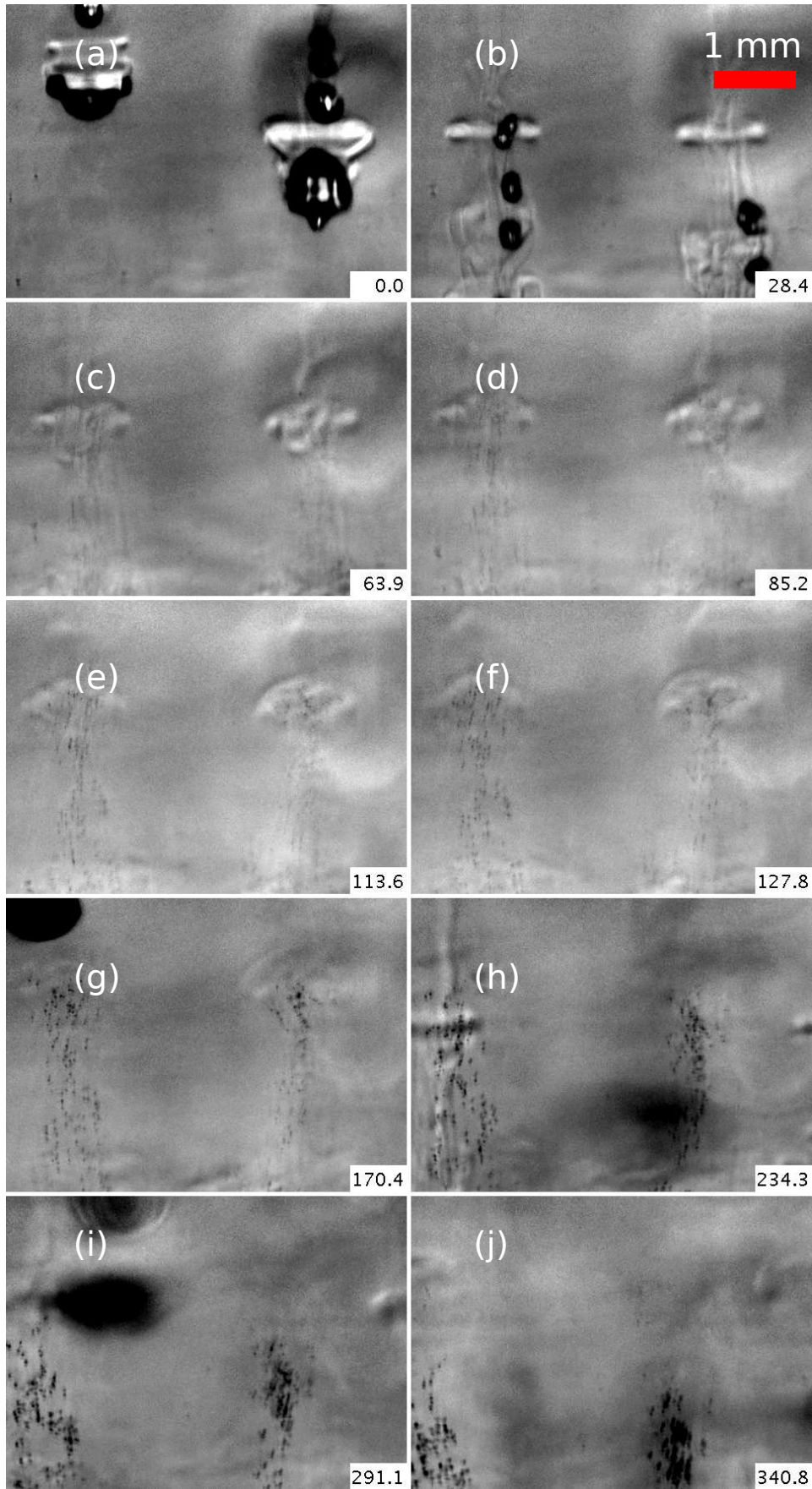


**Figure 4.3:** Contrast enhanced image sequence highlighting the dynamics in the upper half of the cell.  $T_t = 36.00$  °C,  $T_b = 45.00$  °C and  $P = 44.9$  bar. The time stamp (in ms) for each sub-figure is shown at the bottom-right corner.

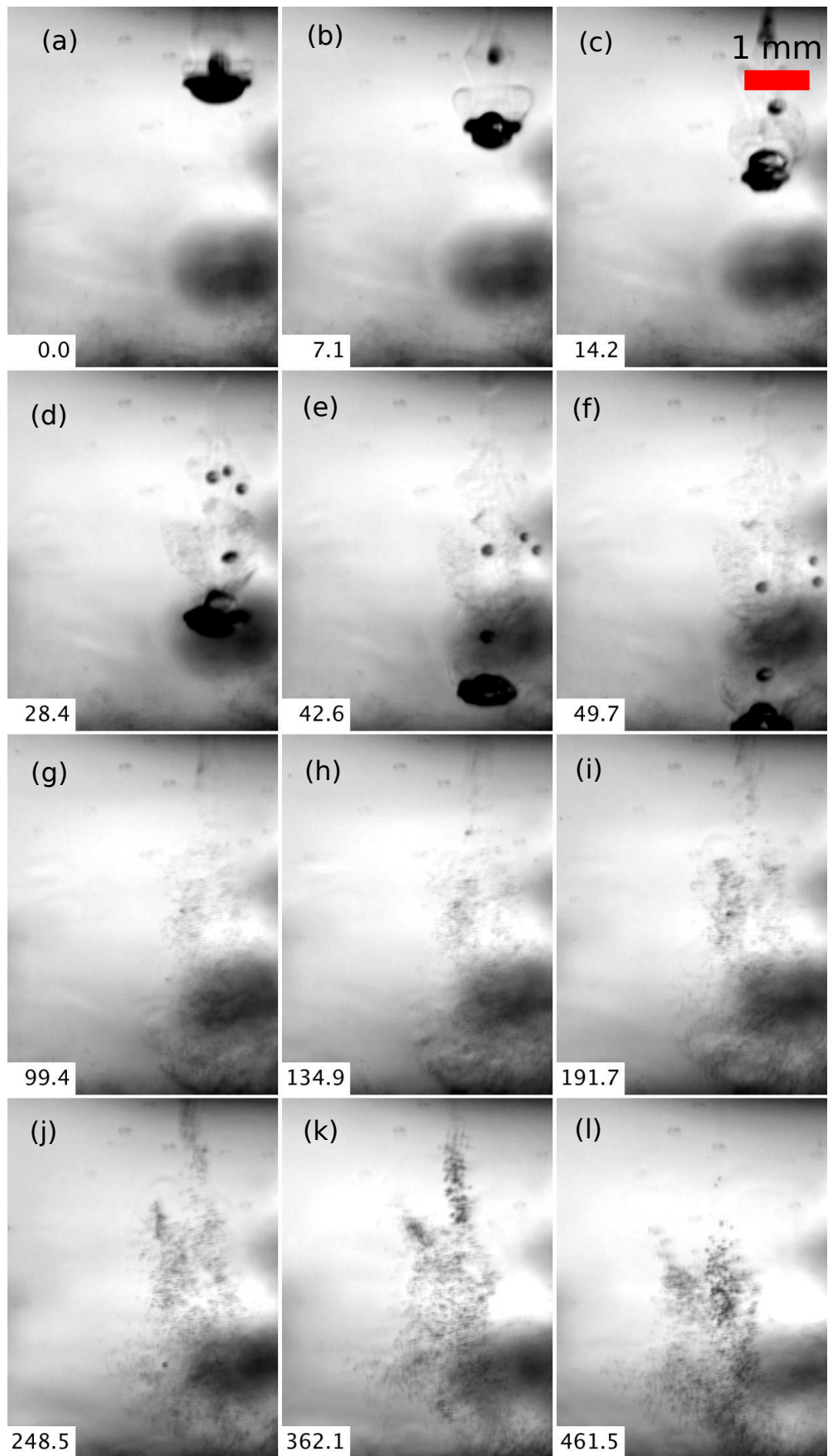


**Figure 4.4:** Contrast enhanced image sequence highlighting the dynamics in the upper half of the cell.  $T_t = 38.00$  °C,  $T_b = 45.00$  °C and  $P = 45.8$  bar. The time stamp (in ms) for each sub-figure is shown at the bottom-right corner.

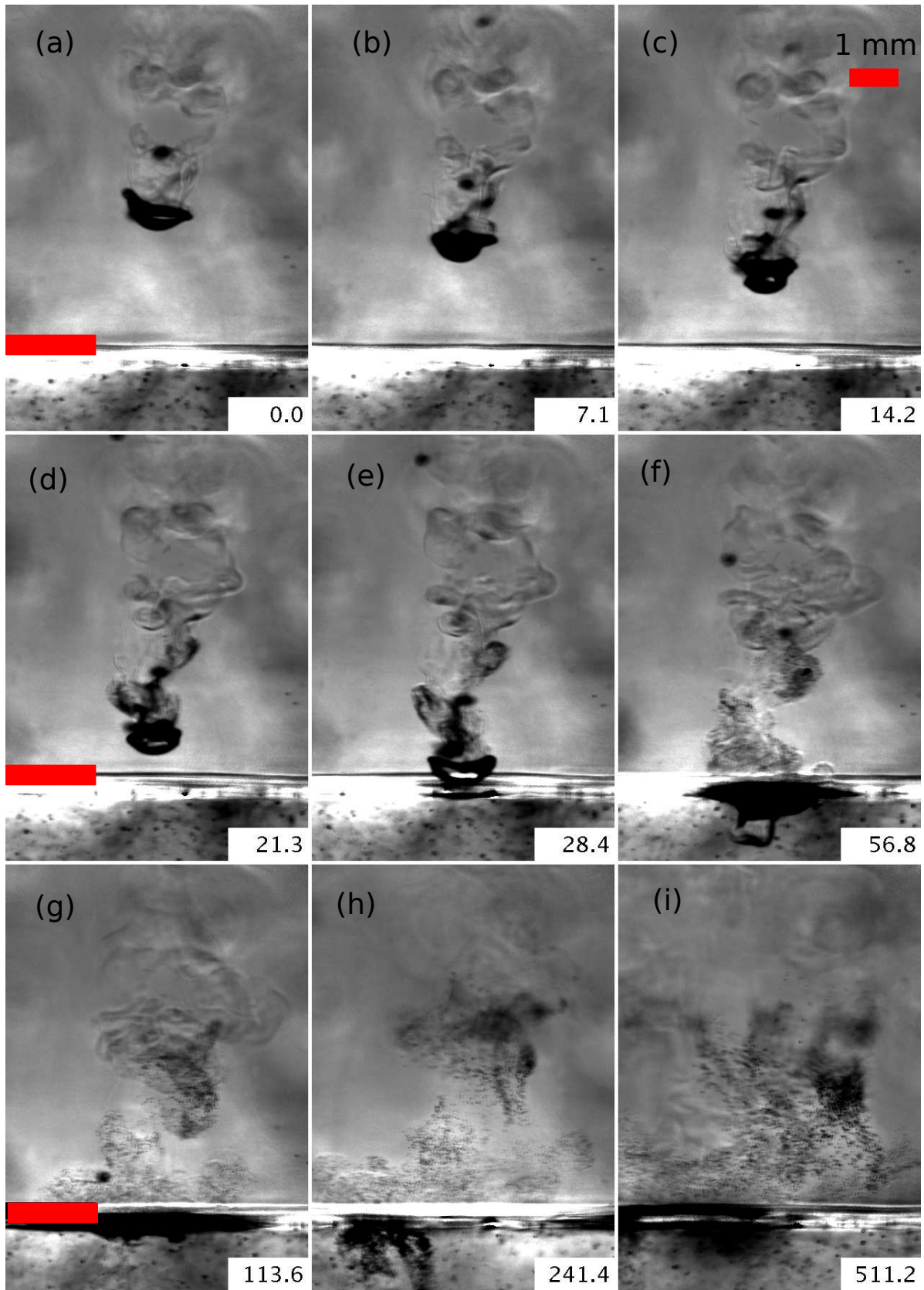


**Figure 4.5:** An image sequence depicting the nucleation of micro-droplets in the lower half of the cell.  $T_t = 40.00$  °C,  $T_b = 44.00$  °C and  $P = 46.9$  bar. The time stamp (in ms) for each sub-figure is shown at the lower-right corner. The red bar on the left indicates the position of the liquid-vapor interface and is about 6 mm from the bottom plate. The details are discussed in the main text.

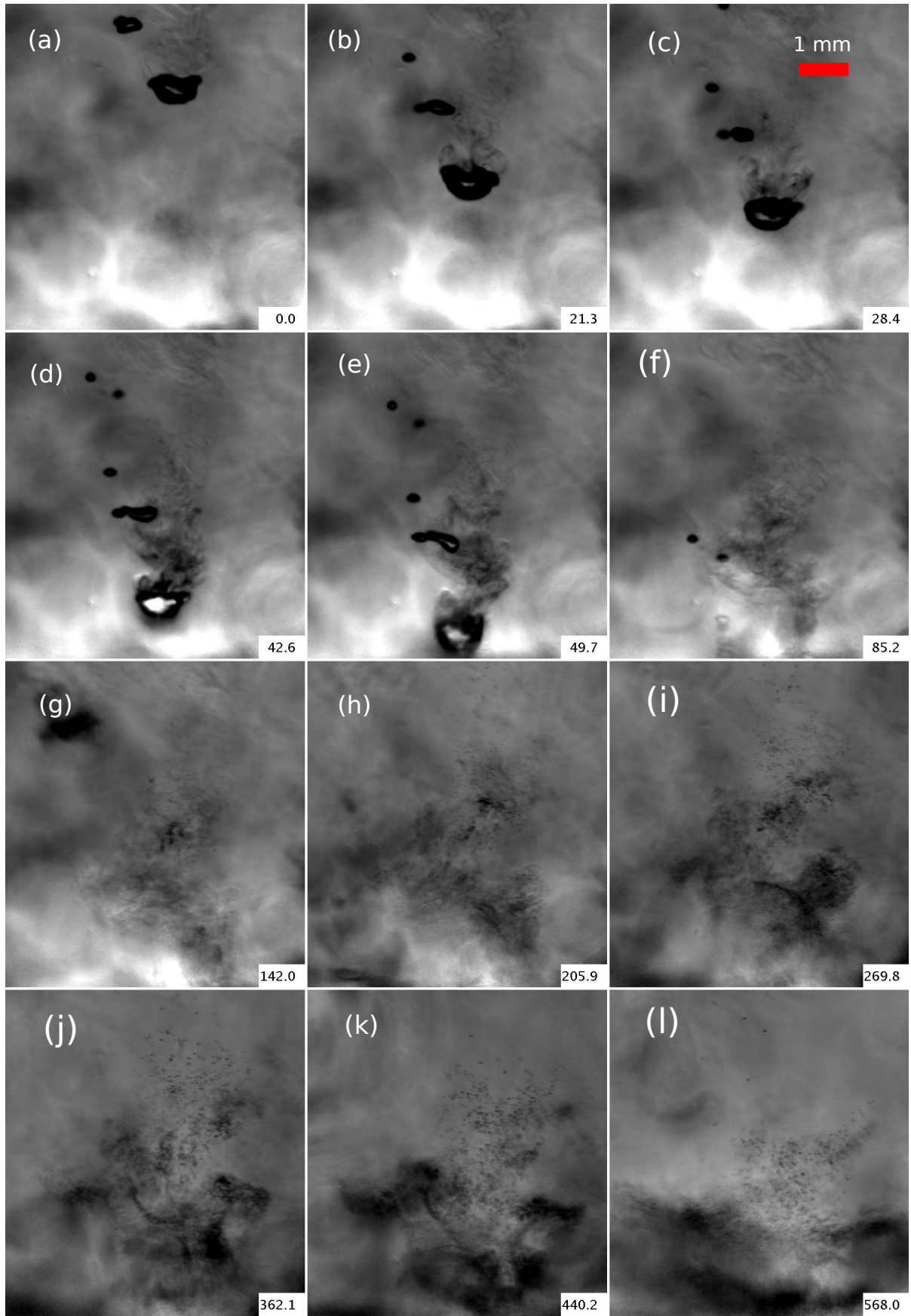


**Figure 4.6:** Contrast enhanced image sequence highlighting the dynamics in the lower half of the cell.  $T_t = 40.00$  °C,  $T_b = 44.00$  °C and  $P = 46.9$  bar. The time stamp (in ms) for each sub-figure is shown at the bottom-right corner.

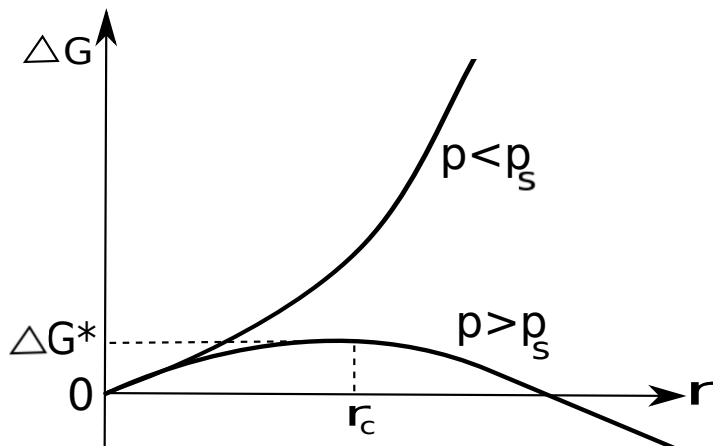
The role of Helium concentration is not explored in this thesis as the concentration of Helium in the vapor phase cannot be controlled in the present experimental setup. Several experiments were conducted at various conditions. Only a select set of images are shown here for the sake of brevity. We discuss in detail the experiments shown in Fig. 4.5. The dynamics is similar in all the cases.

Figure 4.5 shows a deformed large drop with a lateral diameter of  $\approx 1$  mm falling through the SF<sub>6</sub>-He atmosphere from the top plate along with a few satellite drops. The drop is deformed into a pancake like structure due to the surrounding pressure field. The temperatures of such drops are close to  $T_t$  as they originated from the liquid layer attached to the top plate. The wake behind the deformed drop is visible due to the temperature difference between the drop and the ambient. The spatial inhomogeneities in the refractive index caused by the cooling induced by the cold drop in its wake is captured in the shadowgraph image (Fig. 4.5 (a-f)). In the near wake of the deformed drop, the shed vortices entrain saturated warm ambient vapor and mix it with the cold vapor from the boundary layer as shown in Fig. 4.5 (a-f), thus locally altering the temperature and saturation ratio. In particular, the intensity variation is more prominent in Fig. 4.5(c-f). The enhanced contrast in the near wake is due to the nucleation of micro-droplets in the locally supersaturated regions. These micro-droplets are visible in Fig. 4.5 (e, f), and they continue to grow in size by condensation of SF<sub>6</sub> vapor from their supersaturated vicinity until they fall into the liquid pool (Fig. 4.5 (g-h)). The number of nucleated micro-droplets vary strongly for different falling drops for fixed experimental parameters. This suggests that the distribution of SF<sub>6</sub> vapor was non-uniform due to the turbulent convection in the gaseous layer. In this particular case, the cold drop may have fallen through a rising hot plume rich in SF<sub>6</sub> vapor.

For the experiment shown in Fig. 4.5, the temperature at the bottom and top plates were  $T_b = 44.00$  °C and  $T_t = 40.00$  °C respectively, and the pressure  $P = 46.9 \pm 0.1$  bar. We estimate the mole fraction of He in the gaseous layer to be  $x_{He} \approx 26\%$  using Dalton's law of partial pressure [96]. We observed the nucleation of micro-droplets in the wake of a falling cold drop only when  $T_b$  was sufficiently close to the critical temperature of SF<sub>6</sub> ( $T_c = 45.57$  °C) at a fixed temperature difference,  $\Delta T = T_b - T_t$ . As we show below, this is attributed to the lowering of the critical supersaturation required to trigger nucleation as the critical temperature of SF<sub>6</sub> is approached.

### 4.3 Homogeneous Nucleation

The experiments were conducted using SF<sub>6</sub> (purity - 99.999% by volume) and He, and no additional nuclei were added into the convection cell to initiate nucleation. Hence, the nucleation observed in this experiment is due to homogeneous nucleation, i.e., spontaneous formation and growth of droplets under saturated conditions without the aid



**Figure 4.7:** Variation in net change in Gibb’s free energy due to the formation of a droplet of radius  $r$ .  $p$  is the partial vapor pressure in the ambient and  $p_s$  is the saturation vapor pressure on a planar surface.  $\Delta G^*$  is the energy barrier,  $r_c$  is the critical radius. Adapted from [17]

of any surface. Classical nucleation theory (CNT) has successfully explained homogeneous nucleation in many systems [97, 98]. We use CNT to explain our experimental observations. Before we discuss the experimental results we provide a brief introduction to CNT and other relevant material required for understanding the observations. For a detailed account see [17, 44, 99–101].

### 4.3.1 Classical Nucleation Theory (CNT)

Classical nucleation theory is an approximate theory that predicts the rate of formation of a new thermodynamic phase. We discuss CNT in the context of homogeneous nucleation. A similar idea can also be used for heterogeneous nucleation when additional complexities related to the nuclei are taken into account. The details on heterogeneous nucleation will not be discussed here.

In the first step towards homogeneous nucleation, a new thermodynamic phase embryo is created by the random collision of the molecules. We explore under what conditions these embryos are stable. Nucleation of new droplets occurs at constant temperature and pressure, so an appropriate quantity to study this process is the Gibb’s free energy. The net change in Gibb’s free energy  $\Delta G$  due to the formation of a droplet of radius  $r$  is given by [17]:

$$\Delta G = A\sigma - \frac{4}{3}\pi r^3 \Delta g, \quad (4.1)$$

where  $\sigma$  represents the surface tension,  $A = 4\pi r^2$  the surface area of the interface,  $\Delta g$  is the chemical potential or the free energy per volume associated with phase change and  $r$  is the radius of the embryo. The first term in Eq. 4.1 represents the energy spent in

the formation of the new interface and is called the interface energy of the liquid-vapor interface. This term is proportional to the surface area and is always positive. The second term represents the change in Gibbs free energy due to the formation of the new phase and is related to the difference in the chemical potential between the two phases. This term is directly proportional to the volume of the new phase and can be negative or positive depending on the saturation ratio in the ambient atmosphere. We assume that the nucleated phase is spherical. The surface term is proportional to  $r^2$  and the volume term is proportional to  $r^3$ . As a consequence, at small  $r$  the surface term dominates and  $\Delta G$  is positive. If the volume term is positive, then there is a critical radius  $r_c$  above which  $\Delta G$  is negative.  $\Delta G(r_c)$  represents the energy barrier that has to be overcome for the sustained growth of the new phase, in our case for the stable growth of a new droplet. The variation of  $\Delta G$  under various conditions is schematically represented in Fig. 4.7. It shows that only under supersaturated conditions we have a decrease in the total energy of the system beyond the critical radius. So, it is impossible to obtain stable nucleation under sub-saturated conditions. The volume term is rewritten as [17]

$$\Delta g = nk_B T \ln \frac{p}{p_s}, \quad (4.2)$$

where  $n$  is the number density of the molecules,  $k_B$  is the Boltzmann constant,  $p$  is the vapor pressure of the nucleating phase and  $p_s$  is the saturation vapor pressure of the nucleating phase at temperature  $T$ . The energy barrier that has to be overcome for a given saturation ratio is obtained by setting the derivative of  $\Delta G$  with respect to  $r$  to zero. Consequently, we obtain the critical energy barrier  $\Delta G^*$  to be

$$\Delta G^* = \frac{16\pi}{3} \frac{\sigma^3}{(nk_B T \ln S)^2}, \quad (4.3)$$

where  $S = \frac{p}{p_s}$  is the saturation ratio; defined as the ratio of the vapor pressure and the saturation (equilibrium) vapor pressure at that temperature, and the critical radius  $r_c$  is

$$r_c = \frac{2\sigma}{nk_B T \ln S} \quad (4.4)$$

According to CNT, the rate of formation of critical embryos or droplets  $J$  is given as

$$J = nZj \exp\left[\frac{-\Delta G^*}{k_B T}\right], \quad (4.5)$$

where  $n$  represents the number density of the molecules,  $j$  indicates the rate at which molecules diffuse towards the nucleus as the growth is limited by the diffusion process and  $Z$  is the Zeldovich factor. The exponent represents the ratio of the energy barrier and the thermal energy of the molecules. If the ratio is very high then the rate of

nucleation would be significantly low. For instance, at 30 °C a supersaturation of 300% is required for homogeneous nucleation of liquid water. This may explain why homogeneous nucleation of liquid water is not commonly observed in nature. The Zeldovich factor represents the probability that an embryo at the top of the energy barrier would cross over to continue growing. The rate expression Eq. 4.5 is rewritten as [44]

$$J = \frac{1}{\rho_l} \sqrt{\frac{2M\sigma}{\pi N_A}} \left( \frac{p_s}{k_B T} \right)^2 S \exp \left[ -\frac{16\pi M^2 \sigma^3}{3(N_A \rho_l \ln S)^2 (k_B T)^3} \right], \quad (4.6)$$

where  $\rho_l$  is the density of the liquid phase,  $M$  is the molecular weight,  $\sigma$  is the surface tension at the liquid-vapor interface,  $N_A$  and  $k_B$  are Avogadro's and Boltzmann's constants, respectively. By convention [44], the threshold defining a significant rate of homogeneous nucleation is taken to be  $J_c = 1 \text{ cm}^{-3} \text{ s}^{-1}$ . For more information about this expression and CNT in general, please see [44, 99].

We estimate the critical saturation ratio  $S_c$  required for triggering nucleation using Eq. 4.6, and using Kelvin's equation (Eq. 4.5) we estimate the corresponding critical size  $r_c$ , of the liquid embryo, that has to be exceeded for the sustained growth of a droplet. The time required for the concentration of embryos to reach their steady-state values (see, e.g., [44, 97]) is estimated using:

$$\tau = \frac{\sigma}{\phi k_B T (\ln S)^2}, \quad (4.7)$$

where  $\phi = p_v / \sqrt{2\pi(M/N_A)k_B T}$  is the flux of vapor molecules to the embryo surface at the vapor pressure  $p_v$  and the temperature  $T$ . Embryos with radius  $r \geq r_c$  will grow initially by condensation of the molecules from the vapor onto its surface. Using Maxwell's model for diffusion limited growth, the increase in the radius of the droplet with time is calculated as

$$r \frac{dr}{dt} = \frac{D\rho_v}{\rho_l} (S - 1), \quad (4.8)$$

where  $D$  is the molecular diffusion coefficient and  $\rho_v$  is the vapor density away from the droplet.

In the case of heterogeneous nucleation, i.e., in the presence of a favorable nuclei the energy barrier is drastically reduced. The surface interaction between the nuclei and the nucleating phase plays a crucial role in determining the energy barrier. Moreover, in the rate expression Eq. 4.5, the prefactor term is a function of the number of activation sites instead of the number density of the molecules. For more details on heterogeneous nucleation please see [44, 99, 100].

### 4.3.2 Comparison With The Experiment

Let us calculate the parameters required for homogeneous nucleation of SF<sub>6</sub> in the experiment shown in Fig. 4.5. We assume that the ambient was saturated with SF<sub>6</sub> vapor at a mean temperature of 42.00 °C. At  $T_m = 42$  °C, using the parameters for SF<sub>6</sub> in Eq. 4.6, we find  $J = J_c$  at  $S_c = 1.000815$  [80, 102, 103]. The corresponding critical size of the liquid embryo is  $r_c = 21.2$  nm (Eq. 4.5). The time required to establish the steady-state nucleation rate is  $\tau = 1.3$   $\mu$ s (Eq. 4.7). The time for condensation growth from an initial radius of  $r_c$  to  $r = 10$   $\mu$ m using Eq. 4.8 is about 41.5 ms where the values of  $\rho_v = 445.05$  kg/m<sup>3</sup> and  $D = 3.5 \times 10^{-2}$  cm<sup>2</sup>/s were used [104]. This time is consistent with the time stamps in Fig. 4.5. For instance, the time difference between Figs. 4.5(b) and 4.5(f), i.e., the time interval between the passing of a cold drop at a certain location and the first appearance of micro-droplets in its vicinity is about 50 ms. Note that the critical saturation ratio decreases with increasing temperature. In the temperature range of  $30$  °C  $\leq T \leq 44$  °C,  $S_c$  varies between 1.0132 and 1.00015. So far we have deduced the conditions for homogeneous nucleation in the experiment and there are some qualitative agreement amongst some of the calculated quantities. It remains to be seen if these conditions are met in the experiment.

In our experiment, a very small supersaturation is required to achieve the critical nucleation rate. This can be realized by isobaric cooling of SF<sub>6</sub> vapor in the wake of a cold SF<sub>6</sub> droplet falling down from the top. The SF<sub>6</sub> vapor in the neighborhood of the cold drop is cooled due to the heat transfer from the drop. By such isobaric cooling, the temperature in the neighborhood of the drop is reduced to  $T - \Delta T_w$ , where  $T$  is the initial ambient temperature. Thus, the saturation ratio becomes  $S = p_v(T)/p_s(T - \Delta T_w)$  where  $\Delta T_w$  is the difference in temperature between the ambient gas and the wake. For saturated SF<sub>6</sub> vapor at  $T_m = 42$  °C,  $p_v(T_m) = p_s(T_m)$ , a  $\Delta T_w$  of 0.04 K is sufficient to attain the critical saturation  $S_c$ , and at  $T_m = 30$  °C a  $\Delta T_w$  of 0.57 K is required to attain  $S_c$ . A  $\Delta T_w > 0.04$  K is attainable in our experiment as the temperature difference between the top and bottom plate is about 4 °C. But a  $\Delta T_w > 0.57$  °C is not attainable with a temperature difference of 4 °C. This increase in  $\Delta T_w$  as the mean temperature is lowered explains why no nucleation was observed at lower mean temperatures

### 4.3.3 Heat Transfer From a Falling Drop

Let us now model a cold drop falling through a warmer atmosphere with a vertical temperature gradient. We consider a general situation where a spherical drop of diameter  $d$  is falling through an atmosphere at its terminal velocity  $U_t$ . We assume that the temperature of the atmosphere  $T_a$  decreases linearly with increasing height.

$$T_a(z) = T_0 - \beta z \quad , \quad (4.9)$$

where  $\beta$  is the lapse rate ( $\frac{dT_a}{dz}$ ).

The falling drop encounters a warmer environment, and heats up continuously as it falls. The warming rate of the drop  $q$  depends on its mass ( $m = \rho_l \pi d^3 / 6$ ) and its effective heat conductivity  $\lambda_{eff} = \lambda \text{Nu}$ , where Nu is the Nusselt number (ratio between total heat transferred and the heat transferred by conduction),  $\lambda$  is the thermal conductivity of the ambient atmosphere,  $d$  is the diameter of the drop and  $\rho_l$  is the density of the liquid drop.

The equation for the heat transfer rate in the drop is given as:

$$q = c_p m \frac{dT}{dt} = 2\lambda_{eff} \pi d^2 \frac{T_a - T}{d}, \quad (4.10)$$

where  $T$  is the temperature of the drop and  $c_{p,l}$  specific heat capacity of the liquid. We assume that the drop temperature is uniform due to shear enhanced mixing. The Nusselt number which expresses the ratio of convective and conductive heat transfer is estimated for a flow past a heated sphere as [105]

$$\text{Nu} = 2 + (0.4\text{Re}^{1/2} + 0.06\text{Re}^{2/3})\text{Pr}^{0.4}, \quad (4.11)$$

where  $\text{Re} = \rho U_t d / \mu$  is the Reynolds number,  $\text{Pr} = c_{p,g} \mu / \lambda$  is the Prandtl number, and  $\rho$ ,  $\mu$ ,  $c_{p,g}$  are the density, the dynamic viscosity, and the specific heat capacity of the ambient gas, respectively,  $U_t$  is the terminal velocity of the drop. The terminal velocity was obtained from the recorded images from the experiment.

Using Eq. (4.9) and rearranging the terms in Eq. (4.10), we obtain:

$$\frac{dT}{dt} = \frac{6\lambda\text{Nu}}{c_{p,l}\rho_l d^2} (T_0 - \beta z - T). \quad (4.12)$$

The vertical position of the drop after it has attained its terminal velocity is given by

$$z = z_0 - U_t t. \quad (4.13)$$

We thus obtain

$$\frac{dT}{dt} = A [T_0 - T + \beta(U_t t - z_0)], \quad \text{with } A = \frac{6\lambda\text{Nu}}{c_{p,l}\rho_l d^2}. \quad (4.14)$$

Using Eqs. (4.14), (4.9) we write an evolution equation for the difference in temperature between the drop and the ambient temperature  $\Delta = T_a - T$  as

$$\frac{d}{dt} \Delta = \beta U_t - A \Delta, \quad (4.15)$$

The solution of Eq. 4.15 is

$$\Delta = \Delta_0 e^{-At} + \frac{\beta U_t}{A} (1 - e^{-At}), \quad (4.16)$$

where  $\Delta_0 = \Delta(t = 0)$ . Please note that in the present model we do not account for the deformation of the drop and assume the drop to be spherical.

In Fig. 4.5, the initial diameter  $d$  of the cold SF<sub>6</sub> drop detaching from the liquid layer on the top plate is  $\approx 0.5$  mm. From the image sequence, we found that the terminal velocity  $U_t$  of the drop was about 7 cm/s and it was attained after about a 2 – 3 mm fall from the top plate. The time taken for the drops to reach the liquid pool above the bottom plate is about 0.2 s. Using the material parameters of SF<sub>6</sub> at  $T_m = 42^\circ\text{C}$  [103] and the empirical relation between the drop Re and Nu in Eq. 4.11, we obtain  $\text{Re} \approx 600$  and  $\text{Nu} \approx 26$ , and thus using Eq. (4.16),  $1/A \approx 0.18$  s. To neglect the effects of the transients due to  $\Delta_0$  in Eq. 4.16 we assume that as the drop attains its terminal velocity ( $t = 0$ ), the temperature of the drop is the same as its ambient, i.e.,  $\Delta_0 = 0$ . This assumption was made to prevent an over estimation of the induced cooling in the wake. The flow inside the chamber is convecting and therefore the diffusive temperature profile cannot be used for estimating  $\beta$ . To take into account the effects of convective mixing in the bulk we choose a lapse rate  $\beta = 0.5$  K/cm, which is about four times weaker than the temperature gradient without convection of about 2 K/cm across the gas layer. Using Eq. (4.16) we predict that  $\Delta = 0.1$  K at  $t \approx 30$  ms and 0.2 K at about 60 ms. At these instants the drop is well above the liquid pool on the bottom plate.

The cooling  $\Delta T_w$  induced in the wake of the cold drop is a function of the heat transfer rate from the ambient gas to the cold drop, and does depend on the Re of the falling drop and also on the streamwise distance from the drop's surface. The streamwise temperature profile in the wake is also dependent on the nature of the wake, i.e., whether the wake is planar or axisymmetric. The wake behind a spherical drop is axisymmetric. The temperature deficit (difference in temperature between the wake core and the ambient) decay rate in a fully developed self-similar axisymmetric wake is about  $x^{-2/3}$ , where  $x$  is the streamwise distance behind the sphere. In the present scenario, we are interested in the  $\Delta T_w$  variation in the near wake of the cold drop and we do not have any direct measurements from our experiments. Thus, we rely on the data from numerical simulations to understand the instantaneous temperature variation close to the drop. Large eddy simulations (LES) at  $\text{Re} > 300$  [106] of the flow past a hot sphere show that the wake retains up to 20 – 25% of  $\Delta$  till about 2 drop diameters in the downstream direction, therefore we assume that the cooling induced in the near wake up to 2 diameters in the downstream direction is about 20%. At  $T_m = 42^\circ\text{C}$ , the cold drop, with a  $\Delta = 0.2$  K, lowers the temperature of the ambient gas by  $\Delta T_w \approx 0.04$  K at  $t = 60$  ms, which is sufficient to trigger homogeneous nucleation according to

CNT. As the drop falls further, the induced cooling in the near wake is increased as the temperature difference between the drop and ambient increases as described by Eq. 4.16.

Please note that the estimates presented here are based on a simple model system. In this model, the drop is treated as a rigid sphere and from Figs. 4.2 to 4.6 we know that the drop ceases to be spherical within a few millimeters of travel from the top plate. The Nusselt number and drag coefficient will change as the shape of the drop changes. We here assumed that the  $\text{SF}_6$  vapor was saturated at  $T_m$  and the vapor concentration was constant. We account for the heat transfer from the drop to the surroundings, but we do not account for the mass transfer from the surrounding to the drop. The surrounding atmosphere is saturated with  $\text{SF}_6$  and as they encounter the cold surface of the drop,  $\text{SF}_6$  vapor should condense on the drop. This would alter the distribution of  $\text{SF}_6$  vapor in the wake and the boundary layer. Hence, the value of  $\Delta T$  required to trigger nucleation is strongly coupled to the vapor and temperature distribution, and also on the mixing dynamics between the cold air in the boundary layer and the ambient. Accommodating all these effects is necessary to quantify the findings in the observations. This is a separate research problem on its own, which is beyond the scope of the present work as the objective here is to construct a simple model which helps in understanding the observations in our experiment. Due to the above mentioned limitations, the level of supersaturation estimated here by induced isobaric cooling essentially gives an upper bound. The effect of mixing between the drop and the ambient is discussed in the next chapter using a simple mixing model.

## 4.4 Clouds in a Lab

In the experiments discussed so far, the bottom plate was covered with a layer of liquid  $\text{SF}_6$ . The imposed temperature difference between the two plates ensured that there was a continuous supply of vapor into the atmosphere. As a consequence, the atmosphere is on an average saturated or even slightly supersaturated. So if any micro droplet is generated in this environment, they continue to grow absorbing the surrounding  $\text{SF}_6$  vapor till they fall into the liquid pool. Figure 1.1 shows a picture of cumulus cloud in the Earth's atmosphere. These clouds have a finite vertical and horizontal extent. The non-cloudy regions represent a sub-saturated environment not conducive for nucleation of water droplets. The cloud base in a cumulus or a strato-cumulus cloud is well defined and sharp. We try to recreate a similar situation in the laboratory environment where a part of the convection cell is supersaturated and the other half is sub-saturated. The important step is to control the saturation ratio inside the convection cell. The concentration of  $\text{SF}_6$  vapor inside the cell, hence the saturation ratio  $S$ , can be altered (lowered) by completely evaporating the liquid layer on the bottom plate. The vapor

pressure of  $\text{SF}_6$  was adjusted such that it is supersaturated at  $T_t$  but was sub-saturated at  $T_b$ . This would change the supersaturation inside the cell. In such situations, colder, upper part of the cell is supersaturated  $S > S_c$ , while  $S < S_c$  in the lower part of the cell. The extent of these zones depend on the vapor pressure in the cell. Similar variations of the experiment were discussed in the thin cell case in the previous chapter.

Figure 4.8 shows the dynamics observed in the lower half of the cell in the absence of a liquid layer above the bottom plate. The observations in the convection cell were similar to the experiments with a liquid layer at the bottom where micro-droplets nucleated in the wake of the falling cold drop. However, now sustained nucleation was visible only up to a certain height. The vertical level up to which micro-droplets nucleate indicates the horizontal interface where  $S \approx 1$ . In the volume above this interface, new droplets nucleated and grew in the wake of a falling cold drop, and in the sub-saturated zone below the interface these droplets evaporated over time. Below this interface no sustained nucleation was visible. Figure 4.8 (e-h) shows a layer of nucleated micro-droplets suspended in the lab atmosphere. This layer of suspended droplets appear to be stable. Figure 4.9 shows the time averaged (over 15 seconds) view of the cell and the dark band represents the cloud layer. This further suggests that the layer has a well defined base, very similar to a cumulus cloud base in the Earth's atmosphere. At certain instances, the number of nucleated droplets in the supersaturated region was significant such that some of them make it almost all the way to the bottom plate. One such instance is shown in Fig. 4.8 (g). These dynamics are very much like a virga or a rain shaft from a cloud. A virga is a streak or a shaft of visible precipitation from a cloud that usually evaporates before it hits the ground [107]. If it makes it all the way to the Earth's surface, then it is called a precipitation shaft.

The exact dynamics in a cloud is not reproduced here due to the complexity involved, but certain features are captured. The turbulence intensity in the cell is not very high as the thermal driving is low and as a consequence these droplets do not stay afloat for extended periods by the updraft. Moreover, these experiments were conducted fairly close to the critical point of  $\text{SF}_6$  and as a consequence the amount of latent released is quite insignificant which however plays a significant role in the dynamics of clouds. Despite these limitations, our laboratory model with a partially supersaturated convection cell can be used for understanding the interfacial dynamics between cloudy and non-cloudy air. In principle, a similar experimental model can be constructed with water vapor as the working fluid to study the effects of mixing between cloudy and ambient air. This may provide new insights into entrainment and other related interfacial processes.

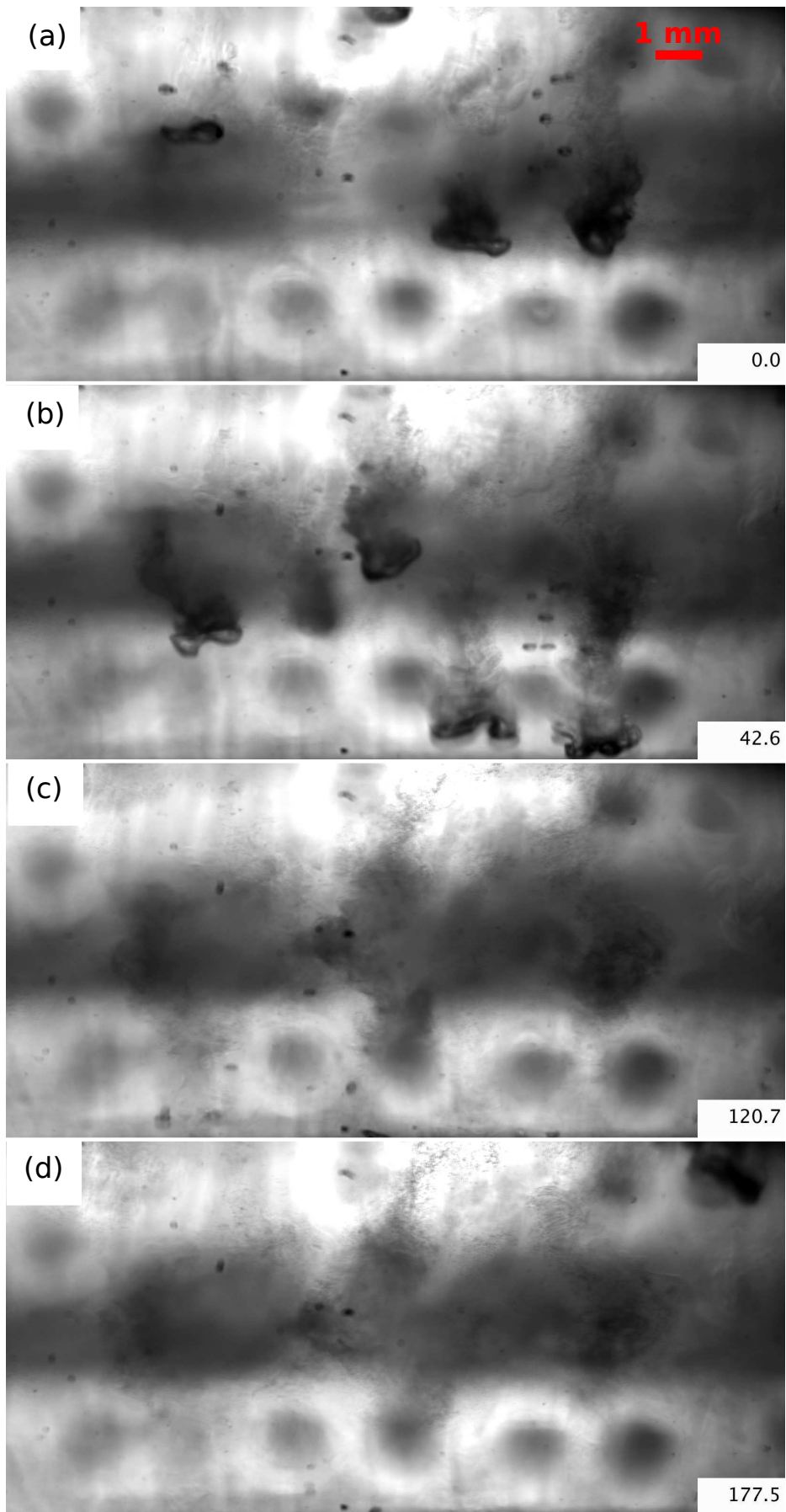
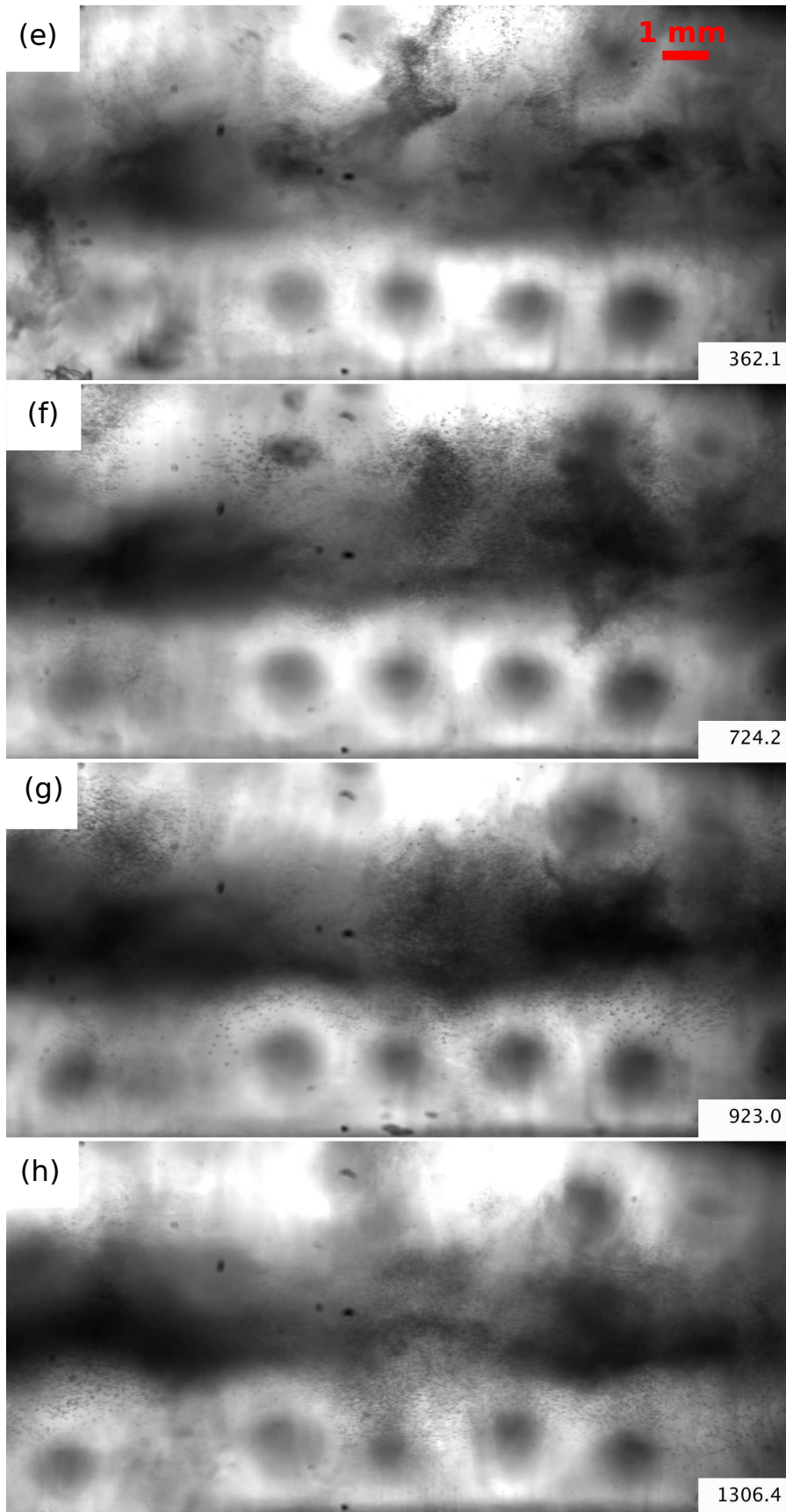


Figure 4.8: See facing page for caption.



**Figure 4.8:** Laboratory cloud - formation of a cloud layer in the lower half of the cell in the absence of a liquid layer on the bottom plate.  $T_b = 45.00$  °C,  $T_t = 36.00$  °C,  $p = 44.9$  bar. The dark circular patches in the lower half of the image are the shadows of the drops attached to the top plate. See main text for description. The time stamp (in ms) is indicated at the lower-right corner of the image.



**Figure 4.9:** Time averaged image over 2150 frames ( $\approx 15$  seconds). The white dashed line vertically separates areas of supercritical (above) and subcritical saturation (below), and thus represents the average position of the base of the cloud layer. See the caption in Fig. 4.8 for the temperature and pressure conditions.

## 4.5 Atmospheric Implications

So far we have shown that new droplets nucleate in the wake of cold drops in a saturated environment under specialized laboratory conditions. We now explore if these observations can be carried over to the Earth's atmosphere and under what conditions it is applicable. In the Earth's atmosphere, the fluid of interest is water and its properties are significantly different from those of  $\text{SF}_6$ . The saturation ratio required to achieve  $S_c$  for homogeneous nucleation in water vapor is much higher than  $\text{SF}_6$  due to its significantly higher surface tension. For instance, a saturation ratio of 3 is required for the homogeneous nucleation of liquid water at a temperature of  $30^\circ\text{C}$ . The supersaturation in the naturally occurring clouds does not exceed more than a few percent [44]. As a consequence, homogeneous nucleation cannot be the mechanism for the formation of water droplets in clouds. Instead, they are formed by heterogeneous nucleation on aerosol particles in the atmosphere. Before we proceed any further, a brief introduction of the Earth's atmosphere is presented along with the definitions of a few terms commonly used in meteorology. For a detailed account please see [17, 18, 44, 96].

### 4.5.1 Earth's Atmosphere

The Earth's atmosphere consists of several gases of which the most important is the water vapor. Under the conditions in which the Earth's atmosphere operates only water vapor undergoes phase transition. The insolation from the Sun warms up the surface of

the Earth. This causes the water vapor to rise from Earth’s surface into the atmosphere. As a parcel of water vapor rises, it undergoes expansion due to the decrease in pressure with altitude. This adiabatic ascent continues until the dew point of the parcel is reached. Assuming that the atmosphere is in hydrostatic equilibrium and that a parcel is displaced vertically without undergoing any phase transition, the “dry” lapse rate,  $\Gamma_d$ , is expressed as [96]

$$\Gamma_d = -\frac{dT}{dz} = \frac{g}{c_p}, \quad (4.17)$$

where  $g$  and  $c_p$  represent acceleration due to gravity and the isobaric specific heat capacity respectively. The lapse rate varies approximately between 9.8 to 6° C km<sup>-1</sup> from equator to the poles [96]. The dry lapse rate is the rate of decrease of temperature with altitude of a parcel of air under adiabatic conditions in a stable atmosphere.

Once the parcel reaches the condensation line (or the dew point line) then the water vapor in the parcel condenses and releases latent heat. This causes the parcel to heat up. So the lapse rate is lower than the dry lapse rate. This lapse rate is called the moist or saturated adiabatic lapse rate  $\Gamma_s$  and is expressed as [96]

$$\Gamma_m = g \frac{1 + \frac{L_v r_v}{R_d T}}{c_p + \frac{L_v^2 r_v}{R_v T^2}}, \quad (4.18)$$

where  $L_v$  is the latent heat of vaporization,  $r_v$  is the mixing ratio of the mass of water vapor to that of dry air,  $R_d$  is the specific gas constant of dry air and  $R_v$  is the specific gas constant of water vapor. The usual value is around 5° C km<sup>-1</sup> [44, 96].

When the air is supersaturated with water vapor, liquid droplets or ice crystals form, resulting in the formation of clouds. The level of supersaturation is determined by the saturation ratio  $S$ . As we had discussed earlier, the level of supersaturation in the clouds are not sufficient to trigger the homogeneous nucleation of water droplets and consequently, droplets form on the surface of atmospheric aerosol through heterogeneous nucleation. Depending on the size and chemical composition of these aerosols water vapor can condense on the surface of these aerosols at a certain supersaturation. The aerosols in the atmosphere can be classified as hygroscopic, hydrophobic or neutral based on their affinity to water [18]. The level of supersaturation required for activating neutral and hydrophobic aerosols are similar to that of homogeneous nucleation of water droplets. For hygroscopic aerosols on the other hand, due to their better wettability characteristics, the critical supersaturation is significantly lower than for homogeneous nucleation. In the presence of solution droplet, *i.e.*, water droplets containing soluble impurities like sodium chloride or ammonium sulphate, the saturation pressure  $p_s$  of water is lower than that of pure water. This reduced vapor pressure can be calculated using Rault’s law, which states that the ratio between the vapor pressure of the solution

( $p$ ) and the vapor pressure of the pure solvent ( $p^*$ ) is proportional to the mole fraction of the solvent ( $\psi$ ) in the solution. Using Rault's law and Kelvin's equation the saturation ratio in the neighbourhood of a solution droplet of radius  $r$  can be expressed as [18, 96]

$$\frac{p'}{p_s} = \exp\left(\frac{2\sigma'}{n'k_BTr}\right) \left(1 + \frac{imM_w}{M_s(\frac{4}{3}\pi r^3\rho' - m)}\right)^{-1}, \quad (4.19)$$

where  $\sigma'$ ,  $\rho'$  &  $n'$  are the surface tension, density and number concentration of the solution,  $m$  is the mass of the solute in the droplet,  $i$  is the number of ions into which the dissolved material disassociates,  $M_w$  is the molar mass of water and  $M_s$  is the molar mass of solute. For a particular solution droplet to grow in a supersaturated environment, the supersaturation barrier needs to be overcome. For instance, for a sodium chloride based aerosol with a  $10^{-18}$  kg mass concentration, a supersaturation of 0.1% is required to overcome the barrier. For sodium chloride solution droplet, Eq. 4.19 can be rewritten in terms of diameter of the salt grain  $d_s$  as

$$\frac{p'}{p_s} = \exp\left(\frac{0.00216}{d}\right) \left(\frac{1 - (d_s/d)^3}{1 + 0.334(d_s/d)^3}\right), \quad (4.20)$$

where  $d$  is the diameter of the solution droplet and  $d_s$  is the grain diameter of the sodium chloride nuclei. More details are available in [96]. Figure 4.10 shows the saturation ratio as a function of sodium chloride solution droplet diameter for various nuclei concentrations. These curves are known as Köhler curves and they represent the saturation pressure in the neighbourhood of solution droplets of various sizes. As the size of the solution droplet increases the effect of solute diminishes and the curves follow Kelvin's equation. Let us discuss the case of a sodium chloride nuclei of diameter  $0.01 \mu\text{m}$ , the saturation ratio of the environment is shown in Fig. 4.10 as a dashed line. A droplet is said to be in stable equilibrium with the surrounding vapor if the diameter of the droplet corresponds to point A marked in Fig. 4.10, *i.e.*, if the relative humidity of the vapor is varied slightly then the droplet diameter would vary according to the Köhler curve until the equilibrium is re-established. A droplet at B is said to be in unstable equilibrium as a small change in the saturation ratio leads to a runaway growth of the droplet. In the process of varying the supersaturation, if the peak in the Köhler curve is overcome then the droplet is said to be activated. The peak in the supersaturation is called the critical supersaturation for the nuclei and the corresponding diameter is the critical diameter of the solution droplet. Beyond the critical diameter no further enhancement in supersaturation is required for the droplet to grow. Droplets of such sizes are therefore in an unstable equilibrium, point B in Fig. 4.10 is in unstable equilibrium. A pre-activated droplet is called haze and the haze droplets form on the stable leg of the Köhler curve. The portion of Köhler curve beyond the critical radius is called the

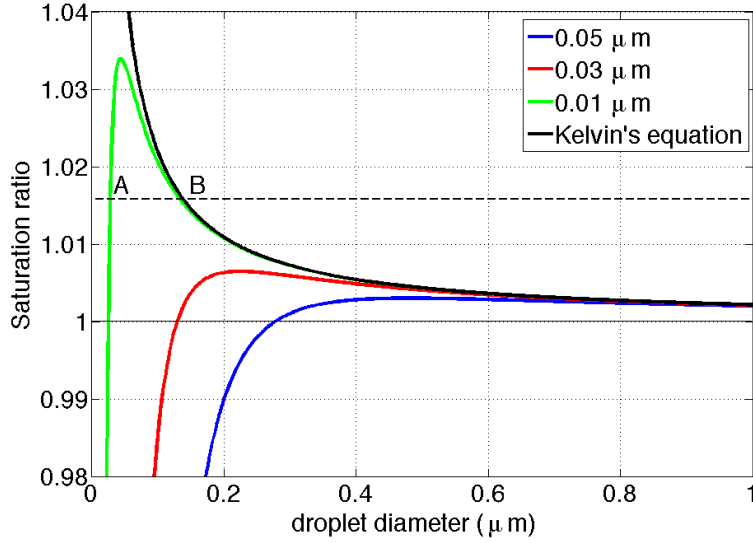


**Figure 4.10:** Köhler curves: Effect of solute (NaCl) diameter on saturation ratio in the neighbourhood of a solution droplet. The solute size is mentioned in the legend. A - a point in the stable leg of Köhler curve, B - a point in the unstable leg of Köhler curve.

unstable leg on the Köhler curve. For additional details please see [18, 96].

There are aerosol particles suspended in the Earth's atmosphere. But not all aerosols can condense water droplets on their surface. Only a fraction of them can eventually grow post activation into cloud droplets. These particles/aerosols are called cloud condensation nuclei (CCN). Before activation, these particles are called cloud nuclei (CN). Some of these particles can also trigger nucleation of ice particles and are called as ice nuclei. A nuclei or a droplet is said to be activated if it surpasses the peak/barrier in the Köhler curve. The concentration of CCN in the atmosphere varies based on the geographical location. The concentration of CCN is significantly higher over the continents than over the oceans. The concentration of CCN is represented as

$$C = A \exp(\beta s), \quad (4.21)$$

where  $s = S - 1$ ;  $A$  and  $\beta$  are fitting parameters which vary based on the geographical location. A detailed description of these parameters are discussed in [44].

#### 4.5.2 Deep Convective Systems

Deep convective clouds play an important role in atmospheric convection. They act as conveyor belts transporting water vapor across the troposphere. Cumulus and cumulonimbus clouds are examples of deep convective systems. Unlike the stratocumulus clouds these clouds are individual convective systems arising out of an unstable atmosphere and the convection is further reinforced by the latent heat released from condensation and glaciation. Such clouds are usually localized cloud systems with their horizontal

extent not larger than a few tens of kilometers, and they are usually aligned along the inter-tropical convergence zones (ITCZ), monsoon bands, slopes or mountain ranges [17]. In certain cases individual cells may merge to form a large mesoscale band [17]. The precipitation from these clouds account for most of the rainfall in the tropics, and hence understanding the dynamics of these systems are of significant importance to the economic health of countries like India. These clouds are usually mixed phase clouds containing both ice and liquid water droplets. The base of these clouds are usually warm with a temperature above  $0^{\circ}\text{C}$  and the cloud top temperatures can be as low as  $-40^{\circ}\text{C}$  [108]. In such clouds a falling rain drop or hail/graupel may nucleate cloud droplets in their wake. In the following subsection we estimate the possible supersaturation in the wake of falling hydrometeors.

### 4.5.3 Secondary Nucleation in Clouds

Let us consider cloudy moist air at a temperature  $T$  and  $S \approx 1$  containing a certain amount of cloud nuclei. When a large cold hydrometeor (rain drop or hail particle), falls through a warm but saturated air, it causes isobaric cooling of the air in its wake and boundary layer, similar in nature to the experiments discussed in the earlier section. This locally enhances supersaturation that may create more CCN, which would eventually grow to become cloud droplets. For instance, at a mean temperature range between  $0^{\circ}\text{C} \leq T_a \leq +30^{\circ}\text{C}$ , to attain a supersaturation  $s$  about 2%, a temperature drop of  $0.27 \text{ K} \leq \Delta T \leq 0.34 \text{ K}$  is required.

In a cloud, the mean temperature decreases with increasing altitude, i.e. if a hydrometeor (raindrop or hail stone) is falling through a cloud it encounters a warmer surrounding environment as it approaches the cloud base. We assume that the rate of variation of the temperature within a cloud is linear and comparable to the moist adiabatic lapse rate, with a typical value of  $\approx 0.005 \text{ K/m}$  [96]. We did not pick any data from field measurements as reliable statistics were not available and the temperature variation is also strongly dependent on the nature of the cloud. Let us consider the case of a raindrop falling through a cloud at its terminal velocity  $U_t$ . The terminal velocity was obtained by solving the equations of motion iteratively. The drag coefficient was obtained from [109]. The steady state temperature difference  $\Delta T$ , between the drop and its surroundings,  $\Delta = \Delta_{\infty} = \beta U_t / A$ , is computed using Eq. 4.16. Similar to the model used for analysing the experimental observations, we only look at the induced cooling in the near wake of the raindrop. We again assume that the cooling induced in the near wake is about 20% of  $\Delta_{\infty}$ . For a raindrop of diameter 1 mm and 4 mm, we find  $\Delta_{\infty}$  is about 0.07 K and 0.95 K respectively. The  $\Delta_{\infty}$  for a 1 mm drop is not large enough to result in any significant supersaturation in its wake. However, for a raindrop of diameter 4 mm, close to the largest values in the size distribution of rain-

fall [44], the cooling induced in the wake,  $\Delta T = 0.2 \Delta_\infty = 0.19$  K is large enough to attain about 1.5% supersaturation. Thus, for large cloud droplets, around 4 mm, which can be found in rainfall, sufficient supersaturation is attained in the wake resulting in enhanced nucleation.

The heat transfer estimates for a drop can also be used in the case of a falling ice particles (hailstones, graupel or ice pellets) as long as the local cloud temperature is below the freezing point of water. This is assuming that the thermal conductivity of ice is much higher than the ambient air and also that the heat added due to the freezing of water droplets is negligible. Such situations are applicable in clouds where liquid water content in the cloud is rather low. If these assumptions fail, then the level of supersaturation in the wake will not be as large as that of the raindrop. Let us consider a hail stone or an ice pellet falling through a saturated environment with the temperature in the surrounding cloudy air above 0°C. Due to the enthalpy of fusion associated with the melting process (a process that extracts heat from its surrounding), the cooling  $\Delta T$  induced in its wake is significantly larger than that of a raindrop of similar dimension. As the hailstone starts to melt, the particle is composed of ice and liquid water. Owing to the lower density of ice compared to liquid water, it will float in the liquid pool. The shear enhanced mixing ensures that the temperature inside the ice drop is homogeneous [110]. Consequently, the temperature of the ice drop remains at 0°C until the ice is completely melted. The rate of heat transfer is also dependent on the shape and size of the ice particle [110]. Let us consider a spherical ice particle of uniform density. The condensation of water vapor results in the addition of latent heat of condensation to the ice-liquid water system. To account for the condensation of water vapor on the surface, we enhance the heat transfer rate between the surroundings and the particle by 25% in comparison to the liquid drop [111].

Within Earth's atmospheric conditions an ice particle would start to melt as the temperature increases above 0°C. Let us assume that the ice particle has attained its terminal velocity before entering the warm parts of a cloud, then we can state that the amount of energy required to melt the ice particle should balance the net heat transferred into this system from the ambient.

$$\frac{\pi d^3}{6} \rho_{ice} l_{ice} = \int_0^t \frac{Nu \lambda}{d} (T_a - T_{ice}) \pi d^2 dt \quad (4.22)$$

where  $l_{ice}$  represents the specific enthalpy of fusion of ice,  $\rho_{ice}$  is the density of the ice.  $T_{ice}$  is 0°C. Using Eq. 4.9 and integrating Eq. 4.22 with respect to time we get

$$t = \sqrt[2]{\frac{d^2 \rho_{ice} l_{ice}}{3Nu \beta \lambda U_t}} \quad (4.23)$$

$$\rho_{ice} = 916 \text{ kg m}^{-3}, l_{ice} = 335 \text{ KJ kg}^{-1}$$

Based on these arguments and assumptions, an ice particle of diameter 1 mm, at a  $Re \approx 230$  (based on terminal velocity), would travel about 450 m and a particle of 5 mm diameter, at  $Re \approx 3600$ , would travel about 2000 m before the melting process is complete. Using the moist adiabatic lapse rate, the maximum  $\Delta_\infty$  attained for these hydrometeors are about 2.2 K and 10 K respectively. Taking into account that  $\Delta T = 0.2 \Delta_\infty$ , the corresponding local supersaturations are around 2% – 10% in the boundary layer and near wake of the particle. We note that much higher levels of supersaturation is attained in the near wake of a hail stone in comparison to a cold raindrop. This enhanced supersaturation may activate several nuclei in the wake and hence increase the concentration of CCNs in the warmer part of the cloud.

## 4.6 Conclusion

The observations and the analysis presented so far revealed a new mechanism for the activation and the growth of droplets under non-equilibrium conditions. The estimates suggest that in a supersaturated laboratory atmosphere, nucleation of new droplets are possible in the wake of a cold drop. The analysis was extended to atmospheric conditions and the calculations suggest that in the wake of cold hydrometeors enhanced nucleation of cloud droplets should occur. In deep convective cloud systems, the dynamics are significantly more complex due to the presence of strong updrafts/downdrafts, variations in the lapse rate due to non-uniform latent heat release from glaciation/condensation, in-homogeneous mixing of cloudy and non-cloudy air due to large scale entrainment of ambient dry air [112]. Despite these limitations, the nucleation mechanism presented in this chapter may play a part in understanding the dynamics of deep convective clouds. The additional droplets nucleated may either collide on settling hail stones/graupel or rain drops, or are entrained into the convective updraft that in turn may reinforce the generation of large rain drops or hailstones. The additional heat released in this process of nucleation may further reinforce the existing updrafts. It is also worth noting that a similar mechanism may play a role in secondary ice nucleation in deep convective systems. Testing these ideas require additional experimental investigations under turbulent atmospheric conditions.



# 5 A Secondary Ice Nucleation Mechanism in Clouds

In this chapter we discuss the possibility of a secondary ice nucleation mechanism in deep convective clouds. The experiments reported in this chapter are inspired by the discussions in the previous chapter. We briefly present an outline of the experimental setup followed by experimental observations and related discussions. Later, we present the possible implications of these observations in the context of atmospheric clouds.

## 5.1 Experimental Setup

The experiment was conducted in the turbulent cloud chamber at Michigan Technological University. The facility is called the  $\Pi$  chamber as the volume inside the chamber with the cylindrical insert is about  $\pi \text{ m}^3$  (diameter of 2 m and height of 1 m). A detailed description of the setup and the available instrumentations are discussed in Chang *et al* (2016) [23]. The chamber is a standard Rayleigh-Bénard convection experiment driven by the thermal gradient imposed between the top and bottom plate. The composition of the working fluid was similar to those in atmospheric clouds, and consisted of water vapor and air as the working fluid. The top and bottom plates were covered with filter paper soaked in water to keep the surface moist (relative humidity  $\text{RH} = 100\%$ , saturation ratio  $S = 1$ ), thus ensuring that the boundaries were saturated. The lateral side walls were maintained at a mean temperature  $T_m = 0.5(T_b + T_t)$  where  $T_t$  and  $T_b$  represent the top and bottom plate temperatures respectively. As a consequence, the water vapor from the bottom plate condenses also on the lateral side walls, resulting in a net loss of water vapor from the chamber over time. The bottom plate was connected to a reservoir of water located below the plate. Thus, the water vapor lost from the chamber was partially restored by the supply from the reservoir. Please note that the side wall temperatures can be regulated independently and thus aid in minor adjustments to the average humidity in the chamber. The conditions were set such that the chamber was nearly saturated with respect to liquid water under warm conditions (*i.e.*  $T_b$  and  $T_t$  are  $> 0 \text{ }^\circ\text{C}$ ) and under cold conditions ( $T_b$  and  $T_t$  are  $< 0 \text{ }^\circ\text{C}$ ) the humidity

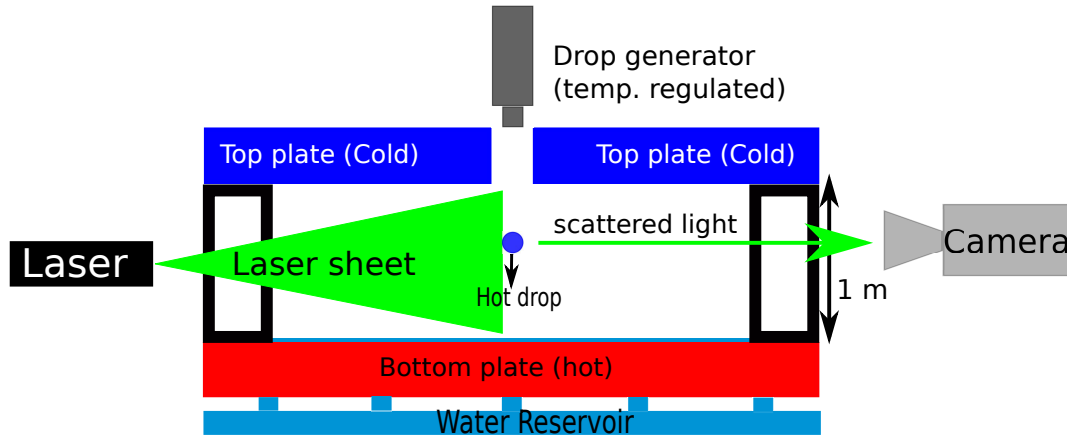


**Figure 5.1:** Schematic of the experimental setup. A detailed description of the facility is provided in [23].

was significantly subsaturated with respect to liquid water, as the water reservoir beneath the bottom plate was frozen. The top, bottom and side wall temperatures were controlled using a PID control loop and were regulated to within  $\pm 0.1$  °C. The pressure was unregulated and thus was at atmospheric pressure.

The objective of the present experiment is to see if water droplets or ice crystals nucleate in the wake of large warm drops through evaporative supersaturation, *i.e.*, supersaturation caused by evaporation from the surface of the warm drop. A drop generator was placed above the top plate and the drops were released into the chamber through a small hole ( $\approx 5$  cm in diameter) in the top plate. The drop diameter was about 2 mm. The drop generator was temperature controlled using a thermostat and was well insulated from the ambient room conditions. The flow rate was adjusted such that a drop was released every few seconds (2 – 5 seconds). The temperature difference between the drop and the thermostat was less than 1 °C. A schematic of the experimental setup and the flow visualization strategy used for image acquisition is shown in Fig. 5.1. The flow field was illuminated using a vertical planar light sheet from a MGL-III 532 nm 300 mW continuous laser. The drop generator was positioned such that the drops fell through the vertical laser sheet, thus illuminating the core of the wake. The nucleation of droplets or ice crystals will scatter light from the laser sheet provided the dimensions of the nucleated particles was larger than the wavelength of the light. The forward scattered light was recorded using a Sony alpha 7S2 camera placed across the chamber (Fig. 5.1).

A TSI atomizer (Model 3076) was used for producing aerosols. The size distribution (dry size) of the sodium chloride (NaCl) aerosols generated from the atomizer is shown in Fig. 5.2. The number concentration from the atomizer was regulated by adjusting the flow rates and salt concentrations in the atomizer. The size distribution measurement was conducted using a TSI scanning mobility particle sizer (Differential Mobility

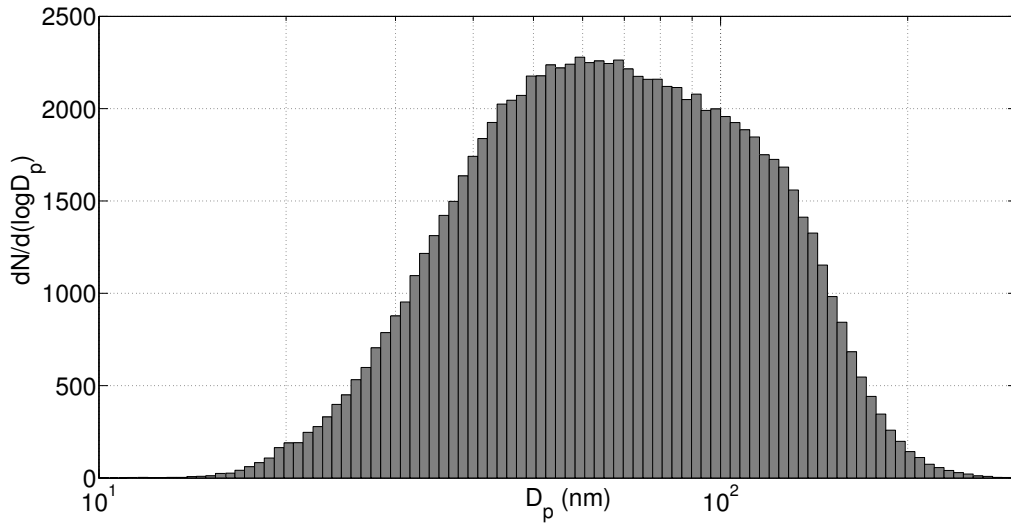


**Figure 5.2:** Sodium chloride aerosol size distribution before injecting into the chamber. The total number concentration is about  $10^5$  per  $\text{cm}^3$ .

Analyzer (DMA)+CPC (3772)). The DMA was also used for size selected injection of aerosol particles of a given diameter. The output from the atomizer was fed into the DMA post desiccation to generate aerosols of a certain diameter. The humidity measurements were carried out using a HUMICAP-HMP7 humidity-temperature sensor from Vaisala. In a near saturated environment ( $\text{RH} < 100\%$ ), the humidity in the chamber was also estimated by injecting size selected aerosols into the moist chamber. These aerosols absorb moisture and grow until they attain their equilibrium size (on the stable leg of Köhler's curve, see section 4.5.1). This equilibrium radius is a function of relative humidity in the chamber.

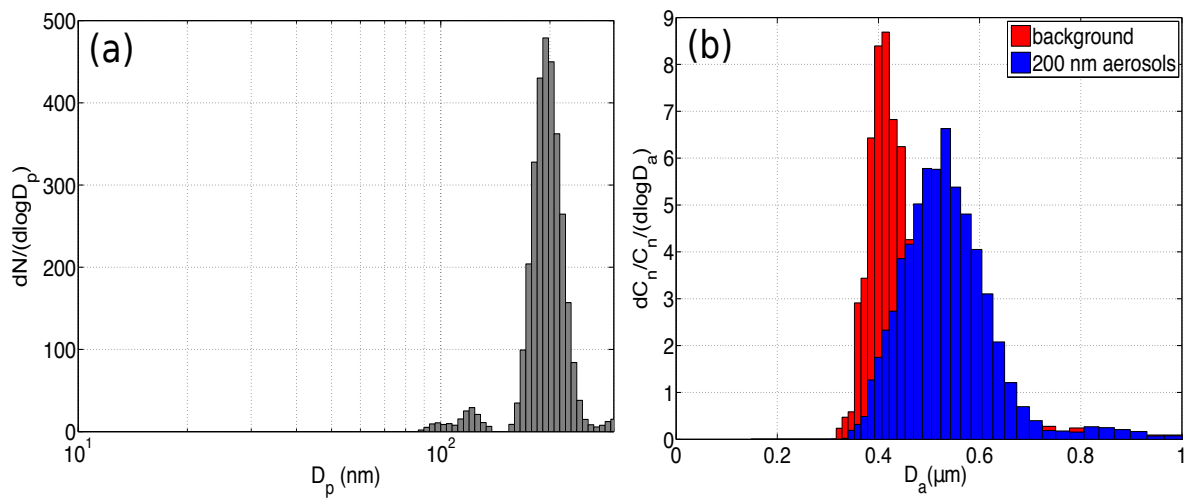


**Figure 5.3:** (a) Size selected NaCl aerosol size distribution. Number concentration  $\approx 120$  per  $\text{cm}^3$ . (b) Particle size distribution measured inside the chamber. Number concentrations: background  $\approx 0.6$  per  $\text{cm}^3$ , 200 nm aerosols  $\approx 35$  per  $\text{cm}^3$ .

Figure 5.3 (a) shows the size selected NaCl aerosol size distribution. The peak in the distribution corresponds to a particle diameter of 198 nm. Please note that the number concentration is significantly lower than the full distribution shown in Fig. 5.2. Figure 5.3 (b) shows the particle size measured inside the chamber using an aerosol sensor (Welas 2100 from Palas, equipped to measure between 0.3 – 10  $\mu\text{m}$ ). The background particle distribution in the chamber before aerosol injection is shown in red and the distribution after the size-selected aerosol injection is shown in blue. Please note that the distributions are normalized and as expected the number concentration for the background measurement was significantly lower compared to the number concentration post aerosol injection (see figure caption for the number concentrations). The blue distribution in Fig. 5.3 (b) corresponds to the hydrated size of the 198 nm dry aerosols pumped into the chamber. The peak in the distribution corresponds to a particle diameter of 0.52  $\mu\text{m}$ . The Köhler equation (Eq. 4.19) can be rewritten as

$$S = \frac{D_{wet}^3 - D_s^3}{D_{wet}^3 - D_s^3(1 - \kappa)} \exp\left(\frac{4\sigma M_w}{RT\rho_w D_{wet}}\right) \quad (5.1)$$

where  $S$  is the saturation ratio,  $D_{wet}$  is the diameter of the solute droplet,  $D_s$  is the dry radius of a solute,  $\kappa$  is the hygroscopicity parameter [113]. The value of  $\kappa$  is around 1.28 for NaCl nuclei. The method for measuring the value of  $\kappa$  is discussed in [113, 114]. The relative humidity computed for the warm condition experiments using Eq. 5.1 is about 93%, and the corresponding measurement from the Vaisala sensor was between 92% and 94% which is consistent with the computed value. Please note that a similar procedure was not applicable for the ice nucleation experiments as the relative humidity in the chamber was about 60% and the corresponding hydration diameter of the droplet was not within the measurable range of the instrument. Moreover, sub-zero temperatures were not favorable for the operation of Welas 2100.

## 5.2 Experimental Observations

The bottom and top plates along with the side walls were set to the desired temperatures such that the average humidity inside the chamber was below water saturation. In the present set of experiments, the average relative humidity in the bulk was between 90% and 92%. The top and bottom plate temperatures were set to 3.5 °C and 14.5 °C respectively. The side wall temperature was set to 10 °C and the temperature measured in the bulk was about 11 °C. Once the system attains steady state the chamber was loaded with sodium chloride (NaCl) nuclei from the atomizer. The size spectrum of the NaCl nuclei in the chamber is shown in Fig. 5.2. Over time, the number concentration of the nuclei in the chamber increases as the nuclei was continuously injected. We introduce the hot drop from the drop generator into the chamber once the number concentration

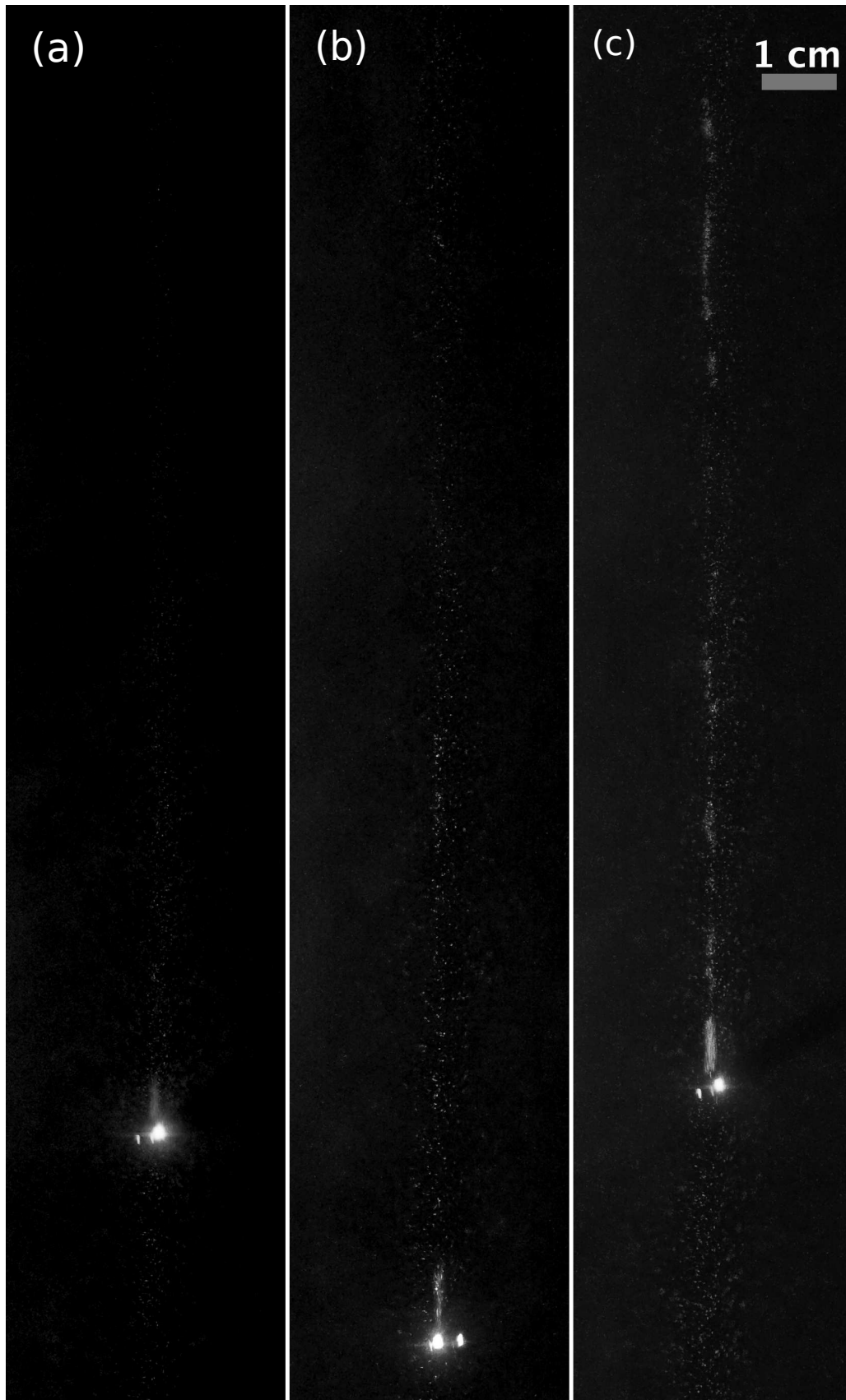


**Figure 5.4:** Nucleation of water droplets in the wake of a hot drop under warm conditions. Ambient temperature  $\approx 11$  °C, humidity  $\approx 92\%$ . The drop temperatures are (a) 25 °C (b) 30 °C (c) 35 °C. The number concentration of the nuclei is about  $1.8 \times 10^4$  per  $\text{cm}^3$ . The images are contrast adjusted.

attains a value around  $10^4$  particles per  $\text{cm}^3$ .

Figure 5.4 shows the dynamics observed in the wake of a falling hot drop at various drop temperatures. The temperature of the drop increases as we move from left to right in Fig. 5.4. The drop diameter is about 2 mm. The drop traverses a distance of about 1 meter in the chamber before reaching the bottom plate. The terminal velocity was estimated by solving the equations of motion iteratively for a spherical drop. The fall distance was not sufficient for the drop to attain terminal velocity and so the drop was accelerating continuously before it hit the bottom plate. At a distance of about 0.5 m from the top, the drop has a velocity of about 3 m/s. Under these conditions the drop does not deform much from the spherical shape.

From Fig. 5.4, we infer that the spatial extent of the nucleated droplets in the wake is a strong function of the drop temperature. We observe that the spatial extent of the nucleated droplets in the wake increases as the temperature difference between the drop and the ambient is increased. The nucleated droplets do not grow indefinitely as the ambient was sub-saturated. As a consequence, the droplet starts evaporating once the transient supersaturation induced in the wake falls below 0%. The ambient was maintained at a few percentage points below saturation (about 8% below) to prevent the activation of droplets to better isolate the role of enhanced supersaturation. We notice that the concentration of the nucleated droplets in the wake is not uniform in space. There are volumes of very high concentrations of the nucleated droplets separated by regions of very low concentrations. This may be related to the spatially intermittent nature of entrainment and mixing in the wake of a bluff body. A detailed argument is presented in the next section.

So far we discussed the observations under warm conditions. Now we present the observations under cold conditions. Figure 5.5 shows temporary nucleation of liquid water droplets and ice crystals in the wake of a hot drop at conditions favorable for ice nucleation. We used aqueous Snomax (proteins from the bacterium *Pseudomonas syringae*) as the ice nuclei. The temperature of the drop increases from left to right in Fig. 5.5. The ambient temperature was between  $-17.5$  °C and  $-18$  °C during the course of the experiments. The top and bottom plate temperatures were set to  $-20$  °C and the wall temperature was set to  $-15$  °C. As a consequence the convection in the chamber was negligible as opposed to the experiments shown in Fig. 5.4. The relative humidity in the bulk w.r.t liquid water was about 60%. The imposition of a temperature gradient resulted in the lowering of relative humidity inside the chamber due to the loss of water vapor to the side walls and the top plate. Unlike in the warm conditions the lost water vapor was not replenished from the reservoir beneath the bottom plate as the water in the reservoir was also frozen. As a consequence, we set the temperature difference across the chamber to  $0$  °C to avoid the loss of water vapor.

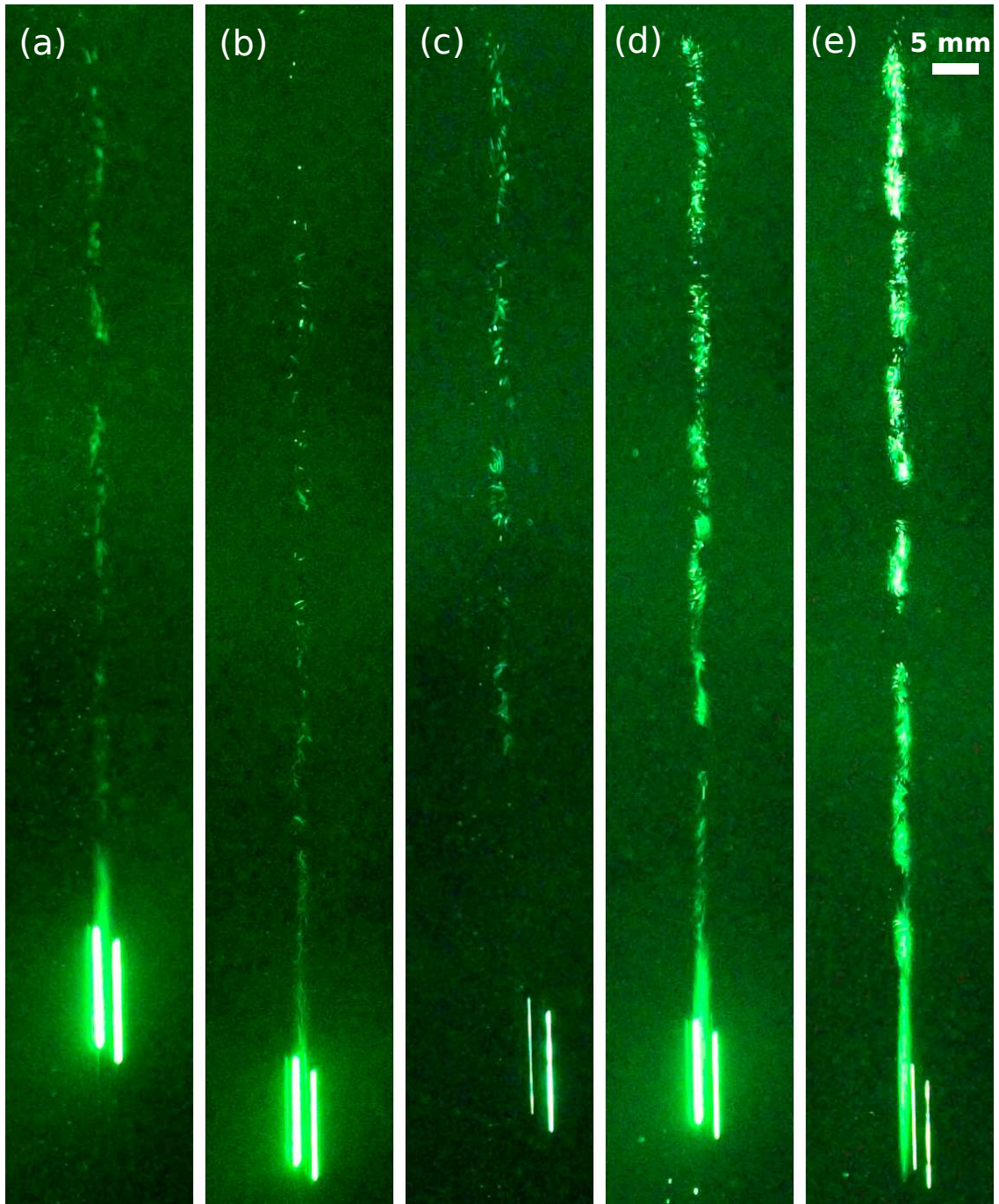


**Figure 5.5:** Nucleation of water droplets and ice particles in the wake of a hot drop under cold conditions. Ambient temperature  $\approx -18$  °C, relative humidity  $\approx 60\%$ . The drop temperatures are (a) 4 °C (b) 10 °C (c) 10 °C (d)  $\approx 20$  °C (e) 50 °C. The number concentration of the nuclei was about  $10^4$  per  $\text{cm}^3$  in all cases except in (b). Number concentration of nuclei in (b)  $\approx 10^3$  per  $\text{cm}^3$ .

In Fig. 5.5, we observe nucleation of water droplets and ice particles in the wake of the hot drop. As expected, we observe that the number concentration of the nucleated particles increased with the increase in the drop temperature. The dynamics of the nucleated particles in the wake in Fig. 5.5 is similar to the dynamics observed in Fig. 5.4. The nucleated particles are not uniformly distributed in the wake. The

nucleated particles have a finite lifetime due to the sub-saturated ambient. Figure 5.5 (b and c) have the same ambient temperature conditions, but the number concentrations of the nuclei were quite different. Figure 5.5 (c) has higher number concentration compared to Figure 5.5 (b) and the same is evident from the number concentration of the nucleated particles in the far wake. In the near wake of Fig. 5.5(c) no nucleated particles are visible and the axis of the wake illuminated by the nucleated particles appear to be shifted from the drop (visible as two bright streaks). This might be due to the oscillations in the path of the drop, induced by vortex shedding in the wake. As a consequence the wake may not have been illuminated by the laser sheet. Please note that the temperatures mentioned in Figs. 5.4 & 5.5 are the drop temperatures at the drop generator, and not at the instant when the image was acquired.

### 5.3 Wake Analysis

In this section we use a mixing parcel model to explain the enhanced supersaturation in the wake of a warm drop. We consider two parcels at different temperatures and humidity, and let these parcels mix isobarically and adiabatically, *i.e.*, no phase change in the system. The variation of the partial vapor pressure and temperature in the mixture as a function of the mixing fraction is called the mixing line. Please refer to any general text on atmospheric thermodynamics for a detailed account on the mixing parcel analysis (for instance, [18, 96]). A brief account on the mathematical formulation is provided in section 5.3.1.

#### 5.3.1 Warm conditions

Figure 5.6 shows the mixing phase diagram for the conditions shown in Fig. 5.4. Please note that we have included an experiment with a drop at 20 °C which was not shown in Fig. 5.4. For this case, no nucleation in the wake was visible. The blue curve represents the equilibrium saturation-vapor pressure curve for liquid water. The equilibrium conditions in the neighbourhood of the drop at various temperatures is marked in the figure along with the ambient conditions. The line connecting the drop conditions with the ambient condition is called the adiabatic isobaric mixing line, which is an outcome of the conservation of enthalpy under the assumption that there is no phase transition in the system [18, 96]. The temperature and pressure from the adiabatic mixing parcel model is expressed as

$$T_w = xT_d + (1 - x)T_a \quad (5.2)$$

$$P_w = xP_d + (1 - x)P_a \quad (5.3)$$

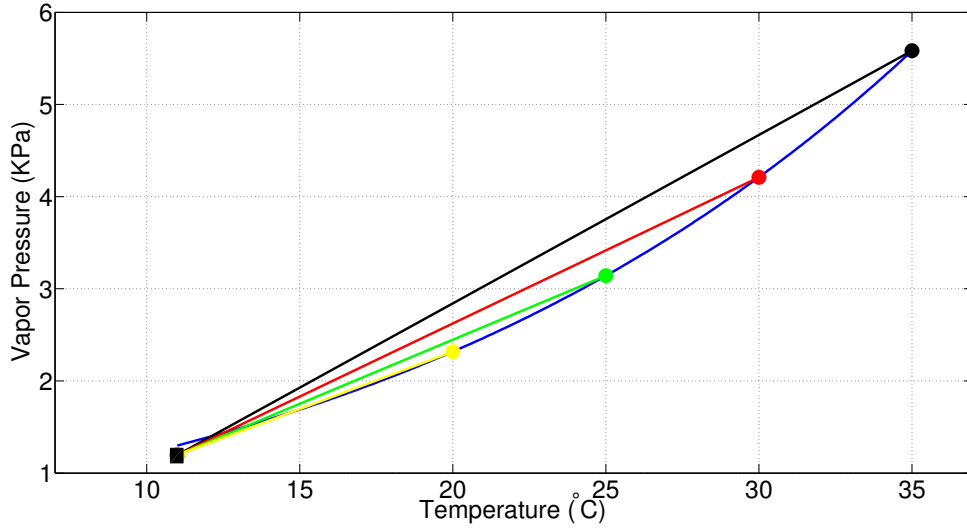


**Figure 5.6:** Mixing phase diagram under warm condition (Fig. 5.4). ■ - ambient condition ( $T = 11$  °C, RH = 92%). The blue curve represents the saturation vapor pressure curve for liquid water. The conditions at the surface of the drop is marked in filled circles (●) of various colors and the corresponding mixing line is represented by a line connecting ● and ■: ● - 35 °C, ● - 30 °C, ● - 25 °C, ● - 20 °C.

where  $x$  is the mixing fraction between the ambient air and the evaporated vapor from the drop.  $T_w$ ,  $P_w$  are the temperature and vapor pressure of water vapor in the wake for a mixing fraction  $x$ ,  $T_d$  represents the drop temperature at a given instant and  $P_d$  is the corresponding equilibrium vapor pressure.  $T_a$  and  $P_a$  represents the temperature and vapor pressure of water vapor in the ambient.

The mixing fraction  $x$  is a measure of mixing between the vapor from the drop and the ambient air. The mixing process is dependent on the nature of the flow field in the wake. The flow field here can be characterized as a buoyant wake as it is a combination of momentum defect and buoyancy flux due to the heat transfer from the drop. Moreover, the no slip velocity boundary condition is not applicable at the liquid vapor interface. To the best of our knowledge there exists no simulation or experiment that has attempted to carry out a systematic study to characterize the flow field in such a system. From the experience in buoyant jets one can conclude that far away from the drop the flow behaves like an axisymmetric plume but the same cannot be said in the near field [115]. From the numerical simulations of a passive wake we can approximate the mean centreline variation in the temperature difference between the wake and ambient as  $\Delta T \propto z^{-1}$ , where  $z$  is the streamwise distance from the drop [106, 116]. On the other hand, we can approximate the mean centreline variation in the  $\Delta T$  in the near wake region as  $z^{-0.5}$  provided we account for the thermal effects and the induced pressure forces on the body [52]. The difference in the decay rate in various numerical simulations may also be due to the difference in the flow Reynolds number.

The ambient was sub-saturated with respect to the drop temperature, which resulted

in continuous evaporation of water vapor from the drop. We assume that the volume in the immediate neighborhood of the drop has a saturation ratio of 1. Its temperature decreases according to Eq. 5.2 as this volume undergoes dilution by mixing with the ambient air. We calculate the variation of the saturation ratio in the wake as  $S = P_w/P_s(T_w)$  where  $P_s(T)$  is the saturated vapor pressure at a temperature  $T$ . Figure 5.7 shows the variation of the saturation ratio traversing along the mixing line shown in Fig. 5.6 for different drop temperatures. We note that the peak supersaturation is attained approximately at the centre of the mixing line.

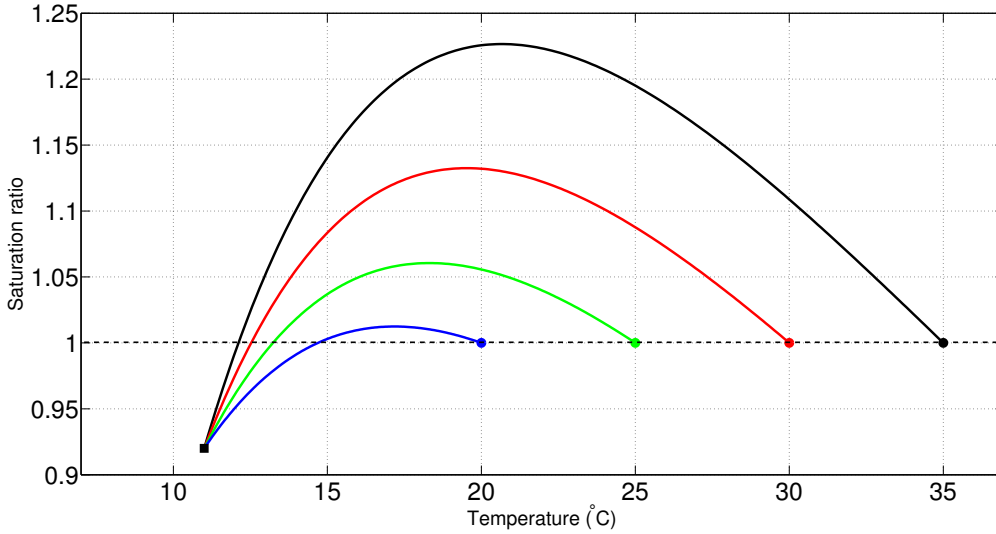


**Figure 5.7:** Saturation ratio along the mixing line plotted in Fig. 5.6. The conditions at the surface of the drop is marked in filled circles (●) of various colors and the corresponding mixing line is represented by a curve connecting ● (of different colors) and ■: ● - 35 °C, ● - 30 °C, ● - 25 °C, ● - 20 °C. The black horizontal line indicates saturation ratio = 1.

The decay in the centre-line temperature difference is an outcome of the mixing of the ambient air with the hot vapor in the wake. The Reynolds number in the experiments discussed so far are about 500 – 600 which suggests that the flow in the wake is not laminar. As a consequence the dilution rate is governed by the large scale motions in the wake [117], and these organized motions are intermittent in time and space [118]. The dilution rate may be higher in the region where the large scale motions are active and as a consequence, the saturation ratio here may rapidly decay to the ambient conditions. The rapid decay of the supersaturation may not activate the nuclei due to insufficient time. This may well explain the localized pockets in the wake without any droplets in Figs. 5.4 & 5.5. One of the other possibilities is that a fluid parcel from the ambient was engulfed into the core of the wake which is a common occurrence in free shear turbulent flows [117]. This parcel is sub-saturated until it mixes with the hot vapor in the wake. Another possibility for the droplet free zones in the wake might be due to the oscillations induced by vortex shedding. This may result in an

undulating trajectory and as a consequence, the planar laser sheet may not illuminate the entire wake. The mixing parcel model does not account for the difference in the mass and thermal diffusion coefficients. The diffusion coefficients of temperature and water vapor are approximately equal (Prandtl number  $Pr$  is about 0.7 and Schmidt number  $Sc$  is about 0.6). We assumed that the diffusivities are equal. As a consequence, the temperature and the water vapor concentration fields are identical. If the difference in diffusivities are considered, it may result in pockets of very high supersaturation, more than what was predicted from the mixing parcel model [52]. Similarly, pockets of sub-saturation may exist even if the two parcels were initially saturated. From the discussions so far it appears that the pockets without droplets in the wake in Fig. 5.4 may be an outcome of several underlying processes: entrainment, drop oscillation and difference in mass/thermal diffusivities. A systematic study is required to understand their contributions which is beyond the scope of the present work.

### 5.3.2 Droplet activation

Let us assume that the convection in the chamber has negligible effect on the dynamics in the wake of the hot drop. This assumption is well founded considering that the fluctuating velocity in the chamber is only a few cm/s [23]. The passage of a hot drop results in the formation of a wake like flow field in the chamber in the neighbourhood of the path traced by the drop. At a given  $z$  location, the wake spreads over time, thus diluting the temperature and water vapor concentration .

Let us consider a fluid parcel in the ambient. The parcel is small enough to contain only one nucleus but is large enough such that the continuum hypothesis is valid. We assume that the ambient temperature and the drop velocity are constant. Let us assume that the fluid parcel with a nucleus is located in the boundary layer near the hot drop and thus has the phase properties (humidity, temperature) of the hot drop. The initial velocity difference  $U - U_a = U_d$  and temperature difference  $T - T_a = \Delta T_d$  between the wake and the ambient of the fluid parcel decays over time where  $U(z)$  and  $T(z)$  are the instantaneous velocity and temperature fields of the parcel respectively.  $U_a$  is the ambient velocity which according to our assumptions is negligible and hence is taken as zero, and  $U_d$  is the velocity of the drop. We assume that the parcel travels downstream with the mean centerline velocity and we take the decay rate to be  $z^{-1}$  in the near wake region [106]. The corresponding decay rate for the mean centre-line temperature difference  $(T - T_a)$  is  $\propto z^{-1}$ , where  $T(z)$  is the mean temperature of the fluid parcel at the centre of the wake.

As was stated earlier, the hot drop does not attain terminal velocity before it reaches the bottom plate. Using the the equations of motion and the drag coefficient values for a rigid sphere [109], we estimate the drop velocity as about 2 m/s at a distance of

0.2 meters from the top, and about 3 m/s at a distance of 0.5 metres. We neglect the acceleration of the drop and assume a value of 3 m/s as  $U_d$  for the model calculations presented below. Based on the discussions so far, the decay of the mean centerline velocity is represented as

$$\frac{U(z) - U_a}{U_d - U_a} = \frac{A_u}{z}; \quad \forall z \geq \frac{d}{2} \quad (5.4)$$

where  $A_u = 0.495d$ ,  $d$  is the diameter of the falling drop,  $z$  is the distance of the fluid parcel from the hot drop. The fluid parcel travels in the wake with the velocity  $U$  and the corresponding temperature  $T$  is represented as

$$\frac{T(z) - T_a}{T_d - T_a} = \frac{A_t}{z}; \quad \forall z \geq \frac{d}{2} \quad (5.5)$$

where  $A_t = 0.5d$ . The constants  $A_u$  and  $A_t$  are calculated assuming that at  $z = 0.5d$ ;  $U = 0.99U_d$  and  $T = T_d$ . The fluid parcel cannot travel at the same speed as the liquid drop, and so we choose a value very close to that of the hot drop (99%  $U_d$ ). Using Eqs. 5.2 & 5.3 we estimate the vapor pressure in the wake, and this gives the saturation ratio.

The diffusional growth of a droplet is computed using the following equation [18]

$$r \frac{dr}{dt} = \frac{(S - 1) - \frac{a}{r} + \frac{b}{r^3}}{F_k + F_d} \quad (5.6)$$

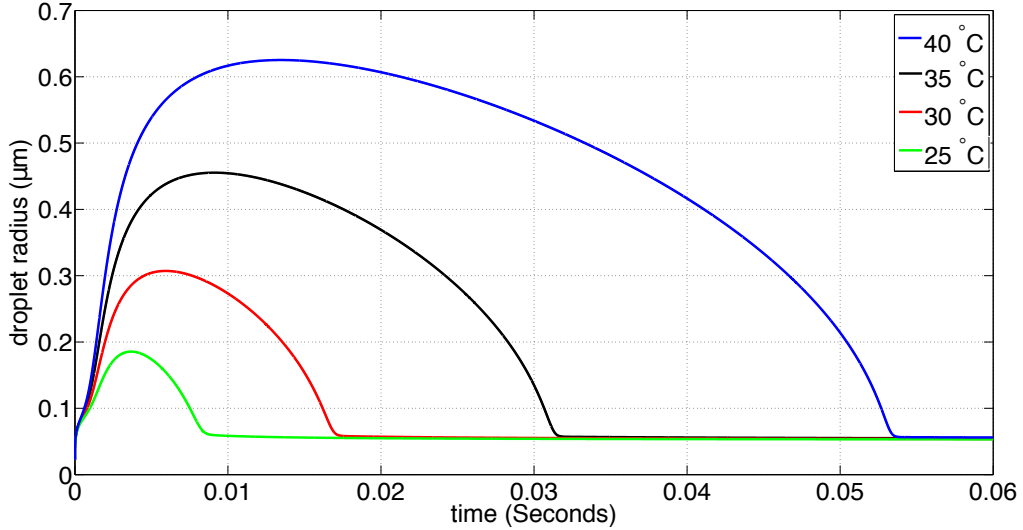
$$F_k = \left( \frac{L}{R_v T} - 1 \right) \frac{L \rho_L}{\kappa T} \quad (5.7)$$

$$F_d = \frac{\rho_L R_v T}{D p_s(T)} \quad (5.8)$$

where  $r(t)$  is the radius of the droplet,  $S$  is the saturation ratio in the neighbourhood of the droplet,  $a$  and  $b$  are the curvature and solution coefficients in Köhler theory and are dependent on the nuclei (see section 4.5.1 for details on Köhler theory),  $L = 2264.7 \text{ kJ/kg}$  is the specific enthalpy of condensation,  $R_v = 461 \text{ J/(K - kg)}$  is the gas constant for water vapor,  $\rho_L = 1000 \text{ kg/m}^3$  is the density of liquid water,  $\kappa$  is the coefficient of thermal conductivity of air,  $D = 2.5 \times 10^{-5} \text{ m}^2/\text{s}$  is the coefficient of diffusion of water vapor in air and  $p_s(T)$  is the saturation vapor pressure at temperature  $T$ . The saturation ratio  $S$  is obtained from the decay rate of  $T$  (Eq. 5.5) and the corresponding variation in  $P_v$  is obtained using the adiabatic mixing model (Eqs. 5.2, 5.3).

The present model has several unknown parameters which we can only estimate based on certain assumptions. The most important parameters are temperature/velocity decay rate in the wake, radius of the nucleus and velocity of the drop. We study the effect of these parameters on the evolution of a droplet starting from a nucleus. In

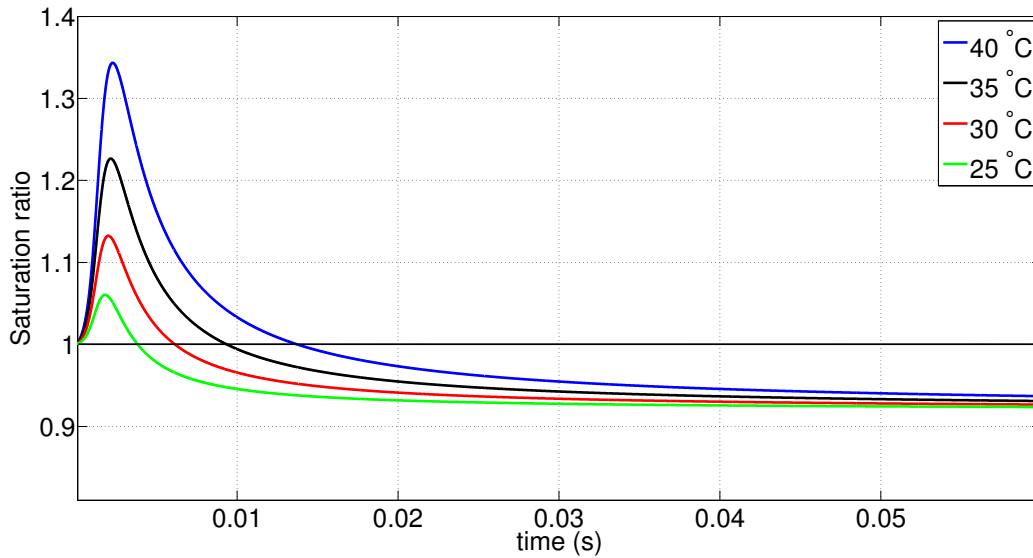
the experiments discussed under warm conditions Sodium Chloride (NaCl) was used as the condensation nuclei. The calculations were carried out for a NaCl nucleus of mass  $10^{-16}$  g, and the corresponding dry radius  $r_s$  of  $\approx 22$  nm. The velocity of the hot drop in the present model is about 3 m/s. Unless stated otherwise, these parameter values are used for the calculations below.



**Figure 5.8:** Effect of drop temperature on the growth of a droplet in its wake.  $U_d = 3$  m/s,  $r_s = 22$  nm.

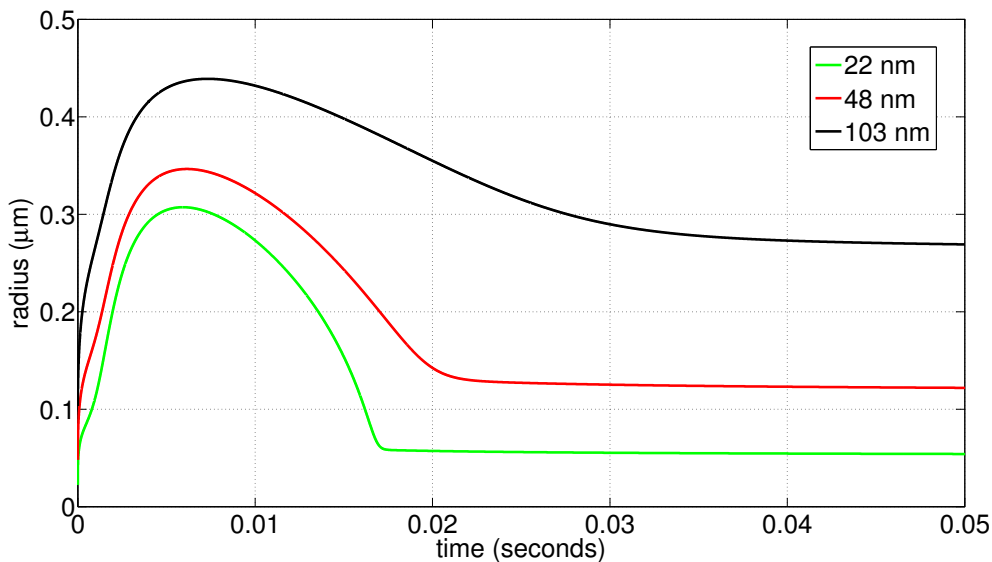
Figure 5.8 shows the size evolution of a droplet based on the adiabatic mixing model (Eq. 5.2 to Eq. 5.8). The model was tested for the hot drop temperatures used in the experiment shown in Fig. 5.4. The ambient conditions were set to the measured values in the experiment. At time  $t = 0$ , the fluid parcel under consideration is assumed to be in the neighbourhood of the warm drop (at  $z \approx 0.5d$ ). The droplet grows from the size of the nucleus  $r_s$ , reaches a maximum and then starts evaporating there after as the ambient was subsaturated. The corresponding variations in the supersaturation is shown in Fig. 5.9. We notice that the drop starts to evaporate once the supersaturation ratio drops below 1. The duration up to which the supersaturation is sustained in the wake increases with the temperature difference between the drop and the ambient. Consequently, the droplet grows for longer duration in the wake of the warmest drop under consideration and also attains higher maximal diameters (Fig. 5.8).

Figure 5.10 shows the evolution of droplets with different radii of their source nucleus. The temperature of the large drop was fixed at 30 °C in all cases. The nuclei with a larger initial radius attains higher maximal diameter before it settles down to its equilibrium hydrated size. The increase in the peak radius appears to be due to the difference in their respective hydration radius. It appears that the growth rate is not strongly influenced by the radius of the source nuclei, but the activation time is strongly dependent on the radius of the nucleus [18]. Larger nuclei require longer time to activate under a



**Figure 5.9:** Variation of saturation ratio encountered by a Lagrangian fluid parcel in the wake of hot drop at various temperatures.  $U_d = 3 \text{ m/s}$ ,  $r_s = 22 \text{ nm}$

given saturation ratio as their critical radius is proportional to the dimensions of the nuclei. The hydration diameter or the equilibrium radius is related to the dry radius of the nucleus. Larger dry radius results in a larger hydrated radius under sub-saturated conditions as can be inferred from Fig. 5.10.



**Figure 5.10:** The growth of droplets with different nucleus radii in the wake of a 30 °C drop falling at a velocity of 3 m/s.

As we had stated earlier, the drop velocity in the experiments presented here increases with time. Figure 5.11 shows the effect of drop velocity on the growth of a droplet in its wake. The radius of the nucleus is 22 nm and the drop temperature is 30 °C. Figure 5.11

shows that a drop with the lowest velocity results in the largest droplet diameter for a fixed set of conditions. The lower velocity results in a relatively slower decay of the supersaturation field in the Lagrangian parcel. This increases the duration for which the droplet encounters a supersaturated environment. If the velocity and diameter of the drop are treated as independent variables then increasing the diameter of the drop will have a similar effect as lowering the velocity. Both variations increase the duration of supersaturation in the fluid parcel.

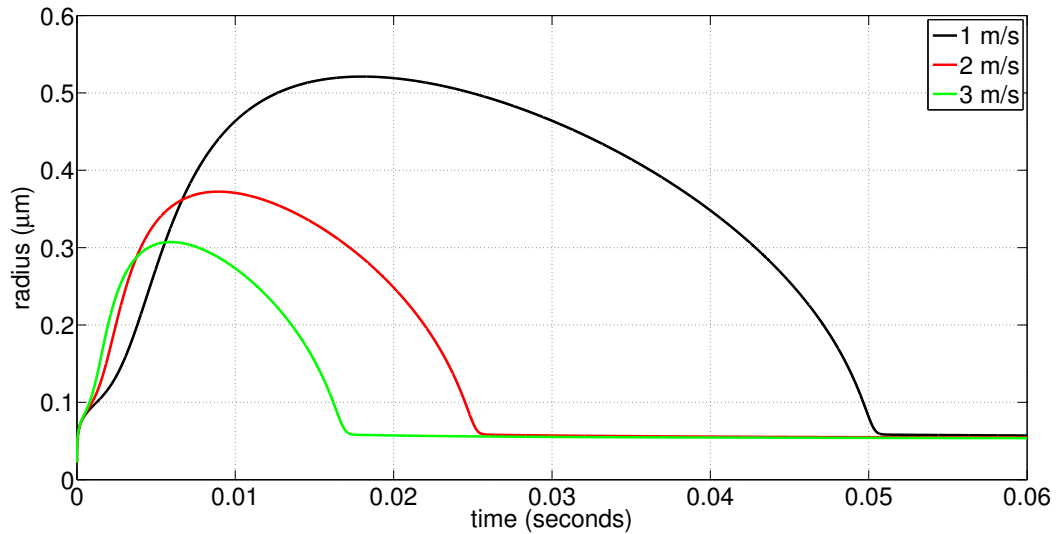


**Figure 5.11:** Effect of drop velocity on the growth of a droplet in the wake of the drop. Drop temperature is set to  $30^{\circ}\text{C}$  and  $r_s = 22\text{ nm}$ . RH in the ambient is 92%.

From the discussions so far, it appears that the temperature difference between the drop and the ambient, and also the velocity of the drop are important parameters in computing the growth of a droplet in the wake of a hot drop. From Fig. 5.8 and Fig. 5.11 we see that the droplets tend to grow ( $\frac{dr}{dt} > 0$ ) for a longer duration in the wake of drops with larger temperature differences and lower velocities. As we show later, drops with a relatively higher velocity would require a relatively larger temperature difference to activate nuclei in their wake. Please note that we have not discussed the activation of droplets so far. Activation is applicable only for droplets in the supersaturated environment. But in the present case, the supersaturation attained is only transient and as a consequence all nucleated droplets eventually evaporate. We discuss activation in the context of Earth’s atmosphere later in this chapter.

An additional parameter that we have not varied is the decay rate of the centre-line temperature and velocity. Figure 5.12 shows the effect of the decay rate of momentum deficit and temperature deficit on the growth of a droplet in the wake. The initial growth up to about  $0.3\text{ }\mu\text{m}$  appear to be independent of the decay rates. But, above  $0.3\text{ }\mu\text{m}$ , the temperature decay rate has a significant influence on the growth of the droplet, and

in comparison, the velocity decay rate does not seem to have such a strong influence on the growth of the droplet. This does not come as a surprise as the supersaturation field is directly coupled to the evolution of the temperature field. The slower the decay rate of the temperature field, the longer is the supersaturation maintained in the wake. As a consequence the droplets tend to grow for a longer duration. Similarly, a slower decay rate in the velocity also sustains supersaturation in the wake for longer duration, but the increase is not as significant as in the case of the temperature decay rate. Please note that we have treated both temperature and velocity as independent variables.

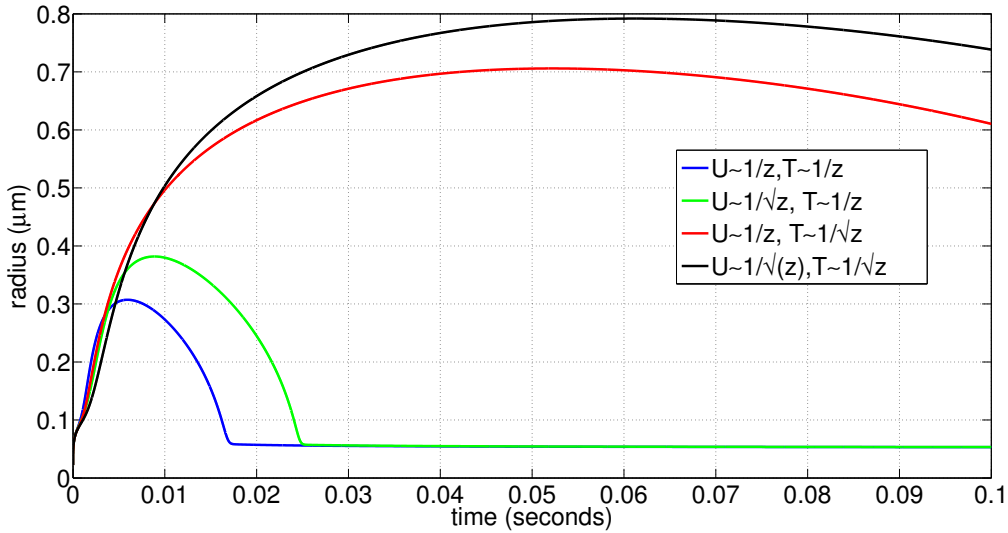


**Figure 5.12:** The effect of temperature and velocity decay rates on the growth of a droplet in the wake of a hot drop. Drop temperature: 30 °C,  $r_s = 22$  nm.

Let us take a closer look at the decay rates from existing numerical simulations. Based on the passive wake calculations where temperature is treated as a passive scalar at  $Re = 10^4$  [106], we note that the decay rate for the temperature up to  $10d$  is about  $z^{-1}$  and beyond  $10d$  it is about  $z^{-\frac{2}{3}}$ . Similarly, the velocity defect in the first  $10d$  is about  $z^{-1}$ , and beyond that it follows the  $z^{-\frac{2}{3}}$  decay rate. On the other hand, in the relatively low Reynolds number passive wake calculations the temperature decay rate is about  $z^{-\frac{1}{2}}$  up to  $10d$  [52]. Unfortunately, the authors do not report the velocity decay rate. They state that their low Reynolds number active wake calculations suggest that the decay rate of the centre-line velocity is slower than  $z^{-1}$ , but they do not report the corresponding decay rates. Similar claims are supported by other numerical calculations [119]. It is important to note that the role of buoyancy is related to the Richardson number  $Ri$  in mixed convective systems.  $Ri$  is defined as the ratio between the buoyancy term and the inertial term in the Navier-Stokes equations and is represented as  $Ri = \frac{g\beta\Delta Td}{U^2}$  where  $d$  is the diameter of the drop and  $\beta$  is the thermal expansion coefficient of air. In the experiments reported here the  $Ri$  is between  $10^{-3}$  and  $10^{-2}$ . Consequently, the

deviations encountered in using the decay rates from a passive scalar computations may not have a strong influence on the model discussed so far.

Based on the discussions so far we use a piecewise decay rate to represent the average temperature and velocity defect in the wake. The velocity decays as  $z^{-1}$  up to  $10 d$  and there after it goes as  $z^{-2/3}$ . The temperature defect decays as  $z^{-1/2}$  upto  $10 d$  and there after it decays as  $z^{-2/3}$ . This new model is called Model A and for comparison we plot the evolution of a droplet with the other decay rates in Fig. 5.13. As expected, Model A lies in between the decay rates of  $z^{-1}$  and  $z^{-1/2}$ . Please note that all the models discussed so far are based on mean quantities and do not account for the effects of fluctuations. On the other hand, the nucleation process is based on the instantaneous value of the variables. As a consequence, the models based on time averaged quantities have their inherent limitations. A detailed DNS study coupled with the droplet growth equations is required to make instantaneous predictions.

Let us take a closer look at Fig. 5.4. In Fig. 5.4 (b), the nucleation in the wake extends to about 12 – 15 cm behind the hot drop. The time for which the nucleated droplets are visible in the wake is about 0.04 – 0.05 seconds (assuming that the drop velocity is about 3 m/s). The wake behind the drop was illuminated by a laser of wavelength 532 nm. The nucleated droplets scatter light from the laser sheet. For the nucleated droplets to be visible, the diameter of the droplet should be at least 532 nm. Let us set a threshold of 300 nm for the radius of the droplet to scatter light from the laser sheet. Based on Model A calculations shown in Fig. 5.13 the nucleated droplet is active for about 0.07 seconds. The model with a decay rate of  $z^{-1}$  results in a droplet activity period of 0.001 second compared to 0.15 second from the model with a decay rate of  $z^{-1/2}$ . Both these predictions are significantly off from the experimental observations. The droplet activity time period calculated from Model A is the best approximation to the observed value in the experiments. We extend this model to drop temperatures of 25 °C and 35 °C, and estimate the nucleated droplet activity time period to be 0 and 0.19 seconds respectively. In Fig. 5.4 (a) we see that the wake length is less than a centimeter for a drop at 25 °C. It appears that the unsteadiness and flow separation in the near wake is not appropriately represented by Model A. In Fig. 5.13 (c), the nucleated droplets appear to be active beyond the observation window (of about 20 cm) for a drop at 35 °C. The predicted wake length with nucleated droplets is about 57 cm under the assumption that the drop velocity does not change.

An additional uncertainty is the temperature of the drop. In the present model the calculations are based on the drop temperature at the drop generator. As the drop falls through the chamber, its temperature decreases due to the heat transfer to the ambient and also due to the latent heat of evaporation. The temperature evolution of the drop

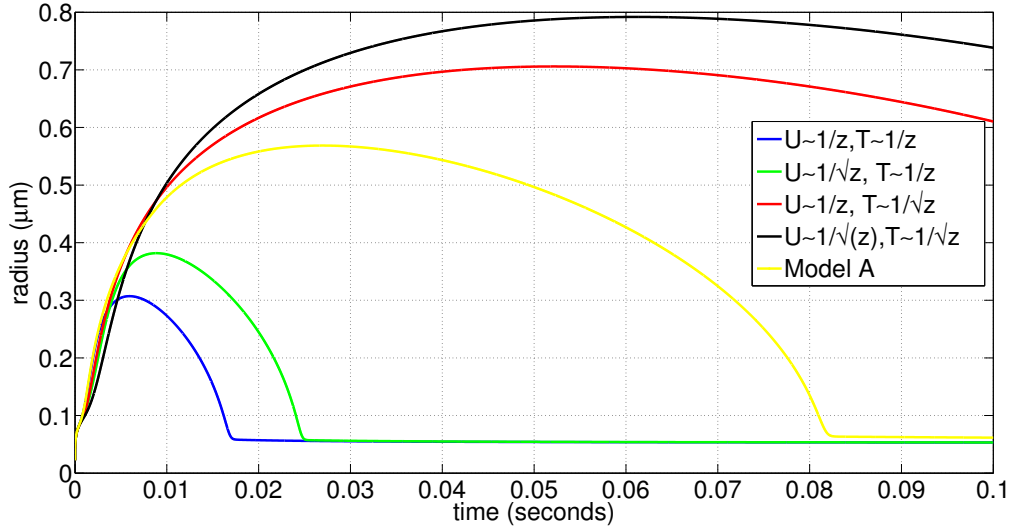


**Figure 5.13:** Comparison of model A with other decay rates. Drop temperature: 30°C,  $r_s = 22$  nm.

is written as [44]

$$\frac{dT}{dt} = \frac{6\lambda\text{Nu}}{c_{p,l}\rho_l d^2}(T_a - T) - \frac{L_e f_v B}{\rho_l \frac{1}{6}\pi d^3 c_p}. \quad (5.9)$$

where  $B = \frac{2\pi d D_v M_w}{R} [\frac{P_d}{T_d} - \frac{P_a}{T_a}]$ ,  $T$  is the drop temperature,  $L_e$  is the specific enthalpy of vaporization,  $f_v$  is the ventilation coefficient and  $D_v$  is the mass diffusion coefficient of water vapor in air. The first term on the right hand side of Eq. 5.9 represents the heat transfer to the ambient and the last term represents the cooling due to evaporative effects. Equation 5.9 can be solved along with the equations of motion for the drop which would aid in computing the temperature of the drop at various instances. Using this model the temperature of the drop in Fig. 5.4 (a), Fig. 5.4 (b) and Fig. 5.4 (c) at a height of 0.5 m from the top are 24.1°C, 28.7°C and 33.2°C respectively. Using these temperatures for the drop in Model A we estimate the corresponding droplet activity distance to be about 0, 15 and 42 cm respectively. The estimated droplet activity length of 15 cm for the drop in Fig. 5.4(b) is in agreement with the experimental observation. In Fig. 5.4(c), the droplet activity extends beyond the image window and as a consequence cannot be compared with the calculations from model A. Nevertheless, the wake length and droplet activity period predictions from model A are broadly consistent with the experimental observations.

Model A has its limitations. For instance, it does not appropriately represent the dynamics in the separated region in the near wake region. Shedding is an inherently unsteady phenomenon and would require phase averaged data to better represent the near wake dynamics. This may explain why the nucleation predictions for the drop temperature of 25°C was not accurate as the droplets were visible only up to a few diameters downstream, hence strongly influenced by the near wake dynamics. Additional

experiments and analysis is required to check this.

### 5.3.3 Cold conditions

Figure 5.14 shows the mixing phase diagram for the conditions shown in Fig. 5.5. The blue curve represents the liquid water saturation line. The ambient experimental conditions are nearly similar in all the experiments and is represented by  $\blacksquare$ . The phase properties in the neighbourhood of the drop at various temperatures are marked in Fig. 5.14 (see figure caption for details). The mixing line plotted in Fig. 5.14 is calculated using the adiabatic mixing parcel model (Eqs. 5.2 & 5.3). The corresponding liquid water saturation ratio along the mixing line is shown in Fig. 5.15 for different drop temperatures. Peak supersaturation is attained below the freezing temperature of water. Before we discuss the details of ice nucleation, we have to discuss the modes of ice nucleation and the role of ice nuclei. In the next sub-section we briefly introduce the modes of ice nucleation. For additional details please see [18, 44].

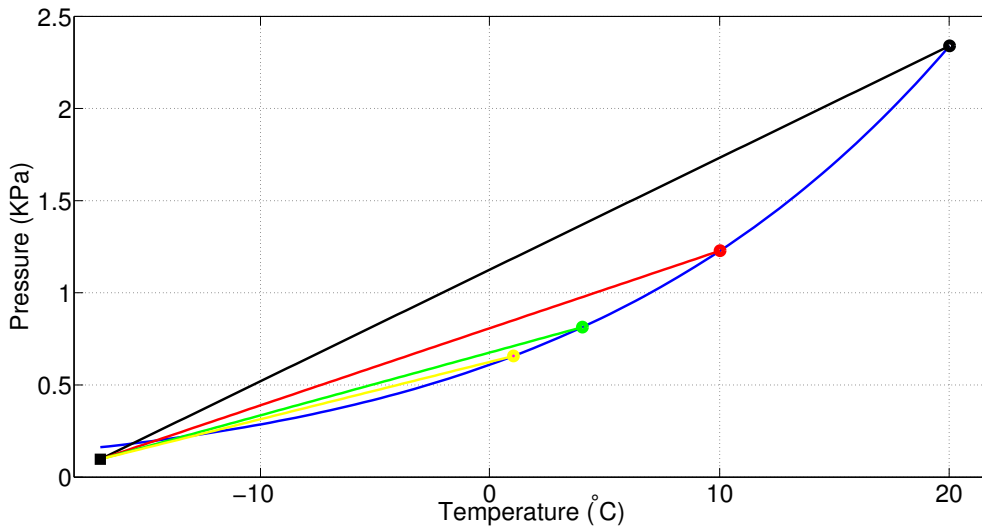


**Figure 5.14:** Mixing phase diagram under cold condition (Fig. 5.5).  $\blacksquare$  - ambient condition ( $T = -18$  °C,  $RH = 60\%$ ). The conditions at the surface of the drop is marked in filled circles ( $\bullet$ ) of various colors and the corresponding mixing line is represented by a line connecting the drop conditions with the ambient conditions.  $\bullet$  20 °C,  $\bullet$  10 °C,  $\bullet$  4 °C,  $\bullet$  1 °C.

#### 5.3.3.1 Ice nucleation

Only a small fraction of cloud nuclei act as ice forming nuclei [44]. Ice crystals are nucleated in four different modes. In the first mode, the nucleus directly adsorbs water vapor onto its surface thus resulting in the formation of ice crystals. This mode is called the direct deposition or deposition mode and is active at sufficiently low temperatures provided the environment is supersaturated with respect to ice. If the environment is

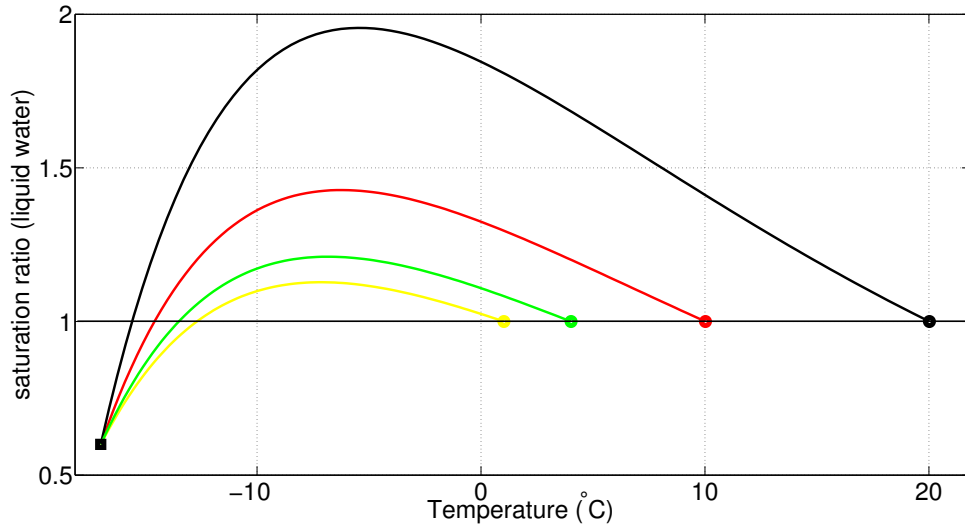


**Figure 5.15:** Saturation ratio along the mixing line plotted in Fig. 5.14. ● 20 °C, ● 10 °C, ● 4 °C, ● 1 °C.

supersaturated with respect to water, then the ice nuclei may act as cloud condensation nuclei to form water droplets, which eventually freezes during the process of condensation. This mode of ice initiation is called the condensation mode. The other two modes are immersion and contact modes. In the immersion mode, a nucleus is immersed into a water drop at a temperature where it is not active and as the temperature of the drop decreases, ice nucleation is initiated. In the contact mode, as the name suggests, ice nucleation is initiated once the ice nuclei makes contact with a supercooled drop. For additional details please see [18, 44]. The different modes of ice initiation are dependent on the temperature and supersaturation of the environment *w.r.t* ice and also on the properties of the nuclei. A detailed review on the modes of ice initiation for various nuclei in the atmosphere and laboratory is provided in [120].

In the experiments shown in Fig. 5.5, aqueous Snomax was used as the ice nuclei. From Fig. 5.15 we see that the saturation ratio in the wake in all the experiments is above water saturation for a certain period of time. This was verified by injecting NaCl nuclei into the chamber, and under these conditions we observed the formation of liquid droplets in the wake. This suggests that the nuclei acts as a condensation nuclei and forms a liquid droplet, which over time freezes. The properties of Snomax aerosols were characterized using a CCN counter. The size distribution of snomax aerosols were similar to that of NaCl. The activation properties of the snomax aerosol was obtained using a DMT CCN counter. For a 90 nm Snomax aerosol particle, the critical supersaturation required for activation as a liquid droplet is about 0.2%. For a NaCl particle of the same diameter, the critical supersaturation required for activation is about 0.13%. The value of  $\kappa$  for Snomax 0.55. The method for measuring the value

Temperature at $z = 0.0$ m ( $^{\circ}\text{C}$ )	1.0	4.0	10.0	20.0	50.0
Temperature at $z = 0.5$ m ( $^{\circ}\text{C}$ )	0.5	3.3	9.0	18.5	45.4

**Table 5.1:** Drop temperature at the center of the chamber calculated using Eq. 5.9

of  $\kappa$  is discussed in [113, 114]. Equation 5.1 coupled together with Eq. 5.6 is solved to compute the growth of solute droplets with Snomax as the nuclei.

### 5.3.3.2 Droplet activation

We estimate the decay rate of the supersaturation in the wake using Model A. The velocity of the hot drop used for the calculations is 3 m/s (same as in the warm conditions). We assume that the temperature in the ambient was  $-18$   $^{\circ}\text{C}$ . The temperature of the drop was corrected using Eq. 5.9 to account for the evaporative cooling effects and also the heat transferred to the ambient. The temperature of the drop at the center of the chamber is shown in Table 5.1.

The growth history of the droplet in the wake of a drop at various temperatures is shown in Fig. 5.16. The dry radius of the nucleus used for these calculations is about 30 nm which approximately corresponds to the peak value in the aerosol size distribution shown. Please note that the large drops are labeled based on their initial temperature (shown in the legend in Fig. 5.16), but the calculations were made using the corrected temperatures shown in Table 5.1. Using the detection criteria discussed for warm conditions we note that the  $1^{\circ}\text{C}$  drop does not result in any detectable droplets. This was corroborated by the experimental observations as no droplets were detected for these conditions. For the drop with an initial temperature of  $4^{\circ}\text{C}$  the estimated activity period for the nucleated droplet is about  $0.01 - 0.015$  seconds which corresponds to a wake length of  $3 - 4.5$  cm. From Fig. 5.4(b), we observe that the wake length is about  $10 - 13$  cm. This may well be due to the fact that we did not account for the freezing of these nucleated droplets. In a sub-saturated environment, an ice particle can survive for a longer duration than an equivalent water droplet as the saturation vapor pressure for ice is lower than the saturation vapor pressure for liquid water at a given temperature below  $0^{\circ}\text{C}$ . Additional analysis is required to include the effects of ice formation. For all the other drop temperatures, the observed wake length extends beyond the window of observation. The predicted wake length for the 10, 20 and  $50^{\circ}\text{C}$  drops are about 21, 90 and over 400 cm respectively. These predictions from Model A are broadly consistent with the observations (based on the recorded movie), but as the drop temperature increases the predicted wake length exceeds the observed wake length or the droplet activity period. This maybe due to the fact that far away from the drop the flow field is significantly different from that of a classical wake and as a consequence the decay rates are different from what has been used in Model A. The evolution of

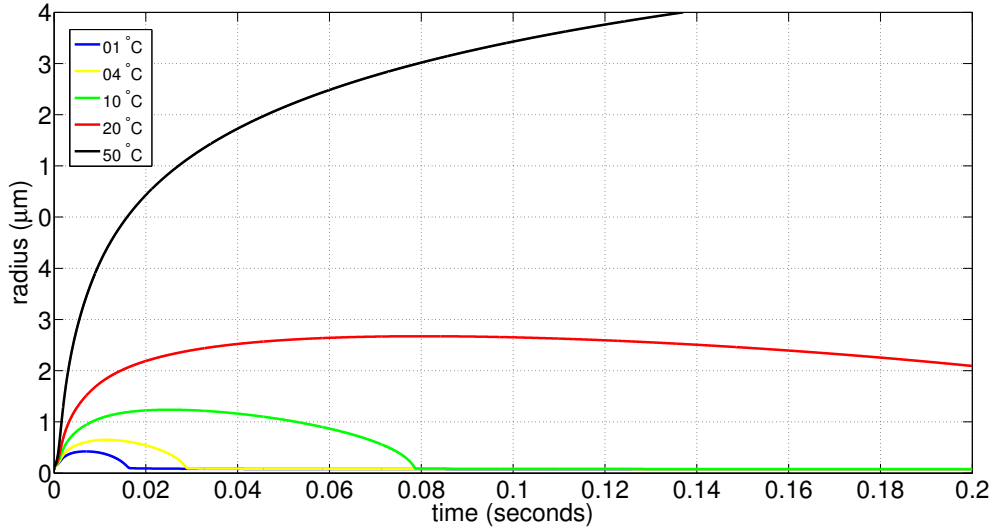


**Figure 5.16:** Effect of drop temperature on the growth of a droplet in its wake under cold conditions.  $U_d = 3 \text{ m s}^{-1}$ ,  $r_s = 22 \text{ nm}$

the wake is also influenced by the underlying convective flow in the chamber, and the decay rates used in Model A are applicable only to a system with a constant drop velocity, which is not true in the present experiments. Despite these limitations, the predictions from Model A are qualitatively consistent with the reported observations.

The discussions so far was based on the behaviour of Snomax as cloud condensation nuclei. Snomax consists of the bacterium *Pseudomonas Syrigae* [120]. These bacteria act as the source of ice nuclei. The experiments to characterize the activity of aqueous solution of Snomax concluded that the heterogeneous nucleation rate was a function of the composition of the nuclei and also of the environmental temperature [121, 122]. Their studies showed that more nuclei are activated as ice particles as the environmental temperature decreases. Furthermore, experiments show that below a temperature of  $-9 \text{ }^\circ\text{C}$  water droplets with a Snomax ice nucleus in them initiate freezing of the droplet [120, 123]. From Fig. 5.15, we note that the wake was supersaturated with respect to liquid water at temperatures below  $-9 \text{ }^\circ\text{C}$ , thus ensuring that at least a fraction of the nucleated droplets must have frozen under these conditions [122]. Incidentally, Snomax is also used for making snow in the ski resorts.

The nucleation of ice crystals and water droplets scatters light from the laser sheet. The nucleated water droplets are spherical and hence the scattered light intensity is independent of the orientation of the droplets. On the other hand, the nucleated ice crystals have a non-spherical geometry and as a consequence the amount of light scattered is dependent on the orientation of the particle. This results in a glittering or twinkling effect. Thus, the light scattered from the nucleated particles are a strong indicator of the phase of these particles. Unfortunately, the optical system used in the present ex-

periments do not capture these effects. One may argue that this difference in character of the scattered light is due to the nuclei used in the experiments. The experiments with Snomax nuclei were repeated at higher ambient temperatures (about  $-5$  °C and  $-12$  °C). Nucleation was observed in the wake of the hot drop and the scattered light from the particles was similar to those from water droplets in Fig. 5.4. This observation suggests that the nuclei has little effect on the scattered light. From the discussions so far it is evident that some of the particles nucleated in the experiments shown in Fig. 5.5 were ice crystals. These observations are consistent with the fact that the environment temperature is an important parameter in ice nucleation [44].

## 5.4 Atmospheric Implications

The experiments and the analysis conducted so far suggests that new droplets nucleate in the wake of a hot drop, and under appropriate conditions, these droplets freeze. In the experiments, these droplets and ice particles evaporated over time as the ambient was sub-saturated. In this section, we examine the possibility of extending these results to atmospheric clouds. Nucleation of ice particles in clouds play an important role in predicting their lifetime [44]. Ice particles tend to grow by diffusion at a faster rate than water droplets as the supersaturation relative to ice is higher than that of supercooled liquid water. Hence, the presence of active ice nuclei may result in a faster formation of precipitation [18, 44]. In this section, we examine the possibility of secondary ice nucleation in the wake of warm hydrometeors. A detailed review of various secondary ice nucleation processes in the Earth's atmosphere was presented in Section 1.4.

### 5.4.1 Secondary Ice Nucleation

In the atmosphere, it is unusual to have a raindrop falling through a cloud with its surface temperature higher than the local ambient cloud temperature. If a raindrop was carried along with an updraft, which is usually warmer than the outer shell of a cloud due to the latent heat released from phase change processes, and later is transported towards the outer shell of a cloud at the top, then for a short duration the temperature of the drop would be higher than that of the ambient. Nevertheless, the induced temperature difference may not be significant enough to nucleate new droplets or ice crystals in the wake of the cloud drop. The shear enhanced mixing inside the drop will equilibrate the temperature of the drop with that of the ambient. Transitional supersaturation also occurs in the immediate vicinity of a freezing supercooled drop. The latent heat released due to the freezing process increases the temperature of the drop to  $0$  °C for a short duration [101]. Experiments suggest that this enhanced transitional supersaturation may result in the nucleation of ice particles by heterogeneous condensation/deposition freezing [72, 73, 124]. A simple quantitative analysis showed

that the effect of this transitional supersaturation was too small to make a significant contribution to secondary ice nucleation [70, 125]. It was argued that the volume of very high transitional supersaturation around a freezing drop was negligible compared to the volume of high ice concentrations in clouds.

A growing hailstone or graupel may have a higher surface temperature than the ambient. In clouds containing sufficient amount of supercooled water droplets, a growing graupel/hailstone may undergo what is known as wet growth [18, 44, 126]. A settling ice particle accumulates supercooled water droplets in a mixed phase cloud. The accumulated water droplets freeze as they come in contact with the ice particle. The latent heat released during the freezing process is transferred to the ice particle by conduction, and to the ambient through convection. If the liquid water content is sufficiently high, then the heat transferred to the ambient and to the core of the ice is smaller than the latent heat released from the freezing process. In such a situation the ice particle is covered with a layer of liquid water, and the surface temperature of the liquid layer is near 0 °C [44, 70, 127]. The freezing process continues as the temperature beneath the liquid water layer is still less than 0 °C. The water accumulated on the surface of the hail/graupel in the accretion process may not be evenly distributed [128]. This may result in an uneven distribution of surface temperature. Nevertheless, a significant temperature difference exists between the surface of the hailstone and the ambient in deep convective clouds. In the wet growth regime, the continuous release of latent heat due to the freezing process maintains the surface temperature of a hailstone at 0 °C, unlike in a freezing cloud drop where the temperature decreases after the drop is frozen. As a consequence, the volume of enhanced supersaturation in the wake is significantly higher for a growing hailstone compared to a freezing cloud drop. Please note that the temperature difference between the hailstone and the ambient varies depending on the altitude, as the ambient temperature in a cloud varies with height.

The hot drop in the experiment was a surrogate for a hailstone in the wet growth regime. So the results from the experiments directly carry over to atmospheric clouds. In the atmosphere, the temperature of a growing hailstone does not increase above 0 °C. On the other hand, in the experiments, nucleation was observed in the wake of the hot drop only if the temperature of the drop was at least 4 °C. This is because the ambient in the experiments was sub-saturated ( $RH \approx 60\%$ ,  $S \approx 0.6$ ). Let us consider a wet convective cloud which is saturated with respect to liquid water, containing supercooled liquid droplets, *i.e.*, the cloud has a local relative humidity of 100%. The liquid water content is high enough for a hailstone/graupel to grow in the wet regime. The red curve in Fig. 5.17 shows the variation of supersaturation in the cloud with respect to ice. The temperature in the cloud varies between  $-20$  °C and 0 °C. The figure also presents the variation of the maximum supersaturation attained in the wake of a growing hailstone

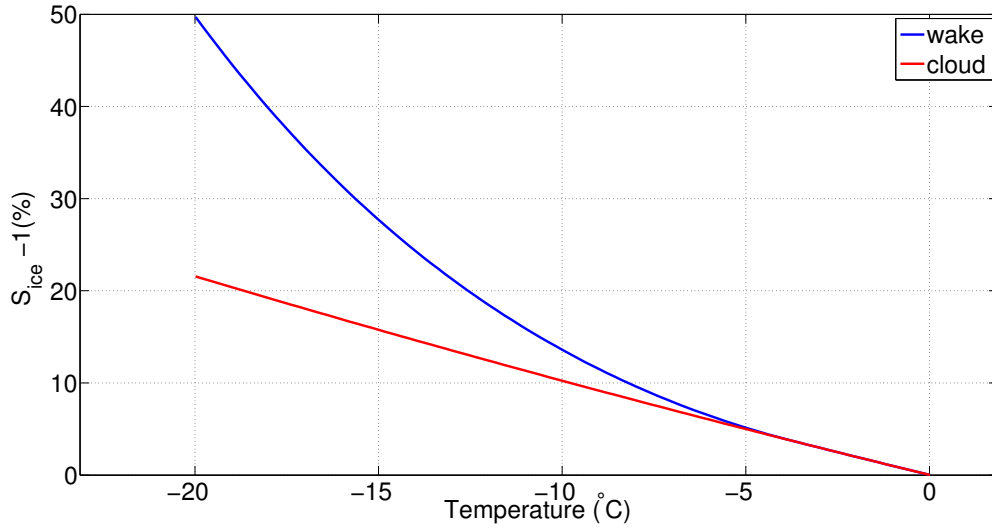


**Figure 5.17:** Variation of ice supersaturation as a function of ambient temperature. The red curve represents the ambient ice supersaturation and the blue curve represents the maximum ice supersaturation in the wake of a hail/graupel in wet growth mode obtained from the mixing model.

using model A assuming that the surface temperature of the hailstone is 0 °C. As expected, the supersaturation in the wake increases as the ambient cloud temperature decreases. Please note that in the calculations based on Model A we do not account for the difference in the temperature and water vapor diffusivity coefficients. Accounting for these differences would result in a higher supersaturation in the wake than what was calculated using the mixing parcel model [52].

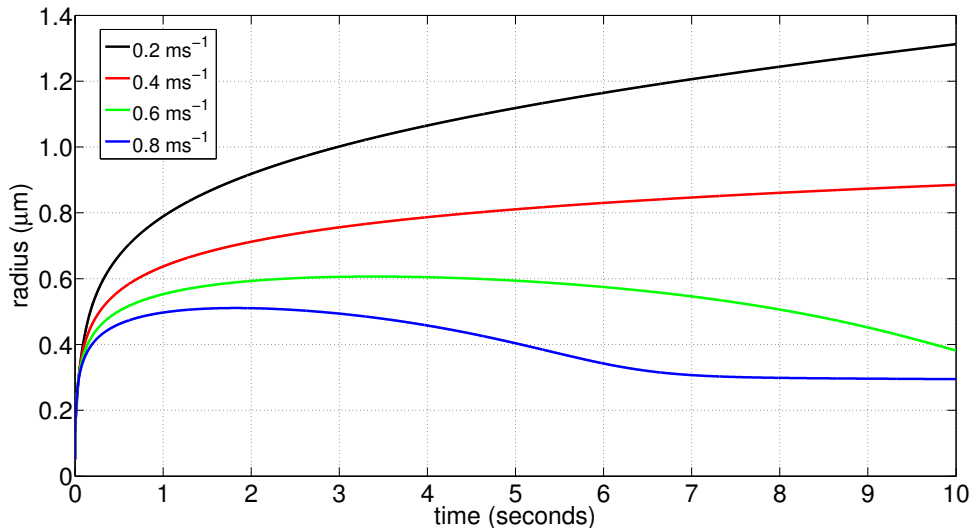


**Figure 5.18:** Effect of velocity of the drop on the growth of a droplet in the wake.  $r_s = 50$  nm,  $S_{ambienet} = 0.1\%$ , drop diameter = 2 mm, drop temperature = 0 °C, ambient tempertaure = -5 °C.

Graupel/hailstones exist in a variety of shapes unlike liquid water drops. As a con-

sequence the drag coefficient ( $C_d$ ) of these particles are very different from those of a settling spherical drop. The  $C_d$  for an ice particle is usually higher than that of an equivalent drop, and the density of the ice particles are lower than that of liquid water. Some of these may contain trapped air pockets. As a consequence the terminal velocity of a hailstone is lower than that of a water drop of equivalent dimension. A detailed discussion on this is presented in [129]. Several experiments were conducted in the past to measure the terminal velocity of various hydrometeors along with other field measurements [130, 131]. They investigated particles with dimensions (effective diameter) between 1 and 10 mm and there was no definite trend as to how the terminal velocity varied as a function of the particle diameter. As was discussed in the previous section, the velocity and diameter of the ice particle plays a crucial role in the growth of droplets in the wake of a hailstones. Figure 5.18 shows the effect of velocity on the growth of a droplet in the wake of a drop at 0 °C in an environment of temperature  $T_a = -5$  °C and a supersaturation of 0.1%. We notice that as the drop velocity is increased the droplet stops growing after a few seconds. For instance, the droplet radius starts to decrease after 4 seconds if the velocity of the hydrometeor is 0.6 m/s. During this time (before it evaporates) the droplet may freeze and would continue to grow as the supersaturation with respect to ice is much higher than that of liquid water. As we increase the velocity of the drop the duration of growth is reduced. So it is a competition between the time required to initiate ice nucleation and the time up to which the enhanced supersaturation is sustained in the wake. On the other hand, for the low velocity drops, the droplets in the wake continue to grow indefinitely as the ambient is supersaturated and the critical supersaturation/radius threshold is surpassed due to the enhanced supersaturation.

A droplet is said to be activated if its radius is above the critical radius determined from the Köhler curve (see Section 4.5.1 for details). This definition for activation is under the assumption that the supersaturation is constant like in the diffusion chamber experiments. In the present scenario, for a Lagrangian fluid parcel in the wake, the supersaturation varies over time. Initially it increases, and then relaxes to that of the ambient condition. So a droplet is said to be activated if the radius of the droplet overcomes the equilibrium radius corresponding to the ambient supersaturation in the unstable leg of the Köhler curve. We call this radius as the dynamic critical radius. Figure 5.19 shows the Köhler curve for a Snomax nucleus of radius 50 nm. The ambient supersaturation of 0.1% is shown in Fig. 5.19. The dynamic critical radius for  $S = 0.1\%$  is marked as A, and B is the corresponding equilibrium radius on the stable leg of the Köhler curve. A haze droplet is initially at B. In the wake of a warm drop, the droplet grows due to the enhanced supersaturation. As the supersaturation in the wake relaxes back to the ambient value, the droplet radius should be at least  $r_A$  for the droplet to be

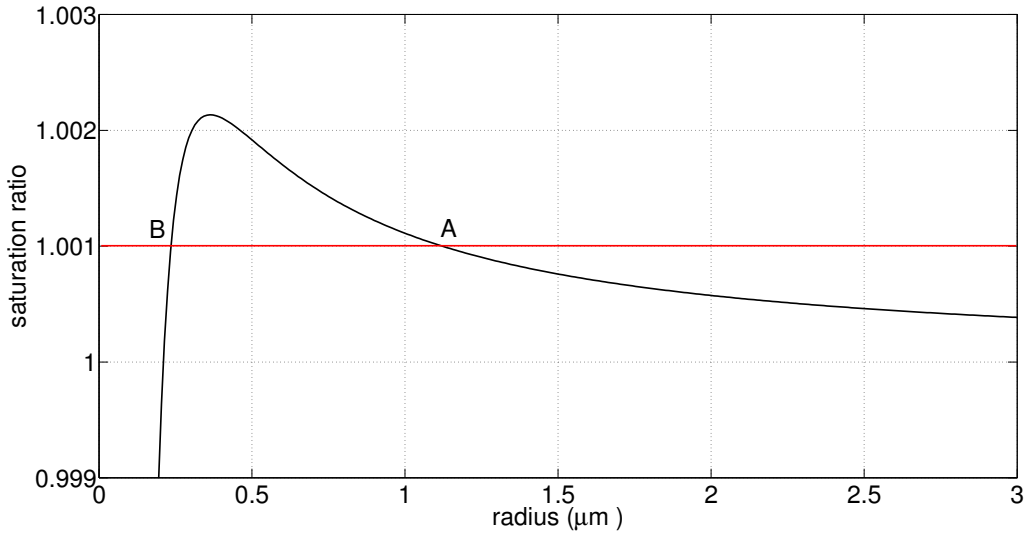


**Figure 5.19:** Köhler's curve for a snomax aerosol with  $r_s = 50$  nm. A - dynamic critical radius for  $S_a = 0.1\%$ , B - equilibrium haze droplet radius. The red line indicates the ambient supersaturation.

active. If at any instance the supersaturation in the wake falls below the equilibrium supersaturation predicted by Köhler's theory then the droplet starts to evaporate till it attains the equilibrium radius in the stable leg of the Köhler's curve. As the drop velocity increases the decay rate is enhanced. As a consequence the droplet does not have enough time to overcome the dynamic critical radius and starts to evaporate over time. The dynamic critical radius is dependent on the ambient supersaturation and also on the properties of the nucleus.

Let us estimate the effect of a growing hailstone on the ice nuclei concentration in a wet deep convective system. Let us consider an ambient cloud temperature of  $-15$  °C with a supersaturation of  $0.1\%$  with respect to liquid water, and an ice nuclei concentration of 1 per liter at these temperatures [132]. The CCN concentration is given as  $Cs^k$  per  $\text{cm}^3$  where  $s$  is the supersaturation in % (see section 4.5.1 for details). The values for  $C$  and  $k$  vary depending on the geographical location [44]. Let us use the data for High Plains, Montana [44] where  $C = 2000$  and  $k = 0.9$ . For  $s = 0.1\%$ , the CCN number concentration is about 252000 per litre. So about 1 in 250000 CCNs act as an ice nucleus. The maximum liquid water supersaturation attained in the wake of a hydrometeor with a surface temperature of  $0$  °C under these conditions is about  $16\%$ . Let us use this maximum value as the reference  $s$  for estimating the number of CCNs activated in the wake. The estimated number concentrations for CCN in the wake is around 100 times greater than the initial concentration. Correspondingly, the activated ice nuclei concentrations also increases by a factor of 100. The numbers calculated above is based on the assumption that ice nuclei concentration also enhances with supersaturation like CCN ( $Cs^k$ ). This assumption is not well founded as the

available laboratory and field measurements suggest that ice nuclei concentration is coupled to the environmental temperature and not on the supersaturation in the cloud, except in the case of deposition nucleation [132, 133]. In deep convective systems, the relative humidity is close to liquid water saturation and so most of the ice nuclei activate in the immersion or the contact mode. In a cloud, more ice nuclei are activated as the environmental temperature decreases, and their activation temperature and active fractions depend on the properties of the nuclei [133]. For instance, bacteria *P. syringae* are active as ice nuclei at about  $-2$  °C, whereas volcanic ash is active only at  $-15$  °C [133]. Moreover, the activity of the nuclei is also dependent on the surface area of the nucleus. The probability of having an ice nucleation site decreases as the size of the nucleus decreases [101, 133].

Let us try to make a refined estimate of the ice nucleation in the wake of a growing graupel/hailstone. As was stated earlier, observations suggest that at a temperature of  $-15$  °C we have about one ice nucleus active per liter and the corresponding CCN concentration is about 250000 for a supersaturation of 0.1%. Let us assume that ice nucleation occurs only in the immersion mode. We assume that the mean diameter of an active cloud nuclei is  $0.5$   $\mu\text{m}$ . At this temperature, we take the active site density  $n_s$  to be about  $10^4$  per  $\text{cm}^2$  [133]. An active site on the surface of a nucleus represents a region favorable for forming an ice embryo, i.e., these sites have a crystallographic structure similar to that of ice [44]. Such sites are found in cracks or defects in a nucleus [133]. Only a small fraction of the activated droplets will contain an immersed ice nuclei. The number concentration of the ice nuclei is expressed as

$$N_i = xN_{CCN}An_s \quad (5.10)$$

where  $N_i$  is the number concentration of ice nuclei per liter,  $N_{CCN}$  is the number concentration of CCN per liter,  $x$  is the fraction of CCN containing an ice nucleus and  $A$  is the surface area of a nucleus  $= \pi d_s^2$  where  $d_s$  is the diameter of the nucleus. Please note that we consider the ice nucleus to be spherical, although in practice one should consider the gas adsorption area which can be 5 to 20 times the spherical surface area [133]. Using Eq. 5.10, we estimate  $x$  to be about 5% assuming 1 ice particle per 250000 cloud droplets. In the wake of a wet hailstone we estimated a cloud droplet concentration of  $25 \times 10^6$  per liter. All the large nuclei (mean diameter of  $0.5$   $\mu\text{m}$ ) are already activated in the cloud, so the additionally nucleated droplets have a smaller mean diameter. Let us assume a mean diameter of  $0.2$   $\mu\text{m}$ . We assume that  $x$  is independent of the size of the nuclei. Using Eq. 5.10, we estimate the ice nuclei concentration to be about 5 per liter. This suggests that the ice nuclei concentration increases by a factor of 5 in the wake of a growing hailstone. Increasing the supersaturation in a liter of cloudy air amounts to a travel distance of approximately 50 m for a 4 mm (in diameter) graupel.

Moreover, the enhanced droplet number concentration in the wake may also enhance contact nucleation of ice crystals as the probability of a deposition nucleus acting as a contact nucleus increases with supersaturation due to the corresponding reduction in the critical radius of the ice embryos [134]. Additional analysis is required to estimate its significance.

The analysis presented so far suggest that in mixed-phase clouds graupel/hailstones undergoing wet growth may activate ice nuclei in their wake due to the enhanced supersaturation in the wake. In deep convective clouds, the hailstones in the wet growth regime shed a lot of melt water from its surface [126]. The shed water has a higher temperature than the ambient and hence may significantly increase the supersaturation in the wake, thus activating ice nuclei in its path. This might be important for a better understanding of the dynamics in deep convective systems. A simplistic analysis by [70] based on the low Reynolds number approximation showed an increased supersaturation in the wake of a growing graupel in the wet growth regime. Their estimates were quite different from the analysis presented here, chiefly due to their assumptions and approximations. They grossly underestimated the supersaturation attained in the wake and their estimated peak supersaturation in the wake was a function of the size of the graupel. The findings from the present analysis is consistent with the DNS calculations of a hailstone undergoing wet growth [52]. These calculations account for the difference in the thermal and mass diffusivities. Therefore, they attain higher supersaturation in the wake compared to what we obtain from the mixing parcel model. Moreover, they do not discuss the micro-physical aspects of the nuclei activation and droplet formation.

It is important to note that the estimates provided here are based on several assumptions. This is partly due to the lack of reliable data on the ice nucleating ability of the atmospheric aerosol. Despite these limitations, the estimates provided here suggest that growing hailstones in deep wet clouds plays an important role in nucleating secondary ice crystals in their wake.

#### **5.4.2 Cloud Engineering**

Several attempts were made in the past to modify the local weather conditions. A commonly used method is to seed the clouds with ice nuclei to initiate rainfall [49]. The level of success obtained from these methods are often questionable [48, 49]. The addition of ice nuclei activates ice phase in mixed phase clouds at relatively higher temperatures. This results in faster initiation of precipitation as the ice particles grow at a much faster rate than the supercooled droplet through diffusion. The observations from the experiments presented here may be applicable in weather modification. Conventional cloud seeding methods involve adding Silver Iodide (AgI) into a developing cloud, as AgI is an excellent ice nuclei [46]. We can improve the existing cloud seeding techniques

efficiency further by adding hot water into a developing cloud system along with the ice nuclei. Addition of hot water may significantly enhance the supersaturation in the cloud, thus activating a wide spectrum (size) of ice nuclei which may trigger intense precipitation. This method may aid in initiating rainfall in the catchment areas under appropriate conditions. Moreover, this may prevent the formation of deep convective systems that result in large hailstones which may be catastrophic in the regions with high population density or agriculture. The formation of precipitation sized hydrometeors initiate strong downdrafts which may suppress the updraft required for sustaining deep convective systems [17]. This may also suppress the formation of multi-cell systems that exists in deep convective clouds with horizontal wind shear.

Addition of hot water alongside ice nuclei may result in rapid growth of ice phase in a developing cloud system. But, this entire process results in adding additional buoyancy to an existing updraft in the cloud through latent heat release from glaciation and also from the hot water. The buoyancy contribution from the latter may not be significant. So the dynamics between the added buoyancy and the downdraft effect from the large hydrometeors may dictate the evolution of a seeded cloud system. This requires a careful parametric study of the system - experimentally and numerically, to quantify the effect of the proposed seeding method.

## 5.5 Conclusion

The experimental observations presented in this chapter showed that ice crystals and water droplets nucleate in the wake of a hot water drop falling in a moist chamber. A mixing parcel model coupled with a one-dimensional wake model was used for explaining these observations. This model was extended to atmospheric clouds in Earth's atmosphere. The analysis revealed that in deep convecting clouds, under appropriate conditions, the ice nuclei concentration increases by a factor of 5 in the wake of a growing hailstone through evaporative supersaturation. This mechanism may play an important role in explaining the anomaly between measured ice particle concentrations and measured ice nuclei concentrations in deep convective systems. Furthermore, these observations and discussions led to the formulation of a methodology for improving the efficiency of existing cloud seeding techniques. This method involves adding hot water into a developing cloud along with the ice nuclei. This may significantly enhance the number of activated ice nuclei and hence may result in the faster formation of precipitation. This may also suppress the formation of catastrophic deep convective systems. A systematic experimental/numerical investigation is required to develop a deeper understanding of this method.

# 6 Additional Observations: Drop Fragmentation, Leidenfrost Patterns and Boundary Layer Visualization

In this chapter we discuss some interesting observations obtained during the experiments discussed in Chapter 3 and Chapter 4. The results and the discussions presented here are preliminary in nature, and require further analysis to arrive at a conclusion.

## 6.1 Drop Fragmentation

Fragmentation of drops plays an important role in combustion (e.g. in a diesel engine). They also play an important role in determining the size distribution of rain drops from a cloud [135]. An interesting question related to drop fragmentation is - what is the largest diameter of a drop that can sustain free fall without undergoing fragmentation? The experiments conducted using water drops in a counter flowing jet (gas) claimed that drops were stable when Weber number  $We = \frac{\rho_a U^2 d}{\sigma} \leq 6$  where  $\rho_a$  is the density of the ambient gas,  $U$  is the free fall velocity scale and is represented as  $U = (\frac{\rho_l - \rho_a}{\rho_a} g d)^{1/2}$ ,  $d$  is the diameter of the drop,  $\sigma$  is surface tension,  $\rho_l$  is the density of the liquid drop [135, 136]. The Weber number represents the ratio between the pressure force and the surface tension force. Above the critical Weber number the surface tension cannot prevent the rupture of the drop. A schematic of the drop fragmentation process is shown in Fig. 6.1. First the drop deforms into a pancake like structure due to the pressure gradient across the drop. The shear imposed by the flow at the interface between the drop and the ambient results in the formation of a rim, which gets thicker due to the accumulation of mass from the center of the drop. The center of the drop becomes thin like a film that stretches and inflates like a bag due to the pressure gradient. This is called the bag instability [136]. The thin membrane ruptures and the rim fragments producing a broad spectrum of drops. This is called “bag break-up” [135]. The analysis by Villermaux

& Bossa (2009) showed that a water drop under free fall conditions was stable if its diameter  $d < 6$  mm [135].

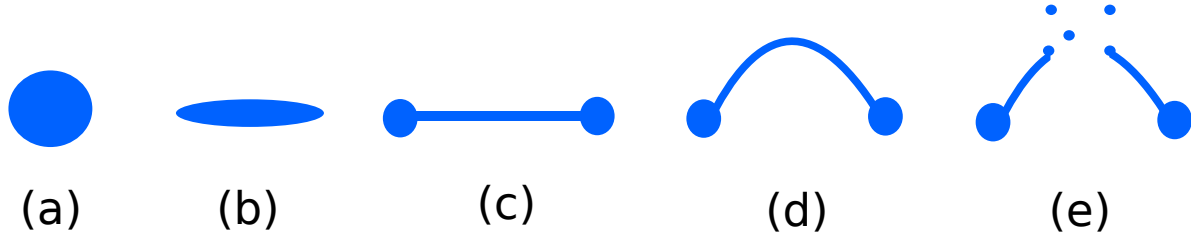


**Figure 6.1:** Schematic of a drop fragmentation. (a) Initial drop (b) pancake drop due to the pressure forces (c) rim formation (d) bag instability and (e) bag break-up.

Experiments in a wind tunnel [137] have shown that water drops as large as 7.5 mm were stable and do not fragment in contrast to the experiments reported by Villermaux and Bossa (2009) [135]. This leads to conflicting experimental observations. One possible explanation for these contradictions is that the velocity profile and the turbulence intensity in the ambient gas in both experiments were significantly different, and so the breakup at 6 mm was due to the limitation in the experimental setup [138]. Close to the center-line the mean streamwise velocity profile in a turbulent jet and a turbulent channel flow can be considered to be similar if the diameter of the drop was relatively small compared to the jet and channel width. Additional experiments are required to investigate the effects of turbulence intensity. Surface contamination of the drop may also explain the contrasting experimental observations [138]. The role of relative humidity was not accounted for in the drop fragmentation experiments.

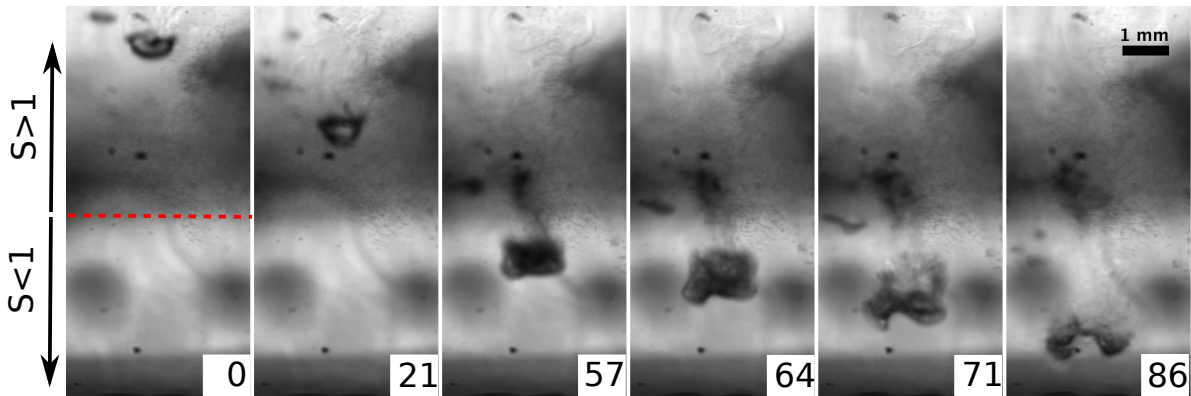


**Figure 6.2:** Image sequence of a  $\text{SF}_6$  drop fragmentation in a  $\text{SF}_6$ -He atmosphere.  $T_b = 45.00$  °C,  $T_t = 36.00$  °C,  $P = 44.9$  bar. The red dashed line separates the supersaturated region from the sub-saturated region. See main text for description. The time stamp (in ms) is indicated in the bottom right corner of the image.  $S$  is the saturation ratio.

Figure 4.5 shows a  $\text{SF}_6$  drop falling through a supersaturated  $\text{SF}_6$ -He atmosphere. The mean temperature in the convection cell was 42.00 °C. Let us assume that the falling drop was at the same temperature as the top plate (40.00 °C). So the Weber number

for this drop is  $We \approx 6$ . If we use the mean temperature as the drop temperature then the Weber number is  $We \approx 9$ . According to the arguments presented by Villermaux and Bossa (2009), these drops are unstable, contrary to our observations. Please note that these drops attain terminal velocity at a distance of 2-4 mm from the top plate and the drop traveled about 14-15 mm before falling into the liquid pool. Figure 6.2 shows a sequence of images showing a  $SF_6$  drop falling through a partially sub-saturated cell (see chapter 4 for details). The mean temperature in the cell was  $40.50^\circ C$  and is similar to the mean temperature in Fig. 4.5. The drop Weber number is  $We \approx 3.5$  at the top plate temperature, and  $We \approx 6.5$  at the mean temperature. In this experiment the falling drop fragmented before touching the bottom plate. Please note that the  $We$  in this experiment was lower than the experiment shown in Fig. 4.5. Figure 6.3 depicts a drop falling through a supersaturated atmosphere at conditions similar to Fig. 6.2. The drop appears to be stable till it falls into the liquid pool. The liquid-vapor interface is about 1 mm above the bottom plate and the gas layer was supersaturated with  $SF_6$  vapor.

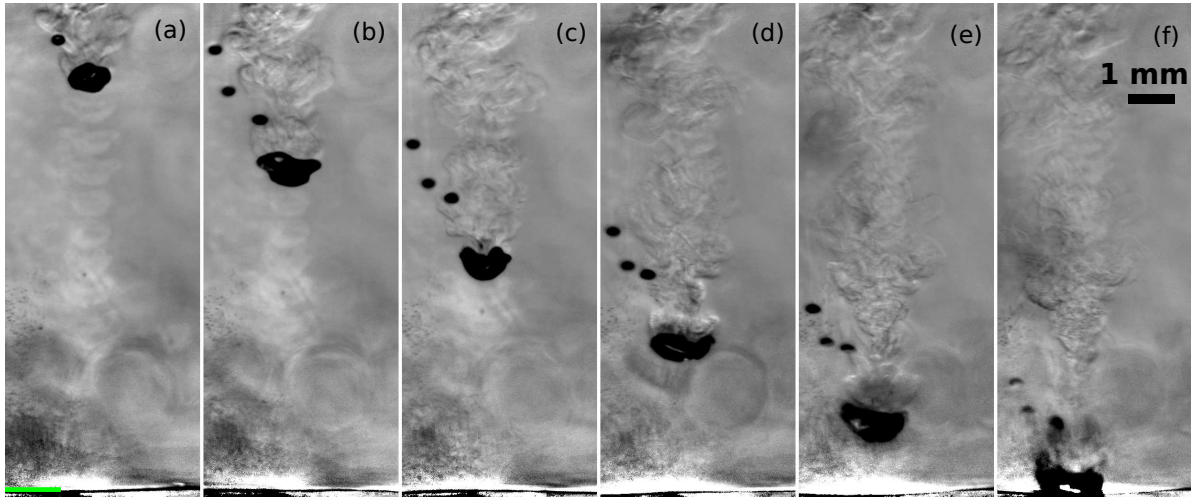


**Figure 6.3:** Image sequence of a  $SF_6$  drop in a supersaturated  $SF_6$ -He atmosphere.  $T_b = 44.00^\circ C$ ,  $T_t = 36.00^\circ C$ ,  $P = 44.3$  bar. The green line marks the position of the liquid-vapor interface. The time difference between each frame is about 22 ms.

In Fig. 6.2 the falling drop fragments before reaching the bottom plate. The fragmentation occurred after the drop entered the sub-saturated region. Please note that this is the case for all the other drops under these conditions. Let us attempt to describe the role of humidity. The schematic in Fig. 6.1 shows that a thin membrane is formed at the center of the drop before the fragmentation of the drop occurs [135]. This membrane is formed due to the transport of liquid from the drop core towards the rim [135]. If the ambient was supersaturated w.r.t the drop temperature then we have condensation occurring on the surface of the drop. This may add additional mass to the core of the drop which may counteract the thinning of the membrane, thus suppressing the

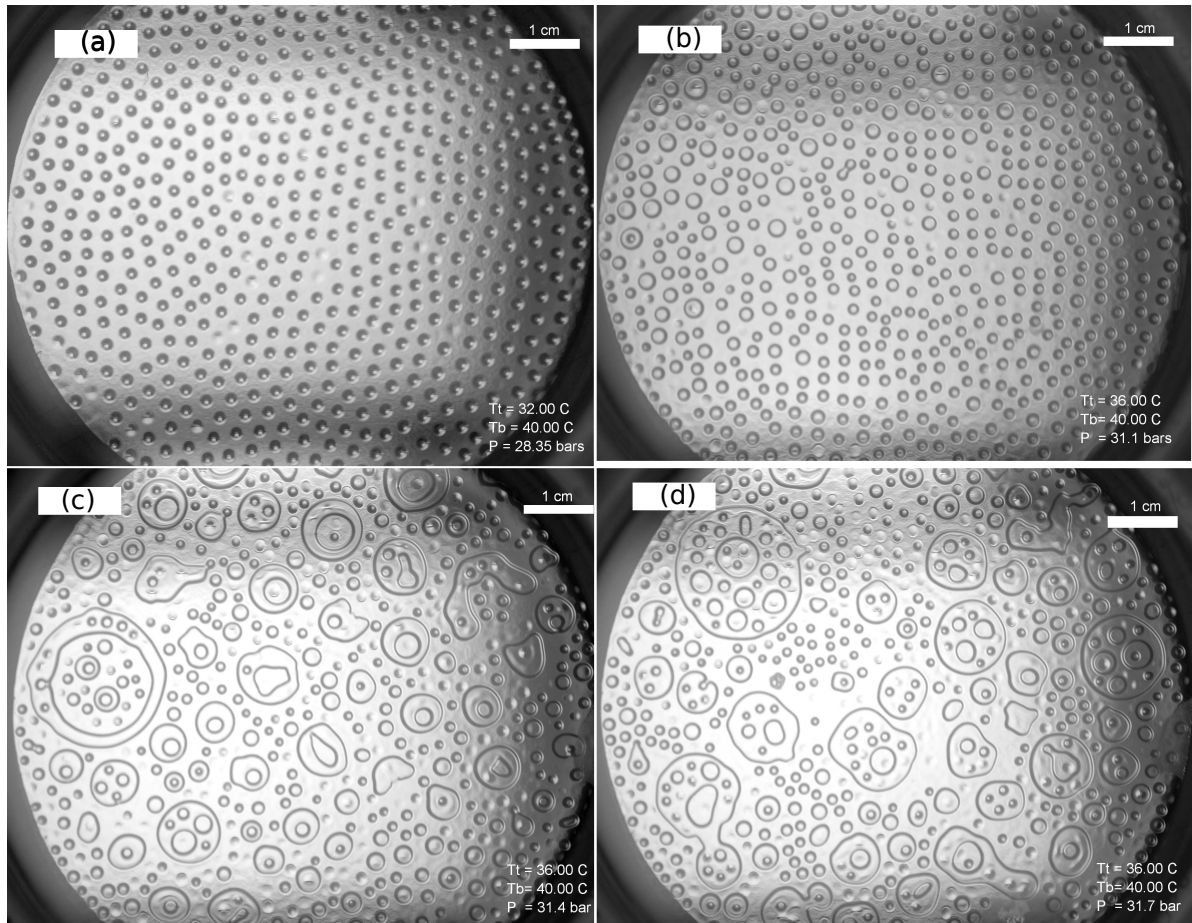
bag instability and the fragmentation. The additional mass accumulation increases the diameter of the drop, which in turn increases the Weber number of the drop. This may eventually lead to the fragmentation of the drop but at a higher Weber number. If the ambient was sub-saturated then evaporation may aid in further reducing the thickness of the core, thus favoring the fragmentation of the drop. This suggests that an equivalent evaporation-condensation number plays an important role in the fragmentation of a drop close to the critical Weber number. This has implications for the stability of a rain drop in a supersaturated or nearly saturated environment like in a deep convective cloud. This could explain the presence of super-large raindrops (8-10 mm in diameter) in some clouds [139].

The parameters involved in our experiments are sensitive to temperature and pressure. Moreover, the presence of Helium makes it difficult to estimate the material properties accurately. Despite these limitations the observations here suggest that humidity plays an important role in the fragmentation of a drop. Additional experiments and analysis are required to quantify these observations.

## 6.2 Leidenfrost Drops

The Leidenfrost effect has important implications in heat transfer from a surface [93]. It significantly reduces heat transfer between a hot plate and a liquid due to the presence of an insulating vapor layer. We stated that the Leidenfrost effect may aid in stabilizing large drops on the top plate (see chapter 3). We studied the effect of pressure on the top plate instability in the medium cell (see Fig. 3.36). As was shown earlier the number of drops on the top plate increases with increasing pressure until they start to drip and form a puddle on the bottom plate.

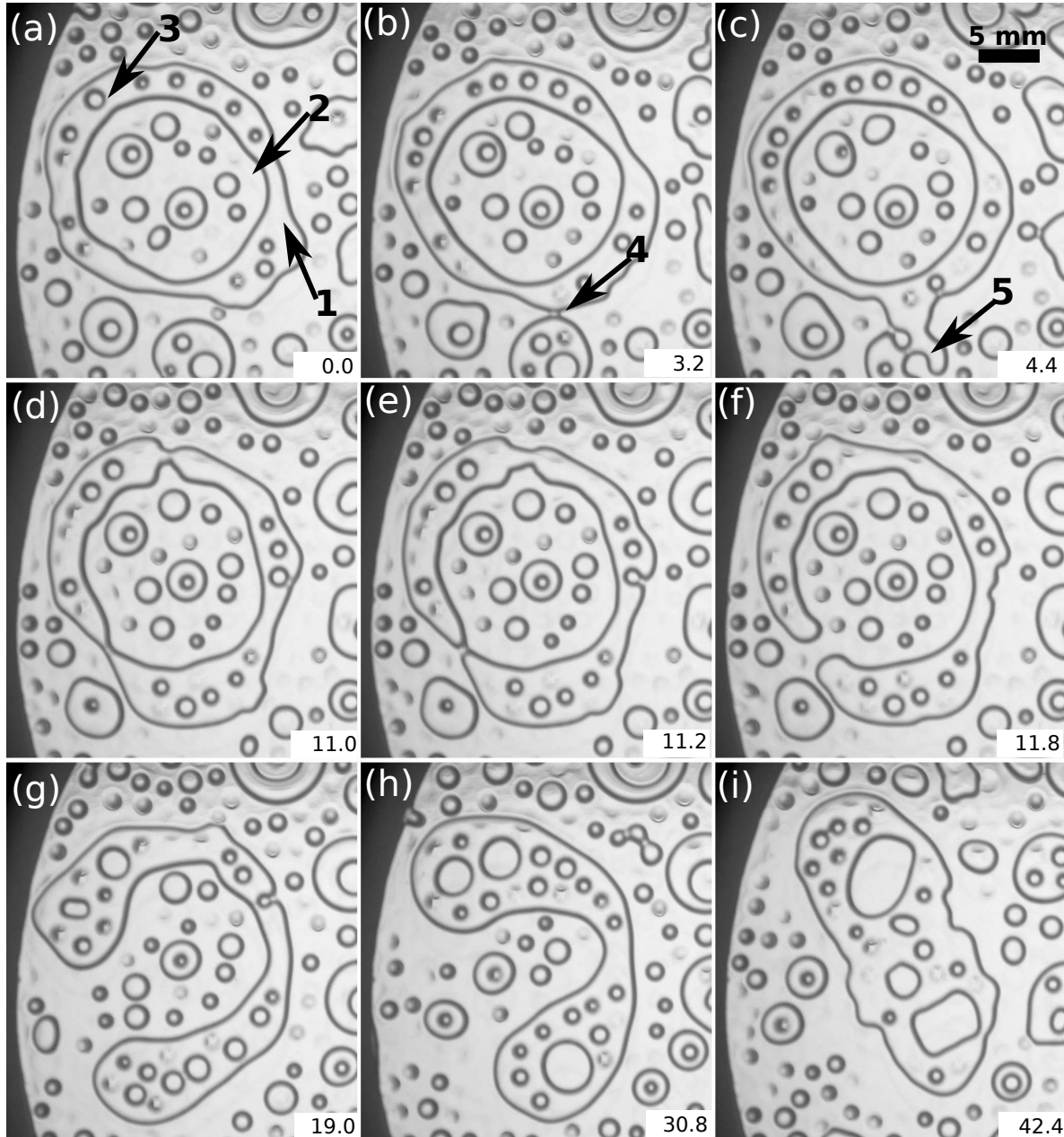
Let us investigate the effect of vapor pressure on the patterns underneath the top plate in the thin cell (cell height  $\approx 0.5$  mm). Figure 6.4 shows the effect of pressure on the drops on the top plate. We observe that the drops get bigger as the vapor pressure in the cell was increased (Fig. 6.4(b)). These big drops are formed by merging of the smaller drops. The increased vapor pressure enhances the supersaturation in the cell. The evaporative effects are confined to the region close to the bottom plate. Please note that the bottom plate is dry and is not covered in a layer of liquid  $\text{SF}_6$  at these conditions. Further increase in pressure increases the lateral diameter of the drops and they start forming holes or chimney like structures inside them (Fig. 6.4(c, d)). A chimney is defined as a vapor region surrounded by liquid. In these experiments we have optical access only from the top and so we do not have any information on the vertical structure of these drops. In particular, it is unclear if these drops are in contact with the top plate. These drops were not in contact with the bottom plate as they were not boiling. The drop like structures occur in a variety of shapes and sizes, and exhibit



**Figure 6.4:** Thin cell - effect of pressure on the drops on the top plate. (a)  $T_b = 40.00$  °C,  $\Delta T = 8.00$  °C,  $P = 28.4$  bar (b)  $T_b = 40.00$  °C,  $\Delta T = 4.00$  °C,  $P = 31.1$  bar (c)  $T_b = 40.00$  °C,  $\Delta T = 4.00$  °C,  $P = 31.4$  bar (d)  $T_b = 40.00$  °C,  $\Delta T = 4.00$  °C,  $P = 31.7$  bar.

interesting dynamics.

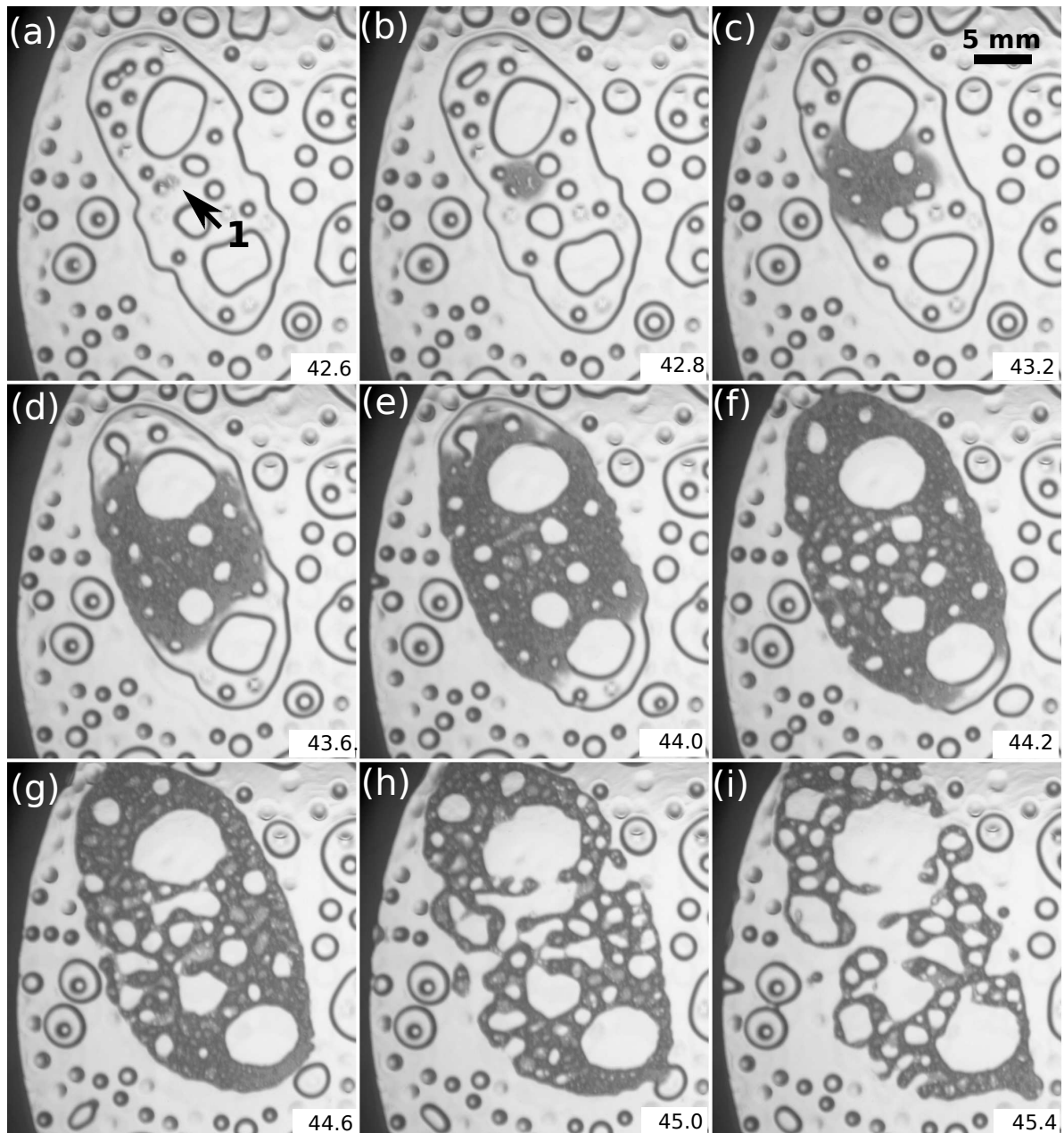
Figure (6.5- 6.7) shows the dynamics of the drops in the experiment shown in Fig. 6.4 (c). In Fig. 6.5 (a), we see a ring-like liquid patch/drop (marked in the figure) levitated above the bottom plate. This drop/patch has several small holes or chimneys in it and also a big chimney in the centre. From these images it is not easy to determine if these chimneys are occupied with vapor only or if there is a liquid layer/film on the top. The big chimney has several smaller drops in it and a few of these drops have a chimney in them. The number of chimneys in a drop is a function of the lateral extent of the drop. A chimney is formed only above a critical size. In Fig. 6.5 (b), we see the merging of the ring shaped drop with another drop. The liquid bridge between these two drops is visible in Fig. 6.5 (b). In Fig. 6.5 (c) we see that the large ring-like drop is reorienting after the merger, and some of the chimneys (bottom center of the image) are exiting the drop. We also see the formation of new drops on the top pate in the big chimney at the center (Fig. 6.5 (b, c)). The sequence from Fig. 6.5 (d) to Fig. 6.5 (i) shows the exiting of the big chimney from the ring-like drop. The narrowing of the ring drop is



**Figure 6.5:** Dynamics of drops in the Leidenfrost regime. (1) ring drop, (2) big chimney, (3) a small chimney, (4) liquid bridge before the merging of two drops and (5) exit of a chimney. The time stamp (in seconds) is indicated in the bottom right corner of the image.

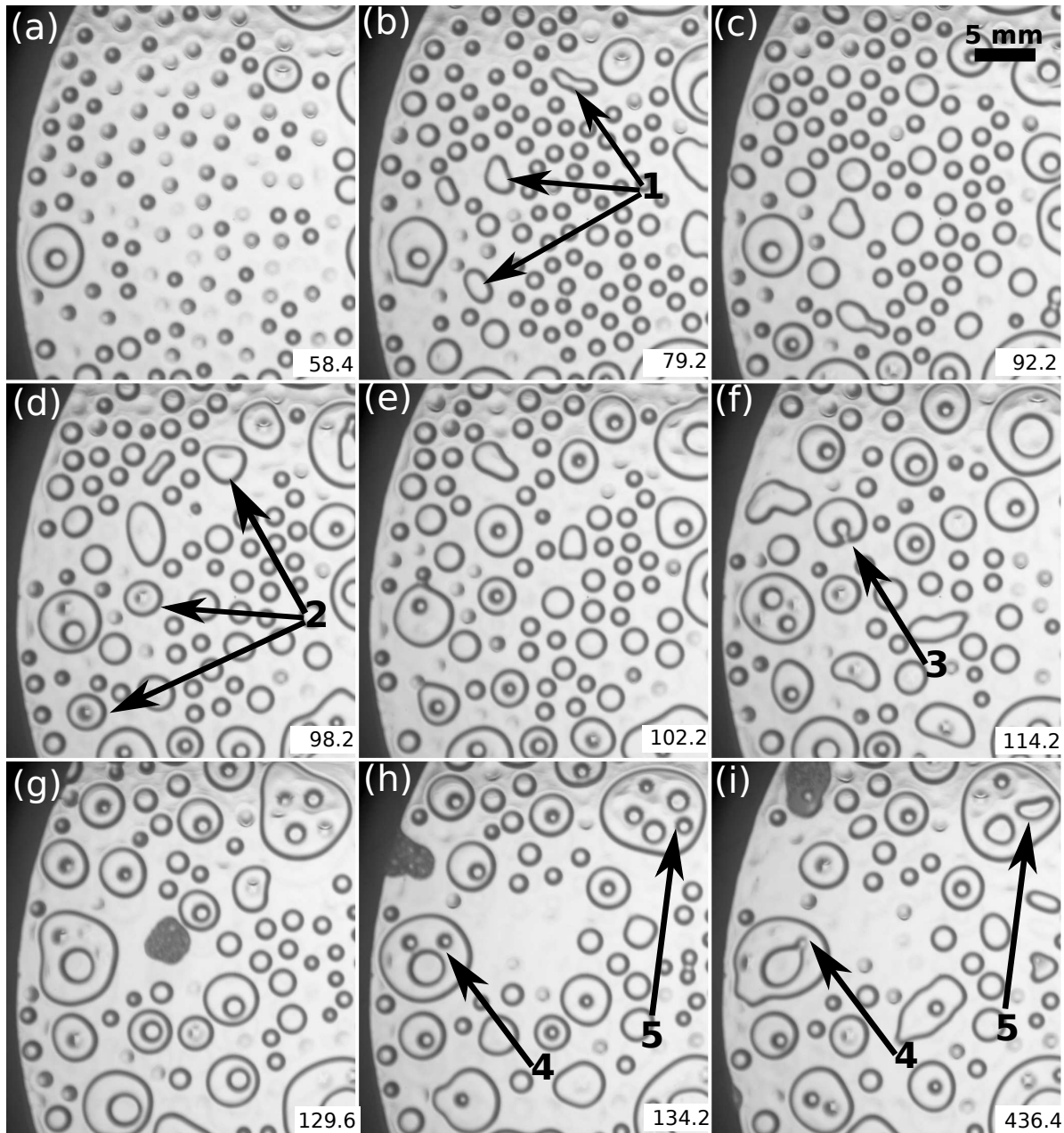
seen in the lower left quarter of Fig. 6.5 (d). The liquid bridge breaks in Fig. 6.5 (e) and we see the reorganization of the ring drop in Fig. 6.5 (f-i). In this process, the drops in the big chimney were pushed out. Some of these drops merge with the large ring like drop. The number of chimneys in the ring drop have decreased post the exit of the big chimney due to merging of some of the chimneys. As a consequence the diameter of the chimneys have increased (Fig. 6.5 (h, i)).

Fig. 6.6 is a continuation of the sequence presented in Fig. 6.5. In Fig. 6.6 (a) we



**Figure 6.6:** Boiling of a drop. (1) Location where boiling started. The time stamp (in seconds) is indicated in the bottom right corner of the image. The time stamp represents the number of seconds from Fig 6.5(a).

see that the drop starts to boil after it comes in contact with the bottom plate. The location where boiling was initiated is marked in Fig. 6.6 (a). Over time the entire liquid drop starts to boil. The spreading of the boiling region is shown in the image sequence in Fig. 6.6. The structure of the relatively large chimneys were preserved until the boiling of the liquid drop was completed. Note that boiling only occurs in a specific drop, while surrounding drops are not affected. It is not clear why the drop touched the bottom plate as it was floating on its vapor for several seconds. One possibility is that



**Figure 6.7:** Formation of large drops with chimney. See text for details. 1) Merged drops exhibiting capillary oscillations. 2) Formation of chimney in a few sufficiently large drops. 3) Exit of chimney from a drop. 4) Merging of small chimney with a large chimney. 5) Merging of two chimneys of similar dimensions. The time stamp represents the number of seconds from Fig 6.5(a).

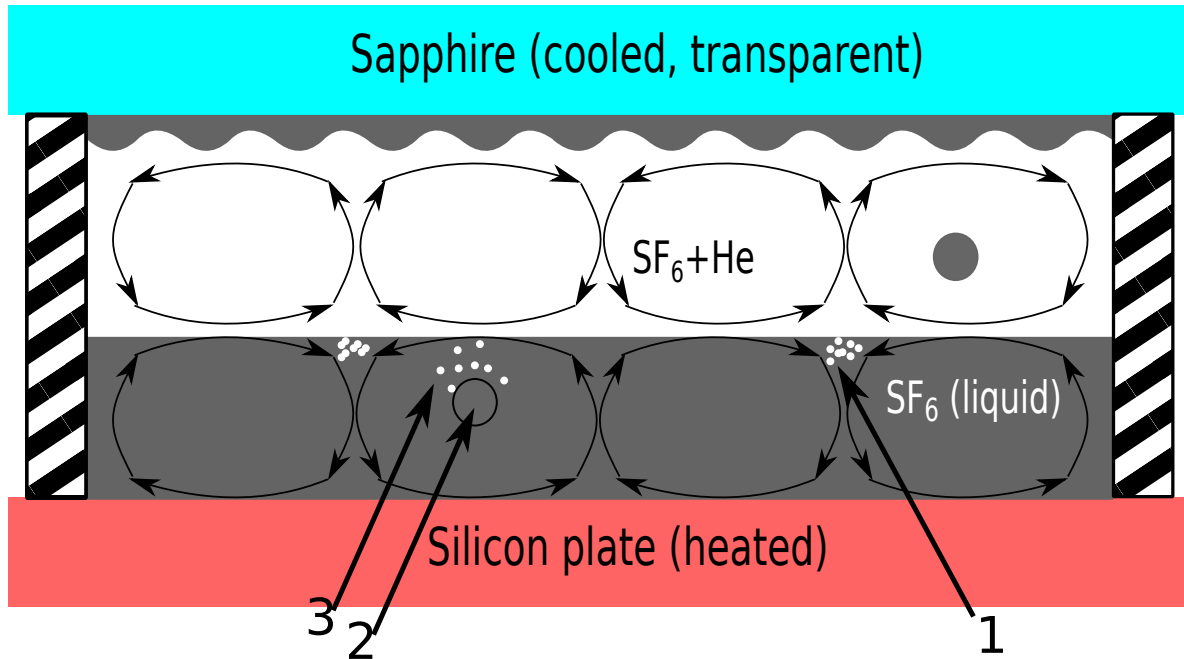
locally the temperature of the bottom plate dropped below the Leidenfrost temperature. If the temperature of the bottom plate locally falls below the Leidenfrost temperature then the vapor pressure generated would not be large enough for sustaining the weight of the drop. As a consequence the drop touched the bottom plate and started boiling immediately due to the enhanced heat transport.

Fig. 6.7 is a continuation of the sequence presented in Fig. 6.5 and Fig. 6.6. The boiling of a large mass of liquid resulted in a very high supersaturation locally. The

vapor condenses on the top plate and undergoes RTI as shown in Fig. 6.7 (a). These drops grow over time through vapor condensation and also by merging with other drops. Some of the merged drops are shown in Fig. 6.7 (b). They exhibit capillary oscillations after the merger event (see section 3.5 for details). Over time the diameter of these drops increases further by merging with other drops in their neighbourhood (Fig. 6.7 (c, d)). Above a critical diameter the drops start to form a chimney as shown in Fig. 6.7(d). As the diameter increases further, multiple chimneys appear in the drop. One such drop is shown in Fig. 6.7 (d). The diameter of these chimneys increases over time. As they expand, they also migrate towards the edge of the drop and eventually exit from the drop. This was shown and discussed in the context of Fig. 6.5. The process of formation of chimneys and exiting from the drop occurs repeatedly until the drop touches the bottom plate. These chimneys also grow by merging with other chimneys in their neighbourhood. Fig. 6.7 (h, i) depicts the merging of a large chimney with a smaller chimney. The drops of various sizes merge together over time and result in large drops with several chimneys, like the drops shown in Fig. 6.5 and Fig. 6.6. As was shown in Fig. 6.4, the size of these merged drops increases with the vapor pressure in the cell. It appears that above a critical size the drop comes in contact with the bottom plate and starts to boil. The maximum size a drop can attain in this experiment is a function of the vapor pressure.

Chimneys have been observed in Leidenfrost drops in the past [93]. The formation of chimneys is attributed to an instability of the vapor cavity below the drop, similar to a RTI [93, 140]. They state that the instability occurs in drops larger than the capillary length of the liquid. The instability results in the formation of a dome like structure in the center with a layer of liquid on the top. Over time this dome bursts resulting in the formation of a liquid torus that however closes again [93, 140]. If the lateral extent of the drop is greater than the capillary length then the gravitational force dominates over the capillary forces. If the drop gets significantly larger than the capillary length then multiple chimneys may form in the drop with a fixed mean distance between these chimneys [93]. The dynamics described above is similar to the dynamics observed in our experiment. Additional analysis is required to characterize the system in order to make a quantitative comparison. The observations reported in this section are qualitatively consistent with the available observations in the literature. Not many experiments report the formation of multiple chimneys and the interaction between these chimneys. Most of the experiments have been conducted using water. We use  $\text{SF}_6$ , and have the advantage of attaining several chimneys in a single drop due to very low surface tension (compared to liquid water). This would aid in studying the interaction between the chimneys. Additional experiments are required to study their behaviour.

### 6.3 Boundary Layer Visualization



**Figure 6.8:** Schematic representation of SF<sub>6</sub>-He boundary layer visualization. 1. accumulated Helium bubbles, 2. a drop from the top plate, 3. nucleated Helium bubbles.

In this section we report a new technique for visualizing the plume emitting zones in the diffusive wall layer in an RBC experiment. The experiments were conducted in the thick cell with SF<sub>6</sub>-He binary mixture as the working fluid. The conditions were set such that the lower half of the cell was filled with liquid SF<sub>6</sub>. Helium is partially soluble in liquid SF<sub>6</sub>. It was observed that the solubility of Helium in liquid SF<sub>6</sub> decreased with the increasing temperature. If the imposed temperature gradient was large enough then the liquid SF<sub>6</sub> starts to nucleate Helium bubbles close to the bottom plate. Moreover, the cold drop from the top plate falling into the liquid SF<sub>6</sub> introduces additional Helium into the liquid pool due to the difference in solubility. Some Helium from the gas layer may also get entrained as the drop hits the liquid pool. As the cold drop falls into the liquid pool a cloud of Helium bubbles is generated in the neighbourhood. A schematic of the flow field in the cell is shown in Fig. 6.8. The nucleated Helium bubbles survive for a longer period of time as the mean temperature in the experiment approaches the critical temperature of SF<sub>6</sub>. Moreover, the size of these bubbles decreases as the critical temperature was approached. The density of these bubbles are significantly lower than that of the liquid SF<sub>6</sub>. As a consequence, these bubbles move towards the low pressure zones in the flow field [141]. In a RBC system, the plume ejecting regions are the low pressure zones and the plume impacting regions are the high pressure zones (from the streamlines in the plane of the large scale circulation [142]). The Helium bubbles were

released in the top layer of the liquid pool. As a consequence, the Helium bubbles align along the plumes ejecting in the liquid pool from the liquid-gas interface boundary layer in the liquid.

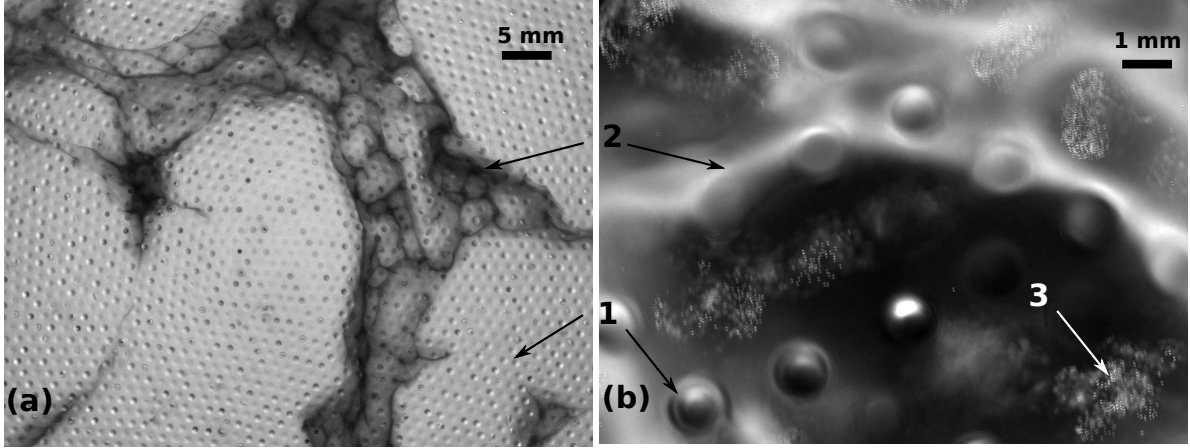


**Figure 6.9:** Boundary layer visualization: (a)  $T_t = 44.50$  °C,  $T_b = 44.95$  °C,  $P = 53.9$ bars,  $\psi_{He} \approx 32\%$ . Image courtesy Dr. Winkel. [78] (b)  $T_t = 43.00$  °C,  $T_b = 45.00$  °C,  $P = 49.2$ bars,  $\psi_{He} \approx 25\%$ . (1) Top plate instability, (2) accumulated Helium bubbles, (3) nucleated SF<sub>6</sub> droplets due to isobaric cooling from the cold drop.

A top view of the convection cell is shown in Fig. 6.9. This experimental observation is discussed in detail in Winkel (2015) [78]. Figure 6.9 (a) was obtained from the experiments reported in Winkel (2015) [78] and Fig. 6.9 (b) was generated as part of the present work. Winkel (2015) argued that these patterns were formed by nucleated SF<sub>6</sub> droplets suspended in the SF<sub>6</sub>-He gas layer, close to the liquid-gas interface. They did not have lateral visual access into the flow field [78]. The addition of sidewall mirrors showed that these dark bands in Fig. 6.9 (a) and white bands in Fig. 6.9 (b) are due to the formation of Helium bubbles in the liquid pool, and not due to the nucleation of SF<sub>6</sub> micro-droplets in the gas layer. The image sequence shown in Fig. 6.10 and Fig. 6.11 captures the dynamics associated with a cold drop falling into the liquid pool. Figure 6.10 shows simultaneously the side and the top view of this process. The portion of the image above the red line represents the side view and the portion below the red line depicts the top view. Figure 6.10 (a-c) shows two cold drops from the top plate falling into the liquid pool. Right after the impact we see two white spots in the top view (Fig. 6.10(c)). These white spots represents a cloud of Helium bubbles in the liquid pool. In the side view, the bubble cloud appears as a dark streak close to the liquid-vapor interface. This cloud slowly drifts along with the flow and in Fig. 6.10 (g-i) the collection of bubbles begin to disperse and disappear. Figure 6.11 shows a similar sequence depicting the side view of a cold drop falling into the liquid pool at a slightly lower concentration of Helium. The dispersion of the bubbles is captured in Fig. 6.11 (e-f). The temperature in the liquid pool was not high enough for the bubbles to survive

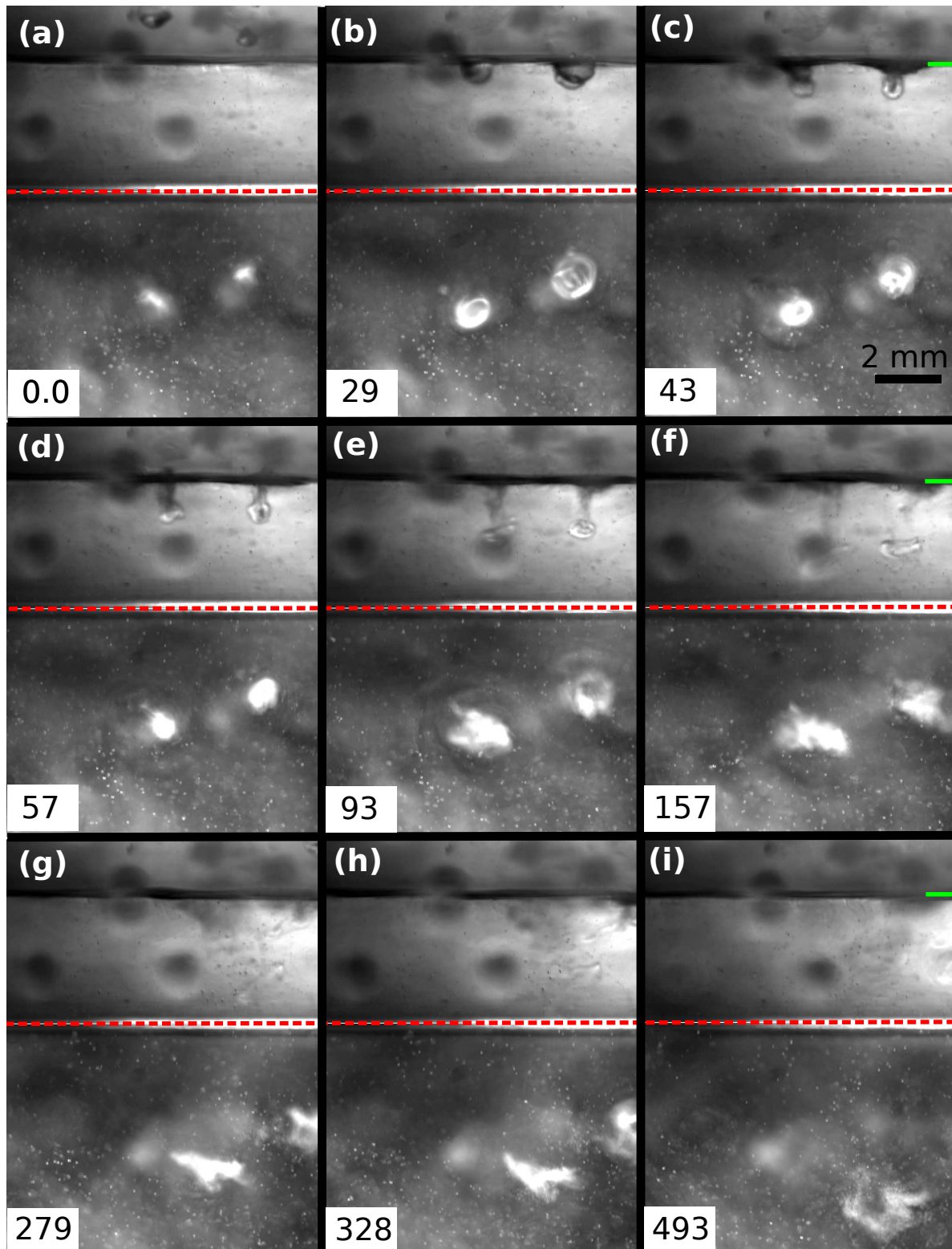


**Figure 6.10:**  $T_t = 40.00$  °C,  $T_b = 44.00$  °C,  $P = 48.3bars$ ,  $\psi_{He} \approx 28\%$ . Side view: portion of the image above the red line, top view: portion of the image below the red line. The time stamps (in ms) are indicated on the bottom left corner. The green line on the right side indicates the position of the liquid-vapor interface in the side view.

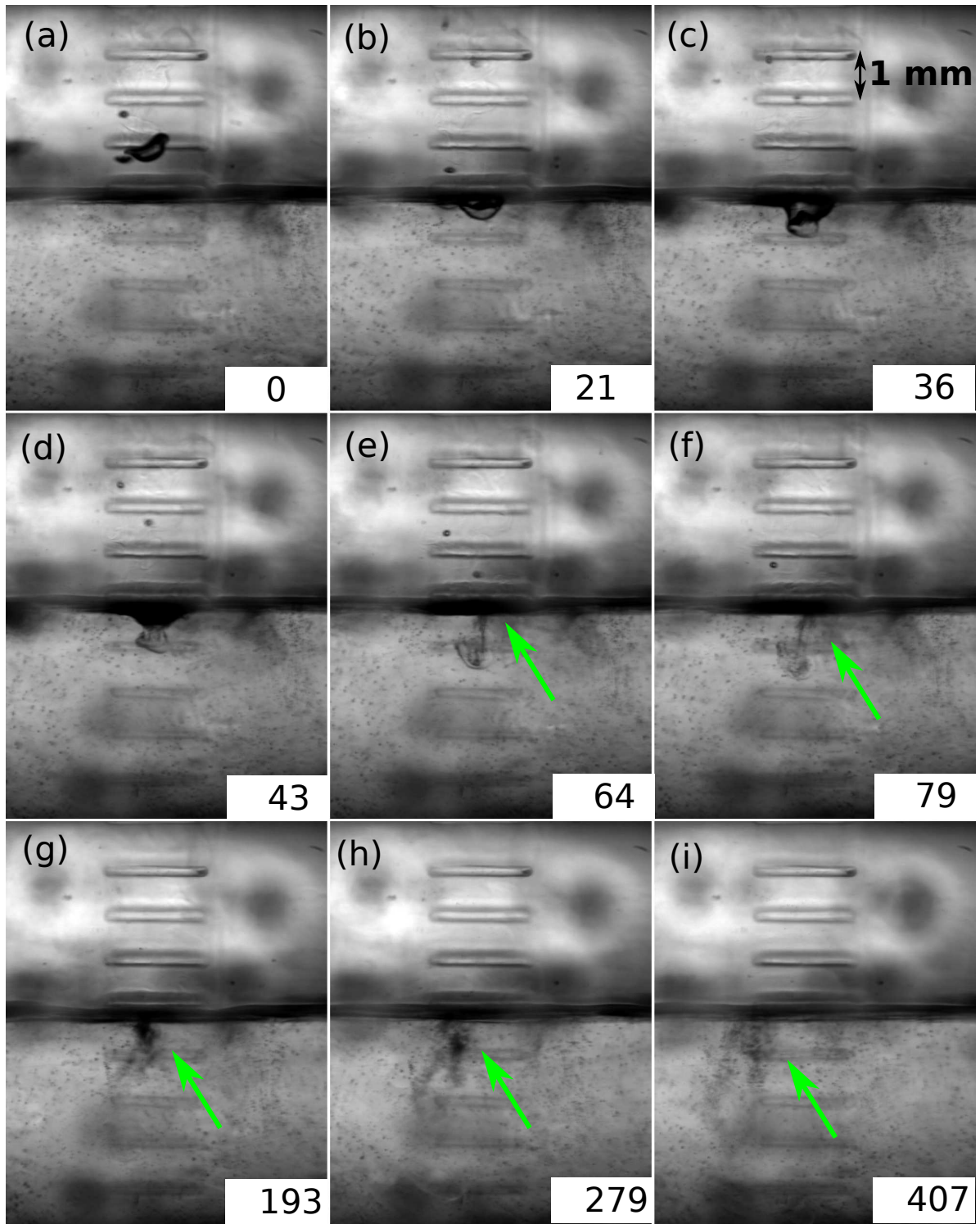


**Figure 6.11:** Side view.  $T_t = 40.00$  °C,  $T_b = 44.00$  °C,  $P = 47.0bars$ ,  $\psi_{He} \approx 26\%$ . The arrows mark the Helium bubbles formed from the cold drop. The time stamps (in ms) are indicated on the bottom right corner.

for a longer duration.

Figure 6.12 depicts Helium bubbles in the liquid pool at a temperature where the bubbles survived for a longer duration. Figure 6.12 (a,b) shows three cold drops falling

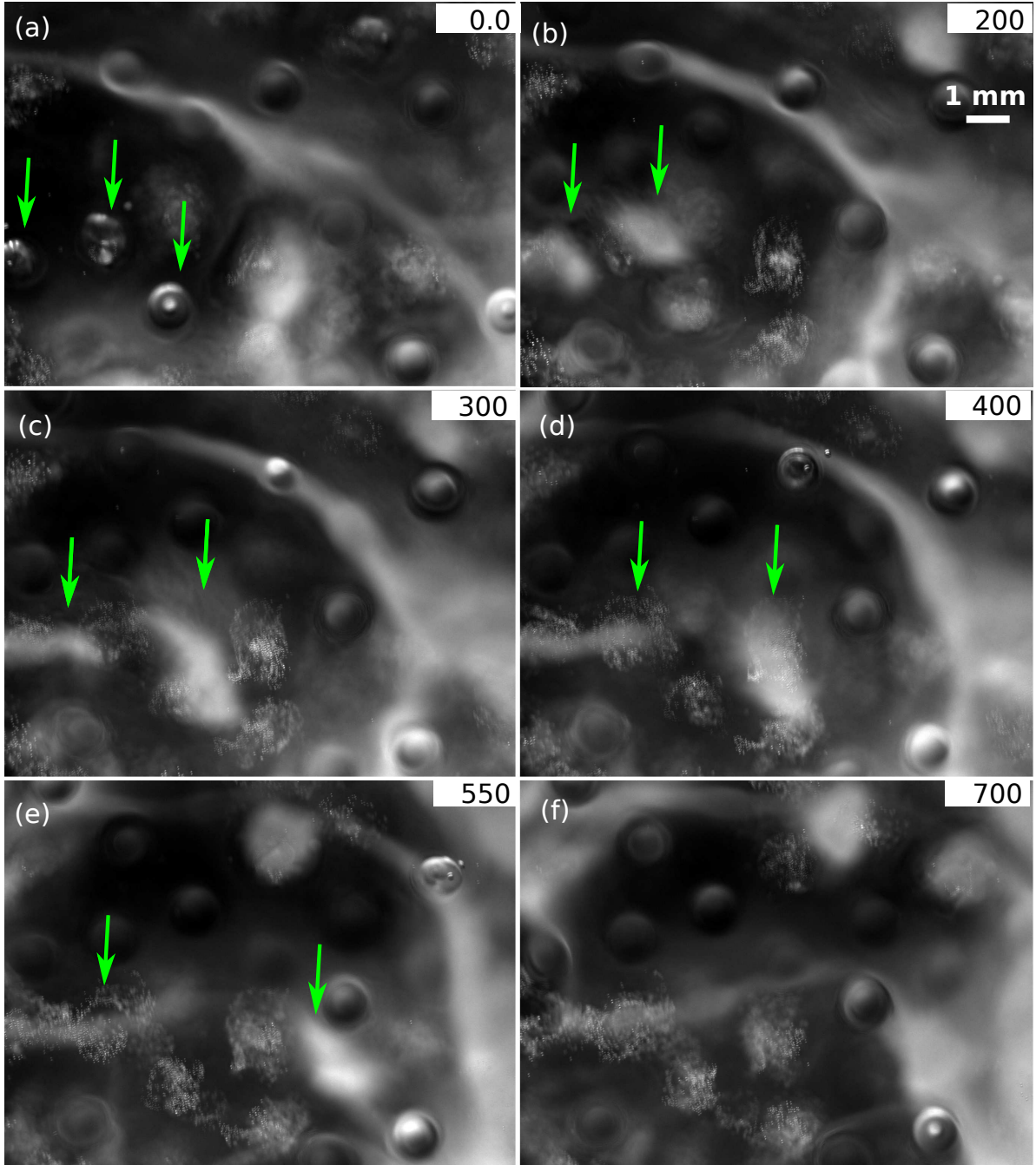


**Figure 6.12:**  $T_t = 43.00$  °C,  $T_b = 45.00$  °C,  $P = 49.2bars$ ,  $\psi_{He} \approx 25\%$ . The arrows mark the falling drops and the Helium bubbles formed from these drops. The time stamps (in ms) are indicated on the top right corner.

into the liquid pool and forming Helium bubbles in the liquid pool. In Fig. 6.12 (c,d) these bubbles start drifting along with the local velocity field and in Fig. 6.12(e,f) the bubbles appear to be aligned along a curve similar to the line plumes in RBC [92, 143].

The structure of the patterns shown in Fig. 6.9 resembles the thermal structure of the boundary layer observed in DNS calculations [92, 143]. Using the properties of pure SF<sub>6</sub> the  $Ra$  in the liquid pool was estimated to be between  $10^8 - 10^9$  and is

comparable to the  $Ra$  in the numerical simulations. Similar plume structure was also visualized experimentally using a high Schmidt number brine solution [144]. In the present experiment, the Helium bubbles are used for visualizing the plumes. It was essential that the bubbles survived for longer duration in the liquid pool. This was possible only if the temperature in the liquid pool was close to the critical temperature of  $SF_6$ . If the temperature was not high enough then the bubbles do not survive long enough to align along the cold plumes ejecting from the liquid vapor interface in the liquid pool. Additional experiments and analysis are required to understand the details of the plume structure observed here.



# 7 Summary and Outlook

## 7.1 Summary

In this work we investigated a variety of problems related to moist convection.

In the first problem, we studied the influence of phase change on the RTI of a thin film on the top plate of an RBC experiment using  $\text{SF}_6$  as the working fluid. We observed two distinct regimes. In regime 1, the bottom plate was covered with a layer of liquid  $\text{SF}_6$ . We showed experimentally that under appropriate conditions, a continuous condensation of  $\text{SF}_6$  on the cold top plate results in a hexagonal arrangement of drops in the thin film. The critical parameter was the rate of condensation of  $\text{SF}_6$  vapor at the top plate. The condensation rate was regulated experimentally by controlling the temperature difference across the convection cell. The drops on the top plate dripped periodically into the liquid pool at the bottom plate. In regime 2, the liquid layer at the bottom plate was eliminated. In the absence of a liquid layer at the bottom plate, the evaporative effects in the vapor layer played an important role in determining the dynamics of the liquid layer at the top plate. The dripping from the thin film was suppressed by enhancing the strength of the evaporative effects in the vapor layer. The evaporative effects were altered by regulating the vapor pressure and temperature difference across the convection cell. The experimental observations were in agreement with the theoretical model proposed by Besterhorn and Merkt (2006) [43] and we demonstrate experimentally the predicted stable (nearly no dripping) hexagonal surface patterns in the liquid layer at the cold top plate. These regular hexagonal patterns were observed when the thermal driving in the vapor layer was weak. As the  $Ra$  number in the vapor layer was increased, the pattern arrangement was influenced by the convection rolls in the vapor phase. In the high  $Ra$  experiments, the drops were clustered in the minimum shear stress zones in the liquid layer.

In the second problem, we establish a laboratory scale cloud model to understand the nucleation processes associated with cloud formation. We used a binary mixture of  $\text{SF}_6$  and He to mimic the moist and dry components in the Earth's atmosphere. The conditions were adjusted such that  $\text{SF}_6$  exists in both liquid and vapor phase like water in the Earth's atmosphere. The bottom plate was covered with a layer of liquid  $\text{SF}_6$ .

Close to the critical point of  $\text{SF}_6$ , we observed the nucleation of  $\text{SF}_6$  micro-droplets in the wake of large cold drops falling through supersaturated  $\text{SF}_6$  environment. Our calculations showed that the droplets were nucleated homogeneously due to the isobaric cooling induced in the wake of the cold drop. The activated droplets grew over time and fell into the liquid layer at the bottom plate. We extended this model to deep convective clouds in the Earth's atmosphere. Our model predicted that secondary nucleation of cloud droplets was possible in the wake of a large cold drop (about 4 mm in diameter) and hailstones/graupel. The supersaturation obtained in the wake of a hailstone/graupel ( $\approx 10\%$ ) was significantly higher compared to large rain drops ( $\approx 1.5\%$ ). We also showed that the supersaturation in the convection cell can be regulated by eliminating the liquid layer at the bottom plate. This resulted in a partially supersaturated and partially sub-saturated cell. In the supersaturated volume, the droplets activated and grew over time. And in the sub-saturated volume, these droplets evaporated and disappeared over time. These differential dynamics in the upper and lower part of the cell resulted in the formation of a layer of nucleated  $\text{SF}_6$  micro-droplets in the interface between the supersaturated and sub-saturated volumes, thus establishing a cloud layer in a moist convection cell. These dynamics of the droplets in the variable supersaturation RBC cell is similar to the cloud droplet dynamics in the Earth's atmosphere where the cloudy air is supersaturated, and the ambient dry air is sub-saturated. Figure 7.1 presents a visual comparison between a laboratory-scale cloud layer and a shallow cumulus cloud layer in the Earth's atmosphere. In both cases, we have a well-defined cloud base, separating the supersaturated and sub-saturated regions in the atmosphere. This cloud model can be used for studying the interactions between moist and dry air in atmospheric clouds.

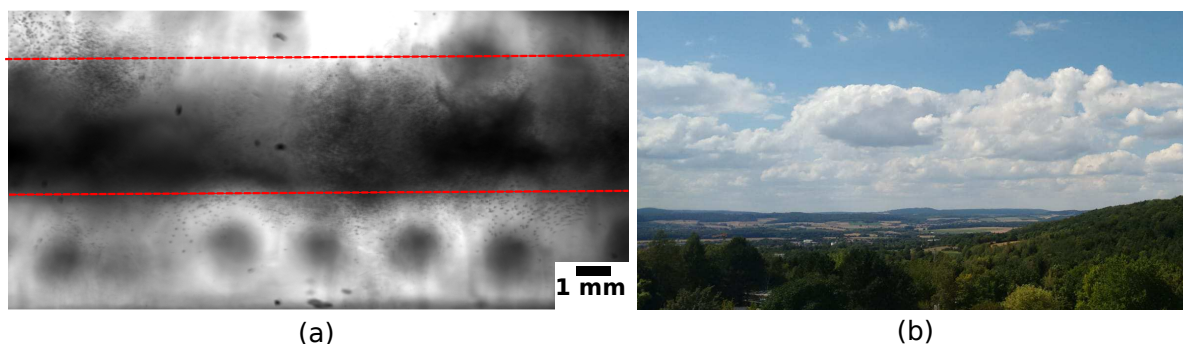


**Figure 7.1:** (a) Laboratory-scale cloud layer (between the red lines). (b) Clouds in Goettingen.

In the third problem, we investigated the possibility of secondary ice nucleation mechanisms in the wake of a growing graupel/hailstone in a deep convective cloud. These experiments were motivated from the observations reported in the  $\text{SF}_6$ -He experiment discussed earlier. The experiments were conducted in a turbulent cloud chamber using a mixture of water vapor and air as the working fluid. A growing hailstone was replaced

with a hot drop. We observed that water droplets and ice crystals were nucleated in the wake of a hot drop falling through a nearly saturated atmosphere. A simple mixing parcel model was used for calculating the supersaturation in the wake. The supersaturation field was coupled with a one dimensional wake model to compute the growth of a droplet from a nucleus. This model was extended to the cloud conditions in the Earth's atmosphere. Our estimates based on the available field measurements suggest that at a temperature of  $-15^{\circ}\text{C}$ , the activated ice nuclei concentration may increase from about 1 per liter to 5 per liter in the wake of a growing hailstone/graupel. This may partly aid in understanding the enhanced ice particle concentrations observed in convective clouds. We also propose a new technique for cloud engineering. The traditional techniques for cloud engineering involves introducing ice nuclei into a developing cumulus/cumulonimbus clouds. Our proposal is to spray hot water along with the ice nuclei for the rapid activation and growth of ice crystals to produce precipitation sized hydrometeors. This may generate sufficient downdraft to suppress the formation of deep convective systems. Additional experiments and numerical modeling are required to study the influence of this proposed technique on weather modification.

Apart from these problems, we also investigated three additional problems. First, we showed experimentally that humidity may play an important role in determining the critical Weber number for the fragmentation of a freely falling drop. We claim that if the ambient gas is supersaturated, then the critical Weber number for fragmentation of a drop increases and if the ambient gas is sub-saturated, then the critical Weber number decreases. A new set of experiments under controlled humidity conditions are required to test this claim. Second, we investigated the formation of chimneys in a Leidenfrost drop. We observed that the number of chimneys in a given drop are proportional to the size of the drop. These chimneys grow in size by merging with other chimneys. Further analysis is required to understand the dynamics of these chimneys. Third, we visualized the thermal boundary layer in a high Rayleigh number Non-Boussenesq RBC. This was done using Helium bubbles generated from the falling of a cold drop from the top plate. Close to the critical temperature of  $\text{SF}_6$ , the Helium bubbles survive for a longer duration in the liquid  $\text{SF}_6$  pool at the bottom plate, and were aligned along the plumes emerging from the boundary layer. The observations here were visually similar to boundary layer visualizations from DNS data. The Helium bubbles, due to their significantly lower density than liquid  $\text{SF}_6$ , moved towards the low pressure regions in the boundary layer which were the plume emitting zones. This technique can be used for visualizing the low pressure zones in the thermal boundary layer in a RBC experiment.

## 7.2 Outlook

### 7.2.1 Secondary Nucleation

In this work, secondary nucleation of cloud droplets and ice particles in the wake of a hot drop was observed experimentally under laboratory conditions. These observations and the subsequent analysis showed that such secondary nucleation mechanisms may play an important role in deep convective systems. To test this claim, these mechanisms have to be parameterized appropriately and then coupled with existing cloud models. Parameterization of this mechanism requires accurate information on all the flow variables. This requires a detailed DNS study of growing hailstones in a turbulent moist environment with appropriate micro-physics models. Later, these models should be incorporated into a cloud-resolving simulation or a LES of a deep convective system. Furthermore, a similar strategy should be followed to quantify the effects of the proposed cloud engineering technique. This can be complemented with a few field campaigns under suitable conditions. This may be a significant step towards cloud-engineering.

### 7.2.2 Laboratory-Scale Clouds

In the present work, we have established a laboratory-scale model for studying cloud formation using a SF<sub>6</sub>-He binary mixture. This model can be extended to study the effects of radiation on the nucleation process. This can be achieved by modifying the experiment to accommodate an infrared laser above the top plate. This laser radiation can mimic the insolation received by the Earth's atmosphere. Furthermore, the cloud model based on partially supersaturated and sub-saturated convection layers can be used for investigating the mixing process between moist-cloudy-air and the dry sub-saturated air. The side wall mirrors can be used for conducting PIV/PTV experiments. This would help in quantifying the experimental observations, and this can be compared against the DNS calculations by Kumar *et al* (2014) [145].

### 7.2.3 Moist Pattern Formation

The pattern formation studies have to be quantitatively compared against the existing theory. This requires the measurement of the thickness of the liquid layer at the top plate. This can be done using an interferometer. At present, the reflection from the bottom silicon plate dominates over the signal from the liquid layer at the top plate. This issue can be resolved by modifying the bottom plate such that the reflection from the bottom plate is minimal. Moreover, the lateral temperature gradient in the convection cell needs to be eliminated for a better comparison with the theoretical predictions. Improving the lateral side wall boundary conditions and the insulation on the lower side of the bottom plate may reduce the radial temperature gradient in the existing

convection cell. This calls for a new design of the convection cell with better insulations from the bottom and the lateral sides.



# List of Figures

1.1	(a) Developing cumulonimbus cloud near Goettingen. Photo taken on July 4, 2015 at 17:53 UTC. (b) Same cloud as in (a) but four minutes later. Image courtesy - Dr. Oliver Schlenczek, MPIDS, Goettingen. . . .	4
1.2	(a) Schematic of classical RBC. (b) Schematic of moist RBC. The arrows represent the LSC in the cell. . . . .	6
1.3	Variation of vapor pressure as function of temperature in supercooled water and ice [51, 52]. . . . .	10
2.1	A schematic representation of the experimental setup. (A) Main pressure vessel (B) Pressure regulation vessel (C) Pressure equilibration vessel (D) convection vessel inside the main pressure vessel. $\text{\textcircled{P}}$ represents the pressure gauge attached to the water and gas side of the experiment. The gas side is marked in yellow and the water side is marked in blue. . . . .	13
2.2	A schematic of the main pressure vessel. The two different water circuits are marked in different shades of blue. Arrows indicate the direction of the flowing water. PW - Sapphire pressure window, TT - Top plate thermistor, BT - bottom plate thermistors, CC - convection cell, SW - side wall of the convection cell, BP - bottom plate, TP - top plate, HC - heating coil. The different shades of blue separates the internal and the external water circuit. A more detailed account on the design is available in [74, 78] . . . . .	14
2.3	$T - P$ phase diagram of $\text{SF}_6$ . Solid black line represents the liquid-vapor coexistence line. $P_c$ and $T_c$ represent the critical pressure and temperature respectively. The data was obtained from the NIST database [80]. . . . .	17
2.4	Schematic representation of the phase diagram of $\text{SF}_6$ -He binary mixture. $\psi_{\text{He}}$ represents the mole fraction of helium in the mixture. The shaded region represents the two phase region for the red curve which corresponds to a certain concentration of He. . . . .	18
2.5	Schematic representation of the shadowgraph setup. . . . .	21

2.6	Schematic representation of the beam splitter setup. . . . .	23
2.7	Cross section of the mirror unit assembly. The lower blocks are colored in black and the upper blocks are semi-transparent. The mirrors are located at the interface between the lower and upper block. See Fig. 2.9 for scale. Image courtesy: Dr. Artur Kubitzek . . . . .	24
2.8	Schematic representation of the mirror unit flow visualization strategy. . . . .	24
2.9	Orthographic projection of the mirror unit. All dimensions are in mm. Image courtesy: Dr. Artur Kubitzek . . . . .	25
3.1	A schematic of the flow field inside the convection cell. The hatched region represents the lateral side walls. Grey region represent liquid SF <sub>6</sub> and the white region between the top and bottom plate represents SF <sub>6</sub> vapor . The arrows indicate large scale circulation in the vapor region. H - height of the cell, L - width of the cell, h - height of the liquid layer above the bottom plate . . . . .	28
3.2	Thick cell. $T_b = 22.00\text{ }^\circ\text{C}$ and $T_t < T_b$ . (a-c) Propagation of the contact line of the liquid layer below the top plate towards the center is marked using red arrows. (d-f) Propagation of the instability towards the center. (g-i) Break up of stripe and axisymmetric patterns into drops like deformations. Time stamp (in seconds) for each of these images is shown in the bottom right corner of the image. . . . .	30
3.3	Evolution of the liquid layer below the top plate in the thick cell at $T_b = 22.30\text{ }^\circ\text{C}$ , $T_t = 22.00\text{ }^\circ\text{C}$ and $P \approx 22.4\text{ bar}$ . Time (in seconds) for each of these figures is indicated on the bottom right corner. Please note that the time stamp indicates the time from (a) and not the absolute time in the experiment. (a-c) evolution of the secondary azimuthal mode from a primary drop. (d-f) breakup of an azimuthal mode into drop like structures. (g-i) loss in symmetry due to dripping. . . . .	31
3.4	Effect of $\Delta T$ on the patterns in the thick cell under steady conditions. $T_t = 24.00\text{ }^\circ\text{C}$ . (a) $\Delta T = 0.55\text{ }^\circ\text{C}$ , $P = 23.4\text{ bar}$ , (b) $\Delta T = 1.30\text{ }^\circ\text{C}$ , $P = 23.5\text{ bar}$ , (c) $\Delta T = 2.05\text{ }^\circ\text{C}$ , $P = 23.9\text{ bar}$ , (d) $\Delta T = 2.55\text{ }^\circ\text{C}$ , $P = 24.0\text{ bar}$ and (e) $\Delta T = 2.90\text{ }^\circ\text{C}$ , $P = 24.1\text{ bar}$ . Scale bar is shown in (b) for all images. . . . .	33
3.5	Thick cell - small $\Delta T$ : Arrangement of drops in the thin liquid layer at the top plate at $T_t = 28.00\text{ }^\circ\text{C}$ , $\Delta T = 0.55\text{ }^\circ\text{C}$ and $P = 25.5\text{ bar}$ . An isolated hexagonal cluster of drops is marked in red and an isolated linear arrangement (stripe) of drops is marked in green. . . . .	34

3.6	Thick cell - Formation of drops in the liquid layer at the top plate. (a, b) Deformation of the liquid film. (c, d) Deformations develop into drops. See Fig. 3.5 for the experimental conditions. . . . .	35
3.7	Thick cell: Sequence of images depicting the evolution of a drop in the liquid layer at the top plate. See Fig. 3.5 for experimental conditions. The red dot indicates the location where the drop was formed and the arrow indicates the drop under discussion. Time stamp in seconds is shown in the bottom right corner of each image. . . . .	36
3.8	Thick cell - Drifting of a drop in the liquid layer. See Fig. 3.5 caption for experimental conditions. The red dot indicates the location where the drop originated (Fig. 3.7(b)) and the arrow indicates the drop under discussion. Time stamp (continuation from Fig. 3.7) in seconds is shown in the bottom right corner of each image. . . . .	37
3.9	Displacement of the drop discussed in Fig. 3.7 & 3.8 from its origin as a function of time. . . . .	37
3.10	Merging of two drops (within the red oval) of nearly equal diameters. See Fig. 3.5 caption for experimental conditions. Time stamp in seconds is shown on the bottom right corner of each image. . . . .	38
3.11	Thick cell - (a-d) Merging of two drops of different sizes. (e-f) Post merger evolution of the drop. See Fig. 3.5 caption for experimental conditions. Time stamp in seconds is shown in the bottom right corner of each image.	38
3.12	Thick cell - large $\Delta T$ : Arrangement of drops in the liquid layer under the top plate in the thick cell at $T_t = 28.00^\circ\text{C}$ , $P = 26.6$ bar and $\Delta T = 3.00^\circ\text{C}$ . Red circle - a defect in the arrangement. . . . .	40
3.13	Thick cell: Drop arrangement processed over time. Each pixel represents the maximum intensity over a certain duration of time. See Fig. 3.12 for the experimental conditions. (a) Image processed over 3 seconds. (b) Image processed over 20 seconds. The arrows indicate the drift direction of the drops. . . . .	41
3.14	Thick cell - large $\Delta T$ - Temporal dynamics of a hexagonal patch in Fig. 3.12. See Fig. 3.12 for experimental details. . . . .	42
3.15	Intensity variation of a drop in Fig. 3.12 as a function of time . . . . .	43
3.16	(a) Averaged image from Fig. 3.13 (a). The circles mark some of the defects in the pattern. (b) Processed image with the identified drop centers. . . . .	43

3.17	2D power spectrum of the drop arrangement on the top plate in the large $\Delta T$ experiments. (a) 2D power spectrum of Fig. 3.16 at $t = 0$ . The arrows represent the wave vectors; (b) $t = 63$ seconds and (c) $t = 111$ seconds. . . . .	44
3.18	Inverse Fourier transform of the wave vectors marked in Fig. 3.17(a). The defect locations are marked in red and green. . . . .	44
3.19	Time lapse of the Fourier transform of a single wave vector. The time difference between each image is 100 ms. The green oval marks a defect location and the green arrow indicates the propagation direction of the defect. . . . .	45
3.20	Measurement overview - thick cell. $\bullet$ , $T_t$ ; $\bullet$ - $T_b$ . The thick black curve indicates the liquid-vapor coexistence curve for SF <sub>6</sub> and the line connecting the top and bottom plate conditions represent the pressure in the experiment. . . . .	46
3.21	Stationary state patterns under different conditions across the liquid-vapor coexistence curve. (a) $T_t = 22.00$ °C, $\Delta T = 3.00$ °C, $P = 23.1$ bar. (b) $T_t = 26.00$ °C, $\Delta T = 2.30$ °C, $P = 25.2$ bar.(c) $T_t = 30.00$ °C, $\Delta T = 3.00$ °C, $P = 27.9$ bar.(d) $T_t = 34.00$ °C, $\Delta T = 1.50$ °C, $P = 29.8$ bar.(e) $T_t = 38.00$ °C, $\Delta T = 1.00$ °C, $P = 32.5$ bar.(f) $T_t = 42.00$ °C, $\Delta T = 0.50$ °C, $P = 35.2$ bar. . . . .	46
3.22	Variation of mean distance between drops as a function of the top plate temperature. The inset shows the variation of capillary length as a function of temperature. Color code represents $\Delta T$ . . . . .	47
3.23	Variation of the pattern wavelength as a function of the top plate temperature. Color code represents $\Delta T$ . . . . .	48
3.24	Normalized (with capillary length) pattern wavelength as a function of the top plate temperature. Color code represents $\Delta T$ . . . . .	48
3.25	Dripping time period as a function of $T_t$ . Color code represents $\Delta T$ . . . .	49
3.26	Rayleigh Taylor instability - (a) gravity vs surface tension and viscosity (b) gravity vs Marangoni forces (c) gravity vs evaporation-condensation: upward arrows indicate condensation and downward arrows indicate evaporation. Dashed line represents the mean position of the interface. . . .	50
3.27	Dispersion curve - (a) gravity vs Marangoni forces (b) gravity vs evaporation-condensation . . . . .	53
3.28	Variation of non-dimensional wavenumbers obtained from the Fourier analysis of the experiments in Fig. 3.24 as a function of $T_t$ . The color code represents the $\Delta T$ . . . . .	56

3.29	Thin cell: Hexagonal arrangement of drops in the liquid layer below the top plate. $T_t = 24.00$ °C, $T_b = 32.00$ °C and $P = 23.7$ bars. The drop inside the red circle is an outcome of a merger event between 3 drops. The inset in the top left corner shows the 2D power spectrum of the hexagonal arrangement. . . . .	58
3.30	Formation of a large drop through coalescence. The red oval circumscribes the merging drops. The red arrow in (f) marks the formation of the new drop. Time stamp in seconds is indicated in the bottom right corner of each image. See Fig. 3.29 for experimental conditions. . . . .	59
3.31	Thin cell: Arrangement of drops in the liquid layer below the top plate. $T_t = 32.00$ °C, $T_b = 40.00$ °C and $P = 28.3$ bars. The inset on the bottom right corner shows the 2D power spectrum of the drop arrangement. . . .	61
3.32	Thin cell: Arrangement of drops in the liquid layer below the top plate. $T_t = 41.00$ °C, $T_b \approx 47.50$ °C and $P \approx 34.7$ bars. Image was acquired using the shadowgraph setup. . . . .	62
3.33	Thin cell: Arrangement of drops in the liquid layer below the top plate. $T_t = 41.00$ °C, $T_b \approx 48.5$ °C and $P \approx 34.8$ bars. Central portion has no drop like deformations. . . . .	63
3.34	Thin cell: Arrangement of drops in the liquid layer below the top plate. $T_t = 41.00$ °C, $T_b \approx 50$ °C and $P \approx 34.9$ bars. . . . .	64
3.35	Thin cell: Arrangement of drops in the liquid layer on the top plate. $T_t = 42.00$ °C, $T_b = 43.80$ °C and $P = 36.1$ bars. The bottom plate is covered with a layer of liquid SF <sub>6</sub> . . . . .	65
3.36	Medium cell - Effect of vapor pressure on the arrangement of drops in the liquid layer on the top plate. $T_t = 35.00$ °C, $T_b = 35.50$ °C. Pressure in (a) 433 psi, (b) 433.1 psi, (c) 433.2 psi, (d) 433.3 psi, (e) 433.4 psi and (f) 433.5 psi. . . . .	66
3.37	Medium cell: Arrangement of drops in the liquid layer on the top plate. $T_t = 35.00$ °C, $T_b = 49.00$ °C and $P = 445$ psi. No liquid layer on the bottom plate. . . . .	67
4.1	Schematic of the convection cell. Mirrors were embedded into the acrylic side walls. Only the two mirrors covering the lower half of the cell are shown for clarity. . . . .	76
4.2	Contrast enhanced image sequence highlighting the dynamics in the upper half of the cell. $T_t = 40.00$ °C, $T_b = 45.00$ °C and $P = 47.1$ bar. The time stamp (in ms) for each sub-figure is shown at the bottom-left corner. (a) and (b) shows the pinch-off instability and the formation of satellite drops. (c-o) nucleation in the wake of cold drop. . . . .	77

4.3	Contrast enhanced image sequence highlighting the dynamics in the upper half of the cell. $T_t = 36.00$ °C, $T_b = 45.00$ °C and $P = 44.9$ bar. The time stamp (in ms) for each sub-figure is shown at the bottom-right corner. . . . .	78
4.4	Contrast enhanced image sequence highlighting the dynamics in the upper half of the cell. $T_t = 38.00$ °C, $T_b = 45.00$ °C and $P = 45.8$ bar. The time stamp (in ms) for each sub-figure is shown at the bottom-right corner. . . . .	79
4.5	An image sequence depicting the nucleation of micro-droplets in the lower half of the cell. $T_t = 40.00$ °C, $T_b = 44.00$ °C and $P = 46.9$ bar. The time stamp (in ms) for each sub-figure is shown at the lower-right corner. The red bar on the left indicates the position of the liquid-vapor interface and is about 6 mm from the bottom plate. The details are discussed in the main text. . . . .	80
4.6	Contrast enhanced image sequence highlighting the dynamics in the lower half of the cell. $T_t = 40.00$ °C, $T_b = 44.00$ °C and $P = 46.9$ bar. The time stamp (in ms) for each sub-figure is shown at the bottom-right corner.	81
4.7	Variation in net change in Gibb's free energy due to the formation of a droplet of radius $r$ . $p$ is the partial vapor pressure in the ambient and $p_s$ is the saturation vapor pressure on a planar surface. $\Delta G^*$ is the energy barrier, $r_c$ is the critical radius. Adapted from [17] . . . . .	83
4.8	See facing page for caption. . . . .	91
4.8	Laboratory cloud - formation of a cloud layer in the lower half of the cell in the absence of a liquid layer on the bottom plate. $T_b = 45.00$ °C, $T_t = 36.00$ °C, $p = 44.9$ bar. The dark circular patches in the lower half of the image are the shadows of the drops attached to the top plate. See main text for description. The time stamp (in ms) is indicated at the lower-right corner of the image. . . . .	92
4.9	Time averaged image over 2150 frames ( $\approx 15$ seconds). The white dashed line vertically separates areas of supercritical (above) and subcritical saturation (below), and thus represents the average position of the base of the cloud layer. See the caption in Fig. 4.8 for the temperature and pressure conditions. . . . .	93
4.10	Köhler curves: Effect of solute (NaCl) diameter on saturation ratio in the neighbourhood of a solution droplet. The solute size is mentioned in the legend. A - a point in the stable leg of Köhler curve, B - a point in the unstable leg of Köhler curve. . . . .	96

5.1	Schematic of the experimental setup. A detailed description of the facility is provided in [23]. . . . .	102
5.2	Sodium chloride aerosol size distribution before injecting into the chamber. The total number concentration is about $10^5$ per $\text{cm}^3$ . . . . .	103
5.3	(a) Size selected NaCl aerosol size distribution. Number concentration $\approx 120$ per $\text{cm}^3$ . (b) Particle size distribution measured inside the chamber. Number concentrations: background $\approx 0.6$ per $\text{cm}^3$ , 200 nm aerosols $\approx 35$ per $\text{cm}^3$ . . . . .	103
5.4	Nucleation of water droplets in the wake of a hot drop under warm conditions. Ambient temperature $\approx 11$ °C, humidity $\approx 92\%$ . The drop temperatures are (a) 25 °C (b) 30 °C (c) 35 °C. The number concentration of the nuclei is about $1.8 \times 10^4$ per $\text{cm}^3$ . The images are contrast adjusted. . . . .	105
5.5	Nucleation of water droplets and ice particles in the wake of a hot drop under cold conditions. Ambient temperature $\approx -18$ °C, relative humidity $\approx 60\%$ . The drop temperatures are (a) 4 °C (b) 10 °C (c) 10 °C (d) $\approx 20$ °C (e) 50 °C. The number concentration of the nuclei was about $10^4$ per $\text{cm}^3$ in all cases except in (b). Number concentration of nuclei in (b) $\approx 10^3$ per $\text{cm}^3$ . . . . .	107
5.6	Mixing phase diagram under warm condition (Fig. 5.4). ■ - ambient condition ( $T = 11$ °C, RH = 92%). The blue curve represents the saturation vapor pressure curve for liquid water. The conditions at the surface of the drop is marked in filled circles (●) of various colors and the corresponding mixing line is represented by a line connecting ● and ■: ● - 35 °C, ● - 30 °C, ● - 25 °C, ● - 20 °C. . . . .	109
5.7	Saturation ratio along the mixing line plotted in Fig. 5.6. The conditions at the surface of the drop is marked in filled circles (●) of various colors and the corresponding mixing line is represented by a curve connecting ● (of different colors) and ■: ● - 35 °C, ● - 30 °C, ● - 25 °C, ● - 20 °C. The black horizontal line indicates saturation ratio = 1. . . . .	110
5.8	Effect of drop temperature on the growth of a droplet in its wake. $U_d = 3$ m/s, $r_s = 22$ nm. . . . .	113
5.9	Variation of saturation ratio encountered by a Lagrangian fluid parcel in the wake of hot drop at various temperatures. $U_d = 3$ m/s, $r_s = 22$ nm . . . . .	114
5.10	The growth of droplets with different nucleus radii in the wake of a 30 °C drop falling at a velocity of 3 m/s. . . . .	114

5.11	Effect of drop velocity on the growth of a droplet in the wake of the drop. Drop temperature is set to 30 °C and $r_s = 22$ nm. RH in the ambient is 92%. . . . .	115
5.12	The effect of temperature and velocity decay rates on the growth of a droplet in the wake of a hot drop. Drop temperature: 30 °C, $r_s = 22$ nm. . . . .	116
5.13	Comparison of model A with other decay rates. Drop temperature: 30 °C, $r_s = 22$ nm. . . . .	118
5.14	Mixing phase diagram under cold condition (Fig. 5.5). ■ - ambient condition ( $T = -18$ °C, RH = 60%). The conditions at the surface of the drop is marked in filled circles (●) of various colors and the corresponding mixing line is represented by a line connecting the drop conditions with the ambient conditions. ● 20 °C, ● 10 °C, ● 4 °C, ● 1 °C. . . . .	119
5.15	Saturation ratio along the mixing line plotted in Fig. 5.14. ● 20 °C, ● 10 °C, ● 4 °C, ● 1 °C. . . . .	120
5.16	Effect of drop temperature on the growth of a droplet in its wake under cold conditions. $U_d = 3$ m s <sup>-1</sup> , $r_s = 22$ nm . . . . .	122
5.17	Variation of ice supersaturation as a function of ambient temperature. The red curve represents the ambient ice supersaturation and the blue curve represents the maximum ice supersaturation in the wake of a hail/graupel in wet growth mode obtained from the mixing model. . . . .	125
5.18	Effect of velocity of the drop on the growth of a droplet in the wake. $r_s = 50$ nm, $S_{ambienet} = 0.1\%$ , drop diameter = 2 mm, drop temperature = 0 °C, ambient tempertaure = -5 °C. . . . .	125
5.19	Köhler's curve for a snomax aerosol with $r_s = 50$ nm. A - dynamic critical radius for $S_a = 0.1\%$ , B - equilibrium haze droplet radius. The red line indicates the ambient supersaturation. . . . .	127
6.1	Schematic of a drop fragmentation. (a) Initial drop (b) pancake drop due to the pressure forces (c) rim formation (d) bag instability and (e) bag break-up. . . . .	132
6.2	Image sequence of a SF <sub>6</sub> drop fragmentation in a SF <sub>6</sub> -He atmosphere. $T_b = 45.00$ °C, $T_t = 36.00$ °C, P= 44.9 bar. The red dashed line separates the supersaturated region from the sub-saturated region. See main text for description. The time stamp (in ms) is indicated in the bottom right corner of the image. $S$ is the saturation ratio. . . . .	132
6.3	Image sequence of a SF <sub>6</sub> drop in a supersaturated SF <sub>6</sub> -He atmosphere. $T_b = 44.00$ °C, $T_t = 36.00$ °C, P= 44.3 bar. The green line marks the position of the liquid-vapor interface. The time difference between each frame is about 22 ms. . . . .	133

6.4	Thin cell - effect of pressure on the drops on the top plate. (a) $T_b = 40.00\text{ }^\circ\text{C}$ , $\Delta T = 8.00\text{ }^\circ\text{C}$ , $P = 28.4\text{ bar}$ (b) $T_b = 40.00\text{ }^\circ\text{C}$ , $\Delta T = 4.00\text{ }^\circ\text{C}$ , $P = 31.1\text{ bar}$ (c) $T_b = 40.00\text{ }^\circ\text{C}$ , $\Delta T = 4.00\text{ }^\circ\text{C}$ , $P = 31.4\text{ bar}$ (d) $T_b = 40.00\text{ }^\circ\text{C}$ , $\Delta T = 4.00\text{ }^\circ\text{C}$ , $P = 31.7\text{ bar}$ . . . . .	135
6.5	Dynamics of drops in the Leidenfrost regime. (1) ring drop, (2) big chimney, (3) a small chimney, (4) liquid bridge before the merging of two drops and (5) exit of a chimney. The time stamp (in seconds) is indicated in the bottom right corner of the image. . . . .	136
6.6	Boiling of a drop. (1) Location where boiling started. The time stamp (in seconds) is indicated in the bottom right corner of the image. The time stamp represents the number of seconds from Fig 6.5(a). . . . .	137
6.7	Formation of large drops with chimney. See text for details. 1) Merged drops exhibiting capillary oscillations. 2) Formation of chimney in a few sufficiently large drops. 3) Exit of chimney from a drop. 4) Merging of small chimney with a large chimney. 5) Merging of two chimneys of similar dimensions. The time stamp represents the number of seconds from Fig 6.5(a). . . . .	138
6.8	Schematic representation of $\text{SF}_6$ -He boundary layer visualization. 1. accumulated Helium bubbles, 2. a drop from the top plate, 3. nucleated Helium bubbles. . . . .	140
6.9	Boundary layer visualization: (a) $T_t = 44.50\text{ }^\circ\text{C}$ , $T_b = 44.95\text{ }^\circ\text{C}$ , $P = 53.9\text{ bars}$ , $\psi_{\text{He}} \approx 32\%$ . Image courtesy Dr. Winkel. [78] (b) $T_t = 43.00\text{ }^\circ\text{C}$ , $T_b = 45.00\text{ }^\circ\text{C}$ , $P = 49.2\text{ bars}$ , $\psi_{\text{He}} \approx 25\%$ . (1) Top plate instability, (2) accumulated Helium bubbles, (3) nucleated $\text{SF}_6$ droplets due to isobaric cooling from the cold drop. . . . .	141
6.10	$T_t = 40.00\text{ }^\circ\text{C}$ , $T_b = 44.00\text{ }^\circ\text{C}$ , $P = 48.3\text{ bars}$ , $\psi_{\text{He}} \approx 28\%$ . Side view: portion of the image above the red line, top view: portion of the image below the red line. The time stamps (in ms) are indicated on the bottom left corner. The green line on the right side indicates the position of the liquid-vapor interface in the side view. . . . .	142
6.11	Side view. $T_t = 40.00\text{ }^\circ\text{C}$ , $T_b = 44.00\text{ }^\circ\text{C}$ , $P = 47.0\text{ bars}$ , $\psi_{\text{He}} \approx 26\%$ . The arrows mark the Helium bubbles formed from the cold drop. The time stamps (in ms) are indicated on the bottom right corner. . . . .	143
6.12	$T_t = 43.00\text{ }^\circ\text{C}$ , $T_b = 45.00\text{ }^\circ\text{C}$ , $P = 49.2\text{ bars}$ , $\psi_{\text{He}} \approx 25\%$ . The arrows mark the falling drops and the Helium bubbles formed from these drops. The time stamps (in ms) are indicated on the top right corner. . . . .	144
7.1	(a) Laboratory-scale cloud layer (between the red lines). (b) Clouds in Goettingen. . . . .	148



# Bibliography

- [1] R. Narasimha. ‘Cumulus clouds and convective boundary layers: a tropical perspective on two turbulent shear flows’. *Journal of Turbulence* 13 (2012), N47.
- [2] P Prasanth. ‘Direct numerical simulation of transient cumulus cloud flow’. PhD thesis. JNCASR, 2014.
- [3] C. Barnett. *Rain: A natural and cultural history*. Broadway Books, 2015.
- [4] B. C. Deva. *Indian music*. Taylor & Francis, 1995.
- [5] H. Le Treut. ‘Historical overview of climate change’. *Climate Change 2007: The Physical Science Basis. Contribution of Working Group I to the Fourth Assessment Report of the Intergovernmental Panel on Climate Change* (2007).
- [6] R. A. Kerr. ‘Clouds appear to be big, bad player in global warming’. *Science* 325.5939 (2009), pp. 376–376.
- [7] J. R. Norris, R. J. Allen, A. T. Evan, M. D. Zelinka, C. W. O’dell and S. A. Klein. ‘Evidence for climate change in the satellite cloud record’. *Nature* 536.7614 (2016), pp. 72–75.
- [8] E. Bodenschatz, S. P. Malinowski, R. A. Shaw and F. Stratmann. ‘Can we understand clouds without turbulence?’ *Science* 327.5968 (2010), pp. 970–971.
- [9] R. Narasimha, S. S. Diwan, S. Duvvuri, K. Sreenivas and G. Bhat. ‘Laboratory simulations show diabatic heating drives cumulus-cloud evolution and entrainment’. *Proceedings of the National Academy of Sciences* 108.39 (2011), pp. 16164–16169.
- [10] S. Gadgil and S. Gadgil. ‘The Indian monsoon, GDP and agriculture’. *Economic and Political Weekly* (2006), pp. 4887–4895.
- [11] S. Gadgil and K. R. Kumar. ‘The Asian monsoon—agriculture and economy’. In: *The Asian Monsoon*. Springer, 2006, pp. 651–683.
- [12] R. A. Shaw. ‘Particle-turbulence interactions in atmospheric clouds’. *Annual Review of Fluid Mechanics* 35.1 (2003), pp. 183–227.
- [13] J. T. Houghton. *Climate change 1995: The science of climate change: contribution of working group I to the second assessment report of the Intergovernmental Panel on Climate Change*. Vol. 2. Cambridge University Press, 1996.
- [14] R. T. Watson, M. C. Zinyowera and R. H. Moss. *Climate change 1995. Impacts, adaptations and mitigation of climate change: scientific-technical analyses*. 1996.
- [15] V Ramaswamy, O Boucher, J Haigh, D Hauglustine, J Haywood, G Myhre, T Nakajima, G. Shi and S Solomon. ‘Radiative forcing of climate’. *Climate change* 349 (2001).

## Bibliography

- [16] R. A. Houze Jr. *Cloud dynamics*. Vol. 104. Academic press, 2014.
- [17] J. M. Wallace and P. V. Hobbs. *Atmospheric science: an introductory survey*. Vol. 92. Elsevier, 2006.
- [18] M. K. Yau and R. Rogers. *A short course in cloud physics*. Elsevier, 1996.
- [19] S. S. Diwan, P. Prasanth, K. Sreenivas, S. Deshpande and R. Narasimha. ‘Cumulus-type flows in the laboratory and on the computer: simulating cloud form, evolution, and large-scale structure’. *Bulletin of the American Meteorological Society* 95.10 (2014), pp. 1541–1548.
- [20] K. K. Chandrakar, W. Cantrell, K. Chang, D. Ciochetto, D. Niedermeier, M. Ovchinnikov, R. A. Shaw and F. Yang. ‘Aerosol indirect effect from turbulence-induced broadening of cloud-droplet size distributions’. *Proceedings of the National Academy of Sciences* 113.50 (2016), pp. 14243–14248.
- [21] J. Voigtländer, D. Niedermeier, H. Siebert, R. Shaw, J. Schumacher and F. Stratmann. ‘LACIS-T-A humid wind tunnel for investigating the Interactions between Cloud Microphysics and Turbulence’. In: *EGU General Assembly Conference Abstracts*. Vol. 19. 2017, p. 6475.
- [22] R. Wagner, H. Bunz, C. Linke, O. Möhler, K.-H. Naumann, H. Saathoff, M. Schnaiter and U. Schurath. ‘Chamber simulations of cloud chemistry: the AIDA Chamber’. In: *Environmental simulation chambers: application to atmospheric chemical processes*. Springer, 2006, pp. 67–82.
- [23] K Chang, J Bench, M Brege, W. Cantrell, K Chandrakar, D. Ciochetto, C. Mazzoleni, L. Mazzoleni, D Niedermeier and R. Shaw. ‘A Laboratory Facility to Study Gas–Aerosol–Cloud Interactions in a Turbulent Environment: The II Chamber’. *Bulletin of the American Meteorological Society* 97.12 (2016), pp. 2343–2358.
- [24] A. Pandey, J. D. Scheel and J. Schumacher. ‘Turbulent superstructures in Rayleigh–Bénard convection’. *Nature communications* 9.1 (2018), p. 2118.
- [25] J.-Q. Zhong, D. Funfschilling and G. Ahlers. ‘Enhanced heat transport by turbulent two-phase Rayleigh–Bénard convection’. *Physical review letters* 102.12 (2009), p. 124501.
- [26] E. Knobloch. *Pattern Formation and Dynamics in Nonequilibrium Systems*. 2010.
- [27] A. M. Turing. ‘The chemical basis of morphogenesis’. *Phil. Trans. R. Soc. Lond. B* 237.641 (1952), pp. 37–72.
- [28] M. Cross and H. Greenside. *Pattern formation and dynamics in nonequilibrium systems*. Cambridge University Press, 2009.
- [29] E. Bodenschatz, W. Pesch and G. Ahlers. ‘Recent developments in Rayleigh–Bénard convection’. *Annual review of fluid mechanics* 32.1 (2000), pp. 709–778.
- [30] G. L. Brown and A. Roshko. ‘On density effects and large structure in turbulent mixing layers’. *Journal of Fluid Mechanics* 64.4 (1974), pp. 775–816.
- [31] P. G. Drazin and W. H. Reid. *Hydrodynamic stability*. Cambridge university press, 2004.
- [32] L. Rayleigh. ‘Investigation of the character of the equilibrium of an incompressible heavy fluid of variable density.’ *Proc. London Math. Soc.* 14 (1883), pp. 170–177.
- [33] G. I. Taylor. ‘The instability of liquid surfaces when accelerated in a direction perpendicular to their planes. I’. *Proc. R. Soc. Lond. A* 201.1065 (1950), pp. 192–196.
- [34] M Fermigier, L. Limat, J. Wesfreid, P Boudinet and C Quiliet. ‘Two-dimensional patterns in Rayleigh–Taylor instability of a thin layer’. *Journal of Fluid Mechanics* 236 (1992), pp. 349–383.

## Bibliography

- [35] S. Chandrasekhar. *Hydrodynamic and hydromagnetic stability*. Courier Corporation, 2013.
- [36] P Brunet, G Gauthier, L Limat and D Vallet. ‘Structure and dynamics of a bidimensional pattern of liquid columns’. *Experiments in fluids* 37.5 (2004), pp. 645–652.
- [37] A. Oron, S. H. Davis and S. G. Bankoff. ‘Long-scale evolution of thin liquid films’. *Reviews of modern physics* 69.3 (1997), p. 931.
- [38] A. Sharma and E Ruckenstein. ‘An analytical nonlinear theory of thin film rupture and its application to wetting films’. *Journal of colloid and interface science* 113.2 (1986), pp. 456–479.
- [39] C. Pirat, C Mathis, P Maissa and L Gil. ‘Structures of a continuously fed two-dimensional viscous film under a destabilizing gravitational force’. *Physical review letters* 92.10 (2004), p. 104501.
- [40] L Limat, P. Jenffer, B Dagens, E Touron, M Fermigier and J. Wesfreid. ‘Gravitational instabilities of thin liquid layers: dynamics of pattern selection’. *Physica D: Nonlinear Phenomena* 61.1-4 (1992), pp. 166–182.
- [41] R. J. Deissler and A. Oron. ‘Stable localized patterns in thin liquid films’. *Physical review letters* 68.19 (1992), p. 2948.
- [42] J. M. Burgess, A. Juel, W. McCormick, J. Swift and H. L. Swinney. ‘Suppression of dripping from a ceiling’. *Physical review letters* 86.7 (2001), p. 1203.
- [43] M. Bestehorn and D. Merkt. ‘Regular surface patterns on Rayleigh-Taylor unstable evaporating films heated from below’. *Physical review letters* 97.12 (2006), p. 127802.
- [44] H. Pruppacher and J. Klett. *Microphysics of Clouds and Precipitation*. Springer, 2010.
- [45] V. J. Schaefer. ‘The production of ice crystals in a cloud of supercooled water droplets’. *Science* 104.2707 (1946), pp. 457–459.
- [46] B. Vonnegut. ‘The nucleation of ice formation by silver iodide’. *J. Appl. Phys.* 18.7 (1947), pp. 593–595.
- [47] I Langmuir. ‘The production of rain by a chain reaction in cumulus clouds at temperatures above freezing’. *J. Meteorol.* 5.5 (1948), pp. 175–192.
- [48] E. B. Kraus and P. Squires. ‘Experiments on the stimulation of clouds to produce rain’. *Nature* 159 (1947), pp. 489–491.
- [49] B. Mason. ‘Personal reflections on 35 years of cloud seeding’. *Contemp. Phys.* 23.4 (1982), pp. 311–327.
- [50] A. J. Heymsfield, P. C. Kennedy, S. Massie, C. Schmitt, Z. Wang, S. Haimov and A. Rangno. ‘Aircraft-induced hole punch and canal clouds: Inadvertent cloud seeding’. *Bulletin of the American Meteorological Society* 91.6 (2010), pp. 753–766.
- [51] Vapor pressure of liquid water -  $\exp(54.842763 - 6763.22/T - 4.210 * \log(T) + 0.000367 * T + \tanh(0.0415 * (T - 218.8)) * (53.878 - 1331.22./T - 9.44523 * \log(T) + 0.014025 * T))$ , vapor pressure of ice -  $\exp(9.550426 - 5723.265./T + 3.53068 * \log(T) - 0.00728332 * T)$ .
- [52] M. Stumpf. ‘DNS of flow around a falling ice ball with heat and mass transfer’. MA thesis.
- [53] P. R. Field, R. P. Lawson, P. R. Brown, G. Lloyd, C. Westbrook, D. Moisseev, A. Miltenberger, A. Nenes, A. Blyth, T. Choulaton et al. ‘Secondary ice production: Current state of the science and recommendations for the future’. *Meteorological Monographs* 58 (2017), pp. 7–1.
- [54] P. V. Hobbs and A. L. Rangno. ‘Ice particle concentrations in clouds’. *Journal of the atmospheric sciences* 42.23 (1985), pp. 2523–2549.

## Bibliography

- [55] S. Mossop. ‘Secondary ice particle production during rime growth: The effect of drop size distribution and rimer velocity’. *Quarterly Journal of the Royal Meteorological Society* 111.470 (1985), pp. 1113–1124.
- [56] W. Cantrell and A. Heymsfield. ‘Production of ice in tropospheric clouds: A review’. *Bulletin of the American Meteorological Society* 86.6 (2005), pp. 795–808.
- [57] J Hallett and S. Mossop. ‘Production of secondary ice particles during the riming process’. *Nature* 249.5452 (1974), p. 26.
- [58] Y. Y. Dong and J. Hallett. ‘Droplet accretion during rime growth and the formation of secondary ice crystals’. *Quarterly Journal of the Royal Meteorological Society* 115.485 (1989), pp. 127–142.
- [59] A. J. Heymsfield and S. Mossop. ‘Temperature dependence of secondary ice crystal production during soft hail growth by riming’. *Quarterly Journal of the Royal Meteorological Society* 110.465 (1984), pp. 765–770.
- [60] R. Oraltay and J. Hallett. ‘Evaporation and melting of ice crystals: A laboratory study’. *Atmospheric Research* 24.1-4 (1989), pp. 169–189.
- [61] Y. Dong, R. G. Oraltay and J. Hallett. ‘Ice particle generation during evaporation’. *Atmospheric research* 32.1-4 (1994), pp. 45–53.
- [62] L. Vardiman. ‘The generation of secondary ice particles in clouds by crystal–crystal collision’. *Journal of the Atmospheric Sciences* 35.11 (1978), pp. 2168–2180.
- [63] C. A. Knight. ‘Ice growth from the vapor at - 5 C’. *Journal of the Atmospheric Sciences* 69.6 (2012), pp. 2031–2040.
- [64] T. Leisner, T Pander, P Handmann and A Kiselev. ‘Secondary ice processes upon heterogeneous freezing of cloud droplets’. In: *14th Conf. on Cloud Physics and Atmospheric Radiation*. 2014.
- [65] W. L. Woodley, G. Gordon, T. J. Henderson, B. Vonnegut, D. Rosenfeld and A. Detwiler. ‘Aircraft-produced ice particles (APIPs): additional results and further insights’. *Journal of Applied Meteorology* 42.5 (2003), pp. 640–651.
- [66] P. V. Hobbs and A. L. Rangno. ‘Rapid development of high ice particle concentrations in small polar maritime cumuliform clouds’. *Journal of the Atmospheric Sciences* 47.22 (1990), pp. 2710–2722.
- [67] R. P. Lawson, S. Woods and H. Morrison. ‘The microphysics of ice and precipitation development in tropical cumulus clouds’. *Journal of the Atmospheric Sciences* 72.6 (2015), pp. 2429–2445.
- [68] A. Heymsfield and P. Willis. ‘Cloud conditions favoring secondary ice particle production in tropical maritime convection’. *Journal of the Atmospheric Sciences* 71.12 (2014), pp. 4500–4526.
- [69] A. Fridlind, A. Ackerman, G McFarquhar, G Zhang, M. Poellot, P. DeMott, A. Prenni and A. Heymsfield. ‘Ice properties of single-layer stratocumulus during the Mixed-Phase Arctic Cloud Experiment: 2. Model results’. *Journal of Geophysical Research: Atmospheres* 112.D24 (2007).
- [70] N Fukuta and H. J. Lee. ‘A numerical study of the supersaturation field around growing graupel’. *Journal of the atmospheric sciences* 43.17 (1986), pp. 1833–1843.
- [71] J. E. Dye and P. Hobbs. ‘The influence of environmental parameters on the freezing and fragmentation of suspended water drops’. *Journal of the Atmospheric Sciences* 25.1 (1968), pp. 82–96.

## Bibliography

- [72] P. V. Hobbs and R. J. Cheng. ‘Microdroplets and water drop freezing’. *Science* 173.3999 (1971), pp. 849–850.
- [73] A. Gagin and H. Nozyce. ‘The nucleation of ice crystals during the freezing of large supercooled drops’. *Journal de recherches atmosphériques* 18.2 (1984), pp. 119–129.
- [74] B. B. Plapp. ‘Spiral pattern formation in Rayleigh-Bénard convection’ (1997).
- [75] K. E. Daniels. *Pattern formation and dynamics in inclined layer convection*. Cornell University, 2002.
- [76] S. Weiß, G. Seiden and E. Bodenschatz. ‘Pattern formation in spatially forced thermal convection’. *New Journal of Physics* 14.5 (2012), p. 053010.
- [77] J. McCoy. ‘Adventures in pattern formation: spatially periodic forcing and self-organization’ (2007).
- [78] F. Winkel. ‘On Turbulent Rayleigh-Bénard Convection in a Two-Phase Binary Gas Mixture’. PhD thesis. Georg-August University, 2015.
- [79] J. R. de Bruyn, E. Bodenschatz, S. W. Morris, S. P. Trainoff, Y. Hu, D. S. Cannell and G. Ahlers. ‘Apparatus for the study of Rayleigh-Bénard convection in gases under pressure’. *Review of scientific instruments* 67.6 (1996), pp. 2043–2067.
- [80] M. M. E.W. Lemmon and D. Friend. “*Thermophysical Properties of Fluid Systems*” in *NIST Chemistry WebBook, NIST Standard Reference Database Number 69*, Eds. P.J. Linstrom and W.G. Mallard, National Institute of Standards and Technology, Gaithersburg MD, 20899.
- [81] J. de Swaan Arons and G. Diepen. ‘Gas—Gas Equilibria’. *The Journal of Chemical Physics* 44.6 (1966), pp. 2322–2330.
- [82] P. Ye, A. Bertelsmann, R. H. Heist, B. N. Hale and M. Kulmala. ‘Nucleation of sulfur hexafluoride’. In: *AIP Conference Proceedings*. Vol. 534. 1. AIP. 2000, pp. 19–22.
- [83] W. Kay. ‘Liquid-vapor phase equilibrium relations in the ethane-n-heptane system’. *Industrial & Engineering Chemistry* 30.4 (1938), pp. 459–465.
- [84] Phantom 65 Gold Camera, Vision Research.
- [85] G. S. Settles. ‘Schlieren and shadowgraph techniques: visualizing phenomena in transparent media, Experimental Fluid Mechanics’. *Springer, Berlin and Heidelberg, DOI 10* (2001), pp. 978–3.
- [86] S. Weiss. ‘Pattern Formation in Spatially Forced Thermal Convection’. PhD thesis. Georg-August University, 2009.
- [87] G. Ahlers, S. Grossmann and D. Lohse. ‘Heat transfer and large scale dynamics in turbulent Rayleigh-Bénard convection’. *Reviews of modern physics* 81.2 (2009), p. 503.
- [88] S. G. Yiantsios and B. G. Higgins. ‘Rayleigh-Taylor instability in thin viscous films’. *Physics of Fluids A: Fluid Dynamics* 1.9 (1989), pp. 1484–1501.
- [89] G. Batchelor. ‘An introduction to fluid’. *Dynamics. Cambridge University* (1967).
- [90] L. Gary Leal. *Advanced Transport Phenomena*. 2007.
- [91] S. VanHook. ‘SJ VanHook, MF Schatz, JB Swift, WD McCormick, and HL Swinney, J. Fluid Mech. 345, 45 (1997).’ *J. Fluid Mech.* 345 (1997), p. 45.

## Bibliography

- [92] F Chillà and J Schumacher. ‘New perspectives in turbulent Rayleigh-Bénard convection’. *The European Physical Journal E* 35.7 (2012), p. 58.
- [93] D. Quéré. ‘Leidenfrost dynamics’. *Annual Review of Fluid Mechanics* 45 (2013), pp. 197–215.
- [94] J. W. Cahn and J. E. Hilliard. ‘Free energy of a nonuniform system. I. Interfacial free energy’. *The Journal of chemical physics* 28.2 (1958), pp. 258–267.
- [95] D. Zwicker, A. A. Hyman and F. Juelicher. ‘Suppression of Ostwald ripening in active emulsions’. *Physical Review E* 92.1 (2015), p. 012317.
- [96] C. F. Bohren and B. A. Albrecht. *Atmospheric Thermodynamics*. Oxford University Press, New York, 1998.
- [97] J. Feder, K. C. Russell, J. Lothe and G. M. Pound. ‘Homogeneous Nucleation and Growth of Droplets in Vapours’. *Adv. Phys.* 15 (1966), pp. 111–178.
- [98] J. B. Zeldovich. ‘On the Theory of New Phase Formation, Cavitation’. *Acta Physicochimica URSS* 18 (1943), pp. 1–22.
- [99] R. P. Sear. ‘Nucleation: theory and applications to protein solutions and colloidal suspensions’. *Journal of Physics: Condensed Matter* 19.3 (2007), p. 033101.
- [100] V. I. Kalikmanov. ‘Classical nucleation theory’. In: *Nucleation theory*. Springer, 2013, pp. 17–41.
- [101] D. Lamb and J. Verlinde. *Physics and chemistry of clouds*. Cambridge University Press, 2011.
- [102] C. Guder and W. Wagner. ‘A Reference Equation of State for the Thermodynamic Properties of Sulfur Hexafluoride (SF<sub>6</sub>) for Temperatures from the Melting Line to 625 K and Pressures up to 150 MPa’. *J. Phys. Chem. Ref. Data* 38 (2009), pp. 33–94.
- [103] Material parameters of SF<sub>6</sub> at  $T = 42^\circ\text{C}$ :  $p_s = 34.715\text{ bar}$ ,  $\rho_l = 1053.7\text{ kg/m}^3$ ,  $\rho_v = 445.05\text{ kg/m}^3$ ,  $M = 146.0554\text{ g/mol}$ ,  $\sigma = 0.1629\text{ mN/m}$ .
- [104] A. Boushehri, J. Bzowski, J. Kestin and E. A. Mason. ‘Equilibrium and Transport Properties of Eleven Polyatomic Gases At Low Density’. *J. Phys. Chem. Ref. Data* 16 (1987), pp. 445–466.
- [105] S. Whitaker. ‘Forced convection heat transfer correlations for flow in pipes, past flat plates, single cylinders, single spheres, and for flow in packed beds and tube bundles’. *AIChE Journal* 18.2 (1972), pp. 361–371.
- [106] M. B. de Stadler, N. R. Rapaka and S. Sarkar. ‘Large eddy simulation of the near to intermediate wake of a heated sphere at  $\text{Re} = 10,000$ ’. *Int. J. Heat Fluid Flow* 49 (2014), pp. 2–10.
- [107] AMS. *Glossary of Meteorology*. [http://glossary.ametsoc.org/wiki/Main\\_Page](http://glossary.ametsoc.org/wiki/Main_Page).
- [108] D. Rosenfeld and W. L. Woodley. ‘Deep convective clouds with sustained supercooled liquid water down to  $-37.5^\circ\text{C}$ ’. *Nature* 405.6785 (2000), pp. 440–442.
- [109] R Clift and W. Gauvin. ‘Motion of entrained particles in gas streams’. *Can. J. Chem. Eng.* 49.4 (1971), pp. 439–448.
- [110] R. Rasmussen, V Levizzani and H. Pruppacher. ‘A wind tunnel and theoretical study on the melting behavior of atmospheric ice particles: III. Experiment and theory for spherical ice particles of radius  $\leq 500\ \mu\text{m}$ ’. *J. Atmos. Sci* 41.3 (1984), pp. 381–388.
- [111] B. J. Mason. ‘On the melting of hailstones’. *Q. J. R. Meteorol. Soc.* 82.352 (1956), pp. 209–216.
- [112] K. Lehmann, H. Siebert and R. A. Shaw. ‘Homogeneous and inhomogeneous mixing in cumulus clouds: Dependence on local turbulence structure’. *J. Atmos. Sci* 66.12 (2009), pp. 3641–3659.

## Bibliography

- [113] M. Petters and S. Kreidenweis. ‘A single parameter representation of hygroscopic growth and cloud condensation nucleus activity’. *Atmospheric Chemistry and Physics* 7.8 (2007), pp. 1961–1971.
- [114] D. Rose, S. Gunthe, E Mikhailov, G. Frank, U. Dusek, M. O. Andreae and U. Pöschl. ‘Calibration and measurement uncertainties of a continuous-flow cloud condensation nuclei counter (DMT-CCNC): CCN activation of ammonium sulfate and sodium chloride aerosol particles in theory and experiment’. *Atmospheric Chemistry and Physics* 8.5 (2008), pp. 1153–1179.
- [115] B. Morton, G. I. Taylor and J. S. Turner. ‘Turbulent gravitational convection from maintained and instantaneous sources’. *Proc. R. Soc. Lond. A* 234.1196 (1956), pp. 1–23.
- [116] P. Bagchi and K. Kottam. ‘Effect of freestream isotropic turbulence on heat transfer from a sphere’. *Physics of Fluids* 20.7 (2008), p. 073305.
- [117] J. Turner. ‘Turbulent entrainment: the development of the entrainment assumption, and its application to geophysical flows’. *Journal of Fluid Mechanics* 173 (1986), pp. 431–471.
- [118] R Narasimha. ‘The utility and drawbacks of traditional approaches’. In: *Whither Turbulence? Turbulence at the Crossroads*. Springer, 1990, pp. 13–48.
- [119] M. Kotouč, G. Bouchet and J. Dušek. ‘Transition to turbulence in the wake of a fixed sphere in mixed convection’. *Journal of Fluid Mechanics* 625 (2009), pp. 205–248.
- [120] C Hoose and O Möhler. ‘Heterogeneous ice nucleation on atmospheric aerosols: a review of results from laboratory experiments’. *Atmospheric Chemistry and Physics*, 12, 9817–9854 (2012).
- [121] H. Wex, S. Augustin-Bauditz, Y. Boose, C. Budke, J. Curtius, K. Diehl, A. Dreyer, F. Frank, S. Hartmann, N. Hiranuma et al. ‘Intercomparing different devices for the investigation of ice nucleating particles using Snomax® as test substance’. *Atmospheric Chemistry and Physics* 15.3 (2015), pp. 1463–1485.
- [122] S Hartmann, S Augustin, T Clauss, H Wex, T Šantl-Temkiv, J Voigtländer, D Niedermeier and F Stratmann. ‘Immersion freezing of ice nucleation active protein complexes’. *Atmospheric Chemistry and Physics* 13.11 (2013), pp. 5751–5766.
- [123] T. Koop and B. Zobrist. ‘Parameterizations for ice nucleation in biological and atmospheric systems’. *Physical Chemistry Chemical Physics* 11.46 (2009), pp. 10839–10850.
- [124] N. Nix and N. Fukuta. ‘Nonsteady-state kinetics of droplet growth in cloud physics’. *Journal of the Atmospheric Sciences* 31.5 (1974), pp. 1334–1343.
- [125] B. A. Baker. ‘On the nucleation of ice in highly supersaturated regions of clouds’. *Journal of the atmospheric sciences* 48.16 (1991), pp. 1904–1907.
- [126] R. M. Rasmussen and A. J. Heymsfield. ‘Melting and shedding of graupel and hail. Part III: Investigation of the role of shed drops as hail embryos in the 1 August CCOPE severe storm’. *Journal of the atmospheric sciences* 44.19 (1987), pp. 2783–2803.
- [127] G. Lesins and R. List. ‘Sponginess and drop shedding of gyrating hailstones in a pressure-controlled icing wind tunnel’. *Journal of the atmospheric sciences* 43.23 (1986), pp. 2813–2825.
- [128] V. T. Phillips, A. Khain, N. Benmoshe and E. Ilotoviz. ‘Theory of time-dependent freezing. Part I: Description of scheme for wet growth of hail’. *Journal of the Atmospheric Sciences* 71.12 (2014), pp. 4527–4557.

## Bibliography

- [129] A. J. Heymsfield and C. Westbrook. ‘Advances in the estimation of ice particle fall speeds using laboratory and field measurements’. *Journal of the Atmospheric Sciences* 67.8 (2010), pp. 2469–2482.
- [130] J. D. Locatelli and P. V. Hobbs. ‘Fall speeds and masses of solid precipitation particles’. *Journal of Geophysical Research* 79.15 (1974), pp. 2185–2197.
- [131] M. Kajikawa. ‘Observation of the falling motion of early snow flakes’. *Journal of the Meteorological Society of Japan. Ser. II* 60.2 (1982), pp. 797–803.
- [132] P. J. DeMott, A. J. Prenni, X. Liu, S. M. Kreidenweis, M. D. Petters, C. H. Twohy, M. Richardson, T. Eidhammer and D. Rogers. ‘Predicting global atmospheric ice nuclei distributions and their impacts on climate’. *Proceedings of the National Academy of Sciences* 107.25 (2010), pp. 11217–11222.
- [133] B. Murray, D O’sullivan, J. Atkinson and M. Webb. ‘Ice nucleation by particles immersed in supercooled cloud droplets’. *Chemical Society Reviews* 41.19 (2012), pp. 6519–6554.
- [134] W. A. Cooper. ‘A possible mechanism for contact nucleation’. *Journal of the Atmospheric Sciences* 31.7 (1974), pp. 1832–1837.
- [135] E. Villerraux and B. Bossa. ‘Single-drop fragmentation determines size distribution of raindrops’. *Nature Physics* 5.9 (2009), p. 697.
- [136] E. Villerraux. ‘Fragmentation’. *Annu. Rev. Fluid Mech.* 39 (2007), pp. 419–446.
- [137] M. Szakáll, K. Diehl, S. K. Mitra and S. Borrmann. ‘A wind tunnel study on the shape, oscillation, and internal circulation of large raindrops with sizes between 2.5 and 7.5 mm’. *Journal of the Atmospheric Sciences* 66.3 (2009), pp. 755–765.
- [138] M. Szakáll, S. K. Mitra, K. Diehl and S. Borrmann. ‘Shapes and oscillations of falling raindrops—A review’. *Atmospheric research* 97.4 (2010), pp. 416–425.
- [139] P. V. Hobbs and A. L. Rangno. ‘Super-large raindrops’. *Geophysical research letters* 31.13 (2004).
- [140] A.-L. Biance, C. Clanet and D. Quéré. ‘Leidenfrost drops’. *Physics of Fluids* 15.6 (2003), pp. 1632–1637.
- [141] A La Porta, G. A. Voth, F Moisy and E. Bodenschatz. ‘Using cavitation to measure statistics of low-pressure events in large-Reynolds-number turbulence’. *Physics of Fluids* 12.6 (2000), pp. 1485–1496.
- [142] S. Wagner, O. Shishkina and C. Wagner. ‘Boundary layers and wind in cylindrical Rayleigh–Bénard cells’. *Journal of Fluid Mechanics* 697 (2012), pp. 336–366.
- [143] O. Shishkina and C. Wagner. ‘Analysis of sheet-like thermal plumes in turbulent Rayleigh–Bénard convection’. *Journal of Fluid Mechanics* 599 (2008), pp. 383–404.
- [144] B. A. Puthenveetil and J. H. Arakeri. ‘Plume structure in high-Rayleigh-number convection’. *Journal of Fluid Mechanics* 542 (2005), pp. 217–249.
- [145] B. Kumar, J. Schumacher and R. A. Shaw. ‘Lagrangian mixing dynamics at the cloudy–clear air interface’. *Journal of the Atmospheric Sciences* 71.7 (2014), pp. 2564–2580.

# Acknowledgment

First and foremost, I would like to thank my advisor Prof. Eberhard Bodenschatz, for his continuous support and encouragement during the last four years. His ability to combine and compare ideas/thoughts from various scientific disciplines stands him out as a scientist. It was a great learning experience working with him. Although he was a very busy person, he always made time for his students. I would like to thank Stephan Weiss for all his help during the last three years. His help with setting up the apparatus was invaluable. His cheerfulness and optimism make him an excellent person to collaborate with. I enjoyed discussing a wide variety of topics with him, ranging from turbulent convection to political philosophy. I would like to acknowledge the contribution of Alexei Krekhov on the theoretical aspects of my work. I am thankful to him for introducing me to nucleation theory and binary phase diagrams. I thank Eberhard, Stephan, and Alexei for proof-reading parts of my thesis.

The work presented in this thesis involves collaboration with groups outside Goettingen. I thank Dr. Alain Pumir from Lyon for all the interesting discussions over the years. I thank Prof. Raymond Shaw and Prof. Will Cantrell for hosting me at Michigan Tech. University. It was a great learning experience visiting their group and conducting the ice nucleation experiments in their cloud chamber facility.

I would like to thank Angela for her help during my early days in Goettingen.

The experiments reported here would not have succeeded without the help from the technical staff of our Institute. I would like to thank Dr. Artur Kubitzek for helping me with the design of the mirror unit for the experiment and also for interacting with the machine shop on my behalf. I would like to thank Andreas Renner, Andreas Kopp and Marcel Meyer for all their help and support in the experimental hall. I would like to thank Mr. Schminke and his team for fabricating the mirror unit, and Mr. Kleinhans from MPIBPC for helping with the aluminum coating on the polished acrylic surfaces for the mirrors. I would like to thank Greg Kinney and Kamalkant Chandrakar for helping with the experiments in Michigan. I would like to thank Holger and Florian for introducing me to the very high-pressure convection experimental setup. I would like to thank Gerhard for his help with the computers and softwares in the past four years.

Special thanks to all my friends and peers with whom I had the chance to interact over

the last four years. Many thanks to Jan for all the fun-filled Volleyball and badminton games; Martin and Vineesh for all the entertaining discussions (most notably - cricket, constitution and politics) and amazing home cooked Kerala cuisine; Martin, Kaumudi, Lukas, Jan, Maddy, Dennis, Smrithika and Estefania for all the interesting trips over the years; Laura for all her help in the last four years and also for informing me about all the new gossips; Albert and John for all the entertaining bowling sessions; Gabriele and Lukas for accompanying me to the gym. Special thanks to our lunch/coffee group over the years including Guus, Johannes, Soda, John, Xuan, Dhawal, Marcel, Mohsen, Freja, Antonio, Nadine, Christian Kuechler, Olga, Christian Westendorf, Holly, Torsten, Hiu Fai for all the entertaining discussions. I thank Oliver for answering some of my trivial questions related to atmosphere and clouds. I would like to thank Freja and Martin for their valuable inputs on a portion of my thesis. I would like to thank Dr. Michael Wilczek for his lectures and interesting discussions in the last few years. I would like to thank Marco, Katharina and Maren for letting me use their chemical hood. I would like to thank Isabella and Azam for all the interesting discussions over the last four years. I would like to thank Yong for all the exciting ping-pong evenings. Special thanks to Lukas, Estefania and Christian for all those memorable kicker afternoons. Special thanks to Maddy, Parry, and Jasmina for all the wonderful weekend parties.

I would like to thank my friends from the badminton club (RSV Goettingen) at Geismar - Heiko, Uschi, Frederike, Detlef, Guni, Hemanth, Anil and Lena for all the interesting games over the years. I would like to thank Ashish Rajput for his help over the last three years.

I thank my thesis committee members - Prof. Andreas Tilgner and Prof. Jens Niemeyer for their help and support. I would like to thank Frauke Bergmann (PBCS/GGNB) for her help over the years. I acknowledge the IMPRS travel grant over the years for attending various conferences. I would like to thank Prof. Roddam Narasimha for all the interesting discussions on turbulence, clouds, jets, and wall-bounded flows over these years. These discussions have helped me develop a better understanding of turbulent flows. Lastly, I would like to thank my family in India for all their support over the years.

# Curriculum Vitae

## Research Interests

---

- Cloud physics, Fluid dynamics

## Education

---

- **Georg-August-Universität** Göttingen, Germany.  
*Ph.D Student, Physics* **2014 - present**  
**Thesis: Moist Convection**
- **Jawaharlal Nehru Centre for Advanced Scientific Research (JNCASR)** Bangalore, India.  
*Master of Science (Engg.), Engineering Mechanics* **2010 - 2014**  
**Thesis: DNS of transient cumulus cloud flows.**  
**CGPA: 7.75/8.0**
- **National Institute of Technology, Tiruchirappalli (NIT T)** Tiruchirappalli, India.  
*Bachelor of Technology, Mechanical Engineering* **2006 - 2010**  
**CGPA: 8.58/10.0**

## Research Experience

---

- **PhD**, Max Planck Institute for Dynamics and Self-Organization, Göttingen Sept. 2014 - present  
**Mentor:** Prof. Dr. E. Bodenschatz  
**Topic:** Nucleation and pattern formation in turbulent moist convection
- **Research Assistant**, Engineering Mechanics Unit (EMU), JNCASR Aug. 2013 - Aug. 2014  
**Mentor:** Prof. R. Narasimha  
**Topic:** Episodic entrainment in a turbulent jet.
- **MS Thesis, JNCASR** Aug. 2010 - Jan. 2014  
**Mentor:** Prof. R. Narasimha, Prof. S. M. Deshpande  
**Topic:** Direct Numerical Simulation (DNS) of transient cumulus cloud flows.
- **Summer Research Fellow, Indian Inst. Tech. (IIT) Madras** May 2009 - Jul. 2009  
**Mentor:** Prof. N.R. Panchapakesan  
**Topic:** Flow inside a 3D lid driven cylindrical cavity.

## Publications

---

### Journal Articles (Peer reviewed articles)

- **P. Prabhakaran**, S. Weiss, A. Krekhov, A. Pumir and E. Bodenschatz, “Can Hail and Rain Nucleate Cloud Droplets?”, *Phy. Rev. Lett.* **119**, 128701 (2017): **Editor’s suggestion, Featured in Physics - Focus article: Drops Falling in Clouds Make More Drops, *Physics* 10, 104**
- Sourabh S Diwan, **P. Prasanth**, K. R. Sreenivas, S. M. Deshpande and R. Narasimha, “Cumulus flows in the laboratory and on the computer: Simulating cloud form, evolution and structure”, *Bulletin of the American Meteorological Society* **95 (10)**, 1541-1548 (2014)

### Conferences

- **P. Prabhakaran**, S. Weiss, A. Krekhov, A. Pumir and E. Bodenschatz: Can Hail and Rain Nucleate Cloud Droplets?. *Bull. Am. Phy. Soc.* 2017

- **P. Prabhakaran**, S. Weiss, A. Krekhov, A. Pumir and E. Bodenschatz: Convecting Cloud Chamber. *Compressible Convection* 2017, Lyon
- S. Shinde, **P. Prabhakaran**, and R. Narasimha: On the outer flow field and episodic entrainment in a round turbulent jet. *Bull. Am. Phy. Soc.* 2016
- **P. Prabhakaran**, S. Weiss, A. Krekhov, H. Nobach, E. Bodenschatz: Pattern-Formation in Moist Turbulent Rayleigh-Bénard Convection. *Bull. Am. Phy. Soc.* 2016
- **P. Prabhakaran**, S. M. Deshpande, and R. Narasimha: Direct Numerical Simulation of Transient Cumulus Flows. *Bull. Am. Phy. Soc.* 2013

---

### Skills

- Programming languages - Matlab, C, C++, Fortran in parallel environments using MPI and OPENMP.
- Visualization tools - Paraview, Tecplot, python

---

### Workshops/Meetings

- Transport of particles in turbulent flows: Experimental, computational and theoretical investigations, 14-18 Oct. 2013, Bangalore.
- Mathematical perspectives on clouds, climate and tropical meteorology, 22 - 26 Jan. 2013, Bangalore.
- Defining guidelines for future extreme simulations of three-dimensional fluid and magnetohydrodynamics, 12 - 16 Dec. 2011, Bangalore.

---

### Teaching Experience

- Co-instructor, Faculty of Physics, Georg-August-Universität, Göttingen  
Current question in turbulence research (Winter 2016/17)
- Teaching Assistant, Faculty of Physics, Georg-August-Universität, Göttingen  
Analytical mechanics (Summer 2016)  
Numerical methods in fluid mechanics (Summer 2016)
- Offered a set of informal lectures on “Introduction to Computational Fluid Dynamics” for the summer students (summer 2011) at EMU, JNCASR, Bangalore.

---

### Awards & Fellowships

- Max Planck Fellowship (Sept. 2014 - Present)
- ICAM Junior Travel Award: 66<sup>th</sup> Annual Meeting of the APS - DFD, Pittsburgh, USA, 2013
- Summer Research Fellowship, Department of Aerospace Engineering, IIT Madras, 2009